ZSoil

for geotechnics & structures

THE HARDENING SOIL MODEL
A PRACTICAL GUIDEBOOK

Report 100701

(revised 2.01.2020)

R. Obrzud
A. Truty

GeoDev.

PO Box CH-1001 Lausanne
Switzerland
https://zsoil.com

Contents

List of Symbols

Stress and Strain Notation

ε	strain
ε_v	volumetric strain $= (\varepsilon_1 + \varepsilon_2 + \varepsilon_3)$
γ_s	shear strain
σ	stress
τ	shear stress
p	total mean stress $= \frac{1}{3}(\sigma_1 + \sigma_2 + \sigma_3)$
p'	mean effective stress
q	deviatoric stress $= \frac{1}{\sqrt{2}}[(\sigma_1 - \sigma_2)^2 + + (\sigma_2 + \sigma_3)^2 + (\sigma_3 - \sigma_1)^2]^{1/2}$

Roman Symbols

s_{u}	undrained shear strength
E_0	maximal soil stiffness
e_0	initial void ratio
E_{oed}	tangent oedometric modulus
E_{50}	secant modulus corresponding to 50% of q_f
E_{ur}	unloading-reloading stiffness
G_0	(or G_{max}) maximal small-strain shear modulus
K_0	coefficient of *in situ* earth pressure "at rest" ($K_0 > K_0^{\mathsf{NC}}$ for $\mathrm{OCR} > 1$)
K_0^{NC}	coefficient of earth pressure "at rest" of normally-consolidated soil
K_0^{SR}	stress reversal K_0 coefficient defining stress point position at intersection between hardening mechanisms
q^{POP}	($=\sigma'_{v0} + \sigma'_c$) preoverburden pressure
B_q	pore pressure parameter for CPTU
c	cohesion intercept
c^*	intercept for M^* slope in $q - p'$ plane ($=6c\cos\phi/(3 - \sin\phi)$)
C_c	slope of the normal compression line in $\log_{10}$ scale ($=2.3\lambda$)
C_k	coefficient of curvature ($=d_{30}^2/(d_{10} \cdot d_{60})$
C_N	overburden correction factor for SPT N_{60}-value
C_r	slope of unload-reload consolidation line in $\log_{10}$ scale
C_u	coefficient of uniformity ($=d_{60}/d_{10}$)
D	scaling parameter (by default =1.0 for HS-Std, =0.25 for HS-SmallStrain)
D_r	relative density
E	Young's modulus
e	void ratio
E_D	dilatometer modulus ($= 34.7(p_1 - p_0)$)
e_{max}	maximal void ratio
f_t	limit tensile strength
G	tangent shear modulus
G_{ur}	unload-reload shear modulus
G_s	secant shear modulus
H	parameter which defines the rate of the volumetric plastic strain
I_D	dilatometer material index ($= (p_1 - p_0)/(p_0 - u_0)$)
I_P	plasticity index ($= w_L - w_P$)
K_D	dilatometer horizontal stress index ($= (p_0 - u_0)/\sigma'_{v0}$)
M	parameter of HS model which defines the shape of the cap surface
m	stiffness exponent for minor stress formulation
M^*	(or M_c^*) slope of critical state line ($= 6\sin\phi'_c/(3 - \sin\phi'_c)$)
M_e^*	slope of critical state line ($= 6\sin\phi'_c/(3 + \sin\phi'_c)$)
M_{DMT}	constrained modulus derived from the Marchetti's dilatometer
M_{D}	one-dimensional drained constrained modulus

m_p	stiffness exponent for p'-formulation
p_0	corrected first DMT reading
p_1	corrected second DMT reading
p_a	atmospheric pressure (average sea-level pressure is 101.325 kPa)
p_c	effective preconsolidation pressure in terms of mean stress
p_{co}	initial effective preconsolidation pressure
q_a	asymptotic deviatoric stress
q_c	cone resistance
q_f	deviatoric stress at failure
Q_t	normalized cone resistance for CPT
q_t	corrected cone resistance
R_f	failure ratio ($= q_f/q_a$)
u	pore pressure
V_s	shear wave velocity
w_L	liquid limit
w_n	water content
w_P	plastic limit
z	depth
OCR	overconsolidation ratio ($= \sigma'_c/\sigma'_{vo}$)
PI	plasticity index

Greek Symbols

γ^{PS}	plastic strain hardening parameter for deviatoric mechanism
γ_{SAT}	saturated unit weight
γ_D	dry unit weight
γ_s	shear strain
γ_w	water unit weight
$\gamma_{0.7}$	value of small strain for which G_s/G_0 reduces to 0.722
κ	slope of unload-reload consolidation line in $\ln$ scale
Λ	plastic volumetric strain ratio ($= 1 - \kappa/\lambda$)
λ	slope of primary consolidation line in $\ln$ scale
ν	Poisson's coefficient
ν_{ur}	unloading/reloading Poisson's coefficient
ϕ	friction angle
ϕ'_c	effective friction angle from compression test
ϕ'_e	effective friction angle from extension test
ϕ'_{cs}	critical state friction angle
ϕ'_m	mobilized friction angle
ϕ'_{tc}	effective friction angle determined from triaxial compression test
ψ	dilatation angle
ψ_m	mobilized dilatation angle
ρ	soil density
σ^{ref}	reference stress
σ'_c	effective vertical preconsolidation stress
σ_L	minimal limit minor stress

Abbreviations

CK$_o$UC	K_o consolidated undrained compression
CK$_o$UE	K_o consolidated undrained extension
CAP	Cap model with Drucker-Prager failure criterion
CIDC	consolidated isotropic drained compression
CIUC	consolidated isotropic undrained compression
CIUE	consolidated isotropic undrained extension
CPTU	cone penetration test with pore pressure measurements (electric piezocone)
CSL	critical state line
DMT	Marchetti dilatometer test
DSS	direct simple shear
FVT	field vane test
HS-Brick	Hardening Soil-Brick model
HS-small	Hardening Soil-small model
HS-standard	Hardening Soil-standard model
MC	Mohr-Coulomb model
MCC	Modified Cam clay model
NCL	normal consolidation line
OED	oedometric test
PMT	pressuremeter test
SBPT	self-boring pressuremeter test
SCPT	static penetration test with seismic sensor
SLS	serviceability limit state analysis
SPT	standard penetration test
TC	triaxial compression

UCS	unified classification system
ULS	ultimate limit state analysis

Sign convention: Throughout this report, the sign convention is the standard convention of soil mechanics, i.e. compression is assigned as positive.

FAQs

1. When should the HS model be applied and what are its advantages?
2. Which formulation to describe the stress dependent stiffness should be chosen?
3. How to migrate stiffness moduli between two different formulations for stress dependent stiffness?
4. How to set model parameters for an "undrained" simulation?
5. How to troubleshoot convergence problem at the initial state analysis?
6. What is a typical ratio $E_{\text{ur}}^{\text{ref}}/E_{50}^{\text{ref}}$?
7. What is a typical ratio $E_{\text{oed}}^{\text{ref}}/E_{50}^{\text{ref}}$?
8. What are typical parameter ranges?
9. Why do three different ratios K_0, K_0^{SR} and K_0^{NC} have to be defined in order to run a simulation with the HS model?
10. What should be specified in $\sigma_{\text{oed}}^{\text{ref}}$ cell?
11. What should be specified in σ_{ref} cell?
12. What is the difference between preconsolidation defined with OCR and q^{POP}?
13. When should I activate the small strain extension?
14. How to identify model parameters?
15. What is the suggested parameter identification sequence?
16. How to use the Virtual Lab v2023 ?

Chapter 1

Introduction

The use of the finite element analysis has become widespread and popular in geotechnical practice as a mean of controlling and optimizing engineering tasks. However, the quality of any prediction depends on the adequate model adopted in the study. In general, a more realistic prediction of ground movements requires using the models which account for pre-failure behavior of soil. Such behavior, mathematically modeled with non-linear elasticity, is characterized by a strong variation of soil stiffness which depends on the magnitude of strain levels occurring during construction stages. Pre-failure stiffness plays a crucial role in modeling typical geotechnical problems such as deep excavations supported by diaphragm walls or tunnel excavations in densely built-up urban areas.

The present study completes the ZSoil® report elaborated by Truty (2008) on the **Hardening Soil models**. It includes also the new **Hardening Soil-Brick** (HS-Brick) version (available in ZSoil® since 2020), after Cudny and Truty (2020), which eliminates important drawbacks (see discussion by Niemunis and Cudny (2018)) of the small strain overlay by Benz (2007) used in the original **Hardening Soil-small** (HS-small) model.

The objectives of the present report can be summarized as follows:

- to highlight the need of using advanced constitutive models in **daily engineering practice**;
- to recall the **main features of the Hardening Soil model** and to **facilitate understanding** its mathematical background;
- to provide to practicing engineers who foresee using the Hardening Soil model with a helpful guideline on specifying an appropriate testing program or making use of already acquired experimental results in order to **identify or estimate model parameters**;
- to show importance of using the Hardening Soil model in typical geotechnical analyses such as shallow footing, retaining wall excavation and tunnel excavation in an urban area;
- to compare predictions obtained with the HS-standard, HS-small and HS-Brick models

1.1 Why do we need small strain extension in the HS model?

It is commonly known that soil behavior is not as simple as its prediction with a simply-formulated linear constitutive models which are commonly used in numerical analyses. Complex soil behavior which stems from the nature of the multi-phase material, exhibits both elastic and plastic non-linearities and, deformations include irreversible plastic strains. Depending on the history of loading, soil may contract or dilate, its stiffness may depend on the magnitude of stress levels, soil deformations are time-dependent, etc. In fact, soil behavior for a given stress level is considered to be truly elastic in the range of small strains as schematically presented in Figure 1.1. In this strain range, soil may exhibit a nonlinear stress-strain relationship. However, its stiffness is almost fully recoverable in unloading conditions. In the aftermath of pre-failure non-linearities of soil behavior, one may observe a strong variation of stiffness starting from very small shear strains, which cannot be reproduced by models such as linear-elastic Mohr-Coulomb model (see Figure 1.2).

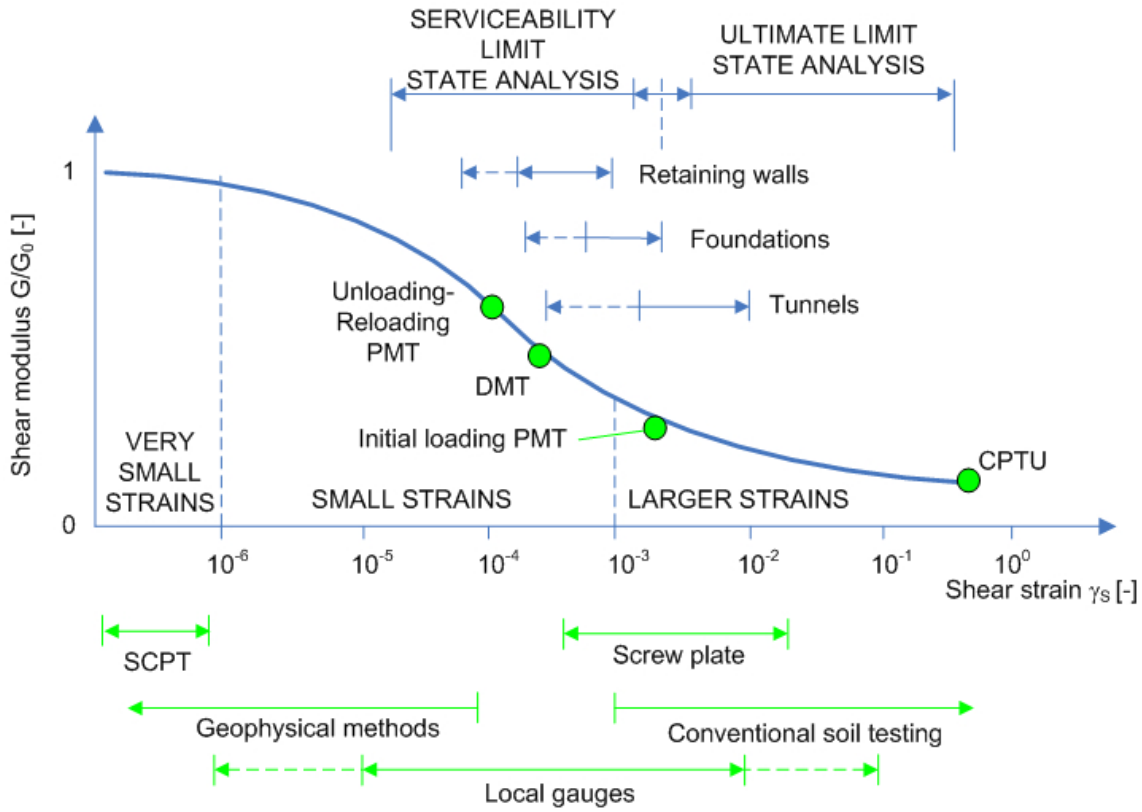

Figure 1.1: Typical representation of stiffness variation in function of the shear strain amplitudes; comparison with the ranges for typical geotechnical problems and different tests (based on Atkinson and Sallfors, 1991, and updated be the author); SCPT - seismic cone penetration test; CPTU - piezocone penetration test; DMT - Marchetti's dilatometer test; PMT - Pressuremeter test.

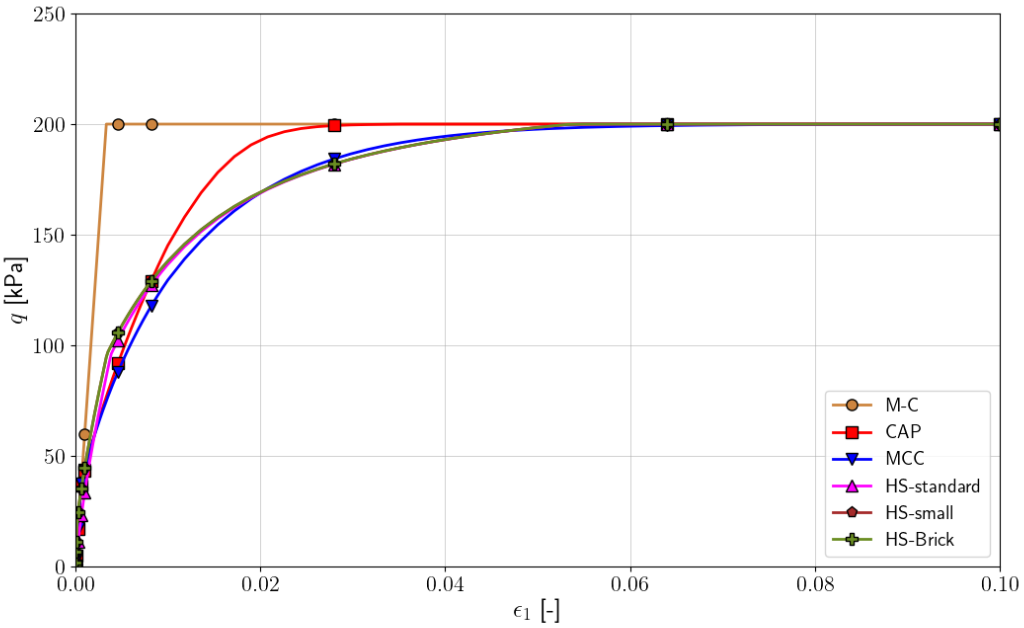

(a) Shear characteristics $q - \varepsilon_1$

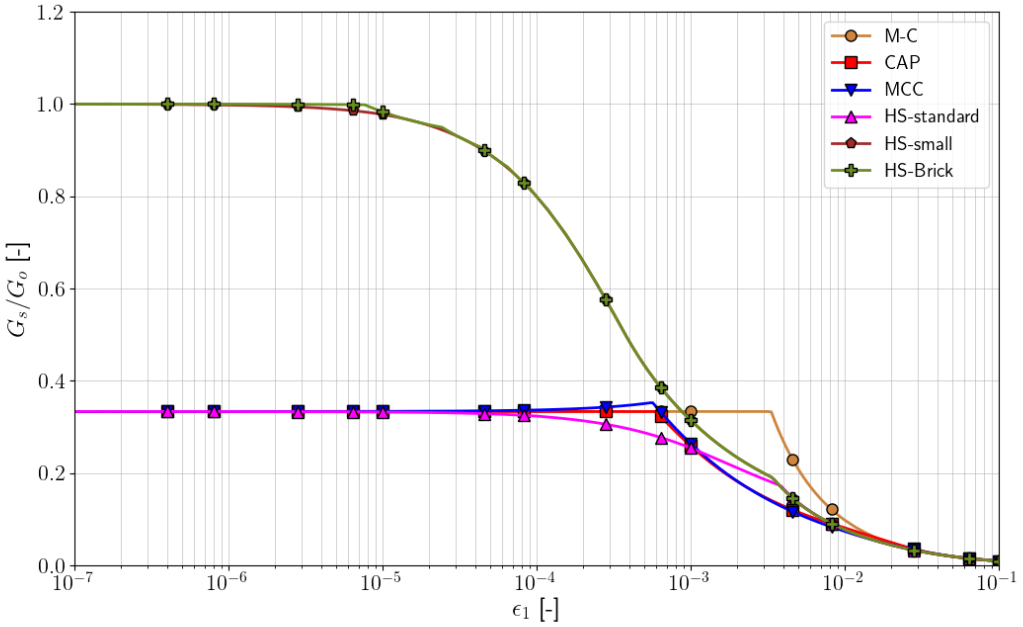

(b) Normalized secant shear stiffness characteristics $G_s/G_o - \varepsilon_1$

Figure 1.2: Comparison of different model responses for drained triaxial compression condition using equivalent parameters and OCR =1.2

Engineers who are looking for reliable predictions of the engineering system response should be aware that by applying linear-elastic, perfectly plastic models in the finite element analysis, soil ground movements may be underestimated, which may influence the magnitude of efforts which are computed in supporting structural elements. The models which account for high stiffness at very small strains concentrate the development of high amplitudes of strain around the close neighborhood of the source of deformations similarly to what is observed in reality. This can be the case of braced excavations (e.g. Figure 1.4) or tunnel excavations (e.g. Figure 1.3) where the varying stiffness increases soil deformations at the unloading boundaries, appropriately reducing them away from the unloaded zone (Addenbrooke et al., 1997). Furthermore, it is often observed in numerical analyses that not differentiating between loading and unloading stiffness moduli in the Mohr-Coulomb model may result in an unrealistic lifting of the diaphragm wall, associated with unloading of the bottom of the excavation (see e.g. Figure 1.4(c)).
The Hardening Soil model in its three variants HS-standard, HS-small and HS-Brick can be a remedy for modeling problems which have been listed above, as they account for most of soil behavior features (see Section 2). Despite the mathematical complexity of the HS model, its parameters have explicit physical meaning and can be determined with conventional soil tests. **There is no difference in parameters estimation between HS-small and HS-Brick models**.

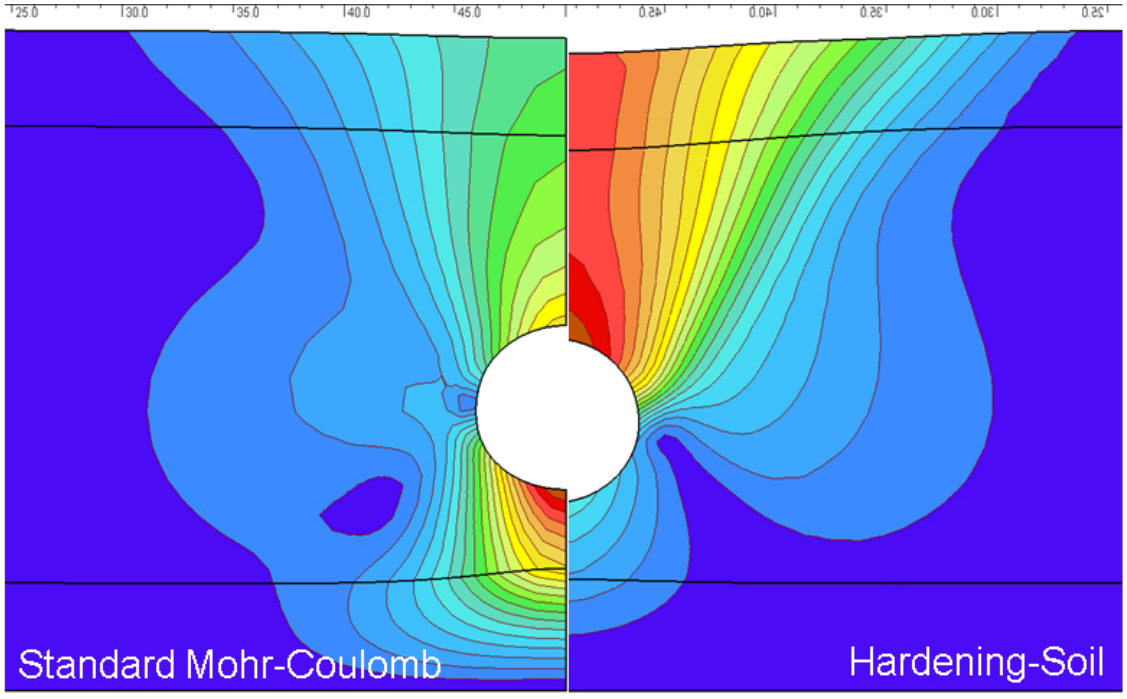

Figure 1.3: Typical model response to the excavation problem using the standard Mohr-Coulomb on the left (unrealistic dominant heaving of the tunnel's bottom) and the Hardening-Soil model on the right (a realistic trough above the tunnel).

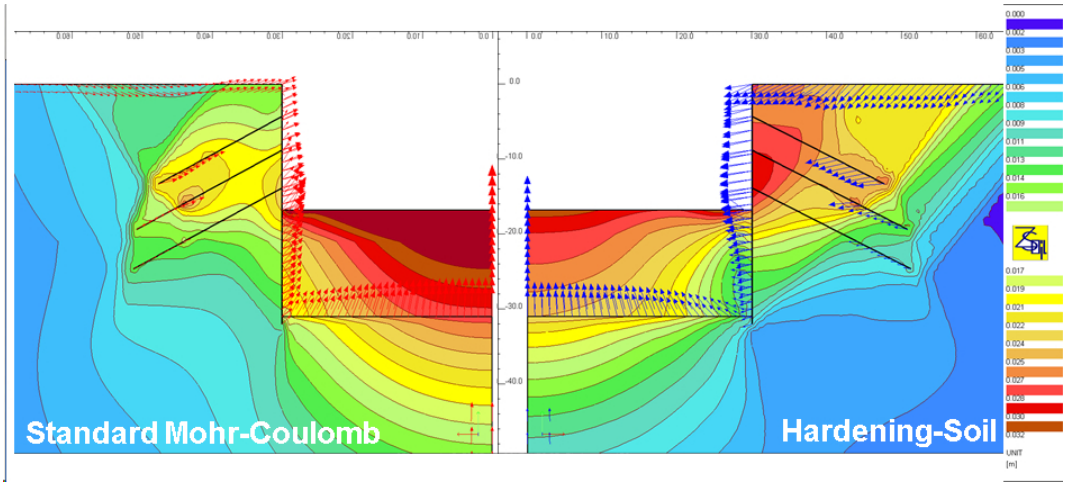

(a)

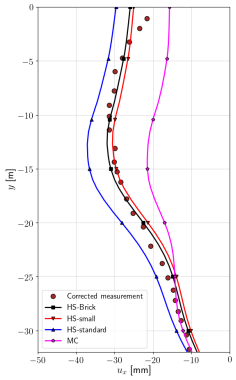

(b)

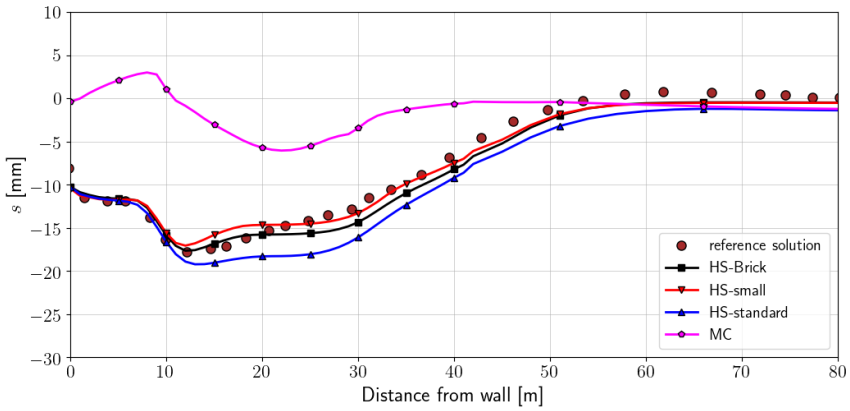

(c)

Figure 1.4: An example of deep excavation in Berlin Sand (after Truty, 2008). Comparison of model predictions: (a) Hardening-Soil vs Standard Mohr-Coulomb model, (b) wall deflections, (c) surface settlements.

Model	Analysis	SANDS	SILTS		CLAYS		
			Dilatant	Non-dilatant	Degree of overconsolidation		
			Low compressible	Compressible	High Stiff clays	Low	Normal Soft clays
Mohr-Coulomb (Drucker-Prager)	SLS						
	ULS	C	D		D		
CAP	SLS	D	D	D	D	C	C
	ULS					C	C
Modified Cam-Clay	SLS			D		C	C
	ULS			C		C	C
HS-standard	SLS					A	A
	ULS	A	A	A	A	A	A
HS-small	SLS	B	B	B	B	B	B
	ULS	A	A	A	A	A	A
HS-Brick	SLS	A	A	A	A	A	A
	ULS	A	A	A	A	A	A

Figure 1.5: Recommendations for the model choice for different soils and two type analyzes: Serviceability Limit State (SLS) and Ultimate Limit State (ULS). Meaning of rating: (A) recommended, (B) recommended except situations when small strain reversals may occur and transient analyses, (C) can be used, (D) can be used but not recommended in terms of quality of results, empty grid cell means not applicable

1.2 Application fields of constitutive models

The finite element code ZSoil® includes soil models from simple linear elastic, perfectly plastic (e.g. Mohr-Coulomb), elasto-plastic cap models (e.g. Cap, Modified Cam Clay) to advanced nonlinear-elasto-plastic cap model HS-small (ZACE, 2010). Table 1.1 summarizes each class of models in terms of basic model attributes. The table includes the main model features, failure criteria, hardening laws, and a comparison of required and corresponding soil parameters. It can be noticed that different models require a specification of different material properties. However, most of them are common to all presented models.

The choice of a constitutive model depends on many factors but, in general, it is related to the type of analysis that the user intends to perform (e.g. ultimate limit state analysis (ULS) or serviceability limit state analysis (SLS)), expected precision of predictions and available knowledge of the soil. In general, SLS analysis requires an application of advanced constitutive models which predict the stress-strain relation more accurately than simple linear-elastic, perfectly plastic models. A perceived general applicability of constitutive models is schematically proposed in Figure 1.5.
It should be emphasized that the classical HS-small model was used in the past and still can be used to carry out SLS analyses. However, this must be done with caution. In certain cases due to small strain reversals the model strain history can be reset causing significant stiffness overshooting. This may lead to severe underestimation of deformations. The HS-Brick model behavior is superior with respect to the HS-small one, moreover it is theoretically much simpler and absolutely free of the aforementioned deficiencies.

First approximation

Typically, the **Mohr-Coulomb model** (MC) is used for testing of the FE mesh discretiza-

tion and should be considered as a first quick approximation in the preliminary analyses. In general, MC model can be applied for the estimation of the ultimate limit state (e.g. stability analyses) or modeling of less influential, massive soil bed layers. The model is often used in the cases where the number of soil tests and the parameter database are limited.
The use of MC is not recommended for clays and soft soils because the model overestimates soil stiffness of normally- and lightly consolidated soils[1] (there is no preconsolidation pressure threshold beyond which important plastic straining occurs)and loading and unloading stiffness are not distinguished.

Soft soils

In many cases, modeling of *soft* and *near normally-consolidated clay type soils* can be performed with the family of volumetric cap models, i.e. **Cap model** and the **Modified Cam Clay** model, under the assumption that the deformation of the considered soil layer are dominated by the volumetric plastic strains. **The Modified Cam clay is however not recommended if soil exhibits a distinct non-associated (dilatant) behavior.** This shortcoming comes from the fact that the direction of strain increment is associated with that of stress increments and the dilatancy cannot be modeled. In addition, natural soils, especially soft clays, may exhibit viscous behavior which can be distinctly observed during secondary consolidation. In the ZSoil® , creep behavior (including swelling) can be modeled by means of constitutive models which exhibit pure linear elastic behavior for stress paths that penetrate the interior of the yield surface (e.g. the Cap model).

All type of soils

Most soil types can be modeled using the family of **HS models** as their formulation incorporates two hardening mechanisms. The shear mechanism deals with the plastic straining which is dominated by shearing what can be observed in *granular soils* and in *overconsolidated cohesive soils*. Having formulated the volumetric hardening mechanism which is governed by the compressive plastic strains, HS models are also suitable for modeling *soft soils*. It was demonstrated on many examples that the HS models, especially the HS-small, give realistic deformations for diaphragm walls and ground movements behind the wall in modeling excavation problems, e.g. Finno and Calvello (2005); Kempfert (2006); Benz (2007); Truty (2008) and Section 5.1.
Since HS models are developed in the isotropic framework for both elastic behavior and hardening mechanisms (uniform expansion of the yielding surfaces in all directions), **modeling of heavily overconsolidated soils which exhibit strong anisotropy should be treated carefully**.
As regards the HS-standard model, it does not include the formulation which deals with the stiffness in the range of small strains, and therefore the stiffness parameters should be chosen according to dominant strain levels in the modeled task. The HS-standard model is not able to reproduce hysteretic elastic behavior nor cyclic mobility (gradual softening due to cyclic loading).
Although the HS-small model reproduces the hysteretic elastic behavior in general, its high sensitivity to presence of small strain reversals precludes its usage

[1] It is generally assumed that a normally consolidated soil has $\mathrm{OCR} = 1$, lightly overconsolidated OCR between 1 and 3, whereas heavily overconsolidated $\mathrm{OCR} = 6 - 8$ (Bowles, 1997).

for cyclic loadings. On the other hand the HS-Brick can be applied to a certain extent for cycling loading as long as the cyclic mobility is not crucial for a given application and as long as dynamically-induced liquefaction effects are not considered.

General limitations

Note that none of the models mentioned above is able to reproduce debonding (destructuration) effects which can be observed as softening in the sensitive soils. It should also be noted that the cap hardening parameter (preconsolidation pressure) is not coupled with the degree of saturation, and therefore modeling of collapsible behavior of partially saturated soils is not possible with the implemented models.

Table 1.1: Comparison of selected soil models implemented in ZSoil® .

Model	**Hardening Soil**	**Cap**	**Mohr-Coulomb**
Type of model	nonlinear elasto-plastic, shear and compression strain hardening	elasto-plastic, compression strain hardening	elastic-perfectly plastic
Basic features	• hyperbolic stress-strain relation • stress dependent stiffness according to power law • non-linear dilatancy according to Rowe's law (+ cut-off for excessive plastic dilatancy) • distinction between primary loading and unloading • evolution of preconsolidation pressure • plastic straining in primary compression • plastic straining in primary deviatoric loading • small strain stiffness (HS-small/HS-Brick) • hysteretic, nonlinear elastic stress-strain relationship (small strains only)	• non-linear stress-strain relation for normally and lightly overconsolidated material • constant stiffness (possibility of introducing linear stress dependent stiffness through superelements) • linear soil dilatancy • distinction between primary loading and unloading • evolution of preconsolidation pressure • plastic straining in primary compression	• linear stress-strain relation • constant stiffness (possibility of introducing linear stress dependent stiffness through superelements) • linear soil dilatancy (+ cut-off for excessive plastic dilatancy)
Failure criterion	Mohr-Coulomb (hexagon in π-plane)	Drucker-Prager (circular in π-plane)	Mohr-Coulomb (hexagon in π-plane)
Cap yield surface	ellipsoidal, defined by van Eekelen criterion in π-plane	ellipsoidal, circular in π-plane	none
Hardening	deviatoric-shear and isotropic-compaction	isotropic-compaction	none
Flow rule	non-associated for shear hardening associated for isotropic hardening	non-associated for shear hardening associated for isotropic hardening	non-associated
Corresponding soil parameters			
Small strain stiffness	E_0 and $\gamma_{0.7}$ (HS-small/HS-Brick only)	none	none
Elastic characteristics	υ_{ur} and E_{ur} E_{50} and m	υ and E	υ and E
Failure criterion	ϕ and c	ϕ and c	ϕ and c
Dilatancy	ψ and e_{max}	ψ	ψ and e_{max}
Cap surface parameters	$E_{\text{oed}}^{\text{ref}}$ (can be determined from λ) OCR and K_0^{NC}	λ OCR	none

Chapter 2

Short introduction to the Hardening Soil models

The Hardening Soil model (**HS-standard**) was designed by Schanz (1998); Schanz et al. (1999) in order to reproduce basic macroscopic phenomena exhibited by soils such as:

- **densification**, i.e. a decrease of voids volume in soil due to plastic deformations, e.g. Figure 2.13;
- **stress dependent stiffness**, i.e. observed phenomena of increasing stiffness moduli with increasing stress level (mean stress), e.g. Figure. 2.4;
- **soil stress history**, i.e. accounting for preconsolidation effects;
- **plastic yielding**, i.e. development of irreversible strains with reaching a yield criterion, e.g. Figure 2.2;
- **dilatation**, i.e. an occurrence of negative volumetric strains during shearing, e.g. Figure 2.13.

Contrary to other models such us the Cap model or the Modified Cam Clay (let alone the Mohr-Coulmb model), the magnitude of soil deformations can be modeled more accurately by incorporating three input stiffness parameters corresponding to the triaxial loading stiffness (E_{50}), the triaxial unloading-reloading stiffness (E_{ur}), and the oedometer loading modulus (E_{oed}).

An enhanced version of the HS-standard, the HS-small strain model (**HS-small**) was formulated by Benz (2007) in order to handle a commonly observed phenomena of:

- strong **stiffness variation** with increasing shear strain amplitudes in the domain of small strains (Figure 1.1);
- hysteretic, nonlinear elastic stress-strain relationship which is applicable in the range of small strains (Figure 2.22).

These features mean that the HS-small should be able to produce more accurate and reliable approximation of displacements which can be useful for dynamic applications or in modeling

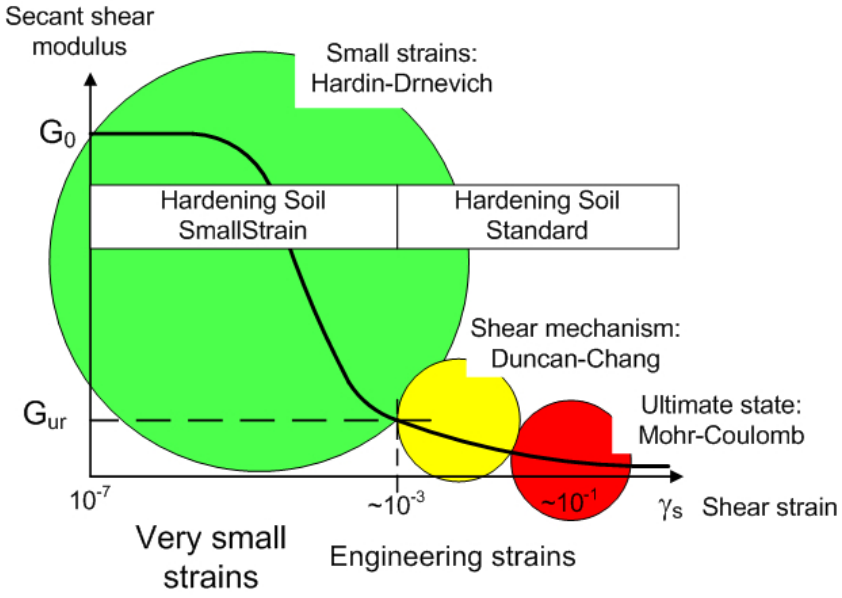

Figure 2.1: Schematic presentation of the Hardening-Soil model framework vis-à-vis the degradation of shear stiffness with increasing shear strains.

unloading-conditioned problems, e.g. deep excavations. This model was used in the practice for several years however recent findings by Niemunis and Cudny (2018) have shown a serious drawback that may show up in an uncontrolled manner in that model. It is related to the spurious reset of the strain history in the model due to tiny strain reversals. Such situations may appear in all kind of transient analyses (consolidation, transient dynamics, creep etc..). To remedy the HS-small model deficiences a new HS-Brick version was recently proposed by Cudny and Truty (2020).

Although all HS models can be considered as advanced soil models which are able to faithfully approximate complex soil behavior, they include some **limitations** related to specific behavior observed for certain soils. These models are not able to reproduce softening effects associated with soil dilatancy and soil destructuration (debonding of cemented particles) which can be observed, for instance, in sensitive soils. As opposed to the HS-small and HS-Brick model, the **HS-standard** does not account for large amplitudes of soil stiffness related to transition from very small strain to engineering strain levels ($\varepsilon \approx 10^{-3} - 10^{-2}$). Therefore, the user should adapt the stiffness characteristics to the strain levels which are expected to take place in conditions of the analyzed problem. Moreover, the HS-standard model is not capable to reproduce hysteretic soil behavior observed during cycling loading.
As an enhanced version of the HS-standard model, the **HS-Brick** accounts for small strain stiffness and therefore, it can be used to some extent to model hysteretic soil behavior under cyclic loading conditions with the exception of gradual softening which is experimentally observed with an increasing number of loading cycles. The **HS-small** should not be used in these situations at all.

2.1 HS-standard model

2.1.1 Shear mechanism

The shear mechanism is introduced in order to handle the soil hardening which is induced by the plastic shear strains. Domination of plastic shear strains can be typically observed for granular materials such as sands, and heavily consolidated cohesive soils.

2.1.1.1 Shear yield mechanism

The hardening yield function for shear mechanism f_1, is described using the concept of hyperbolic approximation of the relation between the vertical strain ε_1 and deviatoric stress q for a standard triaxial drained compression test (Figure 2.2). The yield condition is thus expressed as follows:

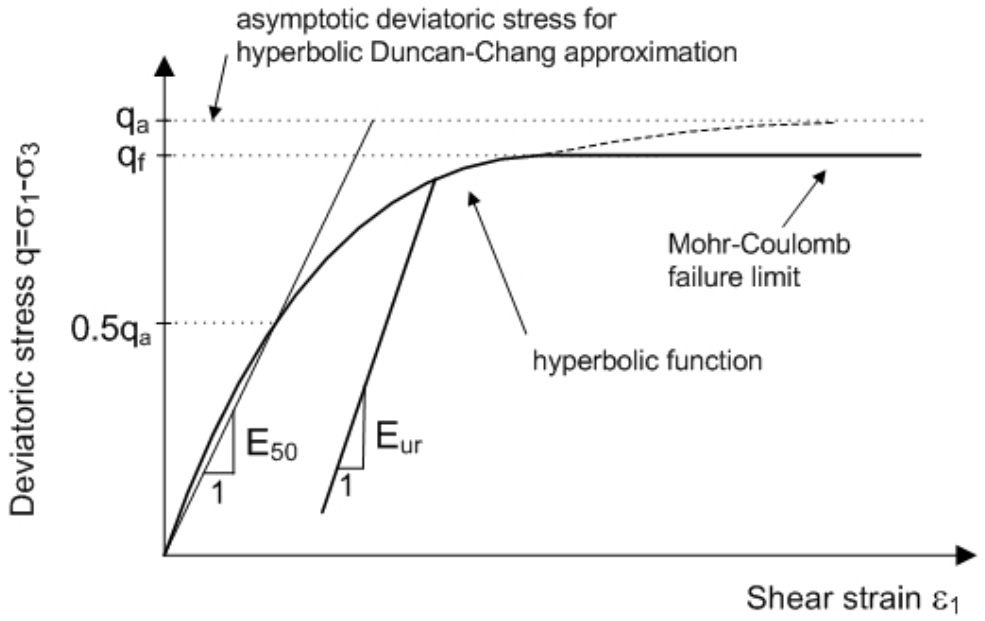

Figure 2.2: Hyperbolic stress-strain relationship and the definition of different moduli in the triaxial drained test condition.

$$f_1 = \frac{q_a}{E_{50}} \frac{q}{q_a - q} - 2\frac{q}{E_{\text{ur}}} - \gamma^{PS} \qquad \text{for } q < q_f \tag{2.1}$$

where γ^{PS} is the plastic strain hardening parameter, q_a is the asymptotic deviatoric stress which is defined by the ultimate deviatoric stress q_f and the failure ratio [1] R_f is defines as:

$$q_a = \frac{q_f}{R_f} \tag{2.2}$$

[1] A suitable value of the failure ratio is set by default $R_f = 0.9$. For most soils, the value of R_f falls between 0.75 and 1. See also Section 3.3.3.

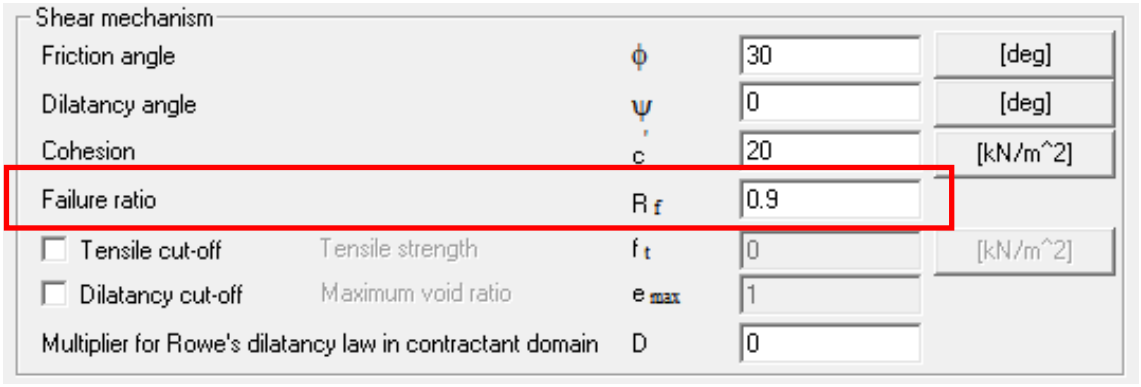

It means that for larger values of the hardening parameter γ^{PS}, the hyperbolic relation is restrained by the ultimate deviatoric stress q_f described by the Mohr-Coulomb criterion (Figure 2.2 and Figure 2.3):

$$q_f = \frac{2\sin(\phi)}{1-\sin(\phi)}\left(\sigma_3 + c\,\mathrm{cot}\phi\right) \tag{2.3}$$

which is defined by the friction angle ϕ and the cohesion c.

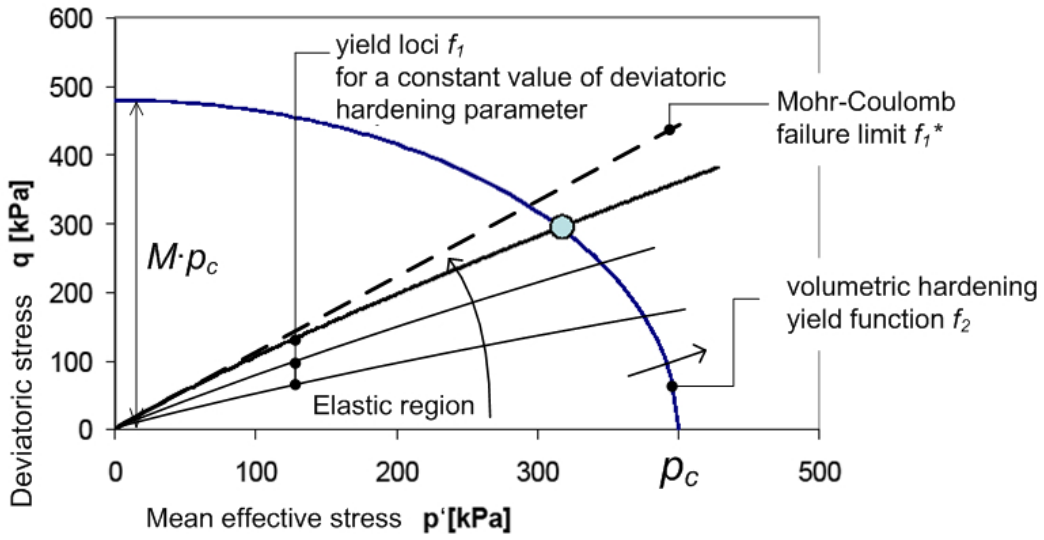

Figure 2.3: Cap surface of the volumetric hardening mechanism, yield loci for the different values of the hardening parameter γ^{PS} and the Mohr-Coulomb criterion limiting the larger values of γ^{PS}.

2.1.2 Stress dependent stiffness

The secant modulus E_{50} which corresponds to 50% of the value of q_f is defined to be **minor stress dependent** using the frequently adopted power law:

$$E_{50} = E_{50}^{\text{ref}} \left(\frac{\sigma_3^* + c \cot\phi}{\sigma^{\text{ref}} + c \cot\phi} \right)^m \tag{2.4}$$

where $\sigma_3^* = \max(\sigma_3, \sigma_L)$, i.e. stiffness degrades with decreasing σ_3 up to the limit minor stress σ_L which can by assumed be default $\sigma_L = 10$kPa; and σ_{ref} is the minor stress at which E_{50}^{ref} has been identified. In the triaxial compression test, σ_{ref} corresponds to the confining stress σ_3 (cf. Figure 3.4).

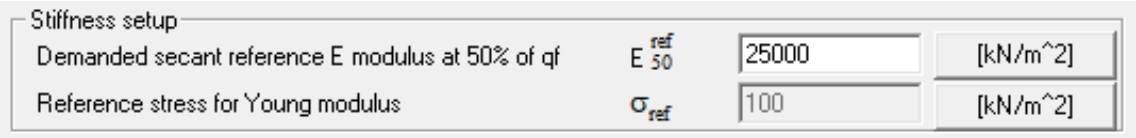

Since ZSoil 2020 another σ_3 based stress dependency is introduced omitting the term $c \cot\phi$ in the original form. The new formula eliminates the drawback which comes out when a total stress undrained analysis is carried out assuming $\phi = 0$ (and $c = C_u$). In the standard form the stiffness stress dependency becomes inactive and current stiffness modulus is always equal to its reference value. The newly added formula takes the following form:

$$E_{50} = E_{50}^{\text{ref}} \left(\frac{\sigma_3^*}{\sigma^{\text{ref}}} \right)^m \tag{2.5}$$

Note that E_{50} largely controls the magnitude of the plastic strains which are related to the shear yield mechanism. In natural soil, the exponent m varies between 0.3 and 1.0. Janbu (1963) reported values of 0.5 for Norwegian sands and silts, whereas Kempfert (2006) provided values between 0.38 and 0.84 for soft lacustrine clays (see also Section 3.3.7). **The user may set the material stiffness to be independent on the stress level by setting** $m = 0$ (i.e. constant stiffness like in the standard Mohr-Coulomb model).
By analogy with E_{50}, the modulus E_{ur} which defines the slope of the unloading-reloading curve is also defined as minor stress dependent:

$$E_{\text{ur}} = E_{\text{ur}}^{\text{ref}} \left(\frac{\sigma_3^* + c \cot\phi}{\sigma^{\text{ref}} + c \cot\phi} \right)^m \tag{2.6}$$

or with the newly introduced stress dependency type without the term $c \cot\phi$ (since ZSoil 2020) as

$$E_{\text{ur}} = E_{\text{ur}}^{\text{ref}} \left(\frac{\sigma_3^*}{\sigma^{\text{ref}}} \right)^m \tag{2.7}$$

Note that the same σ_{ref} applies to the stiffness moduli E_{50}^{ref}, $E_{\text{ur}}^{\text{ref}}$ and E_0^{ref}.

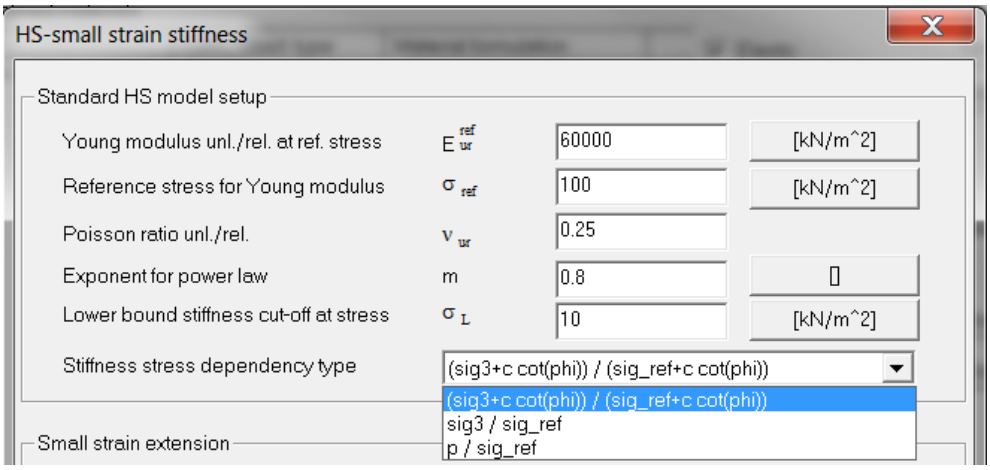

An example of stress dependency is graphically presented in Figure 2.4.

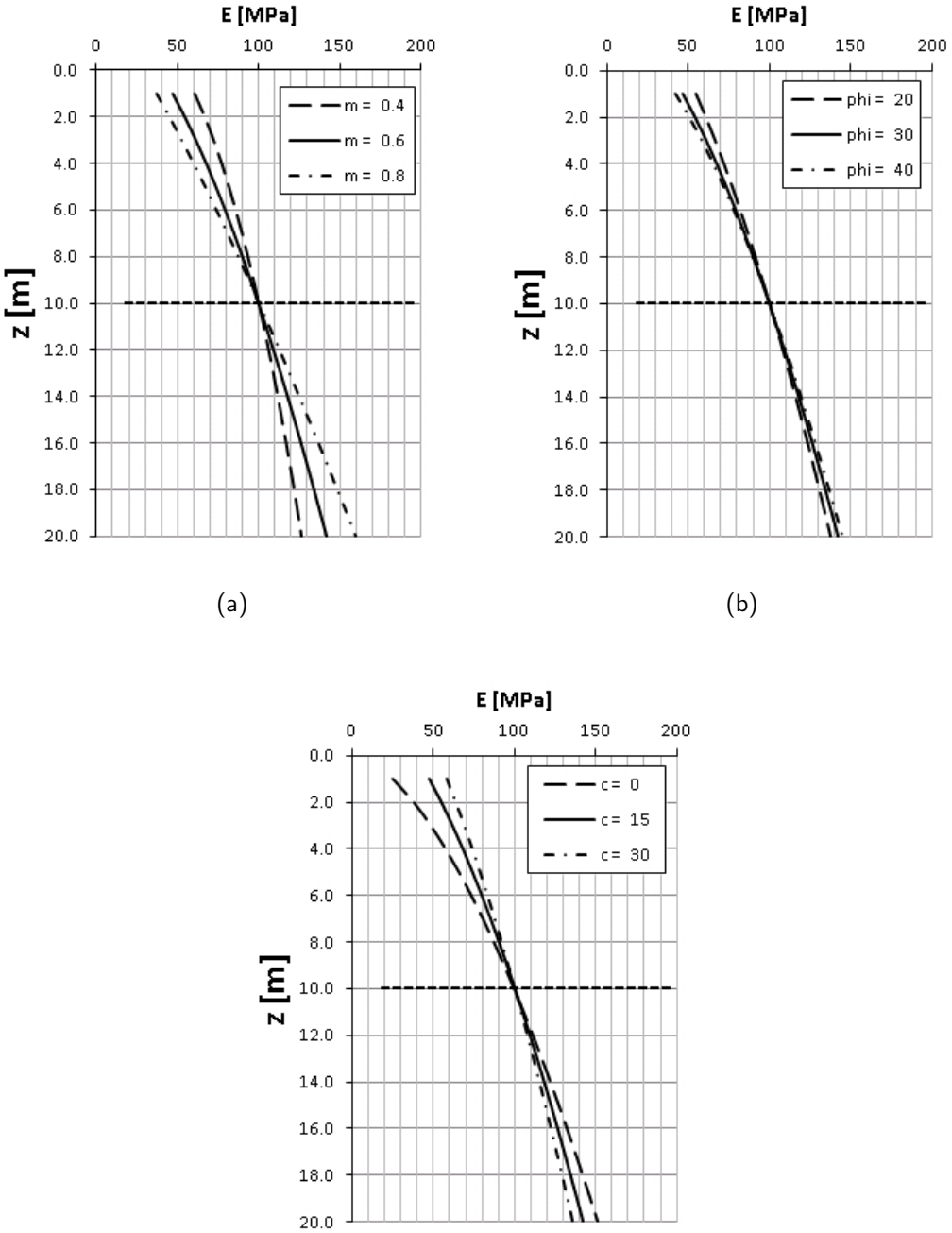

Figure 2.4: Example of stress dependency (based on $\frac{\sigma_3^* + c\cot\phi}{\sigma^{\text{ref}} + c\cot\phi}$) at initial state defined by Eq. (2.6) for different values of parameter (a) m, (b) ϕ, and (c) c.

2.1.2.1 Stress dependent stiffness based on the mean effective stress

In the case of dynamic analyzes or when modeling of excavation problems, a rotation of principal stresses may occur resulting in spurious oscillations of stiffness moduli which, in the classical formulation, depend merely on the minor stress σ_3. For example, in the case of excavation of a circular tunnel, one may observe the rotation of principal stresses at the tunnel sides, and the vertical stress which initially defines the soil stiffness $\sigma_3 = \sigma'_v$ becomes $\sigma_3 = \sigma'_h$ which may lead to a stiffness underestimation. This is because σ'_h decreases almost to zero dropping the unloading-reloading stiffness to its minimal value which is limited by σ_L. Moreover, at the bottom of an excavated tunnel σ_3 which is equal to the vertical stress may also drop to zero resulting in slightly overestimated swelling of the tunnel bottom.

In order to remedy this problem, the user can use the stress dependency formulation which depend on the mean effective stress p' which can be written in a general form as:

$$E = E^{\text{ref}} \left(\frac{p^*}{\sigma_{\text{ref}}} \right)^{m_p} \quad \text{with} \quad p^* = \max(p', \sigma_L) \tag{2.8}$$

where:

σ_{ref} - reference stress
E^{ref} - reference modulus corresponding to the reference stress σ_{ref}
m_p - stiffness exponent for p'-formulation which is equal to $m_p = m$ if $c = 0$, otherwise $m_p \neq m$
p' - mean effective stress $(\sigma'_1 + \sigma'_2 + \sigma'_3)/3$
σ_L - the limiting stress (in order to avoid zero stiffness when p' tends to 0)

A unique σ_{ref} applies to the stiffness moduli E^{ref}_{50}, $E^{\text{ref}}_{\text{ur}}$ and E^{ref}_{0}.
In the current version (ZSoil v2023), the evolution of the preconsolidation parameter (refer to Eq. 2.25) remains the same for all formulations of stiffness dependency and it does not include the component $c \cot \phi$. Note that parameter transformation does not apply to $E^{\text{ref}}_{\text{oed}}$ because this input parameter is not a model parameter but it serves as the reference value for calibrating parameters M and H.

Table 2.1: Comparison of different types of stiffness stress dependency.

Minor effective stress σ'_3	Mean effective stress p'
Drawback: Spurious oscillations of stiffness moduli in the case of dynamic analyzes and excavation problems in materials with $K_0 > 1$	Stiffness oscillations independent of the principal stresses rotation
Drawback: Underestimation of unloading-reloading stiffness in excavation problems	Unloading-reloading stiffness depends on p' which is larger than σ_3 in excavation problems
Direct identification of the stiffness moduli E_{50} and E_{ur} for the constant σ_3 during triaxial compression test	**Drawback:** E_{50} and E_{ur} are not directly identifiable from triaxial test as p' varies during triaxial compression test. A simple transformation method is provided in Figure 2.7.
Drawback: in case of $\sigma_3 + c \cot\phi$ stress dependency type stiffness is not stress dependent in a simplified undrained analysis assuming $\phi = 0$	Stiffness is stress dependent independently on assumed ϕ value

In ZSoil v2023 , p-stress dependency can be activated in *Elastic* dialog window, as illustrated below.

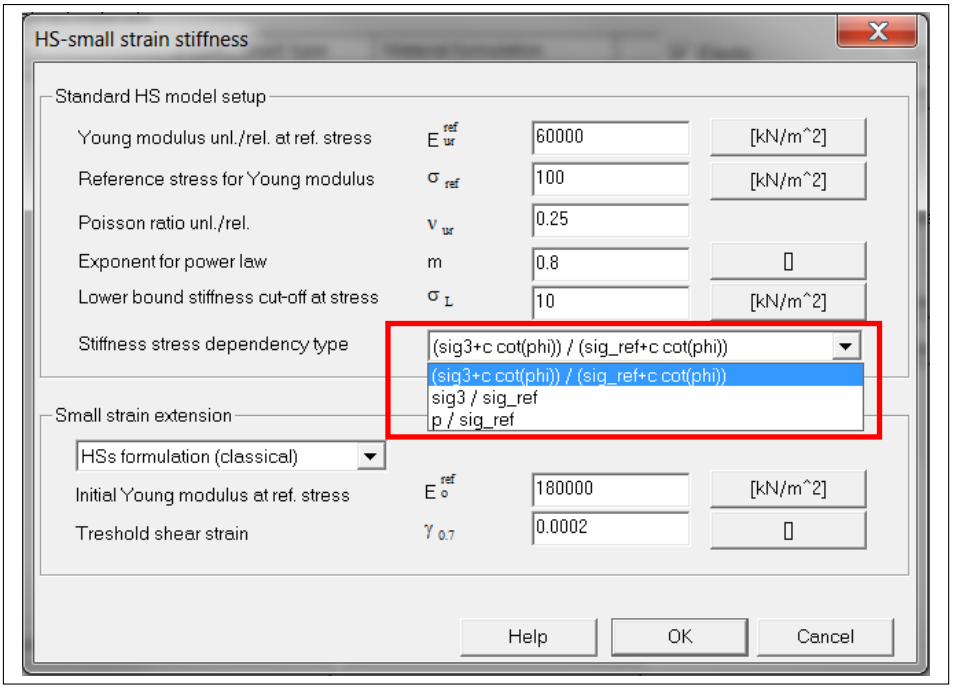

2.1.2.2 Parameter migration between minor and mean stress formulations

Note that material stiffness described with $\sigma_3 + c \cdot \cot\phi$, σ_3 and p' formulations can be different in triaxial conditions in the case when the same values of parameters, $E^{\text{ref}}_{\text{ur}}$, E^{ref}_{50}, m and R_f, are assumed to describe the HS model, as illustrated in Figure 2.5. It is so because the material stiffness is obtained with respect to different scaling variables.

The small strain stiffness described by $\sigma_3 + c\dot{c}\dot{o}t\phi$-formulation and p'-formulation can also be different across the soil initial stiffness profile assuming the same σ_{ref}, if the same reference moduli $E_0^{\sigma,\text{ref}}(\sigma_{\text{ref}}) = E_0^{p,\text{ref}}(\sigma_{\text{ref}})$ and the same value of stiffness exponent $m = m_{\text{p}}$ are taken. In the other words, assuming the same departing stiffness profile for both formulations one should be aware that:

- the reference moduli are different $E_0^{\sigma_3,\text{ref}}(\sigma_{\text{ref}}) \neq E_0^{p,\text{ref}}(\sigma_{\text{ref}})$ if $K_0 \neq 1$
- the stiffness exponents m and m_{p} are different if $c > 0$

Table 2.2 shows in detail equivalency of parameters in terms of compatibility of material stiffness for different initial stress conditions and cohesion value.

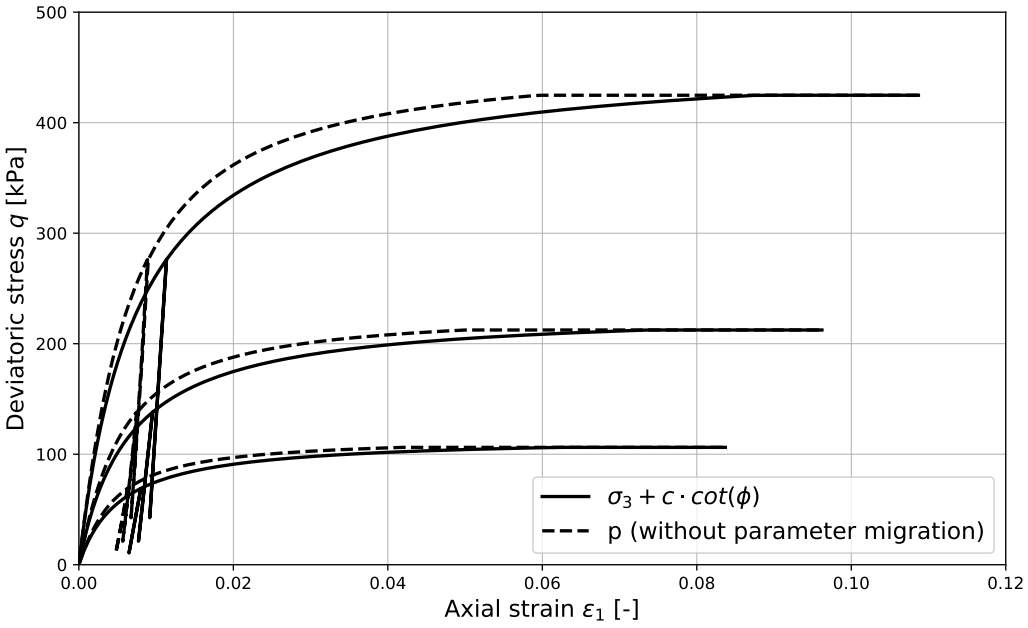

Figure 2.5: Triaxial test curves obtained for $\sigma_3 + c\dot{\cot}\phi$ and p' assuming the same parameter values for $E_{\mathsf{ur}}^{\mathsf{ref}}$, E_{50}^{ref}, m and R_f (without parameter migration)

Table 2.2: Equivalency of model parameters in terms of compatibility of material stiffness for different initial stress conditions and cohesion value

	$c = 0$ $K_0 = 1$	$c = 0$ $K_0 \neq 1$	$c \neq 0$ $K_0 = 1$	$c \neq 0$ $K_0 \neq 1$
$\sigma_3 + c \cdot \cot\phi \rightarrow \sigma_3$	all parameters equivalent	$m = m_{\sigma_3}$ $E_0^{\mathsf{ref}} = E_0^{\sigma_3,\mathsf{ref}}$ $E_{\mathsf{ur}}^{\mathsf{ref}} = E_{ur}^{\sigma_3,\mathsf{ref}}$ $E_{50}^{\mathsf{ref}} = E_{50}^{\sigma_3,\mathsf{ref}}$ $R_f = R_f^{\sigma_3}$	$m > m_{\sigma_3}$ $E_0^{\mathsf{ref}} \neq E_0^{\sigma_3,\mathsf{ref}}$ $E_{\mathsf{ur}}^{\mathsf{ref}} < E_{ur}^{\sigma_3,\mathsf{ref}}$ $E_{50}^{\mathsf{ref}} < E_{50}^{\sigma_3,\mathsf{ref}}$ $R_f = R_f^{\sigma_3}$	$m > m_{\sigma_3}$ $E_0^{\mathsf{ref}} > E_0^{\sigma_3,\mathsf{ref}}$ $E_{\mathsf{ur}}^{\mathsf{ref}} < E_{ur}^{\sigma_3,\mathsf{ref}}$ $E_{50}^{\mathsf{ref}} < E_{50}^{\sigma_3,\mathsf{ref}}$ $R_f < R_f^{\sigma_3}$
$\sigma_3 + c \cdot \cot\phi \rightarrow p$	$m = m_{\mathsf{p}}$ $E_0^{\mathsf{ref}} = E_0^{\mathsf{p,ref}}$ $E_{\mathsf{ur}}^{\mathsf{ref}} > E_{ur}^{\mathsf{p,ref}}$ $E_{50}^{\mathsf{ref}} > E_{50}^{\mathsf{p,ref}}$ $R_f < R_f^{\sigma_3}$	$m = m_{\mathsf{p}}$ $E_0^{\mathsf{ref}} > E_0^{\mathsf{p,ref}}$ $E_{\mathsf{ur}}^{\mathsf{ref}} > E_{ur}^{\mathsf{p,ref}}$ $E_{50}^{\mathsf{ref}} > E_{50}^{\mathsf{p,ref}}$ $R_f < R_f^{\sigma_3}$	$m > m_{\mathsf{p}}$ $E_0^{\mathsf{ref}} \neq E_0^{\mathsf{p,ref}}$ $E_{\mathsf{ur}}^{\mathsf{ref}} > E_{ur}^{\mathsf{p,ref}}$ $E_{50}^{\mathsf{ref}} > E_{50}^{\mathsf{p,ref}}$ $R_f < R_f^{\sigma_3}$	$m > m_{\mathsf{p}}$ $E_0^{\mathsf{ref}} > E_0^{\mathsf{p,ref}}$ $E_{\mathsf{ur}}^{\mathsf{ref}} > E_{ur}^{\mathsf{p,ref}}$ $E_{50}^{\mathsf{ref}} > E_{50}^{\mathsf{p,ref}}$ $R_f < R_f^{\sigma_3}$
$\sigma_3 \rightarrow p$	$m_{\sigma_3} = m_{\mathsf{p}}$ $E_0^{\mathsf{ref}} = E_0^{\sigma_3,\mathsf{ref}}$ $E_{\mathsf{ur}}^{\mathsf{ref}} > E_{ur}^{\sigma_3,\mathsf{ref}}$ $E_{50}^{\mathsf{ref}} > E_{50}^{\sigma_3,\mathsf{ref}}$ $R_f < R_f^{\sigma_3}$	$m_{\sigma_3} = m_{\mathsf{p}}$ $E_0^{\mathsf{ref}} > E_0^{\sigma_3,\mathsf{ref}}$ $E_{\mathsf{ur}}^{\mathsf{ref}} > E_{ur}^{\sigma_3,\mathsf{ref}}$ $E_{50}^{\mathsf{ref}} > E_{50}^{\sigma_3,\mathsf{ref}}$ $R_f < R_f^{\sigma_3}$	$m_{\sigma_3} < m_{\mathsf{p}}$ $E_0^{\mathsf{ref}} \neq E_0^{\sigma_3,\mathsf{ref}}$ $E_{\mathsf{ur}}^{\mathsf{ref}} > E_{ur}^{\sigma_3,\mathsf{ref}}$ $E_{50}^{\mathsf{ref}} > E_{50}^{\sigma_3,\mathsf{ref}}$ $R_f < R_f^{\sigma_3}$	$m_{\sigma_3} < m_{\mathsf{p}}$ $E_0^{\mathsf{ref}} > E_0^{\sigma_3,\mathsf{ref}}$ $E_{\mathsf{ur}}^{\mathsf{ref}} > E_{ur}^{\sigma_3,\mathsf{ref}}$ $E_{50}^{\mathsf{ref}} > E_{50}^{\sigma_3,\mathsf{ref}}$ $R_f < R_f^{\sigma_3}$

In order to preserve compatibility of material behavior in terms of its stiffness between different power law formulations, a migration of parameters should be considered. A parameter migration can be carried out according to a general procedure as follows:

1. Identify or define the parameters of the base power law, i.e. E_0^{ref}, $E_{\text{ur}}^{\text{ref}}$, E_{50}^{ref}, m and R_f ; notice that parameters identified from experimental triaxial curves correspond to $\sigma_3 + c \cdot \cot\phi$ formulation

2. Select a stiffness modulus ($E_{\text{ur}}^{\text{ref}}$ or E_0^{ref}) for which the stiffness exponent m will be adjusted for a selected target power law

3. Make migration of m and the selected modulus by applying either *continuous profile regression analysis* (e.g. for E_0^{ref}) or a *regression analysis based on discrete values* of E_{ur} (e.g. for three values obtained from 3 triaxial tests); both approaches are described below

4. Migrate E_{50}^{ref} and the failure ratio R_f by running optimization of three triaxial curves, i.e. a curve-fitting of numerical triaxial drained compression curves produced with base power law parameters and and sought values of E_{50}^{ref} and R_f describing the target power law

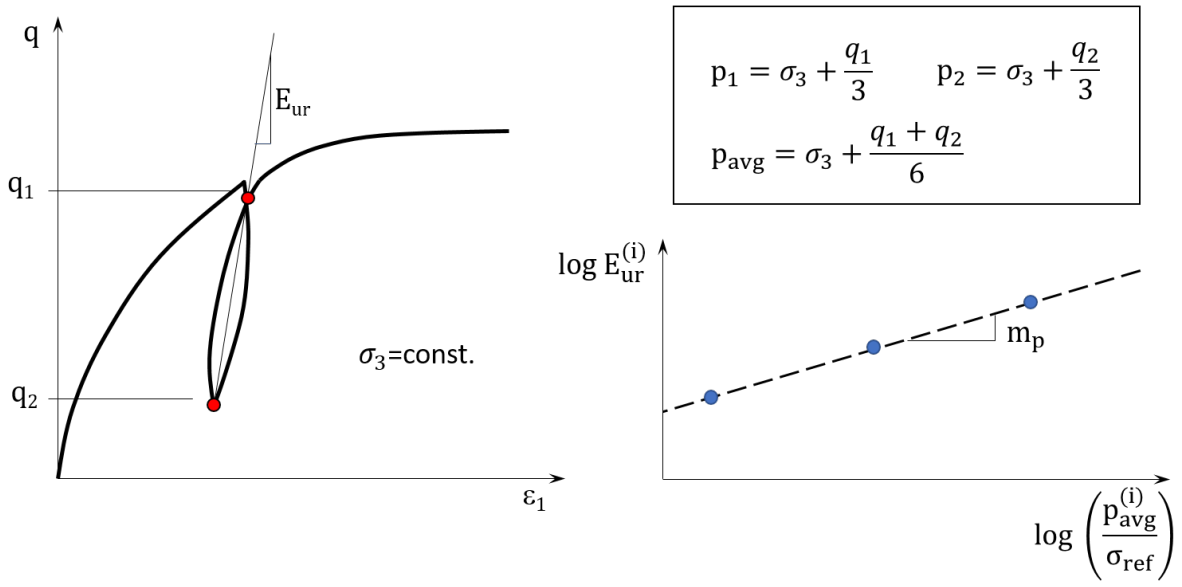

Figure 2.6: Migration of stiffness exponent and unloading-reloading modulus based on unloading-reloading cycles from triaxial curves

Regression analysis based on discrete stress points

In order to obtain a similar response on unloading-reloading cycle for a given stress level for $\sigma_3 + c \cdot \cot\phi$ and p formulations, one may adjust $E_{ur}^{\text{p,ref}}$ to the same value of σ_{ref} by proceeding the following procedure:

1. Determine $E_{\text{ur}}^{\text{ref}}$ (from triaxial test if available), m for given σ_{ref}, ϕ' and, c' assuming σ_3-formulation

   e.g. for $\sigma_{\text{ref}} = 100$kPa, the following parameters were obtained from triaxial compression tests: $E_{\text{ur}} = 64000$kPa, $m = 0.75$, $\phi' = 31^o$ and $c = 5$kPa

2. Specify a discrete number of different initial stress conditions described by the effective vertical stress σ'_{v0} and K_0 (in order to determine σ_3)

   e.g. $\sigma'_{v0} = \{50, 100, 200\}$kPa and $K_0 = 1.0$ (in the case of an isotropic triaxial test), so $\sigma_3 = \min(\sigma'_{h0}, \sigma'_{v0})$

3. Compute three values of the average mean stress which correspond to the half the unloading-reloading cycle, see Figure 2.6 (q_1 and q_2 can be taken from experimental triaxial curves or arbitrarily assumed)
   e.g. the user can assume that the unloading begins at $q_1 = 0.65 \cdot q_f$ and end at $q_2 = 0.65 \cdot q_f$ with q_f denoting the failure stress which can be computed for the known ϕ, c and σ_3

4. Perform a linear regression analysis between logarithmically transformed two factors: the reference stiffness moduli obtained for three different initial stress conditions and the normalizing term of the target power law ($p_{\text{avg}}/\sigma_{\text{ref}}$ in the case of the mean stress formulation), the linear regression allows the power law exponent and the stiffness modulus of the target power law to be found (refer to Figure 2.6)

Continuous profile regression analysis

Parameter migration between the σ_3-formulation and p'-formulation can also be carried out by performing a **simple regression analysis using a spreadsheet** (refer to Figure 2.7). This method requires plotting an evolution of the stiffness modulus computed using σ_3-formulation against the normalized mean effective stress. Two coefficients which define the power-type trendline $y = ax^b$ give the values of $E^{p,\text{ref}}$ and m_{p}, respectively.

 The above procedure optimizes the stiffness exponent m for a continuously populated stress interval and can be used to migrate E_0^{ref} and $E_{\text{ur}}^{\text{ref}}$.

1	σ_3 - dependent stiffness							
2	Input:							
3	E_0^{ref}	260000	kPa					
4	m	0.5	-					
5	σ_3^{ref}	100	kPa					
6	c	5	kPa					
7	ϕ	30	deg					
8	cot(ϕ)	1.73	-					
9	a = c * cot ϕ	8.66	kPa					
10	K_0	0.6	-					
11								
12				$E = E^{ref}\left(\frac{\sigma_3 + a}{\sigma_{ref} + a}\right)^m$				
13	Input	Computed variables					Plotted variables	
14	σ'_v	$\sigma'_h = K_0\,\sigma'_v$	σ_3 = min(σ'_h,σ'_v)	E_0 (sig-3)	p' = (σ'_v+2σ_h)/3		p' / σ_{ref}	$E_0 = E_0$ (sig-3)
15	10	6	6	95501.2	7.33			
16	20	12	12	113372.0	14.67			
17	30	18	18	128786.4	22.00			
18	40	24	24	142543.6	29.33		0.293	142543.6
19	50	30	30	155085.2	36.67		0.367	155085.2
20	60	36	36	166685.8	44.00		0.440	166685.8
21	70	42	42	177530.0	51.33		0.513	177530.0
22	80	48	48	187748.8	58.67		0.587	187748.8
23	90	54	54	197439.5	66.00		0.660	197439.5
24	100	60	60	206676.3	73.33		0.733	206676.3
25	110	66	66	215517.6	80.67		0.807	215517.6
26	120	72	72	224010.2	88.00		0.880	224010.2
27	130	78	78	232192.4	95.33		0.953	232192.4
28	140	84	84	240095.9	102.67		1.027	240095.9
29	150	90	90	247747.4	110.00		1.100	247747.4
30	160	96	96	255169.6	117.33		1.173	255169.6

(a) Input variables and computed data in a spreadsheet

p' - dependent stiffness			
Output (trendline coefficents):			
$E_0^{p.ref}$	239797	kPa	
m_p	0.458	kPa	
$E_0^{p.ref} / E_0^{\sigma 3.ref}$	0.922		

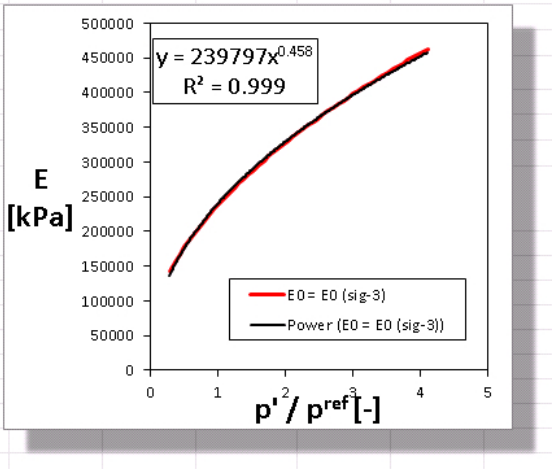

(b) Determination of p'-dependency parameters using regression analysis

Figure 2.7: Migration between the σ_3-formulation and p'-formulation for the initial stiffness parameter E_0^{ref} using a spreadsheet.

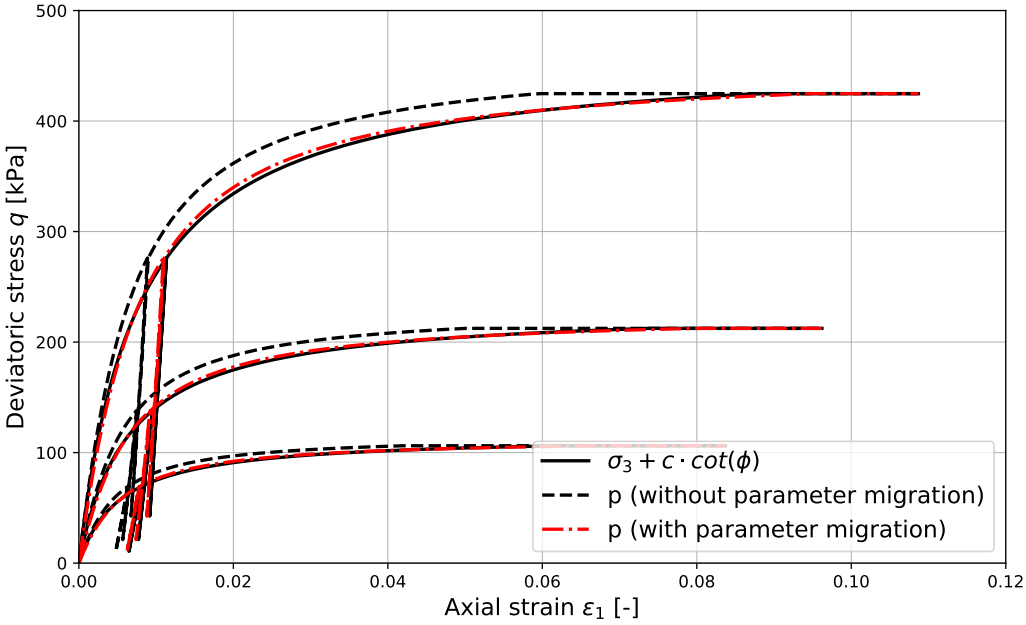

Figure 2.8: Curve-fitting of numerical triaxial drained compression curves produced with base power law parameters and and sought values of E_{50}^{ref} and R_f for the target power law

Migration of E_{50} and R_f - curve-fitting approach

Ensuring compatibility of base and target power laws at larger strains requires migrating the secant stiffness moduli E_{50}^{ref} and the failure ratio R_f which shapes the triaxial curve beyond $0.5q_f$.

Migration of E_{50}^{ref} and R_f consists of running an optimization of three triaxial curves - a curve-fitting of numerical triaxial drained compression curves which are produced with base power law parameters and and sought values of E_{50}^{ref} and R_f for the target power law, as illustrated in Figure 2.8. The optimization should be constrained in terms of R_f value in order to avoid the over-fitting of the failure axial strain. Therefore, the maximum available change of R_f is fixed to 0.02. Moreover, the unloading-reloading branch can be ignored during curve-fitting since $E_{\text{ur}}^{\text{ref}}$ has been previously identified.

2.1.2.2.1 An integrated tool for automatic parameter migration

Virtual Lab v2023 offers and an integrated toolbox for moduli migration (Figure 2.9). The tool includes the migration approaches which are presented above.

The algorithm uses the *regression analysis based on discrete stress points* approach to migrate the stiffness exponent m and E_{ur} and E_0^{ref} and the curve-fitting approach for E_{50} and R_f. Moreover, a continuous profile of E_0^{ref} is plotted in for a stress interval selected for parameter migration. Note that those two values completed with the reference stress value are taken as three discrete stress points for the regression analysis.

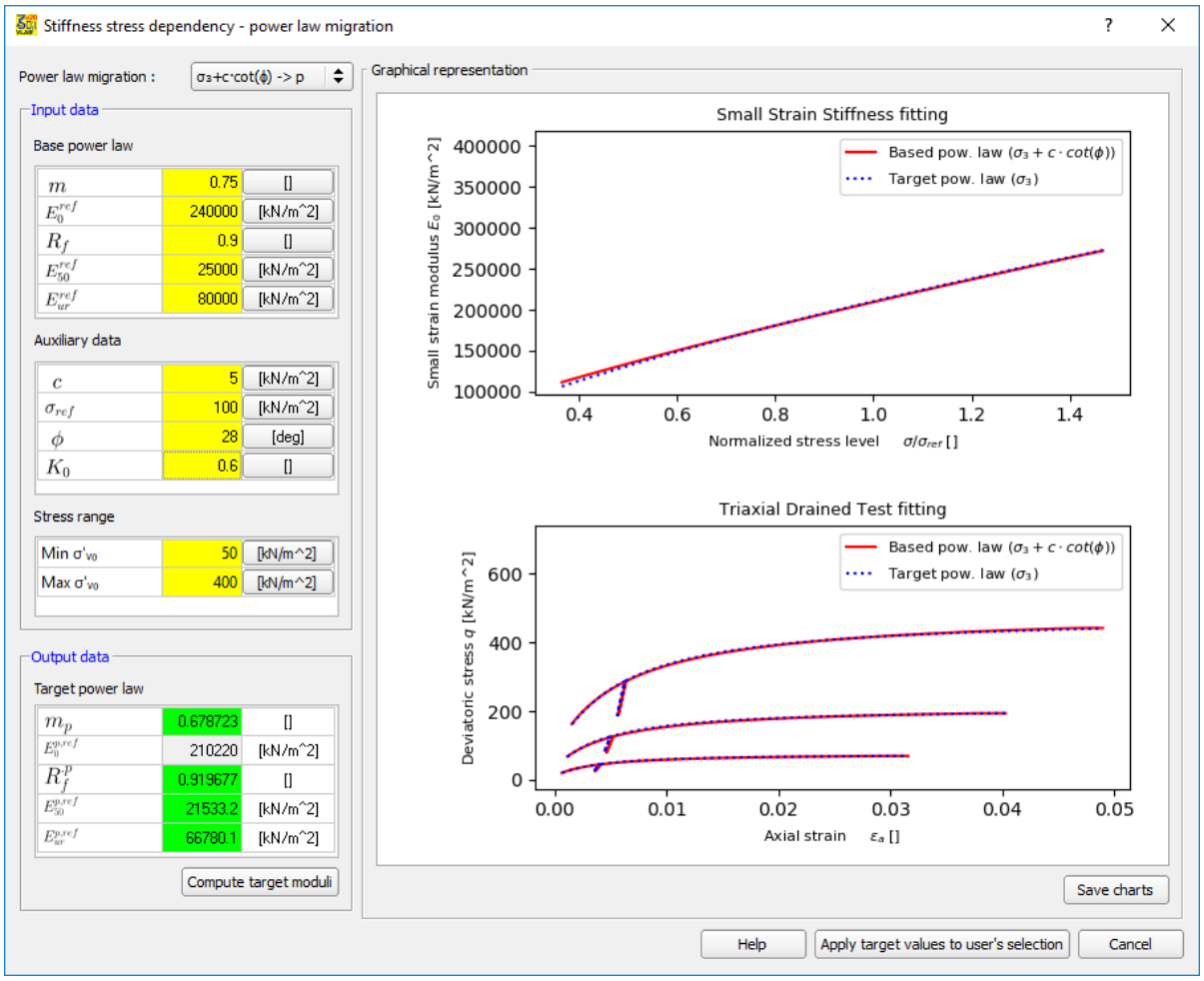

Figure 2.9: A toolbox in Virtual Lab v2023 for the parameter migration between different stress dependent stiffness formulations

2.1.3 Shear hardening law

The shear hardening yield function f_1 can be decomposed into part which is a function of stress - two first components, whereas the last component is a function of plastic strains $\gamma^{PS} = \varepsilon_1^p - \varepsilon_2^p - \varepsilon_3^p$. Assuming that in the contractancy domain, the volumetric plastic strain $\varepsilon_v^p = \varepsilon_1^p + \varepsilon_2^p + \varepsilon_3^p$ is observed to be very small $\varepsilon_v^p \approx 0$, it can thus be written:

$$\gamma^{PS} \cong 2\varepsilon_1^p \tag{2.9}$$

Hence, for the primary loading in drained triaxial conditions, ε_1 is evaluated using the yield condition f_1 (Eq.(2.1)) and decomposition of the elastic and the plastic strains:

$$\varepsilon_1 = \varepsilon_1^e + \varepsilon_1^p = \frac{q}{E_{\text{ur}}} + \frac{1}{2}\left(\frac{q_a}{E_{50}}\frac{q}{q_a - q} - \frac{2q}{E_{\text{ur}}}\right) = \frac{q_a}{2E_{50}}\frac{q}{q_a - q} \tag{2.10}$$

For the drained triaxial conditions and the confining stress remaining constant (i.e. $\sigma_2 = \sigma_3 = const.$), the modulus E_{ur} remains constant and the elastic strains can be computed from:

$$\varepsilon_1^e = \frac{q}{E_{\text{ur}}} \quad \text{and} \quad \varepsilon_2^e = \varepsilon_3^e = \nu_{\text{ur}}\frac{q}{E_{\text{ur}}} \tag{2.11}$$

where ν_{ur} denotes unloading/reloading Poisson's ratio.

The hyperbolic relation between the axial strain and the deviatoric stress presented in Equation 2.10 can be rearranged into:

$$q = \frac{\varepsilon_1}{\dfrac{1}{2E_{50}} + \dfrac{\varepsilon_1 R_f}{q_f}} \tag{2.12}$$

which can also be rewritten in the following form:

$$q = \frac{\varepsilon_1}{a + b\varepsilon_1} \tag{2.13}$$

These equations are graphically presented in Figure 2.10.
Note that for an anisotropically consolidated clay, the initial state deviatoric stress (after consolidation but before compression) which corresponds to the state of zero strains is:

$$q_0 = \sigma_3 \frac{1 - K_0}{K_0} \tag{2.14}$$

so the deviatoric stress after consolidation becomes:

$$q_m = q - q_0 \tag{2.15}$$

and Eq.(2.12) can be rewritten as:

$$q_m = \frac{\varepsilon_1}{\dfrac{1}{2E_{50}} + \dfrac{\varepsilon_1 R_f}{q_{m,f}}} \tag{2.16}$$

with $q_{m,f}$ denoting q_m at failure.

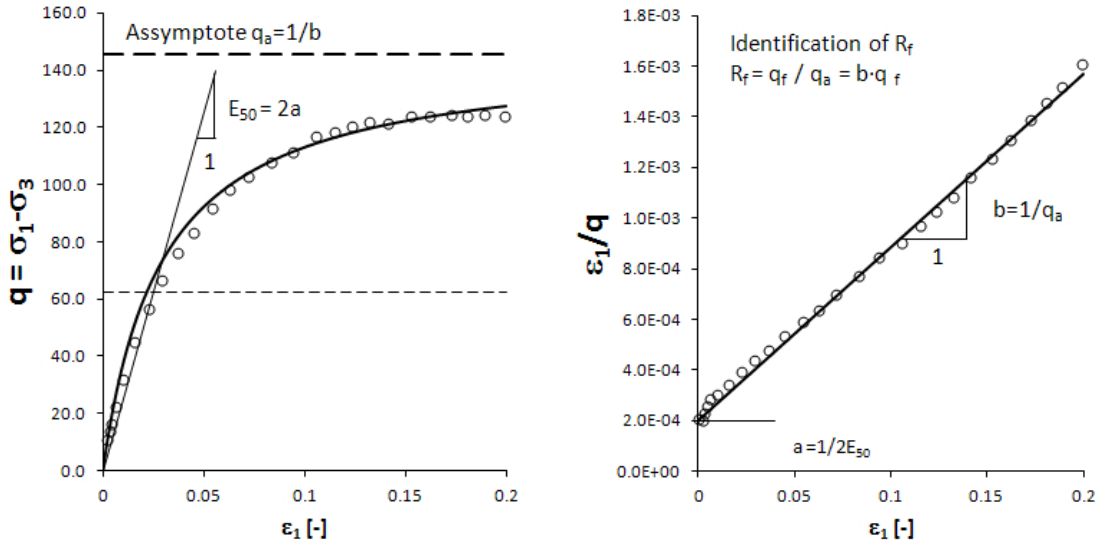

(a) (b)

Figure 2.10: Graphical representation of Eq.(2.12) and identification of failure ratio R_f (a) hyperbolic curve plotted with laboratory data points (b) typical triaxial drained compression results presented in the hyperbolic form (laboratory data from Kempfert, 2006).

2.1.4 Plastic flow rule and dilatancy

The plastic flow rule is derived from the following plastic potential:

$$g_1 = \frac{\sigma_1 - \sigma_3}{2} - \frac{\sigma_1 + \sigma_3}{2} \sin\psi_m \tag{2.17}$$

where the mobilized dilatancy angle ψ_m is calculated in the HS-standard model according to:

$$\sin\psi_m = 0 \quad \text{if} \quad \phi_m < \phi_{cs} \quad \text{(cut-off in contractancy domain)} \tag{2.18a}$$

$$\sin\psi_m = \frac{\sin\phi_m - \sin\phi_{cs}}{1 - \sin\phi_m \sin\phi_{cs}} \quad \text{if} \quad \phi_m \geq \phi_{cs} \quad \text{(Rowe's dilatancy)} \tag{2.18b}$$

The mobilized friction angle[2], ϕ_m, is computed from:

$$\sin\phi_m = \frac{\sigma_1 - \sigma_3}{\sigma_1 + \sigma_3 - 2c\,\cot\phi} \tag{2.19}$$

and the critical state friction angle which is a material property and is independent of the stress conditions, is defined by the friction angle ϕ and the ultimate dilatancy angle ψ as:

$$\sin\phi_{cs} = \frac{\sin\phi - \sin\psi}{1 - \sin\phi \sin\psi} \tag{2.20}$$

The volumetric plastic strain generated by the shear plastic mechanism is expressed as follows ($\mathrm{d}\lambda_1$ is the plastic multiplier for shear mechanism):

$$\mathrm{d}\varepsilon_v^p = \mathrm{d}\lambda_1 \frac{\partial g_1}{\partial \sigma_1} + \mathrm{d}\lambda_1 \frac{\partial g_1}{\partial \sigma_3} = -\mathrm{d}\lambda_1 \sin\psi_m \tag{2.21}$$

[2]The mobilized friction angle ϕ_m describes the stress ratio τ/σ (at the critical state $\phi_m = \phi_{cs}$).

It is worth noting that dilatancy may occur for larger values of the mobilized friction angle $\phi_m > \phi_{cs}$, whereas for smaller stress ratios ($\phi_m < \phi_{cs}$), the material contracts and the mobilized dilatancy angle is controlled by the cut-off criterion as presented in Figure 2.11.

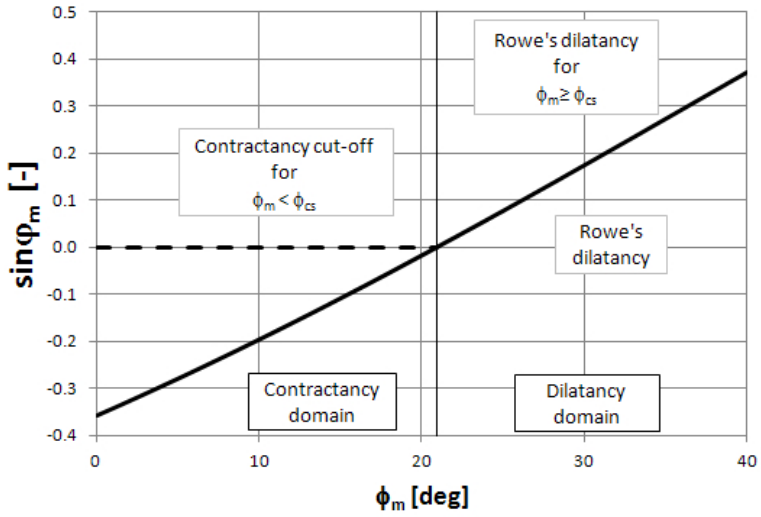

Figure 2.11: Rowe's dilatancy law and the cut-off criterion in the contractant domain for the HS-standard model.

The dilatancy angle ψ can be derived from the maximum slope d of the $\varepsilon_1 - \varepsilon_v$ curve (Figure 2.13):

$$d = \frac{\mathrm{d}\varepsilon_v}{\mathrm{d}\varepsilon_1} \approx \frac{\mathrm{d}\varepsilon_v^p}{\mathrm{d}\varepsilon_1^p} = -\frac{2\sin\psi}{1-\sin\psi} \tag{2.22}$$

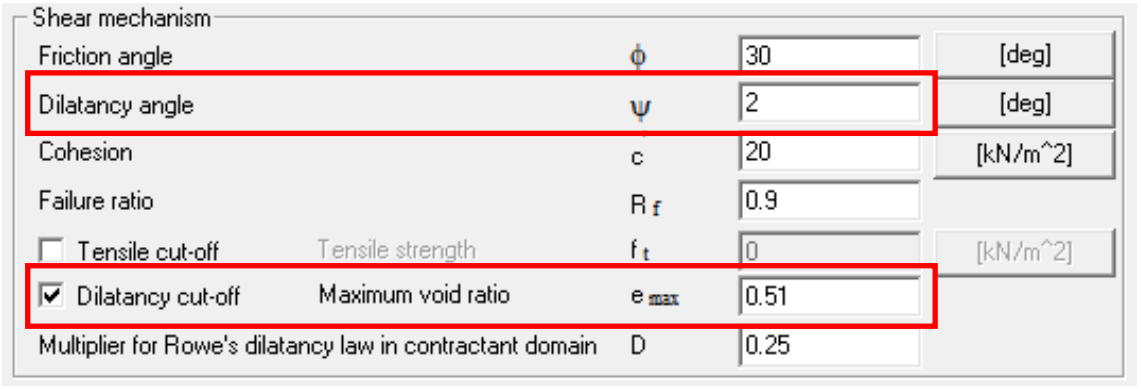

In order to cancel dilatancy which is produced by Rowe's law at the critical state, an additional cut-off criterion is introduced to respect the maximal defined void ratio e_{max} (Figure 2.13):

$$\text{if} \quad e \geq e_{max} \quad \sin\psi_m = 0 \quad \text{(cut-off)} \tag{2.23}$$

otherwise Eq.(2.18b) is used to calculate $\sin\psi_m$.

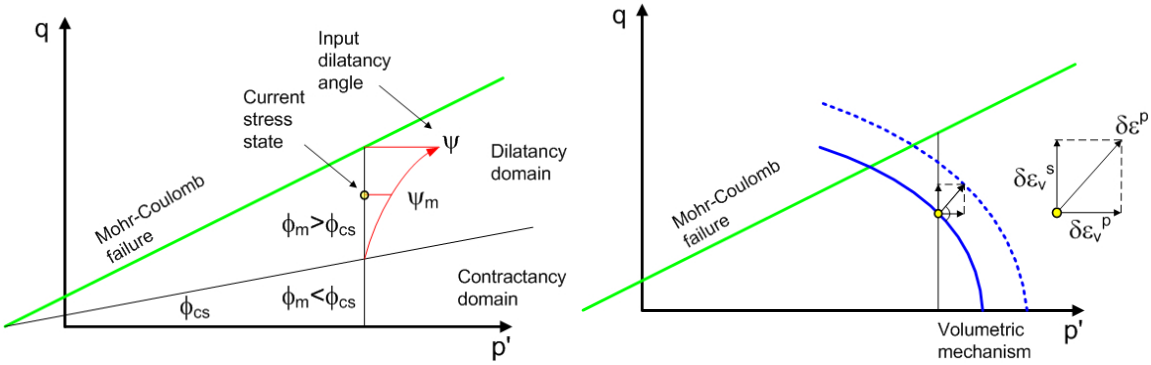

(a) Non-associated flow for deviatoric mechanism (b) Associated flow for volumetric mechanism

Figure 2.12: Plastic flow rules in the HS model (a) graphical explanation of mobilized dilatancy ψ_m which increases from 0 up to the input dilatancy angle ψ once M-C line is reached, (b) contractancy increases with compressive p' stress from zero to maximum value at M-C failure only when cap is mobilized.

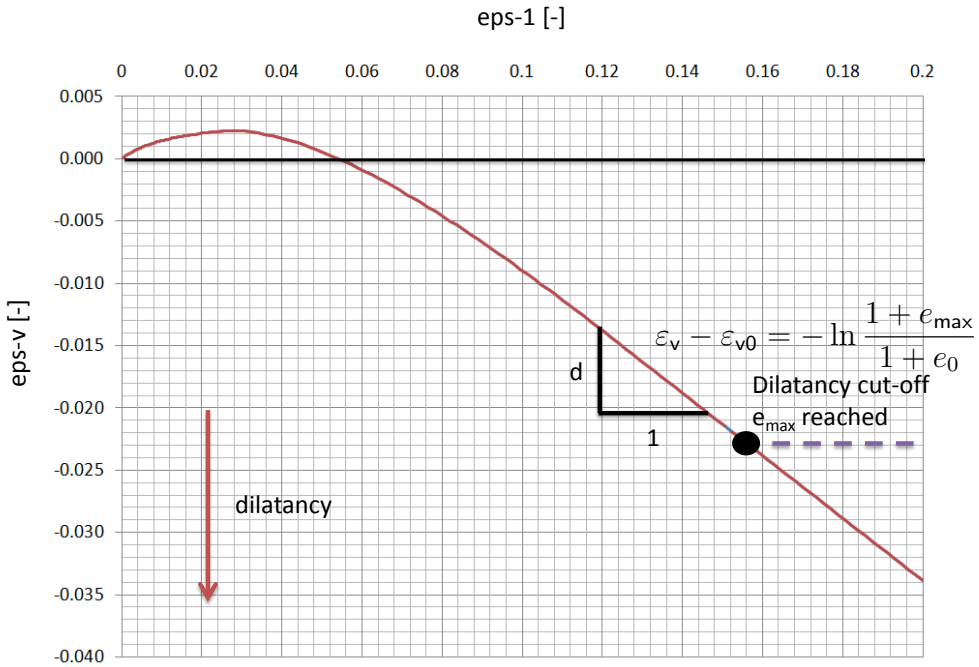

Figure 2.13: Strain curve for a standard triaxial drained compression test with the dilatancy cut-off.

2.1.5 Volumetric mechanism

The volumetric plastic mechanism is introduced to account for a threshold point beyond (preconsolidation pressure) which important plastic straining occur characterizing a normally-consolidated state of soil. Since the shear mechanism generates no volumetric plastic strain in the contractant domain, the model without volumetric mechanism could significantly over-estimate soil stiffness in virgin compression conditions particularly for normally- and lightly overconsolidated cohesive soils. Such a problem can be observed when using, for instance, the Mohr-Coulomb model.

The second yield mechanism is proposed in the form of the cap surface similarly to other hardening models available in ZSoil® , e.g. Modified Cam Clay or Cap. The yield function which is graphically presented in Figure 2.14 and 2.3, is thus defined as:

$$f_2 = \frac{q^2}{M^2 r^2(\theta)} + p'^2 - p_c^2 \tag{2.24}$$

where $r(\theta)$ obeys van Eekelen's formula in order to assure a smooth and convex yield surface (cf. also the formulation of the Modified Cam Clay model); M is the model parameter which defines the shape of the cap surface and is related to K_0^{NC}, and p_c denotes the preconsolidation pressure which defines an intersection of the cap surface with the hydrostatic axis p'.

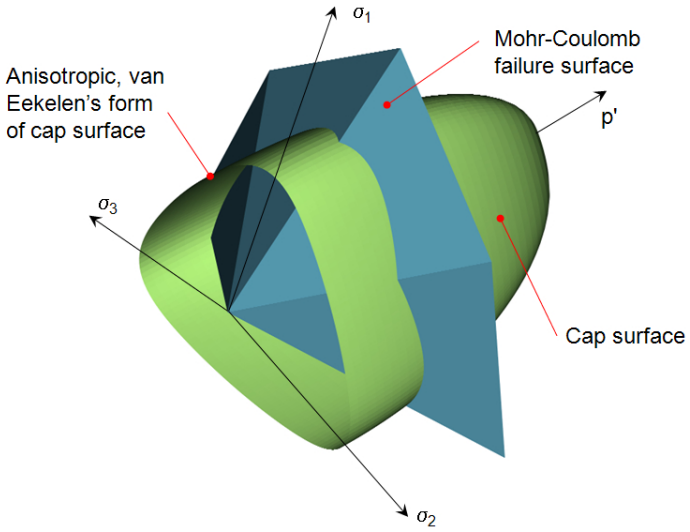

Figure 2.14: 3D representation of strength anisotropy in the HS model with the Mohr-Coulomb failure surface and the cap surface which obeys van Eekelen's formula.

Evolution of the hardening parameter p_c is described by the hardening law (since ZSoil 2020 term $c\cot\phi$ is removed):

$$\mathrm{d}p_c = H \left(\frac{p_c}{\sigma_{\mathrm{ref}}} \right)^m \mathrm{d}\varepsilon_v^p \tag{2.25}$$

where H is the parameter which controls the rate of volumetric plastic strains and is related to the tangent oedometric modulus $\boxed{E_{\mathrm{oed}}}$ at given reference oedometric (vertical) stress level (see Figure 3.7(a)).

The rate of the volumetric plastic strain is then computed:

$$\mathrm{d}\varepsilon_v^p = \mathrm{d}\lambda_2 2\, p' \tag{2.26}$$

Note that the parameters M and H can easily be calculated using internal ZSoil® calculator by providing values of $\boxed{K_0^{\mathrm{NC}}}$ and tangent oedometric modulus $\boxed{E_{\mathrm{oed}}^{\mathrm{ref}}}$ corresponding to the reference oedometric vertical stress $\boxed{\sigma_{\mathrm{oed}}^{\mathrm{ref}}}$; **both must be captured from the primary loading curve (Normal Consolidation Line NCL)**; note that $\boxed{\sigma_{\mathrm{oed}}^{\mathrm{ref}}}$ is used to compute the initial stress point defined by p^* and q^* (see Figure 3.7).

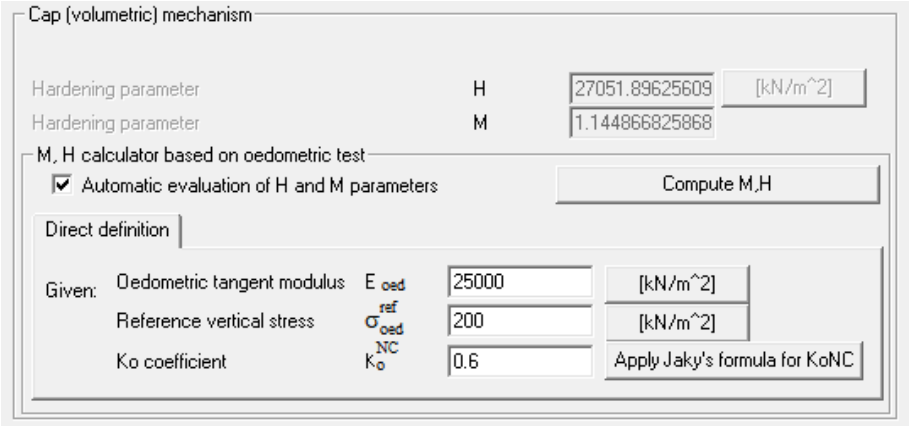

The automatic optimization of M and H must fulfill two conditions:

- K_0^{NC} produced by the model in the oedometric conditions is the same as K_0^{NC} specified by the user.
- E_{oed} generated by the model in the oedometric conditions is the same $E_{\mathrm{oed}}^{\mathrm{ref}}$ specified by the user.

The internal optimization procedure runs a strain driven oedometer test with the vertical strain amplitude $\Delta\varepsilon_v = 10^{-5}$ and the tangent oedometric modulus is computed as $E_{\mathrm{oed}} = \delta\sigma_v/\delta\varepsilon_v \cong \Delta\sigma/\Delta\varepsilon_v$.

The **plastic potential** in the volumetric mechanism is derived from the yield criterion neglecting $r(\theta)$ term (Truty, 2008).

2.1.6 Additional strength criterion

Sometimes, it is necessary to control excessive tensile stresses which are built up during the analysis, particularly when using materials with high values of cohesion. The tensile strength condition is thus described with the Rankine's criterion:

$$f_3 = -\sigma_3 - f_t = 0 \tag{2.27}$$

where $\boxed{f_t}$ is the user-defined tensile strength (default value $f_t = 0$) and σ_3 denotes the minimal principal stress.
The plastic potential is associated with the cut-off condition.

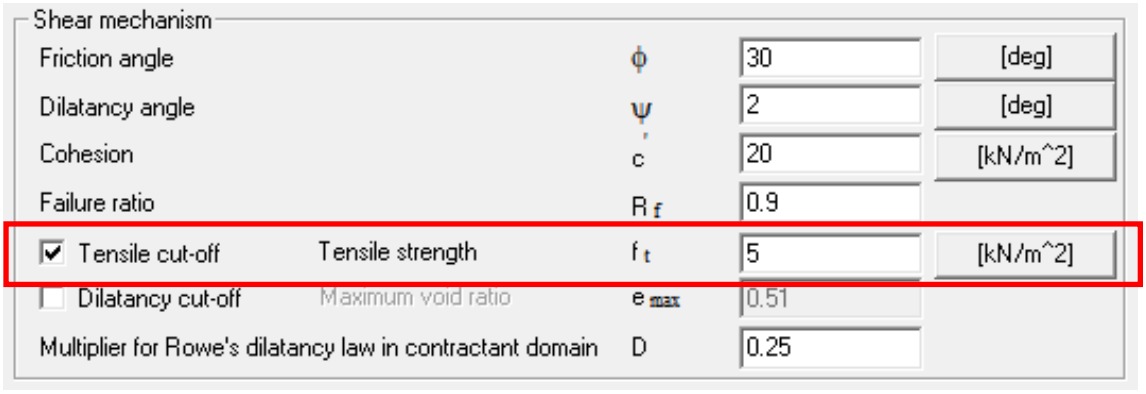

2.1.7 Initial state variables

Setting the initial stress state is necessary for calculating the initial values of hardening parameters γ^{PS} and p_{c0}. This calculation can be performed by a numerical procedure at the beginning of FE analysis based on the initial effective stress conditions $\sigma'_0 = \sigma_0(\sigma'_{x0}, \sigma'_{y0}, \sigma'_{z0})$ and its distance from the maximal stress point $\sigma^{'\mathrm{SR}}$ which is supposed to be experienced by the soil (see Figure 2.17). In order to calculate this distance, the user has to define the following variables:

1. STRESS HISTORY variable which can be set in two ways:
   - through the **overconsolidation ratio** $\boxed{\mathrm{OCR}} = \sigma_{vc}/\sigma'_{v0}$ where σ_{vc} is the **vertical preconsolidation stress** (see Figure 2.15). By applying this option, a constant OCR profile is obtained.
   - through the **maximal preoverburden pressure** offset $\boxed{q^{\mathrm{POP}}} = \sigma_{vc} - \sigma'_{v0}$ (see Figure 2.15). This option is useful to describe the deposits with varying OCR over the depth (typically superficial layers of natural soil subject to mechanical overconsolidation or dessication).

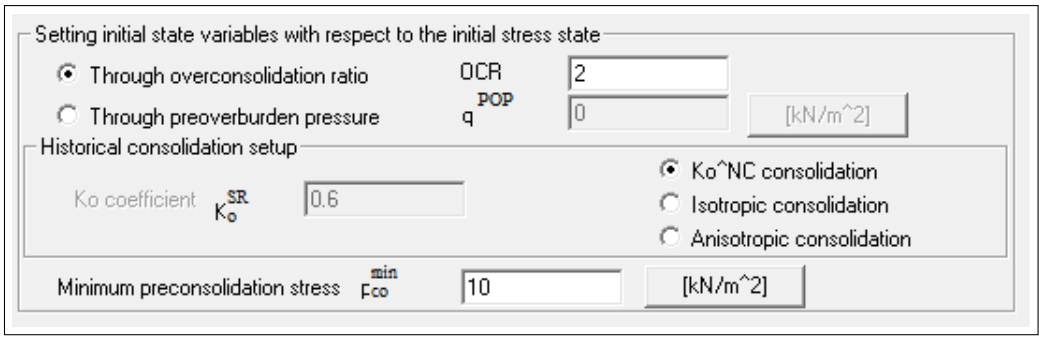

2. HISTORICAL COEFFICIENT OF EARTH PRESSURE AT REST $\boxed{K_0^{\mathrm{SR}}}$ which corresponds to the maximal stress point $\sigma^{'\mathrm{SR}}$ (Figure 2.17), and its value can be assumed as:
   - K_0^{NC} **consolidation**: $K_0^{\mathrm{SR}} = K_0^{\mathrm{NC}}$ (automatically copied from K_0^{NC} cell), applicable to **most study cases** if soil was subject to K_0^{NC} natural consolidation (oedometric conditions), or for simulating a triaxial compression or extension triaxial on a K_0^{NC}-consolidated sample.
   - **Isotropic consolidation**: $K_0^{\mathrm{SR}} = 1$ (automatically assigned) when simulating isotropically consolidated compression or extension triaxial tests.
   - **Anisotropic consolidation**: K_0^{SR} (user-defined) in situations when historical consolidation was different than K_0^{NC}-consolidation specified for $E_{\mathrm{oed}}^{\mathrm{ref}}$.
3. CURRENT IN SITU STRESS CONFIGURATION $\sigma'_0 = \sigma'_0(\sigma'_{x0}, \sigma'_{y0}, \sigma'_{z0})$

$$\sigma'_{y0} = \boxed{\rho} \cdot g \cdot y$$

$$\sigma'_{x0} = \sigma'_{y0} \cdot \boxed{K_{0x}}$$

$$\sigma'_{z0} = \sigma'_{y0} \cdot \boxed{K_{0x}}$$

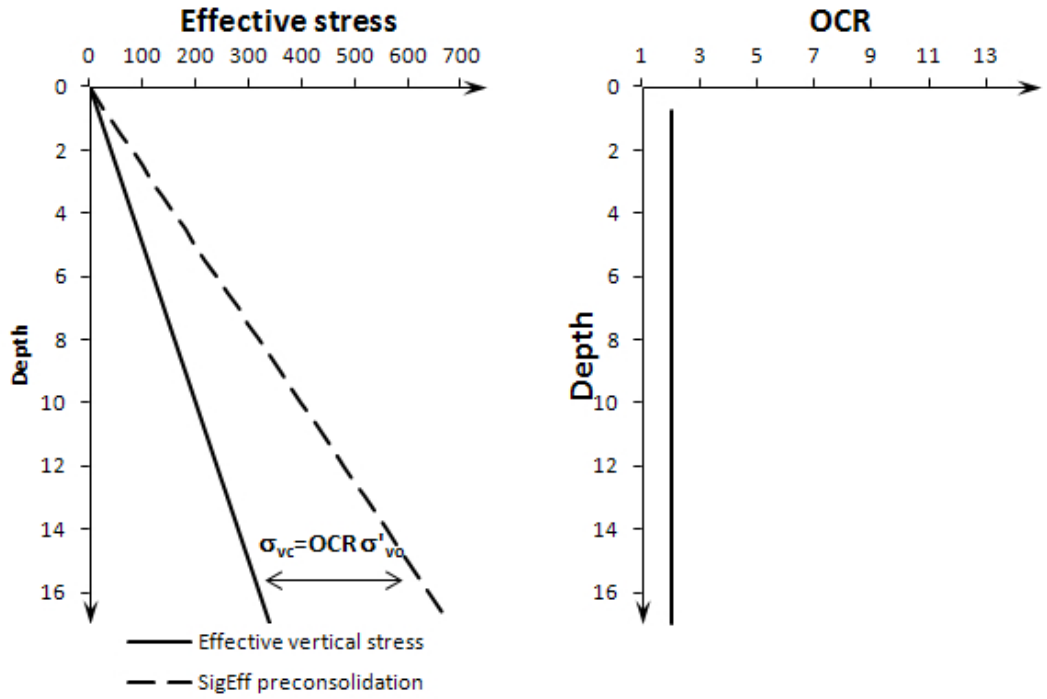

Figure 2.15: Definition of the initial preconsolidation state by means of a constant OCR and the resulting vertical preconsolidation stress σ_{vc}.

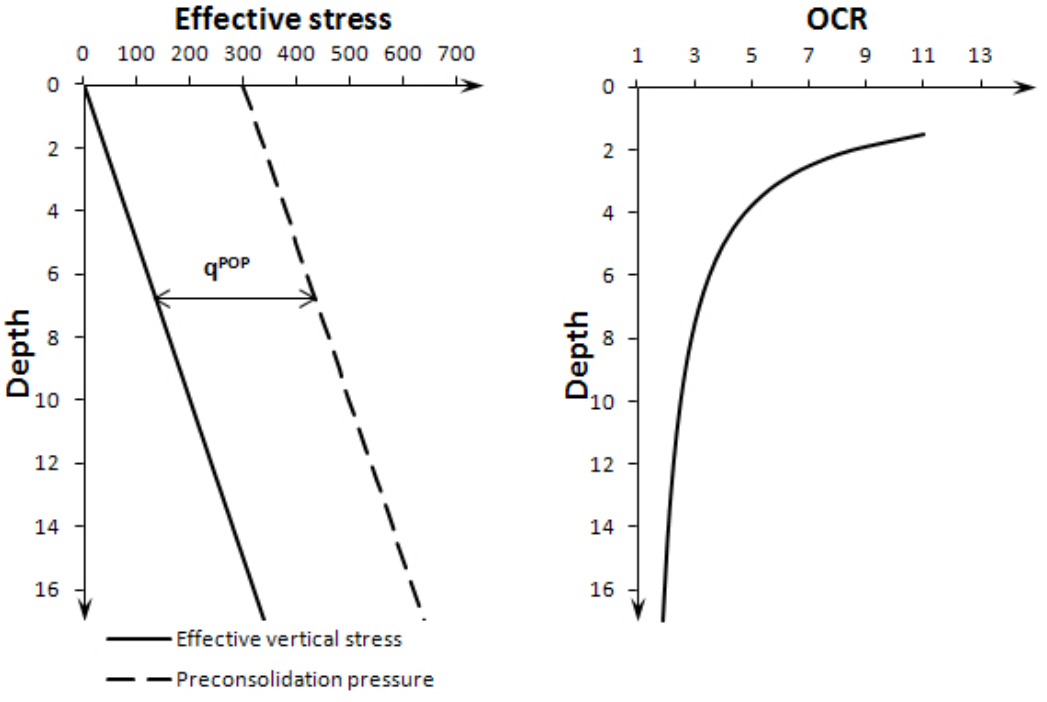

Figure 2.16: Definition the initial preconsolidation state by means of preoverburden pressure q^{POP} and the resulting variable OCR profile (typically observed for superficial soil layers). In such a case, a variable K_0 can also be considered by applying, for instance, Eq. (3.89).

At the beginning of a FE analysis, ZSoil® sets the stress reversal point (SR) with:

$$\sigma_y^{'\mathrm{SR}} = \sigma_y \cdot \mathrm{OCR} \quad \text{or} \quad \sigma_y^{'\mathrm{SR}} = \sigma'_{y0} + q^{\mathrm{POP}} \tag{2.28a}$$

and

$$\sigma_x^{'\mathrm{SR}} = \sigma_y^{'\mathrm{SR}} K_0^{\mathrm{SR}} \quad \text{and} \quad \sigma_z^{'\mathrm{SR}} = \sigma_y^{'\mathrm{SR}} K_0^{\mathrm{SR}} \tag{2.28b}$$

Then ZSoil® uses the calculated $\sigma^{'\mathrm{SR}}$ stress state to compute initial values of the hardening parameter γ_0^{PS} from the condition $f_1 = 0$, and p_{c0} from $f_2 = 0$.

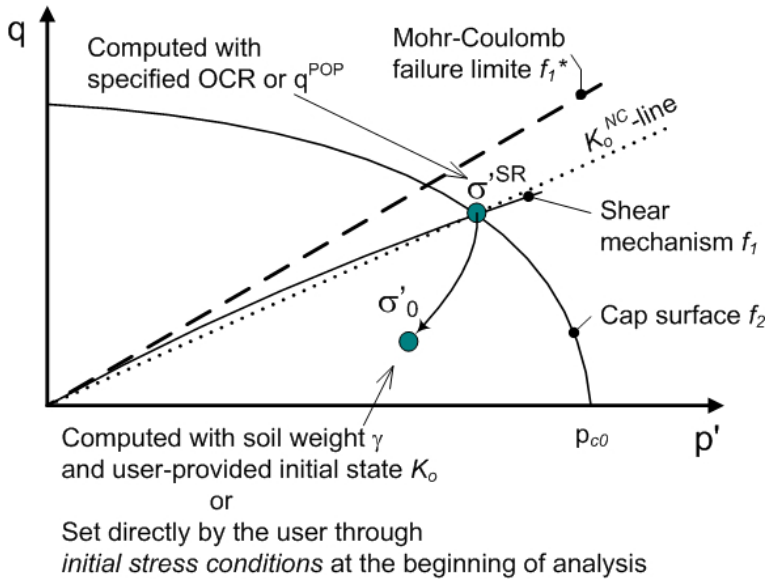

Figure 2.17: Initial stress state setup. Note that for normally-consolidated soil σ'_{SR} coincides with σ'_0, and therefore the *Initial* K_0 *state* which is required to be set by the user is equal to K_0^{NC} specified in the *Non-linear* material menu. For overconsolidated soil, the initial state coefficient K_0 is typically larger than K_0^{NC} (cf. Section 3.3.9).

Note that $\boxed{\sigma'_0}$ in ZSoil® is computed with the *Initial State* driver based on gravity-induced vertical stress and on the user-specified K_0 (*Initial Ko State* menu):

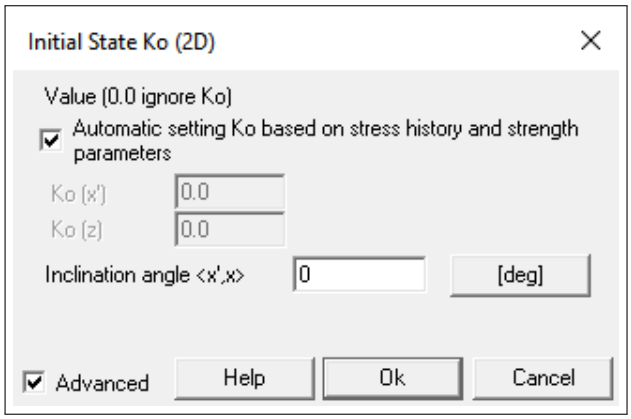

Using the automatic K_0 evaluation option, the initial K_0 profile is computed as a function of the preconsolidation state and the effective friction angle (Mayne and Kulhawy, 1982):

$$K_0 = K_0^{\mathrm{NC}} \mathrm{OCR}^{\sin\phi'} \tag{2.29}$$

with:

$$K_0^{\mathrm{NC}} = 1 - \sin\phi' \tag{2.30}$$

and the upper bound value for K_0 is limited to the passive lateral earth pressure coefficient:

$$K_p = \frac{1 + \sin\phi}{1 - \sin\phi} \tag{2.31}$$

It is worth noting that this option is meaningful for cohesive soils.

The initial K_0 state can also be set via the Preprocessor by applying effective stresses σ'_{x0}, σ'_{y0} ,σ'_{z0} using *Initial stresses* option, Fig.2.18. This option can be useful in the case when imposing a variable K_0 is needed (see an example in Section 5.3).

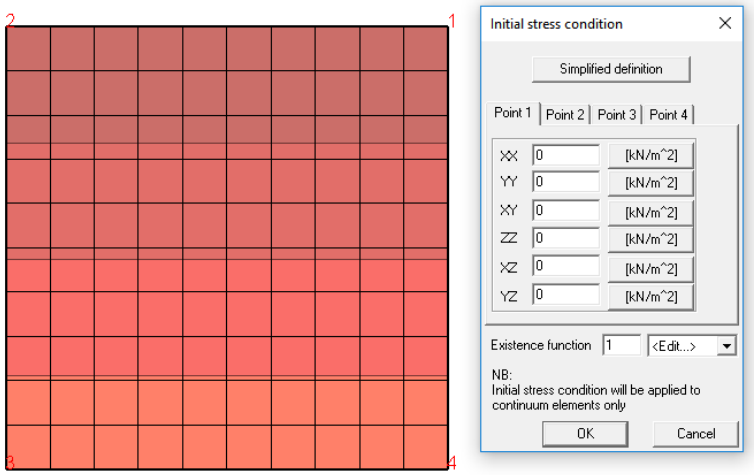

Figure 2.18: Imposing *Initial stresses* option in PrePro.

NB. In whole ZSoil® interface, compressive stresses are negative. In the case of *Deformation+Flow* analysis, the effective stresses have to be introduced when using *Initial stresses* option.

2.1.8 Troubleshooting for Initial State analysis

It may happen that the FE analysis does not converge using the *Initial State* driver. In such a case the following double-check sequence is suggested to be performed:

1. Control whether *Initial* K_0 *State* is specified for each material which is defined by the material formulation *Hardening-Soil*.
2. Control whether K_0 defined in *Initial* K_0 *State* is larger than K_0^{SR} defined in *Non linear* menu of the *HS-small strain stiffness* model.
3. Try to start *Initial State* analysis from a very small *Initial load factor* (e.g. 0.2) applying a very small *Increment* (e.g. 0.1 to 0.4, see below).

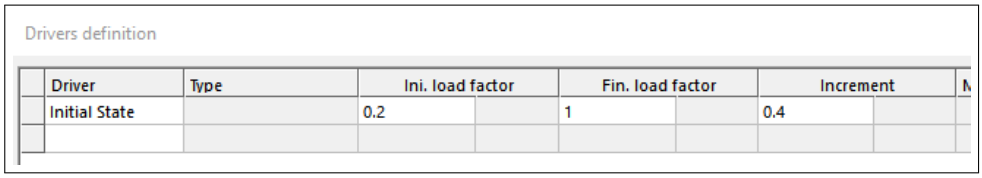

Another efficient way to **converge and accelerate the initial state analysis** is to define the initial stress state via the Preprocessor by means of the *Initial stresses* option (see Fig.2.19). In the *Initial stresses* dialog window, you can put default values for the simplified stress definition which is applied on the whole model domain (i.e. all the soil layers) or bounding box of selected set of elements. This option will help to find the initial guess but the final solution for each soil layer will be computed based on the user-imposed K_0 defined locally in the material definition, Fig. 2.1.7. Setting the initial guess for the initial stresses is also very important when mixture of small and large elements or distorted elements are present in the mesh.

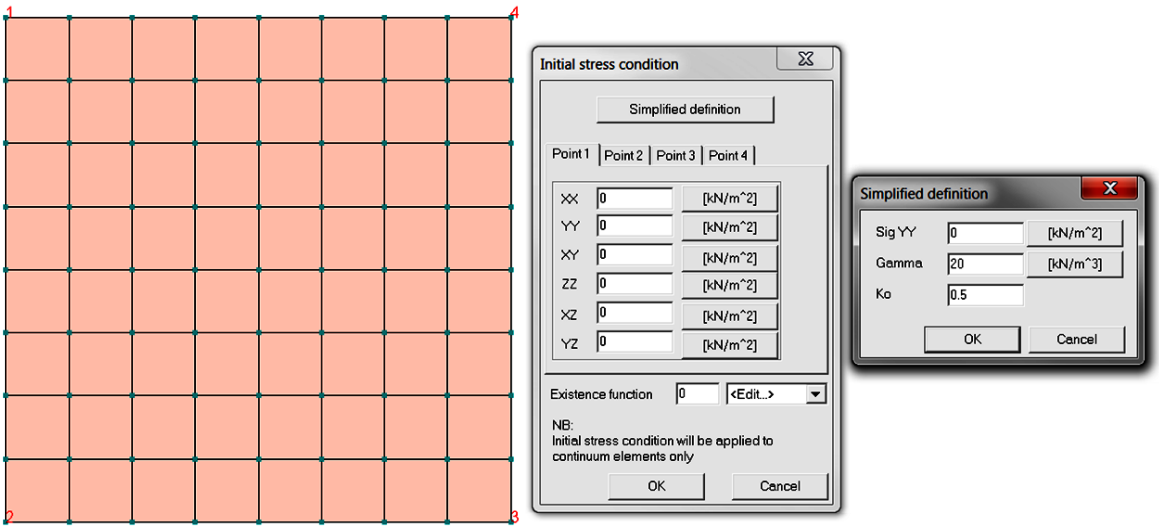

Figure 2.19: Defining initial stresses using simplified definition.

2.2 HS-small and HS-Brick models

The basic HS-standard model can be extended to the HS-small model to account for the S-shaped stiffness reduction as presented in Figure 1.1. In such a case stress paths penetrating the para-elastic domain can be traced using a non-linear elastic stress-strain relationship.

As the HS-small is implemented as an extension of the HS-standard model, the list of model parameters remains the same as for the HS-standard (cf. Table 2.3) and it is only extended with two parameters defining small strain behavior, i.e. the maximal shear modulus $\boxed{G_0}$ and a characteristic shear strain level $\boxed{\gamma_{0.7}}$ at which the secant shear modulus G_s reduces to 70% of its initial value G_0 (alternatively the E_0 modulus can be specified). The effect of small strain stiffness is taken into account in the HS model once the small strain extension is activated (classical HS-small version or the new Brick one)(see below).

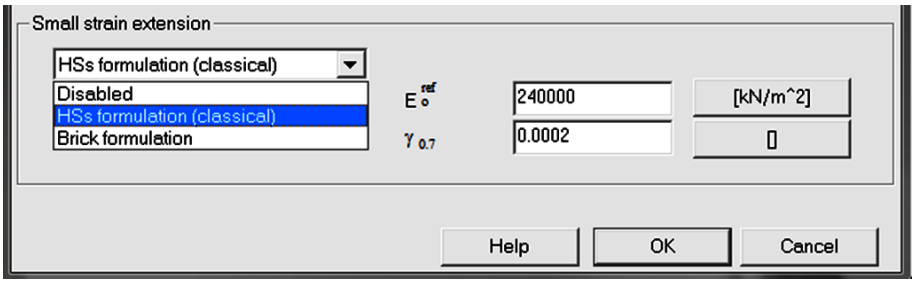

The study cases presented in Section 5.1,5.2 and 5.3 demonstrate sensitivity of numerical simulations to small strain extension. For example, Figures 5.25(a) demonstrate that it is better to run a simulation with underestimated small-strain parameters than not to account for the small-strain stiffness at all.

2.2.1 Non-linear elasticity for small strains

In order to describe the nonlinear S-shaped stiffness reduction, the commonly known in soil dynamics, hyperbolic Hardin-Drnevich relation is adopted. This relation relates the current *secant shear modulus* G_s with an equivalent monotonic shear strain level γ_{hist}, and it takes the following forms:

$$\text{for primary loading:} \qquad \frac{G_s}{G_0} = \frac{1}{1 + a\dfrac{\gamma_{\text{hist}}}{\gamma_{0.7}}} \tag{2.32a}$$

$$\text{for unloading/reloading:} \qquad \frac{G_s}{G_0} = \frac{1}{1 + a\dfrac{\gamma_{\text{hist}}}{2\gamma_{0.7}}} \tag{2.32b}$$

with $a = 0.385$ modifying the original Hardin-Drnevich formula. Note that for $\gamma_{\text{hist}} = \boxed{\gamma_{0.7}}$, the ratio G_s/G_0 is equal to 0.722 which means 72.2% reduction in the case of more accurate considerations (see Figure 2.20).
The equivalent monotonic shear strain is computed from:

$$\gamma_{\text{hist}} = \frac{3}{2}\varepsilon_q \tag{2.33}$$

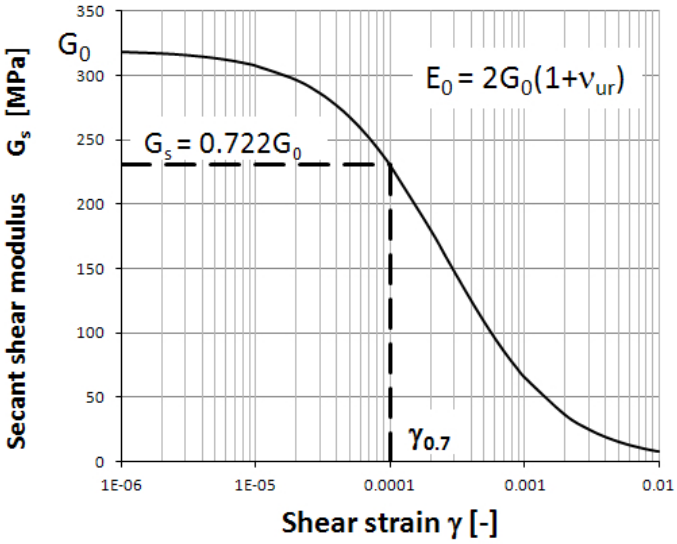

Figure 2.20: Reduction of the secant shear modulus G_s using Eq.(2.32a) and interpretation of the parameter $\boxed{\gamma_{0.7}}$.

with ε_q denoting the second deviatoric strain invariant, and in triaxial test conditions γ_{hist} can be expressed as:

$$\gamma_{\text{hist}} = \varepsilon_1 - \varepsilon_3 \tag{2.34}$$

The corresponding *tangent shear modulus* G can be expressed as:

$$\frac{G}{G_0} = \left(\frac{\gamma_{0.7}}{\gamma_{0.7} + a\gamma_{\text{hist}}} \right)^2 \tag{2.35}$$

The modified Hardin-Drnevich formula is only valid if $\gamma_{\text{hist}} \leq \gamma_c$, with γ_c being the cut-off shear strain at which:

$$G = G_{\text{ur}} \quad \text{where} \quad G_{\text{ur}} = \frac{E_{\text{ur}}}{1 + \nu_{\text{ur}}} \tag{2.36}$$

The *stiffness cut-off* allows applying the Hardin-Drnevich formula in the elastic domain (see Figure 2.21), whereas further stiffness reduction is governed by the hardening mechanism. The cut-off shear strain can be computed from:

$$\gamma_c = \frac{\gamma_{0.7}}{a} \left(\sqrt{\frac{G_0}{G_{\text{ur}}} - 1} \right) \tag{2.37}$$

In Eq. (2.32b), the term $2\gamma_{0.7}$ replaces $\gamma_{0.7}$ appearing in Eq.(2.32a) for virgin loading in order to fulfill Masing's rule which describes the hysteretic behavior in loading/unloading conditions (see Figure). The rule assumes that (*i*) initial tangent shear modulus in unloading is equal to the initial tangent shear modulus during initial loading, and (*ii*) size of the unloading and reloading curves is twice of the initial loading curve.
Although the Hardin-Drnevich law seems to be quite simple its implementation is not straightforward as an efficient tool is needed to detect stress reversal points and the corresponding equivalent shear strain γ_{hist}. Such an implementation was elaborated by Benz (2007) and published in form of a Fortran code in his PhD thesis. However in the recent discussion by

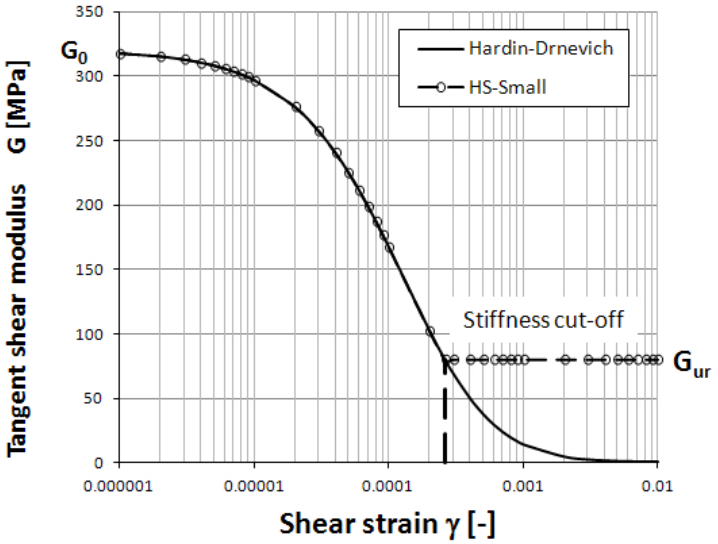

Figure 2.21: Reduction of the tangent shear modulus G in the HS-small model based on Hardin-Drnevich formula (Eq.(2.35)).

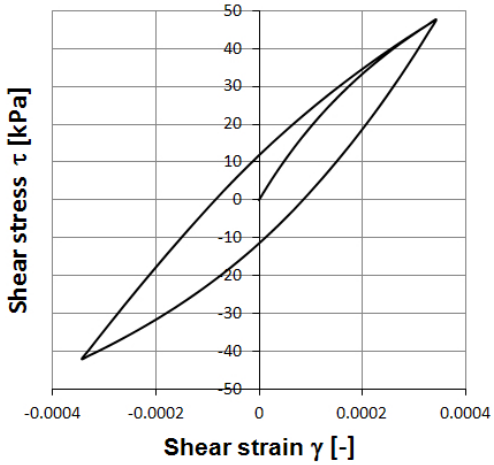

Figure 2.22: Hysteretic soil behavior using Masing's rule.

Niemunis and Cudny (2018) some serious drawbacks of this implementation were detected. In order to shortly describe the problem let us consider a simple triaxial CD test with a complex loading program in which a small stress unloading occurs. The test setup and the vertical loading equivalent to the σ_1 is shown in Figure 2.23. The HS-small vs the new HS-Brick model responses are shown in Figure 2.24. It is clearly visible that the small unloading cycle erases strain history in the HS-small model and a significant stiffness overshooting is generated. This way stress-strain loop becomes open. Such effects may lead to significant deformation underestimation especially in transient analyses (consolidation, dynamics).

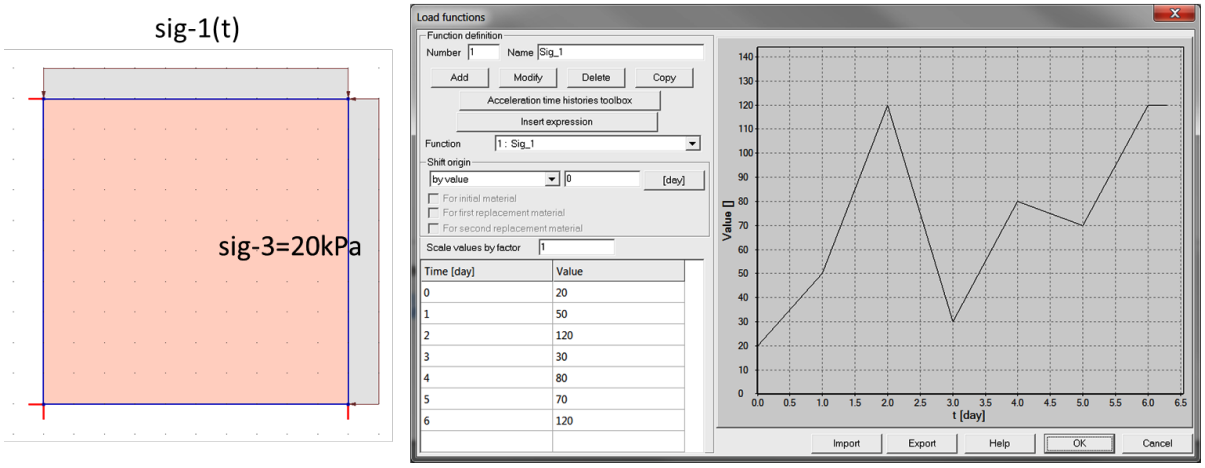

Figure 2.23: Element test on overconsolidated material ($q^{POP} = 150$ kPa) with a complex loading program

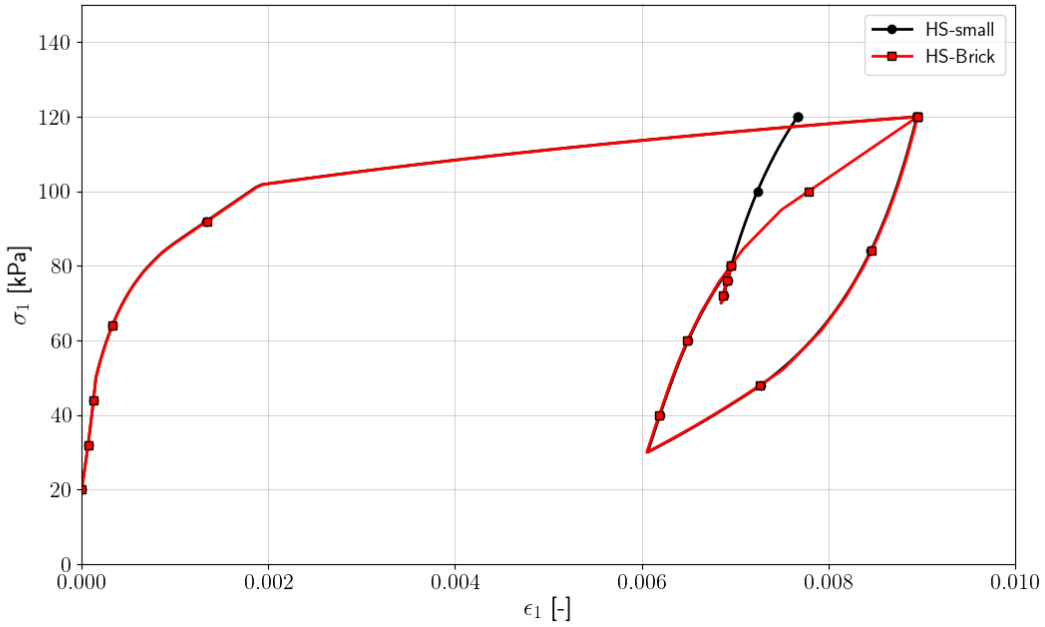

Figure 2.24: $\sigma_1 - \varepsilon_1$ curves for HS-small and HS-Brick small strain extensions

2.2.2 Brick extension to the Hardening Soil model to desribe soil behavior in the range of small strains

The complete theory, equations and all implementation details of the new HS-Brick model are given in the paper by Cudny and Truty (2020). Hence only some basic ideas are presented here. The main goal of the development was to replace the HS-small model tracing strain history algorithm after Benz but to keep the set of HS-small model parameters. The general concept of nested yield surfaces by Mróz et al. (1981) and its specialized version after Simpson et al. (1979); Simpson (1992), called as Brick model, formulated in the strain space, were used to trace stress paths penetrating the interior of current yield surfaces (shear (in the limit the M-C envelope) and cap yield surfaces). This concept is represented in analogy to a man pulling some finite amount of bricks (see Figure 2.25)) on strings. At the initial state strings of different lengths are slack and then when the men is monotonically moving (going in a given direction) strings one by one become progressively taut. The man movement represents strain while strings lengths represent radii of circular yield surfaces in the strain space. Each time the next brick starts to be pulled by a man the reference shear stiffness modulus is degraded in a stepwise manner. This way the S-shaped curve is approximated by a piecewise constant segments (see Figure 2.26). In case when some strings due to the change of the loading direction become loose the high stiffness modulus is regained. In the implemented version of the Brick model, the pulling process is analyzed in general six dimensional strain space. The relative strain distances between the man and $b-$th brick are measured using shear strain invariant γ_b of the strain distance. A general bricks strain history update procedure is given in Win.2-1. In the implementation 10 bricks are used to approximate stiffness degradation curve ($N_b = 10$). Some symbols used in this window are explained in Figure 2.26.

Window 2-1: Updating bricks strain history

Z_Soil

- **For given**:
  - ⋆ bricks strain history: $\boldsymbol{\varepsilon}_n^b \ (b = 1..N_b)$
  - ⋆ total accumulated strain: $\boldsymbol{\varepsilon}_n$
  - ⋆ string lengths: $s^b \ (b = 1..N_b)$
  - ⋆ stiffness degradation factors: $\Delta\omega_G^b$
  - ⋆ reference small strain shear modulus: G_0^{ref}
  - ⋆ strain increment: $\Delta\boldsymbol{\varepsilon}_{n+1}$
- **Update**: $\boldsymbol{\varepsilon}_{n+1}, \ \boldsymbol{\varepsilon}_{n+1}^b$
- **Compute** current reference shear tangent stiffness modulus: $G_{\text{t}}^{\text{ref}}$
- **Initialize**: $\omega_G = 0.0, \ \boldsymbol{\varepsilon}_{n+1} = \boldsymbol{\varepsilon}_n + \Delta\boldsymbol{\varepsilon}_{n+1}$
- **Loop** over each brick b
  - ⋆ Compute strain distance: $\tilde{\boldsymbol{\varepsilon}}^b = \boldsymbol{\varepsilon}_{n+1} - \boldsymbol{\varepsilon}_n^b$
  - ⋆ Compute strain distance deviator: $\tilde{\mathbf{e}}^b = \tilde{\boldsymbol{\varepsilon}}^b - \frac{1}{3}\mathbf{1}^{\mathsf{T}}\tilde{\boldsymbol{\varepsilon}}^b\mathbf{1}$
  - ⋆ Compute: $\gamma_{n+1}^b \left(\tilde{\mathbf{e}}^b\right)$
  - ⋆ **if** $\gamma_{n+1}^b \leq s^b$
    - ♦ string of b-th brick is slack
  - ⋆ **else**
    - ♦ String of b-th brick is taut
    - ♦ Compute relative distance: $d^b = \left(\gamma_{n+1}^b - s^b\right)/\gamma_{n+1}^b$
    - ♦ Update: $\omega_G = \omega_G + \Delta\omega_{\text{G}}^b$
    - ♦ Update brick strain history: $\boldsymbol{\varepsilon}_{n+1}^b = \boldsymbol{\varepsilon}_n^b + d^b \ \left(\boldsymbol{\varepsilon}_{n+1} - \boldsymbol{\varepsilon}_{n+1}^b\right)$
- **Compute** reference tangent shear stiffness modulus: $G_{\text{t}}^{\text{ref}} = (1 - \omega_G) \ G_0^{\text{ref}}$

Window 2-1

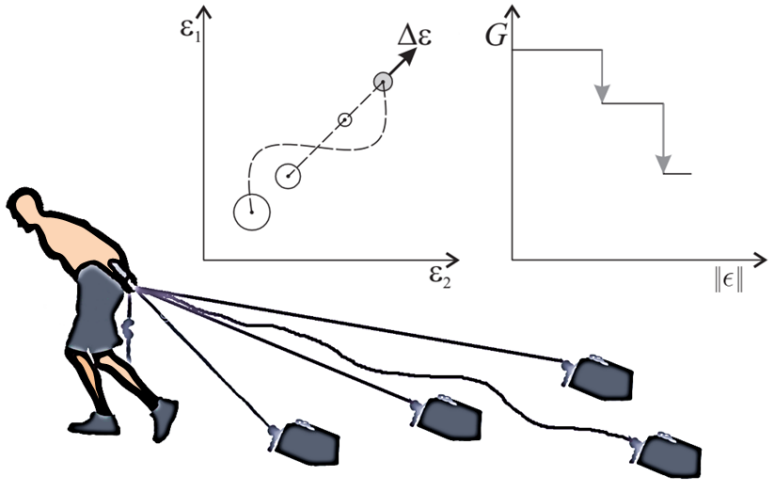

Figure 2.25: Brick model analogy

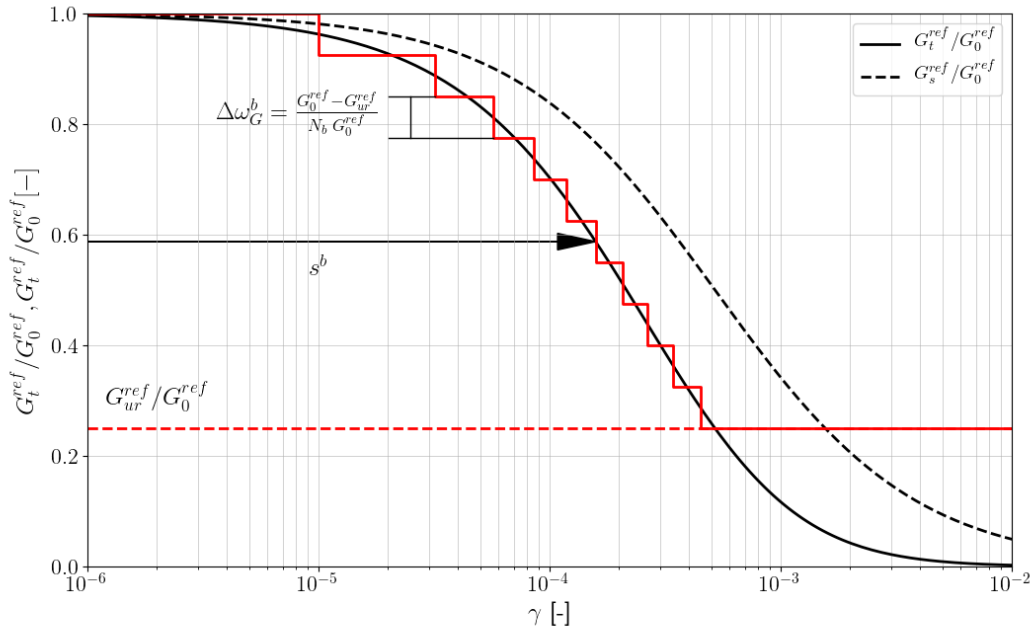

Figure 2.26: Stepwise approximation of shear stiffness reduction curve

As it has been shown in the paper by Cudny and Truty (2020) HS-Brick behavior is superior with respect to the classical HS-small model. All technical details and algorithmic aspects are disscussed in this paper.

2.2.3 Modifications of the plastic part for the HS-small and HS-Brick models

The HS-small and HS-Brick models also require some modifications in the plastic part of the HS-standard code. These modifications concern the plastic flow rule and dilatancy in the domain of contractancy.

Introducing the cut-off for the contractancy domain (as it is in the HS-standard model, cf. Eq.(2.18a)) could yield too small volumetric strains. Therefore, allowing a certain amount of contractancy for the mobilized friction angle ϕ_m before it reaches the critical state ($\phi_m < \phi_{cs}$). Introducing the scaling parameter $\boxed{D}$ into Eq.(2.18b) match Rowe's dilatancy in the contractancy domain to the formula proposed by Li and Dafalias (2000), see Figure 2.27. The Rowe's dilatancy law for the HS-small and HS-Brick models is reformulated as follows:

$$\sin\psi_m = D\frac{\sin\phi_m - \sin\phi_{cs}}{1 - \sin\phi_m \sin\phi_{cs}} \tag{2.38a}$$

where:

$$D = 0.25 \quad \text{if} \quad \sin\psi_m < \sin\phi_{cs} \tag{2.38b}$$

$$D = 1.00 \quad \text{if} \quad \sin\psi_m \geq \sin\phi_{cs} \tag{2.38c}$$

Parameter D is automatically updated to the value 0.25, once the small strain extension is activated.

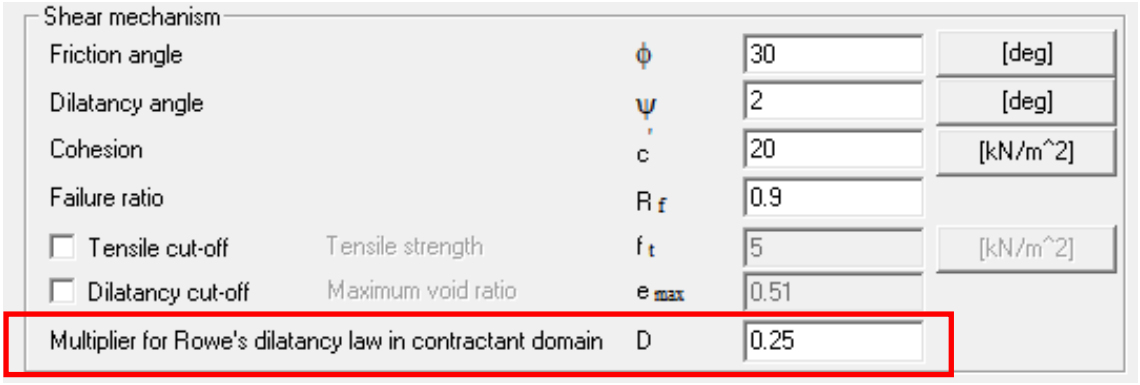

Another modification concerns the hardening laws for parameters γ^{PS} and p_c. The modification is executed by introducing h_i function which is required for an appropriate approximation of $\gamma - G$ curve in the case when a stress path starts directly from one or two yield surfaces. Evolution of the hardening parameters is defined as follows:

$$\mathrm{d}\gamma^{\mathrm{PS}} = \mathrm{d}\lambda_1 h_i \left(\frac{\partial g_1}{\partial \sigma_1} - \frac{\partial g_1}{\partial \sigma_2} - \frac{\partial g_1}{\partial \sigma_3}\right) = \mathrm{d}\lambda_1 h_i \qquad \text{for shear mechanism} \tag{2.39}$$

and

$$\mathrm{d}p_c = \mathrm{d}\lambda_2 2H h_i \left(\frac{p_c}{\sigma_{\mathrm{ref}}}\right)^m p \qquad \text{for volumetric mechanism} \tag{2.40}$$

with the function h_i being defined as:

$$h_i = G_m^{1+\frac{E_{\mathrm{ur}}}{2E_{50}}} \tag{2.41}$$

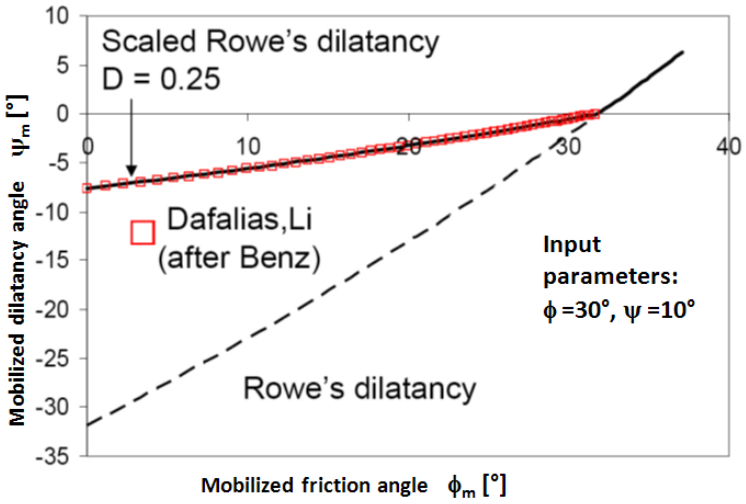

Figure 2.27: Scaled Rowe's dilatancy vs the formula proposed by Li and Dafalias (2000).

where the stiffness multiplier G_m is calculated as:

$$G_m = \min(\frac{G_t}{G_{\text{ur}}}) \tag{2.42}$$

Table 2.3: List of parameters defining the HS-standard and HS-small/HS-Brick models.

Parameter	Unit	HS-standard	HS-small/HS-Brick	Function
Stress dependency type		✓	✓	defines stiffness moduli stress dependency function which is based on $\sigma_3 + c\,\cot\phi$, pure σ_3 or p
Small strain formulation		–	✓	defines whether classical HS-small or HS-Brick (recommended) version is to be used
E_0^{ref}	[kPa]	–	✓	defines the initial tangent slope of $\varepsilon_1 - q$ curve at the reference minor principal stress σ_3^{ref}
$\gamma_{0.7}$	[–]	–	✓	defines a characteristic shear strain level γ_s at which the ratio $G_s/G_0 = 0.722$
$E_{\text{ur}}^{\text{ref}}$	[kPa]	✓	✓	defines unloading/reloading stiffness at engineering strains ($\varepsilon \approx 10^{-3}$) at the reference minor principal stress σ_3^{ref}
E_{50}^{ref}	[kPa]	✓	✓	defines the secant stiffness at 50% of the ultimate deviatoric stress q_f at the reference minor principal stress σ_3^{ref}
σ^{ref}	[kPa]	✓	✓	reference stress used to scale stiffness moduli E_0^{ref}, $E_{\text{ur}}^{\text{ref}}$, E_{50}^{ref} to current values with respect to a current minor principal stress σ_3 (or a current mean stress p' if this formulation is selected)
m	[–]	✓	✓	defines stress dependent stiffness through Eq.(2.6)
ν_{ur}	[–]	✓	✓	defines the ratio $\varepsilon_3/\varepsilon_1$ in an unloading-reloading cycle (elastic deformations)
R_f	[–]	✓	✓	used to compute the hardening parameter γ^{PS} with the use of the asymptotic deviatoric stress q_a defining the hyperbolic function f_2 (default $R_f = 0.9$)
c'	[kPa]	✓	✓	defines the intercept of the Mohr-Coulomb line at null stress condition
ϕ'	[^{o}]	✓	✓	defines the slope of the Mohr-Coulomb yield criterion
ψ	[^{o}]	✓	✓	defines the maximal slope of $\varepsilon_1 - \varepsilon_v$ curve for dilatancy
e_{max}	[–]	✓	✓	defines the cut-off limit corresponding to the maximal void ratio observed in material at the ultimate state
f_t	[kPa]	✓	✓	defines the maximal tensile strength for material
D	[–]	✓	✓	controls Rowe's dilatancy law in the contractancy domain (default $D = 0$ for HS-Std, $D = 0.25$ for HS-SmallStrain)
M	[–]	✓	✓	defines the shape of the elliptical cap yield surface
H	[kPa]	✓	✓	defines the rate of the plastic volumetric strain and the preconsolidation pressure
OCR or q^{POP}	[–] or [kPa]	✓	✓	sets the initial position of stress with respect to the cap surface and it is used to compute the hardening parameter γ^{PS} and p_{c0}
K_0^{SR}	[–]	✓	✓	sets a historical position of the stress point $\sigma^{\text{'SR}}$ ($K_0^{\text{SR}} = \sigma_h^{\text{'SR}}/\sigma_v^{\text{'SR}}$) with respect to the initial stress configuration for an overconsolidated material and it is used to compute the hardening parameter γ^{PS} and and p_{c0}

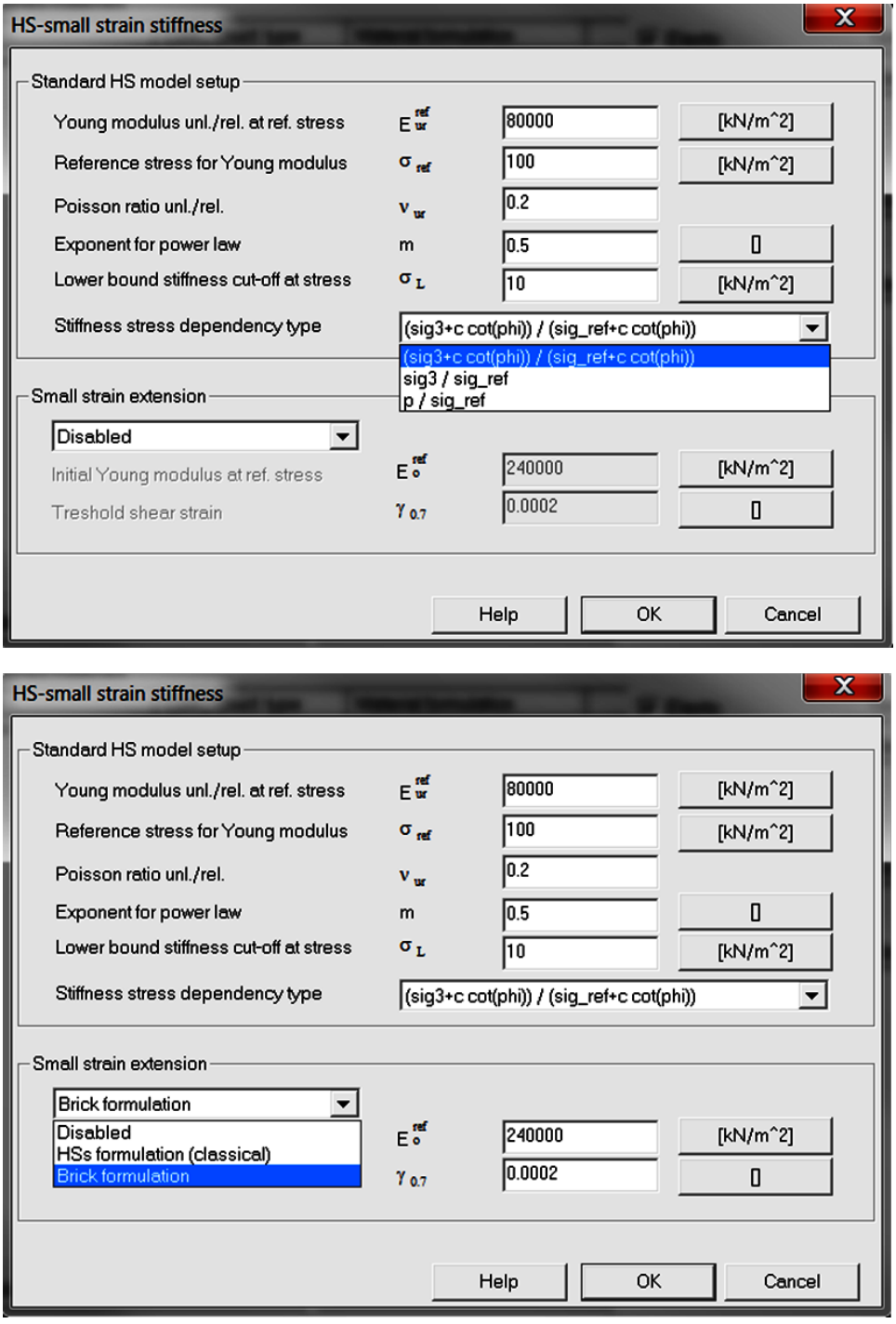

Figure 2.28: Dialog window for the *Elastic* group of parameters which define the HS model including the small strain extension (in the top window possible choices of stiffness stress dependency (barotropy) is shown while in the bottom one possible small strain extensions.

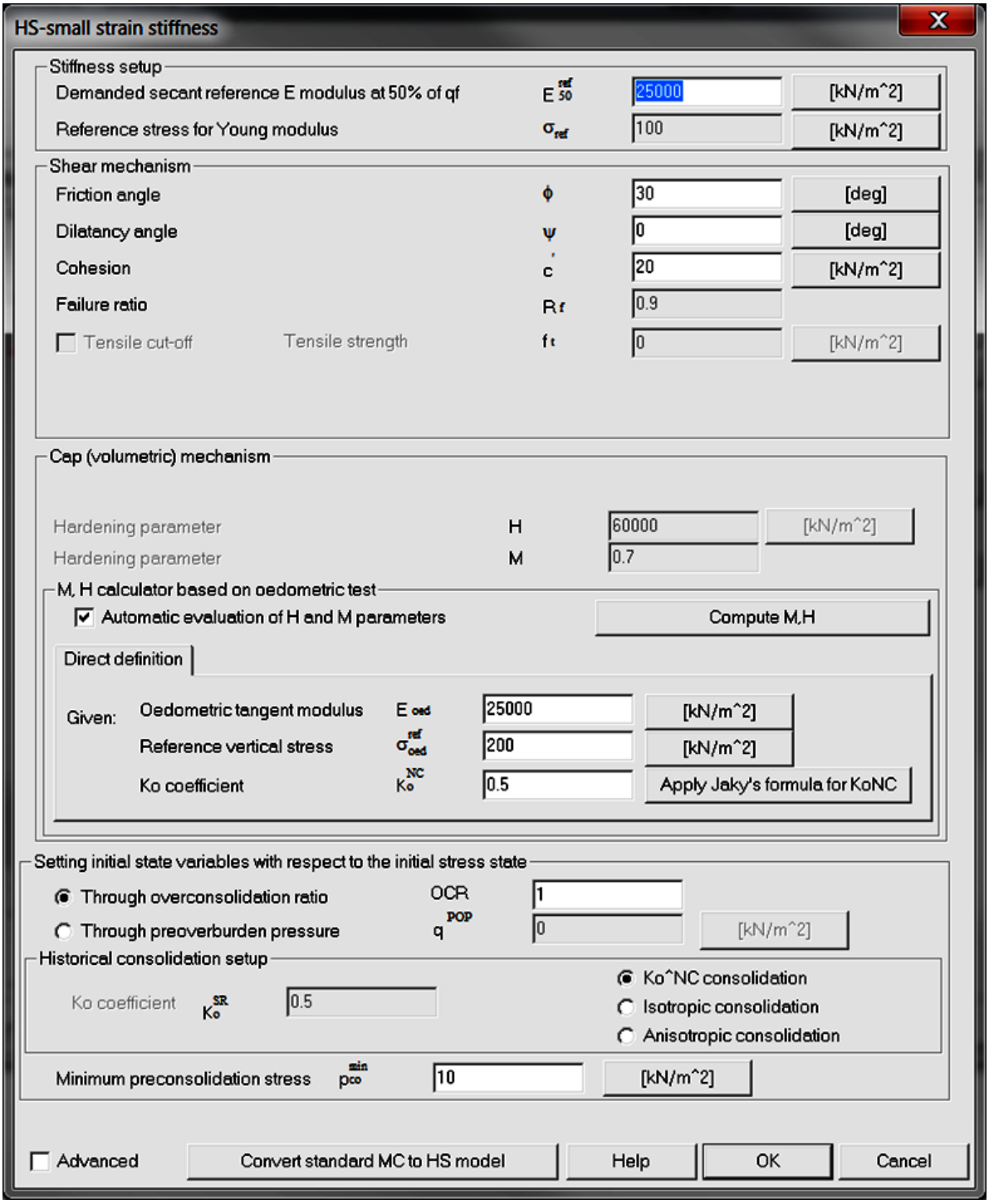

Figure 2.29: Dialog window for the *Nonlinear* group of parameters which define the HS model including the initial state setup.

2.3 Model parameters

Although the HS model is mathematically complex, its parameters have the physical meaning and they can be derived from the standard laboratory test, i.e. the triaxial compression and oedometer tests. A complete list of parameters that the user needs to specify before running application is provided in Table 2.3. The details related to the identification of specific parameters are provided in the subsequent Chapter 3.

The following abbreviations apply to Table 2.4:

- CICD - triaxial test: consolidated isotropically compression drained
- CICU - triaxial test: consolidated isotropically compression undrained
- OED - oedometer test
- CPT - cone penetration test
- CPTU - piezocone cone penetration test
- DMT - Marchetti's dilatometer test
- SCPTU - piezocone cone penetration test with seismic sensor
- DMT - Marchetti's dilatometer test with seismic sensor
- SPT - standard penetration test

Table 2.4: List of parameters which should be provided by the user (advanced parameters in gray).

Model parameter	Unit	Direct estimation test	Alternative test or solution
Small stiffness (HS-SmallStrain only)			
E_0^{ref}	[kPa]	SCPT, DMT or bore-hole, cross-hole or other geophysical method	unloading-reloading branch of CICD; geotechnical evidence; sands: CPT
$\gamma_{0.7}$	[–]	CICD with local gauges	geotechnical evidence
Elastic constants			
$E_{50}^{\text{ref}}(\sigma^{\text{ref}})$	[kPa]	min. 1 CICD at σ_3^{ref}	sands: CPT
$E_{\text{ur}}^{\text{ref}}(\sigma^{\text{ref}})$	[kPa]	min. 1 CICD at σ_3^{ref} geotechnical evidence	
σ^{ref}	[kPa]	1 CICD	
ν_{ur}	[–]	min. 1 CICD with unloading-reloding curve	geotechnical evidence
m	[–]	3 CICD at different σ_3	geotechnical evidence
Shear mechanism			
c	[kPa]	3 CICD or CICU at different σ_3	
ϕ	[^{o}]	3 CICD or CICU at different σ_3	geotechnical evidence; sand: CPT, DMT, PMT, SPT
ψ	[^{o}]	min. 1 CICD	geotechnical evidence
R_f	[–]	min. 1 CICD	default $R_f = 0.9$, geotechnical evidence
e_{max}	[–]	min. 1 CICD on a dense or preconsolidated soil specimen	geotechnical evidence
f_t	[kPa]	isotropic extension	default $f_t = 0$
D	[–]	min. 1 CICD	default D=0 for HS-Standard and D=0.25 HS-SmallStrain
Volumetric (cap) mechanism			
$E_{\text{oed}}^{\text{ref}}(\sigma_{\text{oed}}^{\text{ref}})$	[kPa]	min.1 OED	clays: CPT, DMT
$\sigma_{\text{oed}}^{\text{ref}}$	[kPa]	idem	idem
Initial state variables (soil history)			
OCR or q^{POP}	[–/kPa]	min. 1 OED	clay: CPT, CPTU, DMT
K_0^{SR}	[–]	K_0-consolidation	"Jaky's formula"

The table below presents typical ranges of HS-model parameters in soils. It also indicates relvant sections where the intersted user may find more information about parameter estimation in case of lack laboratory data.

Table 2.5: Typical values and ranges for parameters of the HS model.

Model parameter	Unit	Coarse soils	Fine soils
		Small stiffness (HS-SmallStrain only)	
E_0^{ref}	[kPa]	Sec.3.2.1	Sec.3.3.1
$\gamma_{0.7}$	[–]	$7 \cdot 10^{-5} < \gamma_{0.7} < 4 \cdot 10^{-5}$ cf. Sec.3.2.1	$\gamma_{0.7} > 9 \cdot 10^{-5}$ cf. Sec.3.3.1
		Elastic constants	
$E_{50}^{\text{ref}}(\sigma^{\text{ref}})$	[kPa]	$E_{\text{ur}}^{\text{ref}}/3$, cf.3.2.2	$E_{\text{ur}}^{\text{ref}}/3$, cf. Sec.3.3.5
$E_{\text{ur}}^{\text{ref}}(\sigma^{\text{ref}})$	[kPa]	Sec.3.2.2	Sec.3.3.5
σ^{ref}	[kPa]	typically taken as 100 kPa, cf. also in Virtual Lab report	
ν_{ur}	[–]	$0.15 < \nu_{\text{ur}} < 0.25$, cf. Sec.3.2.4	
m	[–]	0.5, cf. Sec.3.2.5	$0.5 < m < 1.0$, cf. Sec.3.3.7
		Shear mechanism	
c'	[kPa]	$0 \div 5$	≥ 0
ϕ'	[^{o}]	$25^o < \phi < 50^o$ cf. Sec.3.2.6	$18^o < \phi < 42^o$ cf. Sec.3.3.2
ψ	[^{o}]	Sec.3.2.7	cf. Sec.3.3.4
R_f	[–]	$0.75 < R_f < 1$ with average $R_f = 0.9$, cf. Sec.3.3.3	
e_{max}	[–]	Sec.3.2.9	Sec.3.3.10
f_t	[kPa]	default $f_t = 0$	
D	[–]	default D=0 for HS-Standard and D=0.25 HS-SmallStrain	
		Volumetric (cap) mechanism	
$E_{\text{oed}}^{\text{ref}}(\sigma_{\text{oed}}^{\text{ref}})$	[kPa]	$\approx E_{50}^{\text{ref}}(\sigma_{\text{ref}})$, cf. Sec.3.2.3 and 3.3.6	
$\sigma_{\text{oed}}^{\text{ref}}$	[kPa]	$\approx \sigma_{\text{ref}}/K_0^{\text{NC}}$, cf. Sec.3.2.3	
K_0^{NC}	[–]	good-working equation: $K_0^{\text{NC}} = 1 - \sin\phi'$	
		Initial state variables (soil history)	
OCR or q^{POP}	[–/kPa]	$\text{OCR} \geq 1$ or $q^{\text{POP}} \geq 0$	
K_0^{SR}	[–]	$= K_0^{\text{NC}}$ for natural soils, cf. Sec. 2.1.7	
K_0	[–]	good-working equation: $K_0 = K_0^{\text{NC}}\text{OCR}^{\sin\phi'}$, cf. Sec.3.3.9	

Chapter 3

Parameter determination

As most of the constitutive models for soils, the **HS-standard** model has been designed based on behavior of soil specimen which is observed during laboratory tests with the use of standard devices such as triaxial cell and oedometer. Therefore, still responding to certain test requirements such as drained compression, model parameters can be derived directly from the experimental curves. Direct parameter identification is presented in Section 3.1. Sometimes, the test requirements cannot be fulfilled (e.g. performing drained compression test on low permeable clay specimen may prove to be too time consuming). Then, the model can still be calibrated using, for instance, the measurements derived from the undrained triaxial compression test or the model parameters can be estimated based on results obtained through *in situ* tests or approximated using parameter correlations observed in geotechnical practice. Such an indirect parameter determination is presented in Section 3.2 for sand type materials, and in Section 3.3 for cohesive soils.
Additional parameter which describes the small stain stiffness in **HS-small** and **HS-Brick** models can easily be determined using the measurements derived from one of the *in situ* probes equipped with a seismic sensor which allows measuring the velocity of shear waves. Owing to time and economical constraints of laboratory testing, and the effect of specimen disturbances during soil sampling, the use of laboratory devices to determine G_0 seems less reasonable. Nevertheless, an approximate value of G_0 can be derived from unloading-reloading branch derived from the triaxial compression test.

The following sections provide a comprehensive guideline on parameter identification which may help the user to effectively apply the advanced constitutive models. In this context, the guideline may be helpful in specifying an appropriate testing program or making use of already acquired experimental results which need a specific treatment in order to estimate model parameters.

3.1 Experimental testing requirements for direct parameter identification

3.1.1 Direct parameter identification for the Hardening-Soil Standard

Direct parameter identification for the HS-standard model requires the use of two commonly used laboratory devices:

- **triaxial cell** with consolidated isotropically drained compression test (CICD); three programmed compression tests at different confining pressures σ_3 should provide:
  - ⋆ stress paths in $p' - q$ plane which are used to determine strength parameters $\boxed{\phi}$ $(= \phi')$ and $\boxed{c}(= c')$, according to Figure 3.1 or Mohr's circles;
    Note that ϕ and c can also be derived from the undrained compression test[1] (CU) considering that the failure stress envelopes derived from drained and undrained tests are essentially similar, see an example in Figure 3.2;
  - ⋆ relationships $\varepsilon_1 - q$ which is used to determine unloading-reloding modulus $\boxed{E_{\text{ur}}}$[2,3], as shown in Figure 3.4; secant modulus $\boxed{E_{50}}$ and failure ratio $\boxed{R_f}$ according to Figure 3.3; and stiffness stress dependency parameter $\boxed{m}$ according to Figure 3.5;
  - ⋆ relationships $\varepsilon_1 - \varepsilon_v$ which is used to determine the dilatancy angle $\boxed{\psi}$ and the maximal void ratio $\boxed{e_{max}}$, as shown in Figure 3.6.
- **oedometer**; the test should provide pre- and post-yield evolution of the void ratio (or specimen height) with respect to changes of vertical effective stress, $\sigma'_v - e$, which is used to estimate:
  - ⋆ the preconsolidation pressure σ'_c for cohesive deposits, which is then used to determine the overconsolidation ratio $\boxed{\text{OCR}}$ defined as:

$$\text{OCR} = \frac{\sigma'_c}{\sigma'_{v0}} \tag{3.1}$$

  - ⋆ the tangent oedometric stiffness $\boxed{E_{\text{oed}}}$ for corresponding $\boxed{\sigma^{\text{ref}}_{\text{oed}}}$ which have to be captured from the primary loading curve[4] (postyield branch), see Figure 3.7.

The preconsolidation pressure σ'_c understood as a threshold point beyond which the important plastic straining occur, is difficult to establish unambiguously. Among a number of methods proposed in literature for determining σ'_c, the following ones are commonly used owing to their simplicity:

[1] In the case of the undrained test, the maximum principal stress ratio $(\sigma'_1/\sigma'_3)_{\text{max}}$ and the maximum deviatoric stress $(\sigma_1 - \sigma_3)_{\text{max}}$ can be considered as the failure criteria.

[2] Note that E_{ur} corresponds to Young's modulus E which is specified by the user in Mohr-Coulomb or Cap model.

[3] Note that $E_0 > E_{\text{ur}} > E_{50}$ or $G_0 > G_{ur} > G_{50}$.

[4] This condition implies that at given oedometric pressure, both shear and volumetric mechanisms are active following K_0^{NC} consolidation line, as shown in Figure 3.7(b).

- empirical, graphical Casagrande's method (Casagrande, 1936), see Figure 3.9(a),
- simple graphical method proposed by Pacheco-Silva (1970), see Figure 3.9(b),
- and as a last resort, σ'_c can be taken as the vertical stress which corresponds to the intersection point of the reloading and the virgin compression lines, cf. Figure 3.9(a).

It should be noticed that the *in situ* preconsolidation pressure may vary from that derived from laboratory tests considering specimen disturbances due to sampling, transporting or specimen trimming, etc. Leroueil et al. (1983a) demonstrated that the *in situ* preconsolidation pressure is observed as:

$$\sigma'_{c,\text{in situ}} = \alpha \cdot \sigma'_{c,\text{lab}} \tag{3.2}$$

where $\alpha = 1.1$ for normally consolidated clays ($\mathrm{OCR} < 1.2$), $\alpha = 1.0$ for lightly overconsolidated clays ($1.2 < \mathrm{OCR} < 2.5$), and $\alpha = 0.9$ for overconsolidated clays ($2.5 < \mathrm{OCR} < 4.5$).

$\boxed{E_{\text{oed}}}$ and $\boxed{\sigma^{\text{ref}}_{\text{oed}}}$ are the input variables which are used to calculate parameters M and H with the aid of the internal ZSoil® calculator, see material interface for nonlinear characteristics of the HS model.
Clearly, the tangent oedometric modulus E_{oed} can also be determined from:

$$E_{\text{oed}} = \frac{2.3(1+e_0)}{C_c}\sigma_v \tag{3.3}$$

Note that the above definition is correct when the stress point is on the primary loading curve.

In the case of incompleteness of experimental results, the input model parameters can be estimated using approximative parameter correlations which are provided in Section 3.2 and 3.3.

Sometimes, the compression index C_c can also be expressed through the isotropic compression index λ which is the slope of the virgin compression line plotted in $\ln p' - e$ axes. Since $\log_{10} x = 0.43 \ln x$, one can derive:

$$C_c = 2.3\lambda \tag{3.4}$$

A number of correlations for estimating C_c are provided in Appendix B.

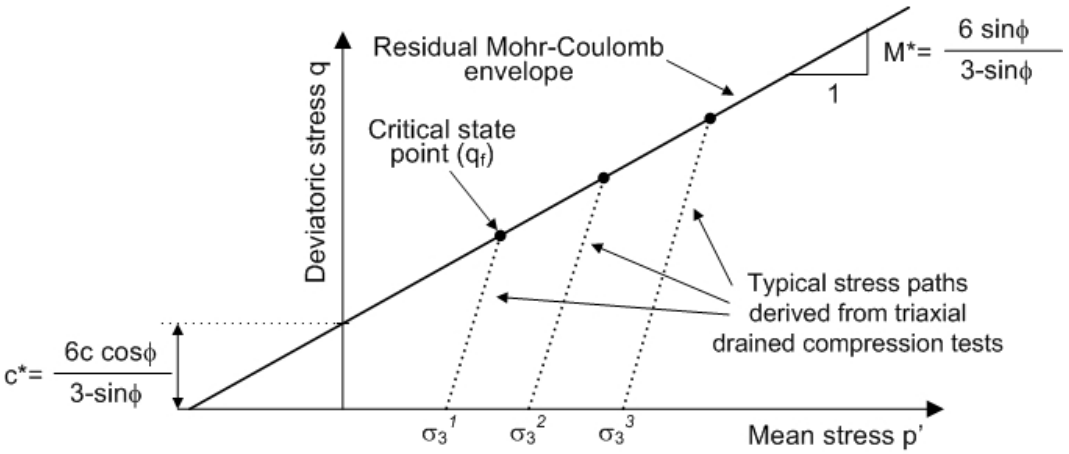

$$\text{then} \quad \phi = \arcsin\left(\frac{3M^*}{6+M^*}\right) \qquad c = c^*\frac{3-\sin\phi}{6\cos\phi} \tag{3.5}$$

Figure 3.1: Determination of the residual Mohr-Coulomb envelope and strength parameters ϕ and c from typical stress paths derived from the triaxial drained compression tests driven at three different confining pressures σ_3.

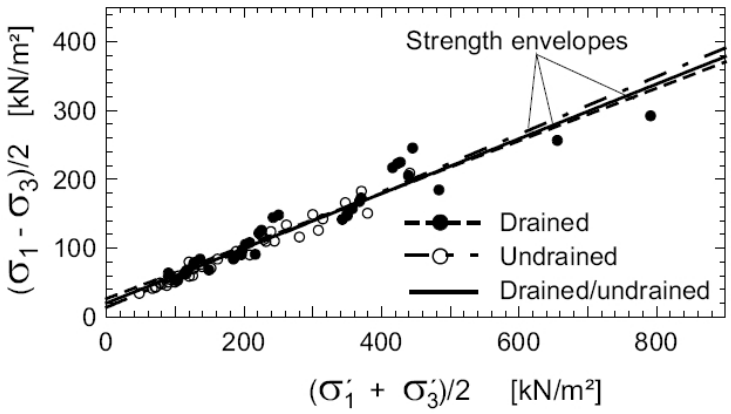

Figure 3.2: Compatibility of strength envelopes derived from drained and undrained triaxial tests (from Kempfert, 2006).

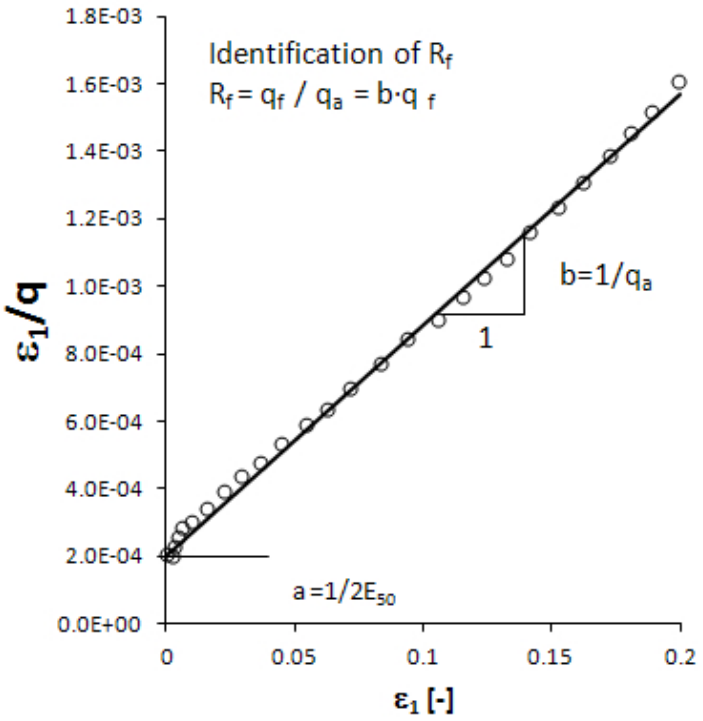

Figure 3.3: Determination of the slope a and b for identification of the secant modulus E_{50} and failure ratio R_f from typical triaxial drained compression results $\varepsilon_1 - q$. Best precision of the interpreted parameters is obtained by plotting the trendline for two closest data points adjacent to $0.5q_f$.

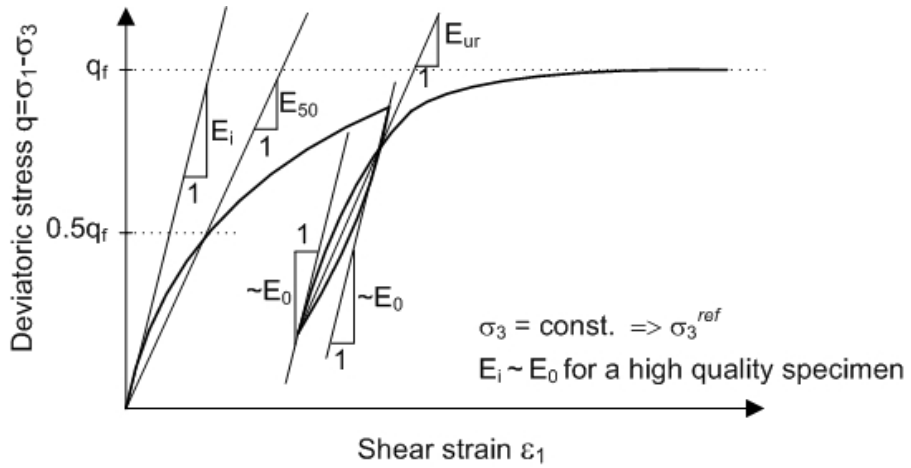

Figure 3.4: Determination of E moduli (input model parameters) from a typical curve derived from the triaxial drained compression tests.

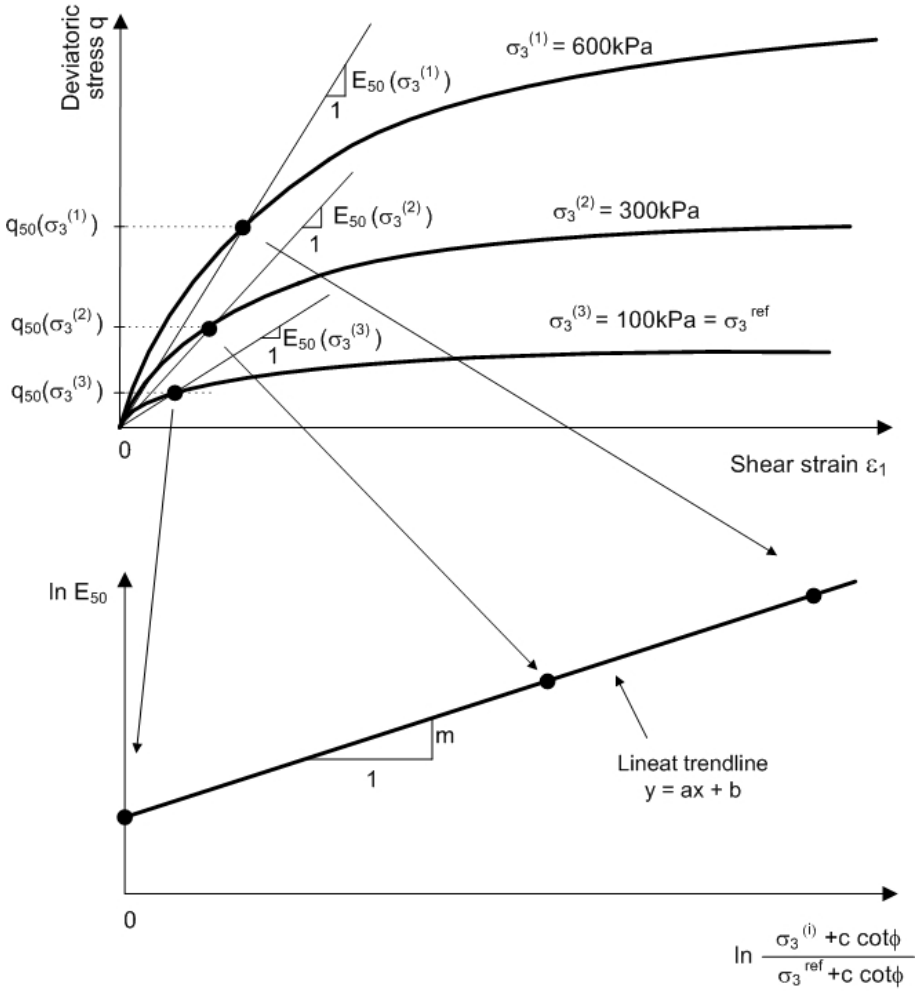

Identification algorithm:

1. Find three values of $E_{50}^{(i)}$ corresponding to $\sigma_3^{(i)}$ respectively.
2. Find a trend line $y = ax + b$ by assigning variables
   y as $\ln E_{50}^{(i)}$ and
   x as $\ln\left(\dfrac{\sigma^{(i)} + c\,\cot\phi}{\sigma_{\text{ref}} + c\,\cot\phi}\right)$
   and assuming σ_{ref} (typically equal to 100kPa)
3. Then the determined slope of the trend line a is the parameter m.

Figure 3.5: Determination of the stiffness stress dependency parameter m from three curves derived from the triaxial drained compression tests.

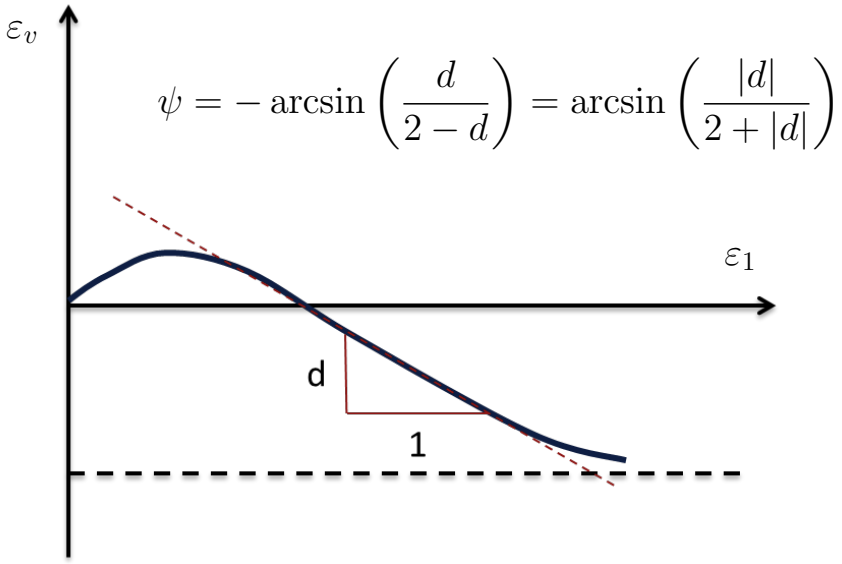

Figure 3.6: Determination of the dilatancy angle ψ from $\varepsilon_v - \varepsilon_1$ curve obtained in the triaxial drained compression test (note that d is negative in the classical notation used in soil mechanics).

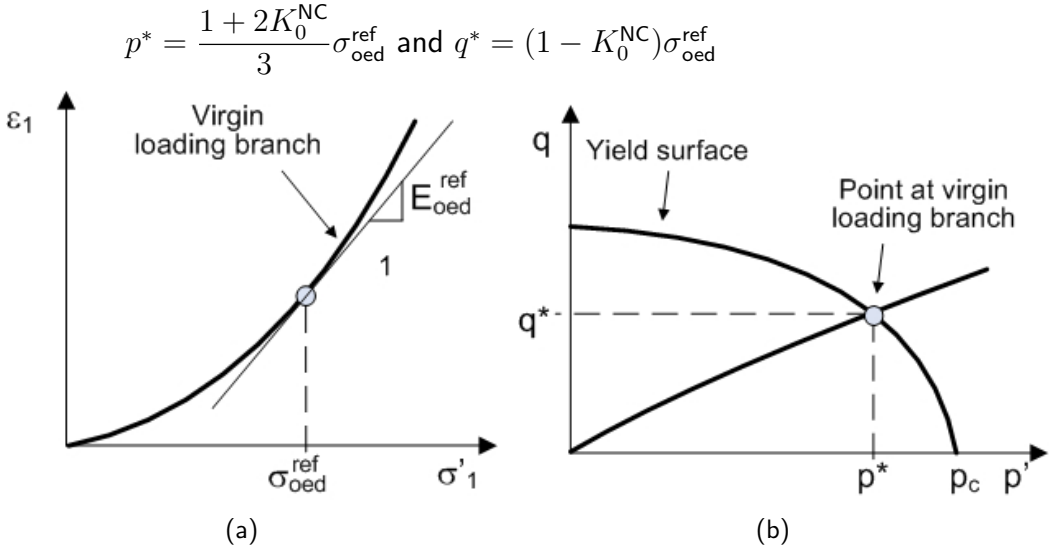

Figure 3.7: Assumptions to the automatic determination of parameters M and H: at given σ_{oed}^{ref} which is located at post-yield plastic curve, both shear an volumetric mechanism are active.

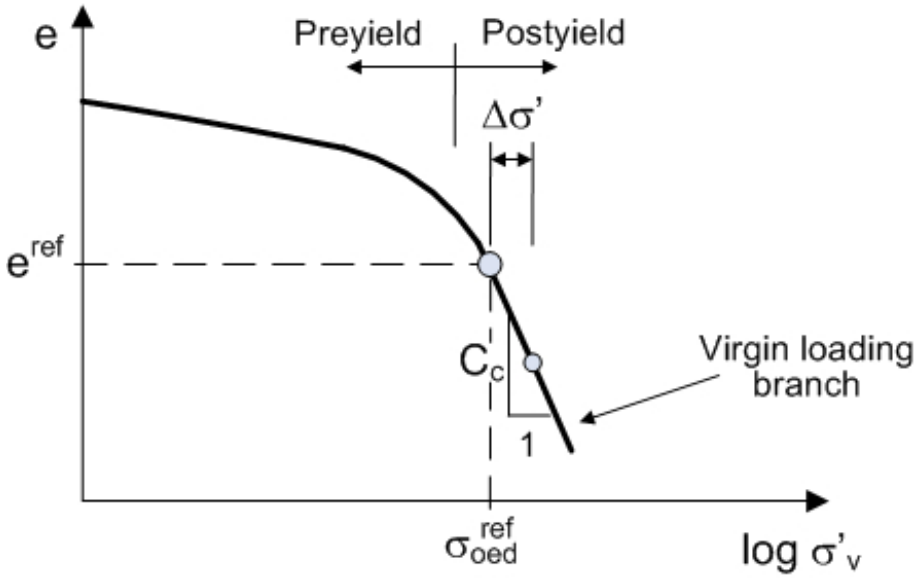

Figure 3.8: Determination of the compression index C_c from typical results derived from oedometer test for estimating the tangent modulus E_{oed}.

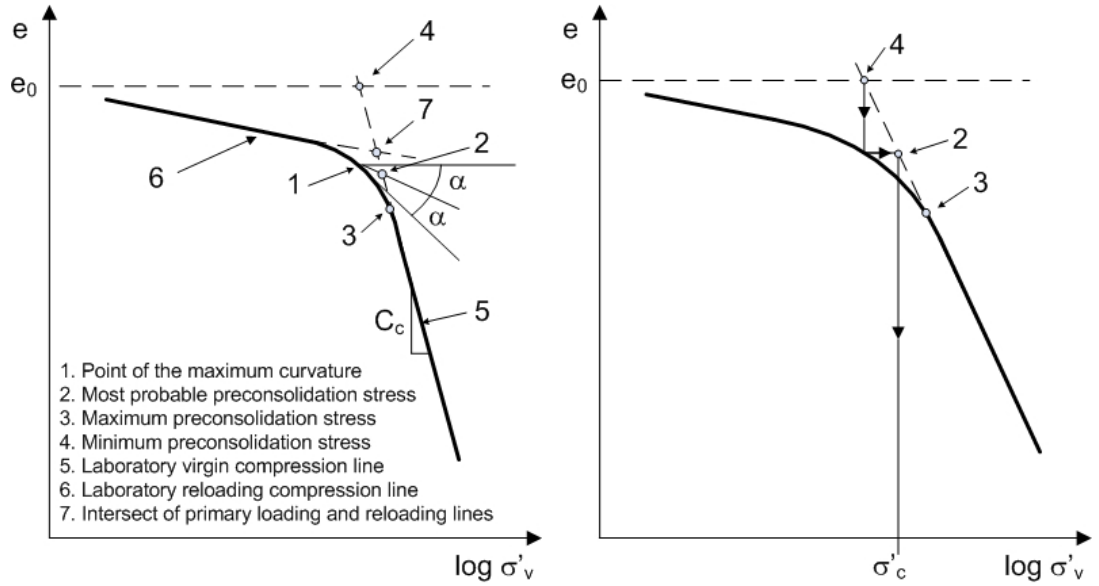

Figure 3.9: Estimation of preconsolidation pressure σ_c' (a) Casagrande's method, (b) Pacheco Silva's method.

3.1.2 Direct parameter identification for the HS-small

Direct parameter identification for the HS-small and HS-Brick models requires the measurements derived from **geophysical tests** or one of the advanced *in situ* probes equipped with a seismic sensor which allows measuring the shear wave velocity V_s in the subsoil. Two commonly known devices, i.e. the **seismic piezocone** (SCPT or SCPTU) or **seismic Marchetti's dilatometer** (SDMT), can be used to determine small strain stiffness G_0 (or G_{max}) from the following expression:

$$G_0 = \rho V_s^2 \tag{3.6}$$

where ρ is a density of soil. Typical ranges for V_s in different types of soils, as well as a variety of methods that can be used to estimate V_s from *in situ* tests (SPT, DMT, CPT, PMT) are given in Appendix C.
Note that in natural conditions G_0 is stress dependent and, in the HS-small/HS-Brick model, this parameter is defined by analogy to other stiffness moduli using one of the selected expressions:

$$G_0 = G_0^{\text{ref}} \left(\frac{\sigma_3^* + c\ \text{cot}\phi}{\sigma^{\text{ref}} + c\ \text{cot}\phi} \right)^m \tag{3.7}$$

$$G_0 = G_0^{\text{ref}} \left(\frac{\sigma_3^*}{\sigma^{\text{ref}}} \right)^m \tag{3.8}$$

$$G_0 = G_0^{\text{ref}} \left(\frac{p^*}{\sigma^{\text{ref}}} \right)^m \tag{3.9}$$

Having determined G_0, the parameter $\boxed{E_0}$ which is defined by the user in the material dialog, can be calculated from:

$$E_0 = 2(1 + \nu_{\text{ur}})G_0 \tag{3.10}$$

assuming that Poisson's coefficient ν_{ur} is a constant in the model.

Soil stiffness at very small strains can also be approximated based on the initial part of the $\varepsilon_1 - q$ curve or the unloading-reloading branch derived from the triaxial compression test, as demonstrated on Figure 3.4. However, an exact determination of the initial soil stiffness E_i may prove to be difficult, especially in soft soils. Therefore, one should realize that the initial slope E_i derived from triaxial test can be more than once lower than soil stiffness $\boxed{E_0}$ observed in natural conditions.

Identification of the parameter $\boxed{\gamma_{0.7}}$ at which the secant shear modulus G_s^{ref} is reduced to $0.722G_0^{\text{ref}}$, requires the use of advanced laboratory devices in order to determine the S-shape curve at very small strain levels. In practice, it may prove to be time-consuming and expensive and therefore, it is suggested to estimate $\boxed{\gamma_{0.7}}$ by means of typically observed experimental curves. In the case of granular materials $\boxed{\gamma_{0.7}}$ mostly depends on the mean effective stress p' (see Figure 3.19) but also on overconsolidation. In cohesive materials, $\boxed{\gamma_{0.7}}$ may mostly depend on the plasticity index I_P (PI) (see Figures 3.38 or 3.40), however the stress level (p') and the overconsolidation (OCR) may also increase the value of $\boxed{\gamma_{0.7}}$. Having assumed all other model parameters, it is also recommended to run a one-element simulation of the triaxial compression test in order to examine the shape of $\log(\varepsilon_1) - G$ (or E) curve derived from the computed $\varepsilon_1 - q$ results.

3.1.3 Parameter identification sequence

The following sequence should be followed during parameter identification for the HS model:

1. Identify ϕ' and c' (e.g. Figure 3.1)
2. Identify ψ (e.g. Figure 3.6)
3. Identify R_f and $E_{50}^{(\mathrm{i})}$ for different confining pressures $\sigma_3^{(\mathrm{i})}$ (e.g. Figure 3.3)
4. Identify $E_{\mathrm{ur}}^{(\mathrm{i})}$ for different confining pressures $\sigma_3^{(\mathrm{i})}$ (the value of ν_{ur} can be assigned between 0.1 and 0.2)
5. Identify m based on the identified values of $E_{50}^{(\mathrm{i})}$ or/and $E_{\mathrm{ur}}^{(\mathrm{i})}$ (e.g. Figure 3.5)
6. Assign the reference stress σ_{ref} (it can be the confining pressure in the triaxial test that best corresponds to *in situ* stress conditions)
7. Evaluate E_0 and $\gamma_{0.7}$
8. Calculate E_0^{ref}, $E_{\mathrm{ur}}^{\mathrm{ref}}$, E_{50}^{ref} in terms of σ_{ref} (note that by applying the stress stiffness dependency law such as Eq.(2.4) the stiffness moduli also depend on ϕ, c and m)
9. Double-check the following relationships:
   - $E_0^{\mathrm{ref}} > E_{\mathrm{ur}}^{\mathrm{ref}} > E_{50}^{\mathrm{ref}}$
   - $E_{\mathrm{ur}}^{\mathrm{ref}} / E_{50}^{\mathrm{ref}} > 2$
   - $3.6 < E_0^{\mathrm{ref}} / E_{50}^{\mathrm{ref}} < 30$ (typically $6 < E_0^{\mathrm{ref}} / E_{50}^{\mathrm{ref}} < 14$)
10. Evaluate K_0^{NC} and $E_{\mathrm{oed}}^{\mathrm{ref}}$ for the corresponding vertical reference stress $\sigma_{\mathrm{oed}}^{\mathrm{ref}}$ in order to compute M and H (note that M and H should be recomputed if one of the following parameters has been changed: E_{ur}, ν_{ur}, m, E_{50}, ϕ, ψ, c, R_f)
11. Evaluate the profile of soil preconsolidation in order to specify a constant OCR or a variable OCR profile by means of q^{POP}
12. Set $K_0^{\mathrm{SR}} = K_0^{\mathrm{NC}}$
13. Evaluate the *in situ* stress state in order to specify K_0 (for example accounting for preconsolidation state Eq.(3.89))

An example of parameter identification using a spreadsheet is given in Table 5.8.

3.1.4 Model parameters for "undrained" simulations

In ZSoil® , the undrained behavior can be obtained in the **two-phase analysis** (`Deformation+flow`) by running on of the following drivers:

- `Consolidation` driver (undrained or partially-drained conditions can be obtained depending on the action time and soil permeability [5])
- `Driven Load (Undrained)` (perfectly undrained conditions)

Since the constitutive models are formulated in effective stresses, it is recommended to use the effective stress parameters:

- Effective stiffness parameters E'_0, E'_{ur}, E'_{50}, ν'_{ur} permeability)
- Effective strength parameters ϕ', c'

The main advantages of working with the effective parameters are as follows:

- deviatoric stress at failure (that corresponding to the undrained shear strength $q_f^u = 2S_u$) depends on preconsolidation history (cf. Figure 3.45)
- undrained shear strength is stress dependent

Another approach which can be considered for simulating the undrained behavior is that relying on **"undrained" strength parameters**, i.e. $\phi = \phi^{\text{u}} = 0$, $c = S_u$, $\nu_{\text{ur}} = 0.4999$. Note, however, that for this approach the undrained shear strength is constant and stress independent.
In such approach, the following parameters should be considered:

- Effective strength parameters $\phi = \phi^{\text{u}} = 0$, $c = S_u$ ($\psi = 0$ for normally- and lightly cohesive soils in order to avoid excessive gain in material resistance after reaching the failure stress point)
- Effective stiffness parameters E'_0, E'_{ur}, E_{50}^{ud}, $\nu_{\text{ur}} = 0.4999$
- High OCR, e.g. 1000 to skip the cap mechanism in computations (no plastic volumetric deformations)

The following sequence should be respected when setting the "undrained" parameters:

1. Insert the effective parameters E'_0, E'_{ur} in `Elastic` dialog window and the "undrained" Poisson's coefficient $\nu_{\text{ur}} = 0.4999$.

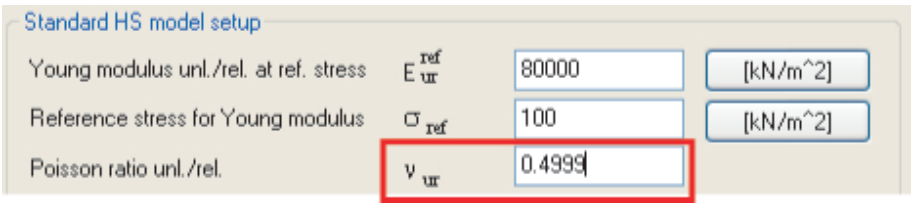

[5] In order to obtain perfectly undrained conditions for consolidation driver use very short time steps. For real problems this may require two-phase stabilization to be active.

In the `Nonlinear` dialog window, disable
`Automatic evaluation of H and M parameters` in order to avoid unfeasible calculation of M and H parameters for the null friction angle.

2. Set "undrained" parameters $\phi^{\mathrm{u}} = 0^o$, $c = S_u$, and $\psi = 0$ for normally- and lightly cohesive soils in order to avoid excessive gain in material resistance after reaching the failure stress point (cf. Truty and Obrzud (2015)).

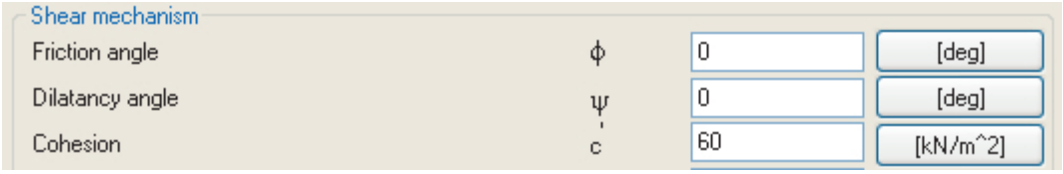

3. Set high OCR, e.g.1000, in order to skip the cap mechanism during analysis

4. Set input E_{50} equal to undrained one E_{50}^{u}. The "undrained" secant modulus can be computed from:

$$E_{50}^{\mathrm{u}} = \frac{3E'_{50}}{2(1+\nu)} \tag{3.11}$$

where ν should correspond to the ratio $\varepsilon_3/\varepsilon 1$ obtained for plastic straining and the efective secant modulus E'_{50}, i.e. $\nu \approx 0.3$.

3.2 Alternative parameter estimation for granular materials

3.2.1 Initial stiffness modulus and small strain threshold

The present section provides a number of approaches for estimating the initial soil stiffness and the small strain threshold $\gamma_{0.7}$. Some correlations allows to directly approximate the input parameter E_0, the others provide solutions for estimating the initial shear modulus G_0. Then the input parameter E_0 can be obtained through:

$$E_0 = 2(1 + \nu_{\text{ur}})G_0 \tag{3.12}$$

assuming a constant value of the unloading-reloading Poisson's coefficient ν_{ur}.

Geotechnical evidence. Experimental data shows that the initial stiffness of soils may depend on the stress level, soil porosity and overconsolidation. These factors can be taken into account using a modified equation proposed by Hardin and Black (1969):

$$G_0 = A \cdot f(e) \cdot \text{OCR}^k \left(\frac{p'}{p_{\text{ref}}}\right)^m \quad \text{, in [MPa]} \tag{3.13}$$

where G_0 is the maximum small-strain shear modulus in MPa, p' is the mean effective stress in kPa, p_{ref} is the reference stress equal to the atmospheric pressure $p_{\text{ref}} = 100$ kPa, OCR is the overconsolidation ratio and A, $f(e)$, k, m are the correlated functions and parameters which are given in Table 3.1 and 3.2 for different types of soils. It is observed that the empirical exponent k varies from 0 for sands and 0.5 for high plasticity clays.

Biarez and Hicher (1994) proposed a simple relationship for all soils with $w_L < 50\%$:

$$E_0 = \frac{140}{e}\left(\frac{p'}{p_{\text{ref}}}\right)^{0.5} \quad \text{, in [MPa]} \tag{3.14}$$

Table 3.1: Parameters for estimation of G_0 in different types of granular soils using Eq.(3.13).

Soil tested	D_{50} [mm]	C_u [-]	A [-]	$f(e)$ [-]	k [-]	m [-]	Reference
Kenya carbonate sand	0.13	1.86	101-129	$e^{-0.8}$	0	0.45-0.52	Fioravante (2000)
Quiou carbonate sand	0.75	4.40	71	$e^{-1.3}$	0	0.62	Lo Presti et al. (1993)
Ottawa sand No.20-30	0.72	1.20	69	$\frac{(2.17-e)^2}{1+e}$	0	0.50	Hardin and Richart Jr (1963)
SLB sand (subround)	0.62	1.11	82-130	$\frac{(2.17-e)^2}{1+e}$	0	0.44-0.53	Hoque and Tatsuoka (2004)
Toyoura sand (subangular)	0.16	1.46	71-87	$\frac{(2.17-e)^2}{1+e}$	0	0.41-0.51	Hoque and Tatsuoka (2004)
Toyoura sand (subangular)	0.19	1.56	84-104	$\frac{(2.17-e)^2}{1+e}$	0	0.50-0.57	Chaudary et al. (2004)
Toyoura sand (subangular)	0.22	1.35	72	$e^{-1.3}$	0	0.45	Lo Presti et al. (1993)
Ticino sand (subangular)	0.50	1.33	61-64	$\frac{(2.17-e)^2}{1+e}$	0	0.44-0.53	Hoque and Tatsuoka (2004)
Ticino sand (subangular)	0.54	1.50	71	$\frac{(2.27-e)^2}{1+e}$	0	0.43	Lo Presti et al. (1993)
Ticino sand (subangular)	0.55	1.66	79-90	$e^{-0.8}$	0	0.43-0.48	Fioravante (2000)
Ham River sand (subangular)	0.27	1.67	72-81	$\frac{(2.17-e)^2}{1+e}$	0	0.5-0.52	Kuwano and Jardine (2002)
Silica sand (subangular)	0.20	1.10	80	$\frac{(2.17-e)^2}{1+e}$	0	0.5	Kallioglou et al. (2003)
Hostun sand (angular)	0.31	1.94	80	$\frac{(2.17-e)^2}{1+e}$	0	0.47	Hoque and Tatsuoka (2000)
Silica sand (angular)	0.32	2.80	48	$\frac{(2.17-e)^2}{1+e}$	0	0.50	Kallioglou et al. (2003)
Silica sand	0.55	1.80	275	$\frac{(1.46-e)^2}{1+e}$	0	0.42	Wichtmann and Triantafyllidis (2004)
Hime gravel (subround)	1.73	1.33	53-94	$\frac{(2.17-e)^2}{1+e}$	0	0.45-0.51	Chaudary et al. (2004)
Chiba gravel (subround)	7.90	10	76	$\frac{(2.17-e)^2}{1+e}$	0	0.50	Modoni et al. (1999)

Table 3.2: Parameters for estimation of G_0 in granular soils using Eq.(3.13).

Soil tested	e_{min} [-]	e_{max} [-]	A [-]	$f(e)$ [-]	m [-]	Reference
Clean uniform sands with $C_u < 1.8$	0.5	1.1	57	$\frac{(2.17-e)^2}{1+e}$	0.4	Iwasaki and Tatsuoka (1977)
All soils with $w_L < 50\%$	0.4	1.8	58*	$\frac{1}{e}$	0.5	Biarez and Hicher (1994)
Undisturbed crushed sands	0.6	1.5	33	$\frac{(2.97-e)^2}{1+e}$	0.5	Hardin and Black (1969)

*obtained from Eq. 3.14 assuming $\nu = 0.2$

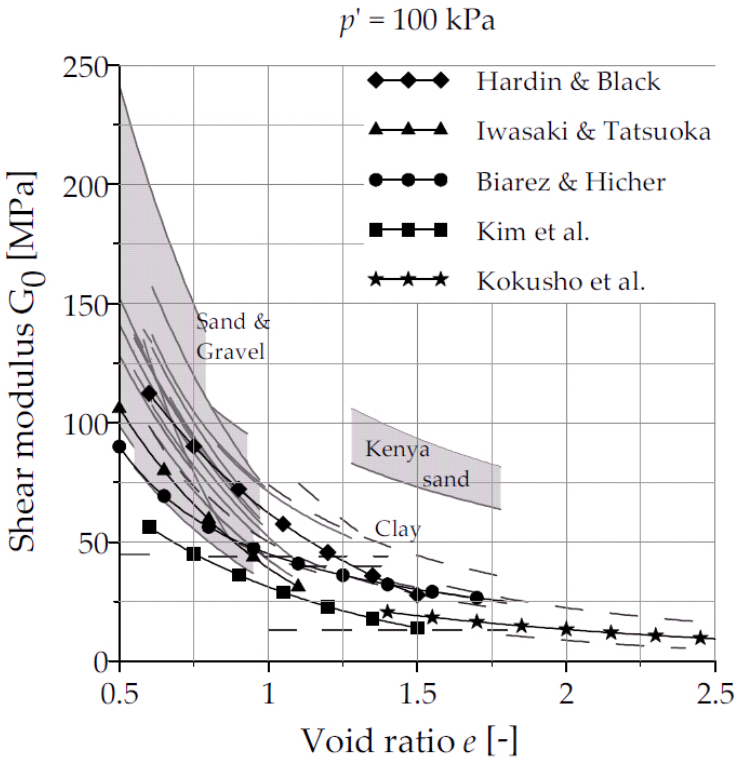

Figure 3.10: Graphical representation of empirical relations presented in Table 3.6 and 3.18 (after Benz, 2007).

Geotechnical evidence. In case of lack of test data at very small strain levels, E_0 can be evaluated from an empirical relation proposed by Alpan (1970). This relation which is presented in Figure 3.11, relates so-called "static" modulus E_s to the "dynamic" modulus E_d. For the sake of HS-SmallStrain model, E_s can be considered as E_{ur} obtained at engineering strain levels ($\varepsilon \approx 10^{-3}$), whereas E_0 can be considered as $\approx E_d$.

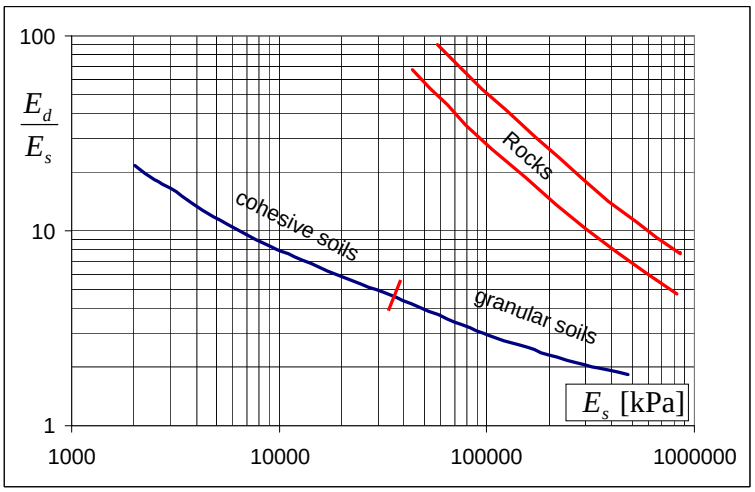

Figure 3.11: Approximative relation between "static" soil stiffness (here $E_s \approx E_{\text{ur}}$) and "dynamic" modulus E_d corresponding to E_0 proposed by Alpan (1970).

Geotechnical evidence. It can be observed in laboratory test that secant stiffness reduces with mobilization of the shear strength. Mayne (2007) provides a selection of secant modulus curves, represented by the ratio G_s/G_0 or E_s/E_0. The collected results were derived from monotonic laboratory shear tests performed on an sorted mix of clayey ans sandy materials, and they are presented in Figure 3.13. Such experimental results can be approximated with a hyperbolic model by Fahey and Carter (1993) (see Figure 3.12):

$$\frac{G_s}{G_0} = 1 - F\left(\frac{q}{q_{\text{max}}}\right)^g \tag{3.15}$$

where f and g are soil-specific model parameters (typically $0.8 < f < 1.0$).

Experimental results reported in Lo Presti et al. (1998) show that g increases (E_0/E_{50} decreases) with overconsolidation, especially for quartz and calcerous sands. It has also been recognized that E_0/E_{50} increases with soil cementation and structurization. Therefore, higher values of E_0/E_{50} can be expected for sensitive clays.

Experimental results and Eq. (3.15) have been used in this report to develop a method which provides reasonable first-guess values of E_0 based on a known value of E_{50}. Considering that q/q_{max} corresponding to E_{50} is equal to 0.5, and assuming that $F = 1$, the hyperbolic equation can be used to find lower and upper limits of E_{50}/E_0 by adjusting g parameter. The adjustment of g with respect to overconsolidation or the consolidation stress ratio K_c (which for natural soils increases with overconsolidation) was carried out using the experimental results for Toyura sand presented in Figure 3.14. A summary of adjusted g values and corresponding E_0/E_{50} ratios with respect to overconsolidation is provided in Table 3.3.

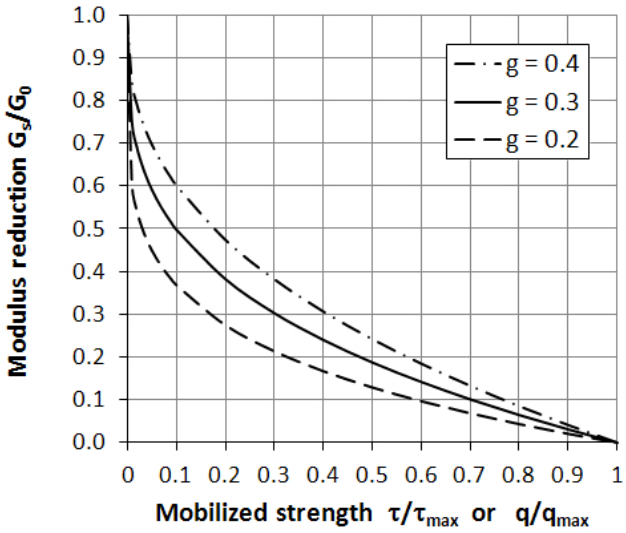

Figure 3.12: Reduction of G_0/G_{50} by the hyperbolic model - Equation (3.15) (assuming $F = 1$).

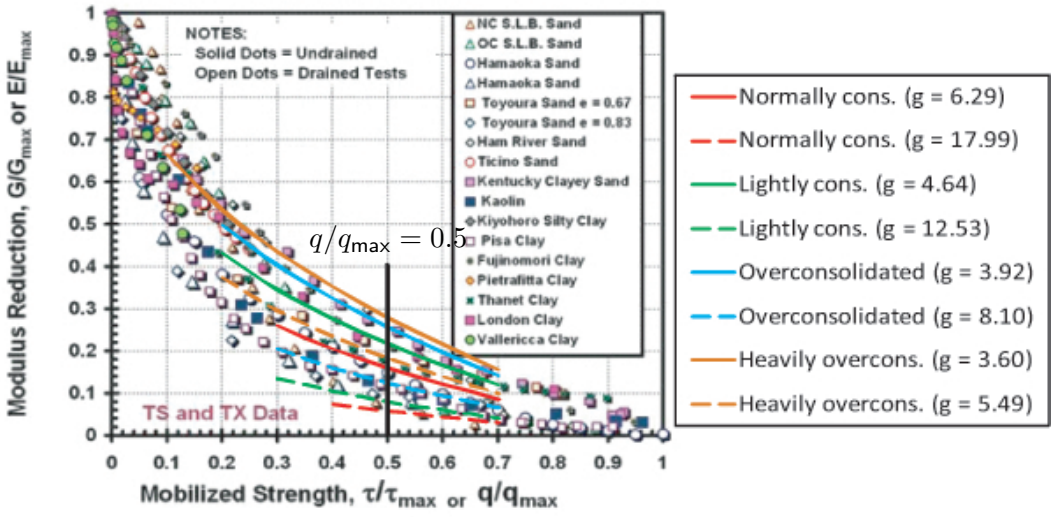

Figure 3.13: Observed secant stiffness modulus reduction curves from static torsional and triaxial shear data on clays and sands (from Mayne, 2007) and the superposed hyperbolic curves obtained for different g values. The adjusted g values provides reasonable first-guess lower and upper limits for estimating E_0 from a determined E_{50} value (see Table 3.3).

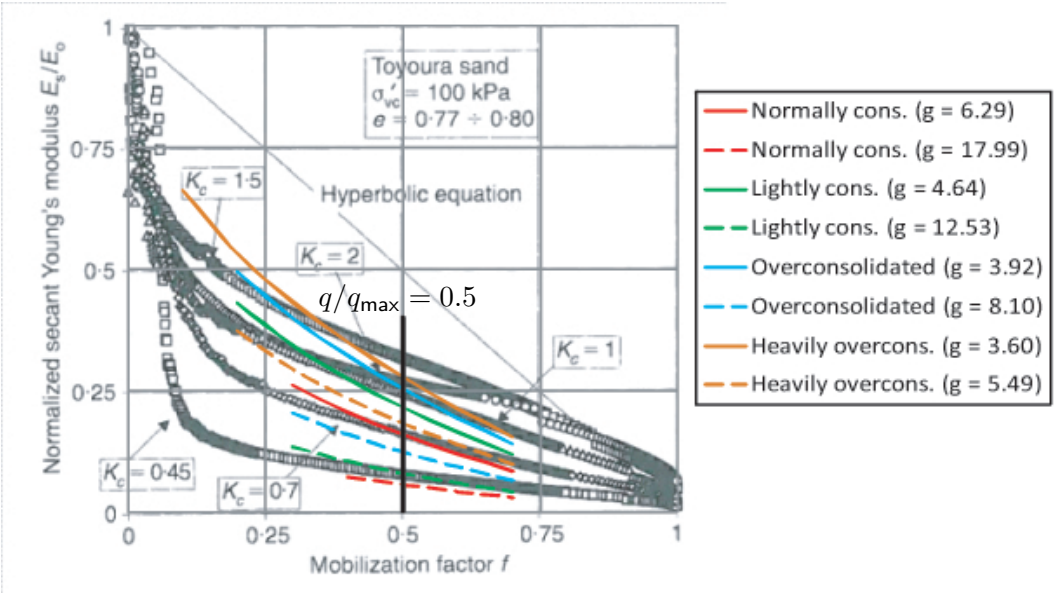

Figure 3.14: Normalized secant modulus of Toyura vs mobilized shear strength (Lo Presti et al., 1998, from) and adjusting of g parameter with respect to stress consolidation ratio.

Table 3.3: Typical values of E_0/E_{50} ratio for granular soils with respect to the preconsolidation state (this table has been developed based on literature review and Fahey's stiffness reduction model).

	OCR [–]	E_0/E_{50} [–]		Corresponding g [–]	
Degree of preconsolidation		"Min"	"Max"	For "Min"	For "Max"
Unknown		4.1	18.0	0.40	0.083
Normally consolidated	$1 \div 1.2$	6.3	18.0	0.25	0.083
Lightly overconsolidated	$1.2 \div 2.5$	4.6	12.5	0.35	0.12
Overconsolidated	$2.5 \div 4.5$	3.9	8.1	0.43	0.19
Heavily overconsolidated	$4.5 \div 10$	3.6	5.5	0.47	0.29

The higher values of E_0/E_{50} ratio are suggested for aged, cemented and structured sands.

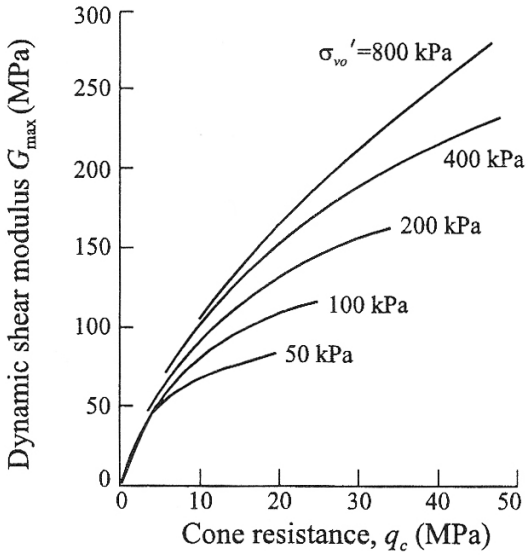

Figure 3.15: Cone resistance vs. maximal shear modulus G_0 for sands (after Robertson and Campanella, 1983).

CPT. Initial small strain stiffness for sands can be approximated from cone resistance measurements q_c derived from CPT. Robertson and Campanella (1983) related the maximal shear modulus G_0 with q_c for different effective vertical stresses σ'_{v0}, as presented in Figure 3.15.

CPT. Based on calibration chamber and field measurements Rix and Stokoe (1992) proposed the correlation for uncemented quartz sands (cf. Figure 3.16). The wide range of G_0/q_c at low values of normalized cone resistance is explained by variations in soil compressibility; more compressible sands may give lower values of Q_t and hence higher values of G_0/q_c (Lunne et al., 1997).

$$\left(\frac{G_0}{q_c}\right)_{\text{avg}} = 1634 \left(\frac{q_c}{\sqrt{\sigma'_{v0}}}\right)^{-0.75} \qquad (3.16)$$

$$\text{Range} = \text{Average} \pm \frac{\text{Average}}{2}$$

with G_0, q_c and σ'_{v0} in kPa.

DMT. In general, G_0 in sands can be estimated based on dilatometer modulus E_D using the correlations obtained based on calibration chamber tests by Baldi et al. (1986) and on field tests by Belotti et al. (1986):

$$\frac{G_0}{E_D} = 2.72 \pm 0.59 \qquad (3.17a)$$

$$\frac{G_0}{E_D} = 2.20 \pm 0.7 \qquad (3.17b)$$

The relations are graphically presented in Figure 3.17.

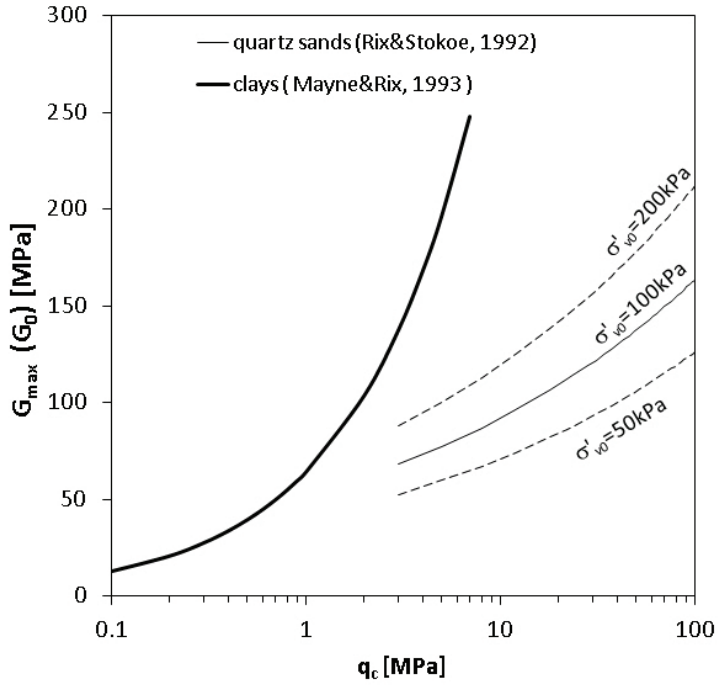

Figure 3.16: Comparison of empirical correlations for estimating G_0 (G_{max}) in sands (Eq.(3.16)) and clays (Eq.(3.47)) from CPT data (correlations interpreted for typical q_t ranges).

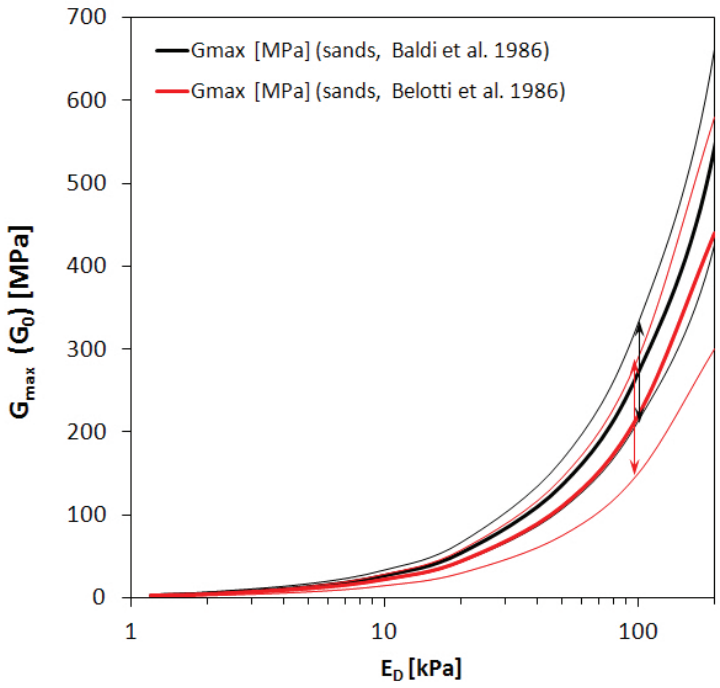

Figure 3.17: Comparison of empirical correlations for estimating G_0 (G_{max}) in sands from DMT data (Eq.(3.17a) and Eq.(3.17b).

SPT. G_0 can be estimated for sands from the correlation proposed by Ohta and Goto (1976, as referred in Kramer (1996)), cf. Figure 3.18:

$$G_0 = 438 N_{1,60}^{0.3333} p_a \left(\frac{p'}{p_a}\right)^{0.5} \tag{3.18}$$

with G_0 and p'-mean effective stress in kPan and $p_a = 100$kPa, $N_{1,60}$ - "overburden-corrected" N_{60}-value (cf. Table 3.10).

Another correlation for sand based on SPT date was proposed by Imai and Tonouchi (1982, as refered in Kramer (1996)), cf. Figure 3.18:

$$G_0 = 15600 N_{60}^{0.68} \tag{3.19}$$

(G_0 in kPa.)

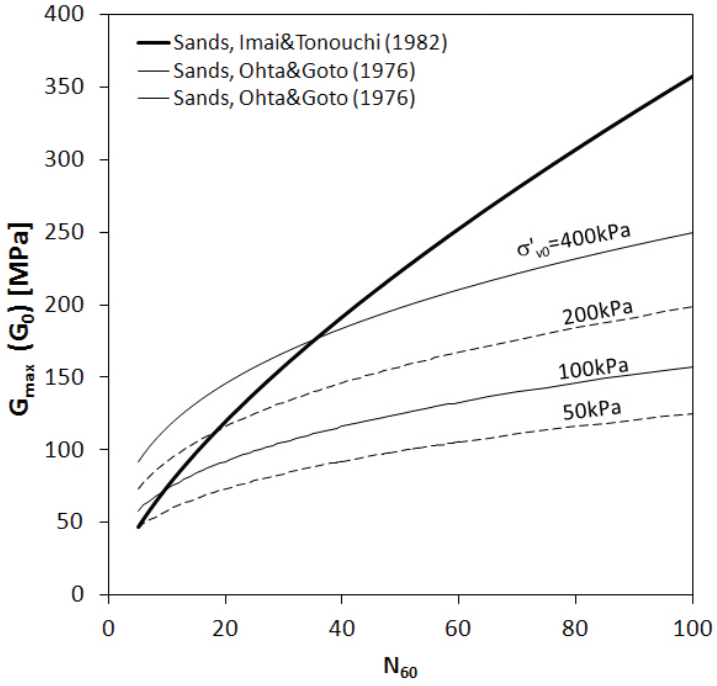

Figure 3.18: Comparison of empirical correlations for estimating G_0 (G_{max}) in sands from SPT data, Eq.(3.18) plotted for $K_0 = 0.4$ and Eq.(3.19).

Geotechnical evidence. It has been proved experimentally that the strain threshold $\gamma_{0.7}$ does not depend on soil density in the case of non-cohesive granular soils (cf. 3.19). On the other hand, $\gamma_{0.7}$ can be affected by the magnitude of the confining pressure σ'_0 which corresponds to the mean effective stress p' for *in situ* conditions (cf. Darendeli and Stokoe (2001); Wichtmann and Triantafyllidis (2004)). Hence, the parameter $\gamma_{0.7}$ can be approximated from a diagram presented in Figure 3.19. Note that the model formulation does not account for stress dependency of $\gamma_{0.7}$. If needed this parameter can be incorporated into boundary value problems through definition average mean effective stress for defined sub-layers.

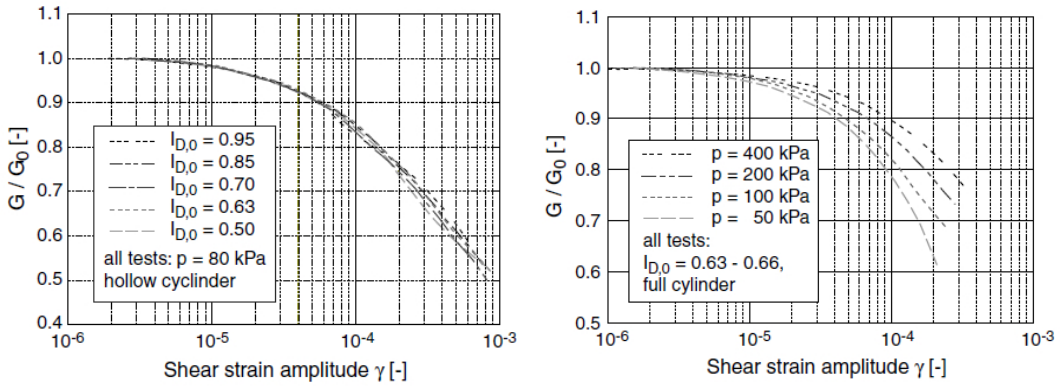

Figure 3.19: Influence of relative density I_D and the confining pressure p' on strain threshold $\gamma_{0.7}$ for sands (from Wichtmann and Triantafyllidis, 2004).

Experimental evidence for sands reported in Darendeli and Stokoe (2001), Figure 3.20, allows to write the following approximating relationship:

$$\gamma_{0.7} = \gamma_{0.7}^{\text{ref}} \left(\frac{p'}{p_a} \right)^{0.35}$$

with (3.20)

$\gamma_{0.7}^{\text{ref}}(p_a) = 1.26 \cdot 10^{-4}$ - reference strain threshold at p_a

$p_a = 1\text{atm} \approx 100\text{kPa}$ - atmospheric pressure

An estimation of $\gamma_{0.7}$ for granular soils can also be carried out using a linear interpolation which is obtained through interpretation of the results presented in Figure 3.19:

$$\gamma_{0.7} = 8.75 \cdot 10^{-5} \frac{p'}{p^{\text{ref}}} + \gamma_{0.7}^{\text{ref}} \quad \text{for } p' \leq < 400\text{kPa}$$

with (3.21)

$\gamma_{0.7}^{\text{ref}}\left(p^{\text{ref}}\right) = 1.0 \cdot 10^{-4}$ - reference strain threshold at p^{ref}

$p^{\text{ref}} = 100\text{kPa}$ - reference pressure

where $p^{\text{ref}} = 100\text{kPa}$.
A fit of the above correlation to the experimental curves is presented in Figure 3.21.

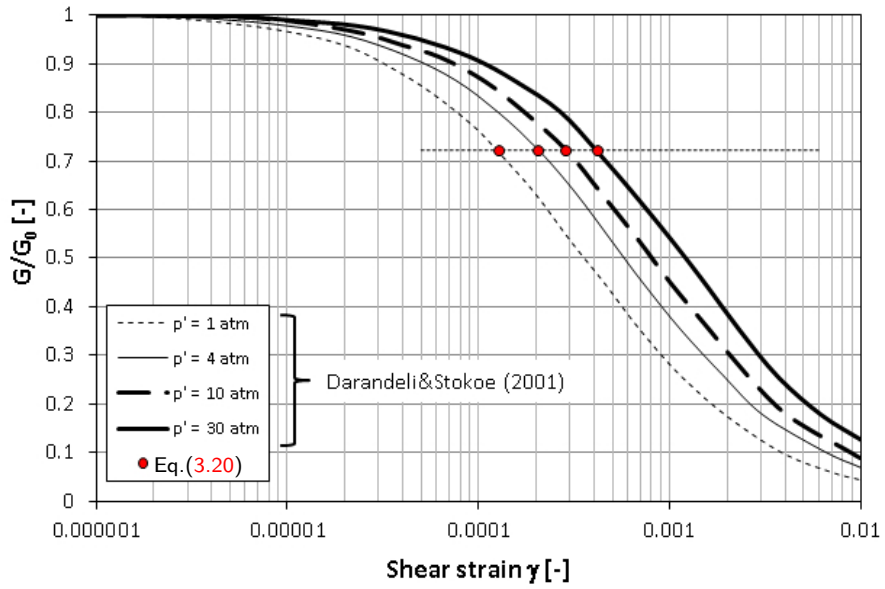

Figure 3.20: Comparison of predictions for $\gamma_{0.7}$ at different mean stresses p' using Eq.(3.20) for the data reported in Darendeli and Stokoe (2001).

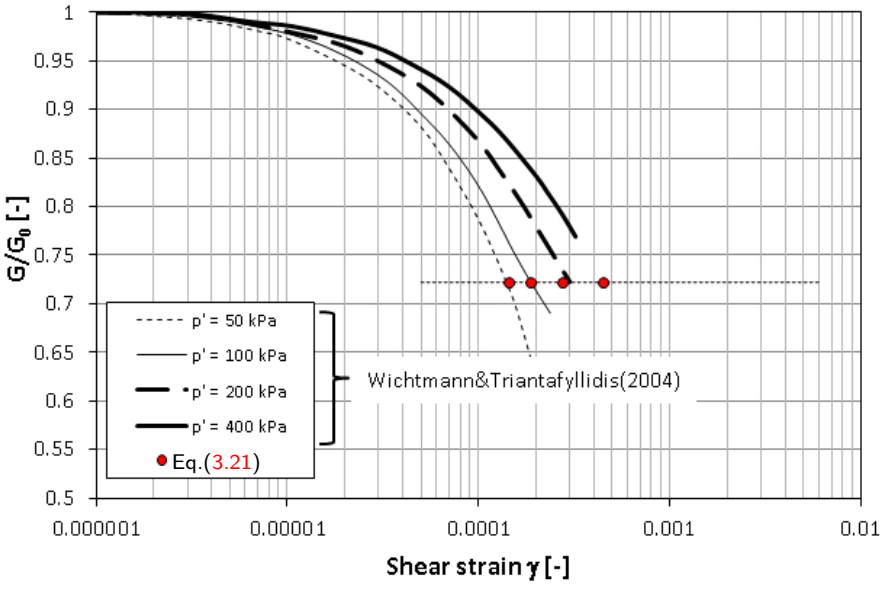

Figure 3.21: Comparison of predictions for $\gamma_{0.7}$ at different mean stresses p' using Eq.(3.21) with experimental data for sands reported in Wichtmann and Triantafyllidis (2004).

In the case of granular soils, it is also observed that the strain threshold may be affected by OCR and for sands with high content of fines additionally on I_P. In order to account these effects, the correlation presented in Eq.(3.54) can be used (this generalized formula by Darendeli (2001) was developed based on a database containing four groups of soils, i.e. "clean" sands, sands with high content of fines, silts and clays.

3.2.2 Secant and unloading-reloading moduli

In general, the relation between the stiffness moduli is as follows:

$$E_{50} < E_s < E_{\text{ur}} \tag{3.22}$$

where E_s denotes "static" modulus or secant modulus taken from the initial part of the $\varepsilon_1 - q$ experimental curve at $\varepsilon_1 = 0.1\%$.

In the case when E_{50} or E_{ur} cannot be directly determined from experimental curves, it may be relevant for many practical cases to set:

$$\frac{E_{\text{ur}}^{\text{ref}}}{E_{50}^{\text{ref}}} = 2 \text{ to } 6 \qquad \text{(an average can be assumed equal to 3)} \tag{3.23}$$

Higher ratios can be assumed for loose sands (3 to 6), whereas lower ones for dense sands (2 to 4). However, note that the following condition should be satisfied: $\frac{E_{\text{ur}}^{\text{ref}}}{E_{50}^{\text{ref}}} > 2$.

However, note that the following condition should be satisfied: $\frac{E_{\text{ur}}^{\text{ref}}}{E_{50}^{\text{ref}}} > 2$.

In absence of laboratory results, the stiffness moduli can be approximated based on typically observed order of magnitudes of "static" modulus E_s which are given in Table 3.4. Assuming that soil behavior follows the stress-strain relation described by Equation 2.10 and assuming $\varepsilon_1 = 0.1\%$, the "static" modulus can be represented with:

$$E_s = \frac{q}{0.001} = \frac{1}{\frac{1}{2E_{50}} + \frac{0.001 \cdot R_f}{q_f(\phi, c)}} \tag{3.24}$$

The above equation can be represented graphically in Figure 3.22, and can be used to estimate E_{50} from the known value of E_s.

Table 3.4: Typical values for the "static" modulus E_s [MPa] (compiled from Kezdi, 1974; Prat et al., 1995, and extended by the authors).

	Soil Density									
	Very loose		Loose		Medium		Dense		Very dense	
Soil Type	Min	Max	Min	Max	Min	Max	Min	Max	Min	Max
Gravels/Sand well-graded	10	30	30	80	80	160	160	320	320	480
Sand, uniform	5	10	10	10	30	30	50	50	80	120
Sand/Gravel silty	3	7	7	12	12	20	20	30	30	40
Sand/Gravel clayey	2	6	6	10	10	15	15	21	21	29

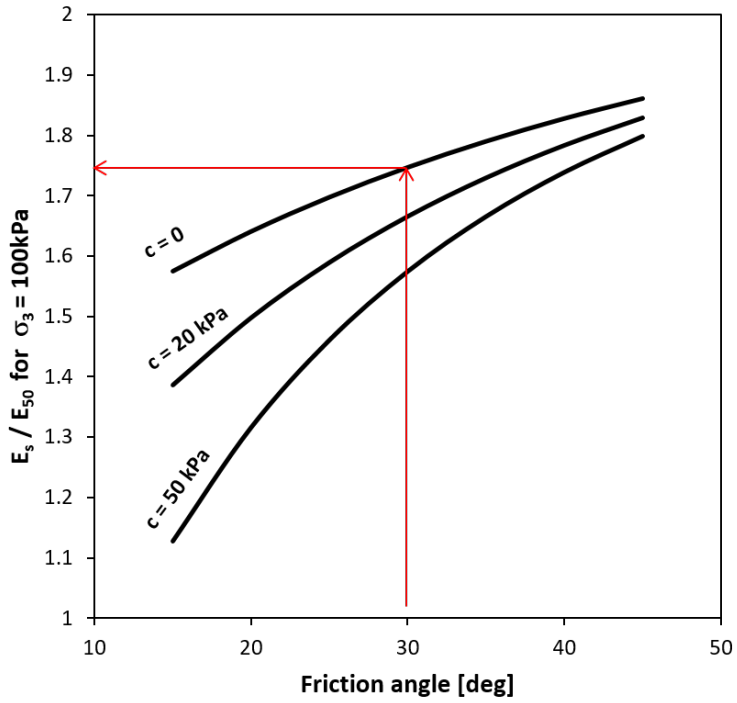

Figure 3.22: Estimating the ratio between the static modulus E_s and secant modulus E_{50}.

For sands, the secant modulus E_{50} can be estimated based on the known porosity, Figure 3.23.

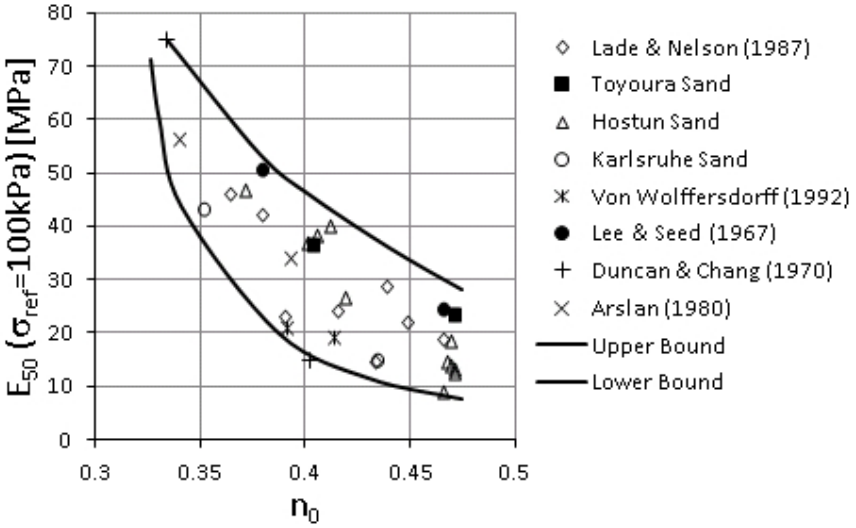

Figure 3.23: Normalized secant modulus E_{50} vs. porosity n_0 for different sands (after Schanz and Vermeer, 1998).

CPT. Secant modulus E_{50} for sands can be approximated from cone resistance measurements q_c derived from CPT. Robertson and Campanella (1983) related E_{50} with q_c for different effective vertical stresses σ'_{v0}, as presented in Figure 3.24.

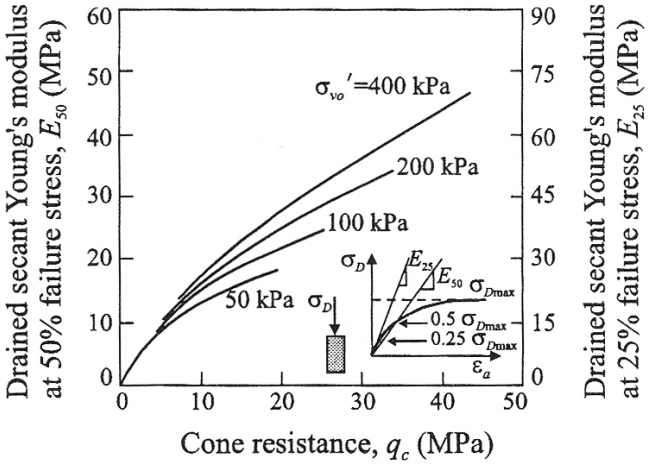

Figure 3.24: Cone resistance q_c vs. secant E_{50} modulus for sands (after Robertson and Campanella, 1983).

DMT. The "static" modulus corresponding to E_{ur} can be evaluated for silty sands and sand from the vertical drained constrained modulus M_{DMT} which is derived from three intermediate dilatometer parameters, i.e. the material index I_D, the horizontal stress index K_D, and the dilatometer modulus E_D. Note that M_{DMT} may correspond to E_{oed} only for normally-consolidated soil. The unloading-reloading modulus E_{ur} can be evaluated assuming that:

$$E_{\text{ur}} = E_s = aE_{\text{oed}} = aM_{\text{DMT}} \tag{3.25}$$

where $a \approx 0.9$ as $a = (1+\nu_{\text{ur}})(1-2\nu_{\text{ur}})/(1-\nu_{\text{ur}})$ and the dilatometer vertical drained constrained modulus M_{DMT} :

$$M_{\text{DMT}} = R_M E_D \tag{3.26}$$

with $E_D = 34.7(p_1 - p_0)$ and R_M depending on soil type behavior, i.e.

- silty sand $(1.8 < I_D < 3)$: $R_M = R_{M,0} + (2.5 - R_{M,0}) \log K_D$ and $R_{M,0} = 0.14 + 0.15(I_D - 0.6)$
- sand $(I_D \geq 3)$: $R_M = 0.5 + 2 \log K_D$
- if $K_D > 10$: $R_M = 0.32 + 2.18 \log K_D$
- if $R_M < 0.85$: set $R_M = 0.85$

SPT. Table 3.5 gives some empirical equations which can be used to evaluate the "static" modulus based on SPT N-value. A graphical interpretation of correlation performance and a comparison with typical values for the "static" modulus E_s is presented in Figure 3.25.

Table 3.5: Empirical correlations relating the "static" modulus E_s with SPT N-value.

Soil Type	Empirical formula E_s in [kPa]	Remarks	Reference
Gravels/Sands well-graded	$6000N_{55}$	can be considered as a **good approximation** for E_{ur} in well-graded sands and gravels	Bowles (1997)
Gravelly sand	$1200(N_{60}+6)+4000$	seems to give **too low values** for in for E_{ur} in gravelly sand	Begemann (1974)
	$600(N_{55}+6)$	seems to gives too	Bowles (1997)
	$+2000$ if $N>15$	low values for E_{ur} in gravelly sands	
Sand	$(3.5 \text{ to } 5.0)\times 10^4 \log(N_{60})$	perceived as a **good approximation** of lower and upper bound for E_{ur} in uniform sands	Tromienkov (1974)
Sand NC	$2750N_{55}$	can be considered as a good approximation for E_{ur} in **loose to medium NC sands**	Bowles (1997)
	$7000\sqrt{N_{55}}$	can be considered as a **lower-bound approximation** for E_{ur} in NC uniform sands	Bowles (1997)
Sand NC or sand & gravel	$\frac{780N_{60}+20000}{1-\nu^2}$	can be considered as a **good approximation** for E_{ur} in uniform NC sands	authors' equation from plot of D'Appolonia et al. (1970)
Sand OC	$\frac{1100N_{60}+40000}{1-\nu^2}$	can be considered as a **good approximation** for E_{ur} in uniform OC sands	authors' equation from plot of D'Appolonia et al. (1970)
Sand saturated	$500(N_{60}+15)$	gives **too low values** for E_{ur}	Webb (1969)
Fine sands and silty sands	$100(44N_{60})^{0.75}\pm 5000$	can be considered as the **lower-bound approximation** for E_{ur} in silty sands	Schultze and Menzenbach (1961)
Clayey sand	$333(N_{60}+15)$	can be considered as the **lower-bound approximation** for E_{ur} in clayey sands	Webb (1969)

N_{60} corresponds to the energy ratio $E_r = 60$. Since the energy $\times$ blow count should be a constant for any soil, the following equation can be applied $E_{r1}\times N_1 = E_{r2}\times N_2$ (Bowles, 1997). For example, $N_{55} = N_{60}\times 60/55$.

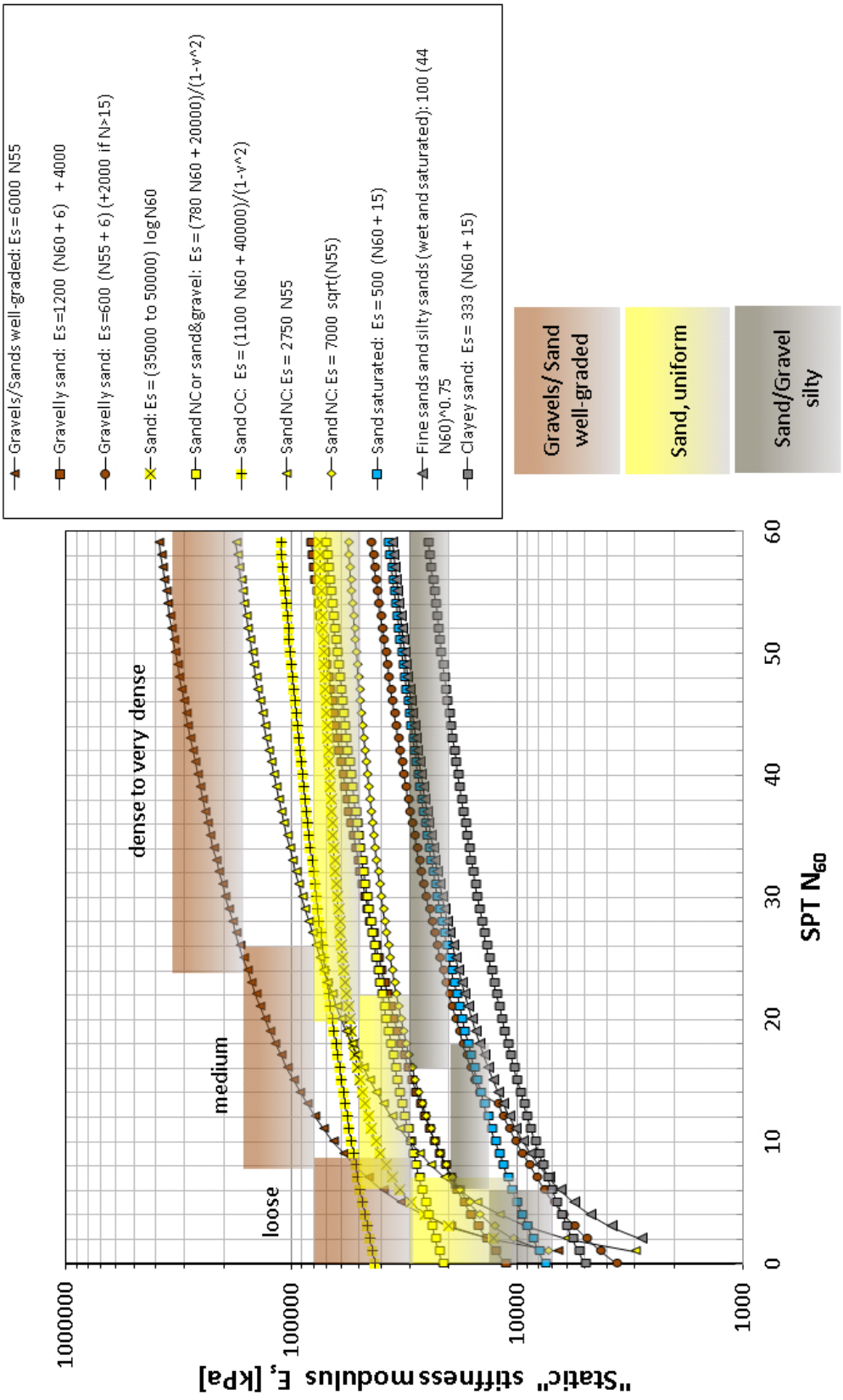

Figure 3.25: Performance of empirical correlations from Table 3.5 compared with typical values for the "static" modulus E_s from Table 3.4.

3.2.3 Oedometric modulus

In case of lack of oedometric test data for granular material the oedometric modulus can approximately be taken as:

$$E_{\text{oed}}^{\text{ref}} \cong E_{50}^{\text{ref}} \tag{3.27}$$

In such a case, the oedometric vertical reference stress $\sigma_{\text{oed}}^{\text{ref}}$ should be matched to the reference minor stress σ_{ref} since the latter typically corresponds to the confining (horizontal) pressure $\sigma_{\text{ref}} = \sigma_3 = \sigma'_h$:

$$\sigma_{\text{oed}}^{\text{ref}} = \sigma_{\text{ref}} / K_0^{\text{NC}} \tag{3.28}$$

On the other hand, when defining $\sigma_{\text{oed}}^{\text{ref}} = \sigma_{\text{ref}}$ in the model, the following relationship should be taken:

$$E_{\text{oed}}^{\text{ref}} \cong E_{50}^{\text{ref}} \left(K_0^{\text{NC}}\right)^m \tag{3.29}$$

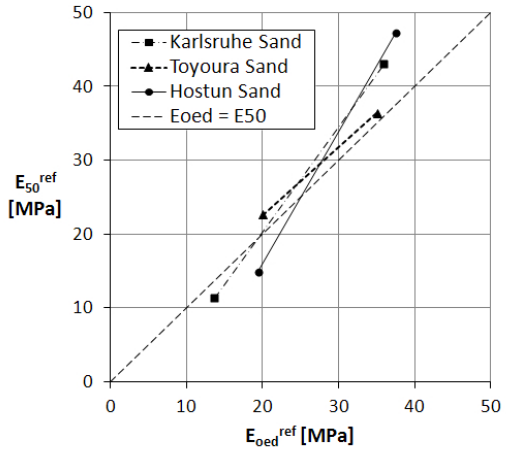

Figure 3.26: Comparison of reference stiffness moduli for sands from oedometer and triaxial tests (after Schanz and Vermeer, 1998).

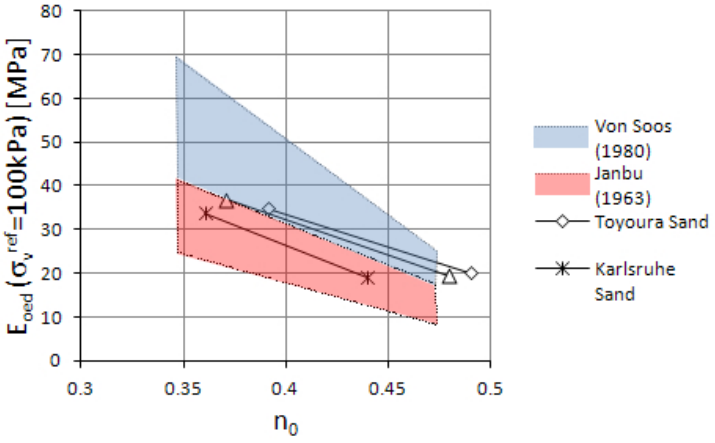

Figure 3.27: Normalized stiffness modulus of various sands derived from oedometer tests (after Schanz and Vermeer, 1998).

DMT. The constrained tangent modulus M_{D} (corresponding to E_{oed} in oedometer test) can be interpreted from three intermediate DMT parameters, i.e. the material index I_D, the horizontal stress index K_D, and the dilatometer modulus E_D, by applying the correlation presented in Eq.(3.26).

Important note. In the case of the HS model, $E_{\mathsf{oed}}^{\mathsf{ref}}$ can be taken as equal to M_{DMT} if the latter has been derived from DMT but **only for normally-consolidated soil**. In such a case σ_{oed} can be taken as σ'_{v0} which corresponds to the testing depth for which M_{DMT} has been evaluated.

3.2.4 Unloading-reloading Poisson's ratio

Experimental measurements from local strain gauges show that the initial values of Poisson's ratio in terms of small mobilized stress levels (q/q_{max}) varies between 0.1 and 0.2 for clays, sands and rocks (Figure 3.28). Therefore, the characteristic value for the *elastic unloading/reloading Poisson's ratio* of $\nu_{\text{ur}} = 0.2$ can be adopted for most soils.

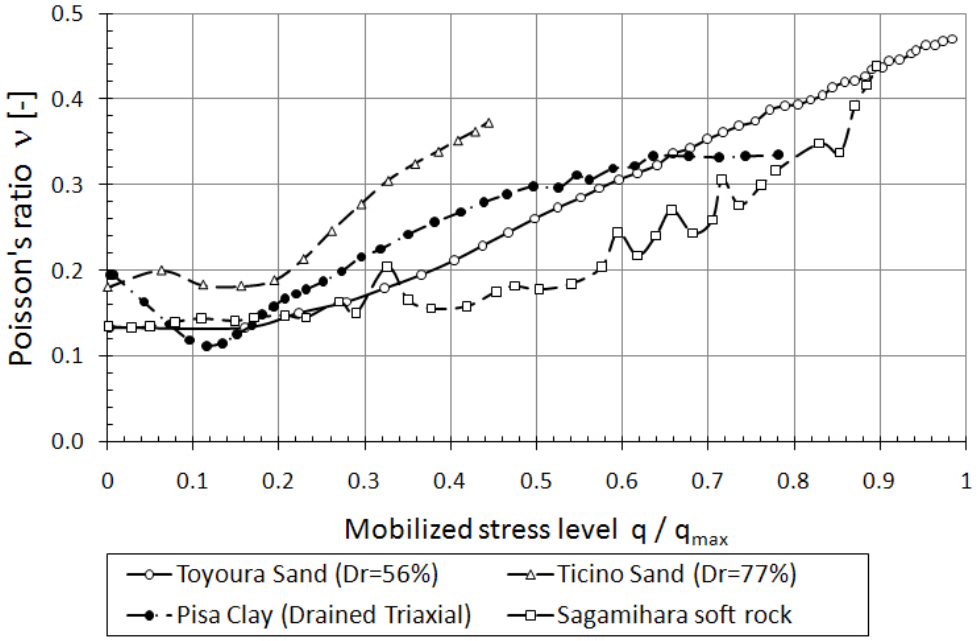

Figure 3.28: Poisson's ratio ν vs. mobilized stress level derived from local strain measurements on sand, clay and soft rock (after Mayne et al., 2009).

3.2.5 Stiffness exponent

Geotechnical evidence. In natural soil, the exponent m varies between 0.3 and 1.0. Janbu (1963) reported values of 0.5 for Norwegian sands ans silts. Typical values for m obtained in clean sands and gravels are provided in Table 3.6.

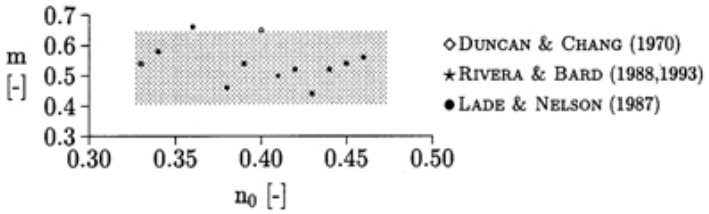

Figure 3.29: Typical values for m obtained for sands from triaxial test vs. initial porosity n_0 (from Schanz and Vermeer, 1998).

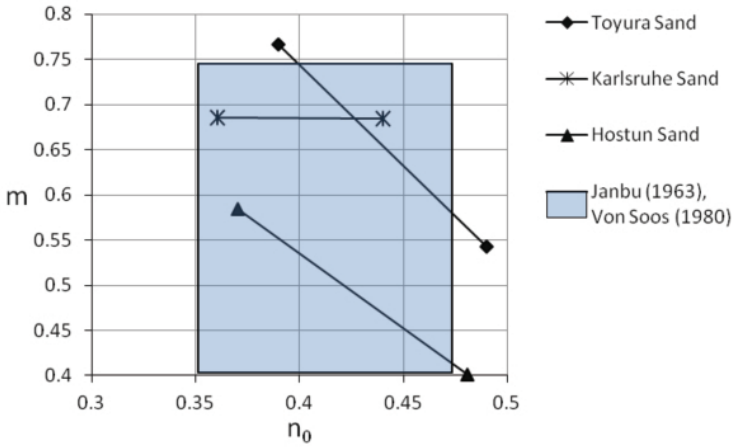

Figure 3.30: Typical values for m obtained for sands from oedometric test vs. initial porosity n_0 (after Schanz and Vermeer, 1998).

Table 3.6: Typical values for m observed in clean sands and gravels for the shear modulus G_0 (from Benz, 2007).

Soil tested	m [-]	Reference
Kenya carbonate sand	0.45-0.52	Fioravante (2000)
Quiou carbonate sand	0.62	Lo Presti et al. (1993)
Ottawa sand No.20-30	0.50	Hardin and Richart Jr (1963)
SLB sand (subround)	0.44-0.53	Hoque and Tatsuoka (2004)
Toyoura sand (subangular)	0.41-0.51	Hoque and Tatsuoka (2004)
Toyoura sand (subangular)	0.50-0.57	Chaudary et al. (2004)
Toyoura sand (subangular)	0.45	Lo Presti et al. (1993)
Ticino sand (subangular)	0.44-0.53	Hoque and Tatsuoka (2004)
Ticino sand (subangular)	0.43	Lo Presti and Jamiolkowski (1998)
Ticino sand (subangular)	0.43-0.48	Fioravante (2000)
H.River sand (subangular)	0.5-0.52	Kuwano and Jardine (2002)
Silica sand (subangular)	0.5	Kallioglou et al. (2003)
Hostun sand (angular)	0.47	Hoque and Tatsuoka (2000)
Silica sand (angular)	0.50	Kallioglou et al. (2003)
Silica sand	0.42	Wichtmann and Triantafyllidis (2004)
Hime gravel (subround)	0.45-0.51	Chaudary et al. (2004)
Chiba gravel (subround)	0.50	Modoni et al. (1999)

Table 3.7: Suggested ranges of stiffness exponent m observed for oedometric modulus E_{oed} (von Soos, 1991).

Soil type	m [-]
Gravel: poorly-graded (uniform)	$0.4 \div 0.6$
Gravel: sandy, well-graded	$0.5 \div 0.7$
Gravel: silty or clayey, well-graded, not crushed	$0.5 \div 0.7$
Gravel-sand-clay mixture, crushed	$0.7 \div 0.9$
Sand: fine, uniform	$0.6 \div 0.75$
Sand: coarse, uniform	$0.55 \div 0.7$
Sand: well-graded and gravelly sand	$0.55 \div 0.7$
Sand: with fines, not crushed	$0.65 \div 0.8$
Sand: with fines, crushed	$0.75 \div 0.9$

3.2.6 Friction angle

In coarse soils, the value of friction angle is mostly influenced by soil density, shape of particles and soil gradation. Friction angle can be approximated from Table 3.8 or estimated based on in situ test results from SPT, CPT or DMT.

Brinch Hansen and Lundgren (1958) proposed to estimate the friction angle with the following empirical correlation:

$$\phi = 36^o + \phi_1 + \phi_2 + \phi_3 + \phi_4 \tag{3.30}$$

using the following corrections to account for different soil features:

Soil type		Relative density	
• gravel	$\phi_1 = +2^o$	• very loose	$\phi_2 = -6^o$
• gravel+sand	$\phi_1 = +1^o$	• loose	$\phi_2 = -3^o$
• sand	$\phi_1 = 0^o$	• medium	$\phi_2 = 0$
		• dense	$\phi_2 = +3^o$
		• very dense	$\phi_2 = +6^o$
Soil gradation		Particles shape	
• well-graded	$\phi_3 = +3^o$	• angular	$\phi_2 = +1^o$
• medium	$\phi_3 = 0^o$	• subangular	$\phi_2 = 0^o$
• poorly-graded	$\phi_3 = -3^o$	• subrounded	$\phi_2 = -3^o$
		• rounded	$\phi_2 = -5^o$

Table 3.8: Empirical values for ϕ and D_r of granular soils based on SPT at about 6 m depth and normally consolidated (after Bowles, 1997, and modified by the authors).

Description	Very loose	Loose	Medium	Dense	Very Dense
Relative density D_r	0	0.15	0.35	0.65	0.85
SPT N_{70} :					
fine	1-2	3-6	7-15	16-30	
medium	2-3	4-7	8-20	21-40	> 40
coarse	3-6	5-9	10-25	26-45	> 45
SPT ϕ					
fine	26-28	28-30	30-34	33-38	
medium	27-28	30-32	32-36	36-42	< 50
coarse	28-30	30-34	33-40	40-50	

N_{70} corresponds to the energy ratio $E_r = 70$. Since the energy $\times$ blow count should be a constant for any soil, the following equation can be applied $E_{r1} \times N_1 = E_{r2} \times N_2$ (Bowles, 1997). For example, $N_{60} = N_{70} \times 70/60$.

SPT. The friction angle for granular soils with a small content of fine grains can be determined using the chart suggested by Peck et al. (1974). This chart also correlates the SPT number with the bearing factors N_γ and N_q which are standardly used for dimensioning of foundations.

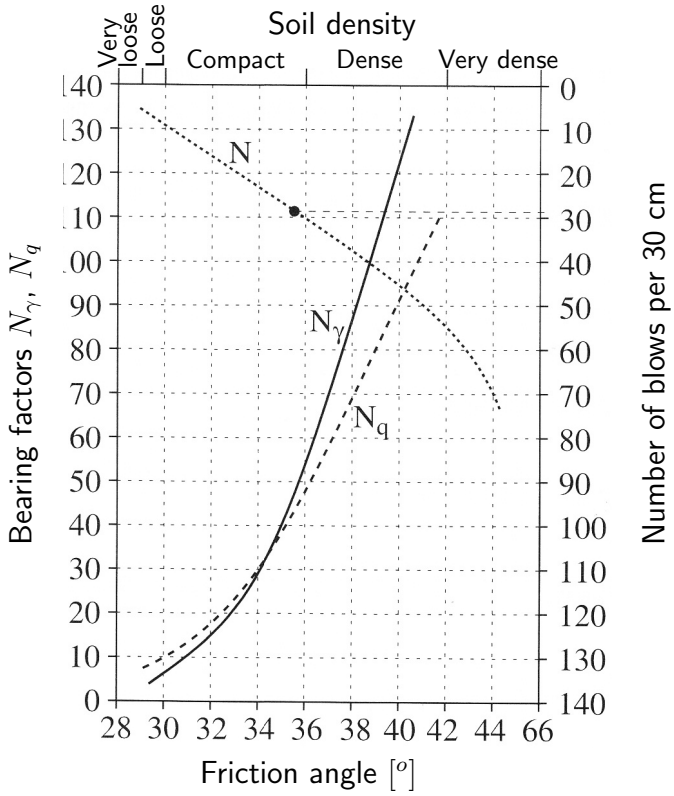

Figure 3.31: Determination of the friction angle ϕ' and bearing factors for granular soils based on the SPT number (from Peck et al., 1974).

Table 3.9: Estimation of the friction angle ϕ' from the SPT number.

	Standard Penetration Resistance	Friction angle, ϕ [^{o}]	
Soil type	N_{60}, blows/0.3m	Peck et al. (1974)	Meyerhof (1956)
Very loose sand	< 4	< 29	< 30
Loose sand	4-10	29-30	30-35
Medium sand	10-30	30-36	35-40
Dense sand	30-50	36-41	40-45
Very dense sand	> 50	> 41	> 45

Table 3.10: Empirical correlations relating SPT N-value with the effective friction angle for sands.

Empirical formula	Reference	Remarks
$\phi'_{\text{peak}} = \sqrt{15.4N_{1,60}} + 20^o$	Hatanaka and Uchida (1996)	tends to overestimate ϕ' in very dense sands $\sigma'_{v0} < 100$kPa
$\phi'_{\text{peak}} = \sqrt{15.4N_{60}} + 20^o(\pm 3^o)$	Hatanaka and Uchida (1996) without overburden correction	simplification: $\sigma'_{v0} = p_a$
$\phi' = \sqrt{20N_{1,60}} + 15^o$	Teixeira (1996)	tends to overestimate ϕ' in very dense sands $\sigma'_{v0} < 100$kPa
$\phi' = \tan^{-1}\left(\frac{N_{60}}{12.2 + 20.3\frac{\sigma'_{v0}}{p_a}}\right)^{0.34}$	Schmertmann (1975)	tends to overestimate ϕ' in very dense sands $\sigma'_{v0} < 100$kPa
$\phi' = \tan^{-1}\left(\frac{N_{60}}{32.5}\right)^{0.34}$	Schmertmann (1975) without overburden correction	simplification: $\sigma'_{v0} = p_a$
$\phi' = 25^o + 28\sqrt{\frac{N_{55}}{\sigma'_{v0}}}$	after Townsend et al. (2003)	tends to overestimate ϕ' in very dense sands $\sigma'_{v0} < 100$kPa
$\phi' = 15^o + \sqrt{18N_{70}}$	Shioi and Fukui (1982)	Japan Road Association standards
$\phi' = 27^o + 0.36N_{70}$	Shioi and Fukui (1982)	Japanese National Railway standards

N_{60} corresponds to the energy ratio $E_r = 60$. Since the energy $\times$ blow count should be a constant for any soil, the following equation can be applied $E_{r1} \times N_1 = E_{r2} \times N_2$ (Bowles, 1997). For example, $N_{55} = N_{60} \times 60/55$.

$N_{1,60} = N_{60}C_N$ ("overburden-corrected" N_{60}-value)
with the overburden correction factor $C_N = (p_a/\sigma'_{v0})^{0.5}$ (Liao and Whitman, 1986)
use $C_N = 1.7$ if $C_N > 1.7$
p_a - atmospheric pressure (average sea-level pressure is 101.325 kPa)

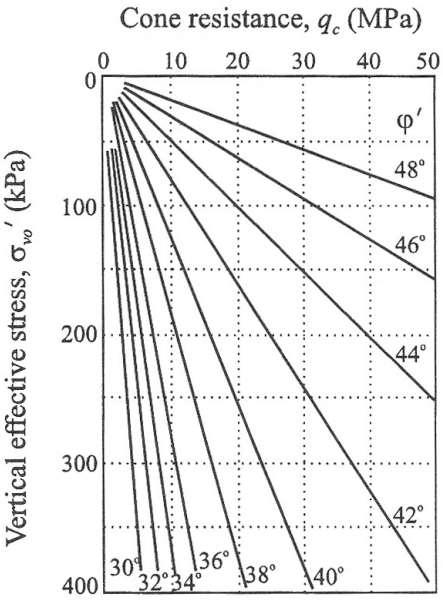

Figure 3.32: Cone resistance vs. peak friction angle ϕ' for sands (after Robertson and Campanella, 1983).

CPT. The most widely accepted relationship which relates the cone resistance q_t with ϕ' for granular materials is the expression proposed by Robertson and Campanella (1983) (Figure 3.32):

$$\phi' = \arctan\left[0.10 + 0.38 \log\left(\frac{q_t}{\sigma'_{v0}}\right)\right] \tag{3.31}$$

DMT. Two direct empirical correlations suggested in Totani et al. (1999) can be used to estimate lower and upper bounds of the range of the friction angle:

$$\phi'_{max} = 31 + K_D/(0.236 + 0.066K_D) \tag{3.32}$$

$$\phi'_{min} = 28 + 14.6 \log K_D - 2.1(\log K_D)^2 \tag{3.33}$$

with K_D denoting horizontal stress index which is calculated based on the first dilatometer reading p_0, i.e. $K_D = (p_0 - u_0)/\sigma'_{v0}$.

Geotechnical evidence. Typical values of the friction angle for granular soils are provided in Tables 3.11, 3.12, 3.13 and 3.14.

Table 3.11: Representative values of ϕ observed in sands (after Schmertmann, 1978).

Relative density D_r [%]	Friction angle ϕ [^{o}] Fine Grained Uniform	Fine Grained Well-graded	Medium Grained Uniform	Medium Grained Well-graded	Coarse Grained Uniform	Coarse Grained Well-graded
40	34	36	36	38	38	41
60	36	38	38	41	41	43
80	39	41	41	43	43	44
100	42	43	43	44	44	46

Table 3.12: Representative values of ϕ observed in cohesionless soils (after Carter and Bentley, 1991).

Soil type	ϕ [^{o}] Loose	Dense
Uniform sand, round grains	27	34
Well-graded sand, angular grains	33	45
Sandy gravels	35	50
Silty sand	27-33	30-34
Inorganic silt	27-30	30-35

Table 3.13: Representative values of ϕ observed in compacted sands and gravels (after Carter and Bentley, 1991).

Soil type	UCS class	ϕ [^{o}]
Well-graded sand-gravel mixtures	GW	> 38
Poorly-graded sand gravel mixtures	GP	> 37
Silty gravels, poorly graded sand-gravel-clay	GM	> 34
Clayey gravels, poorly graded sand-gravel-clay	GC	> 31
Well-graded clean sand, gravelly sands	SW	38
Poorly-graded clean sands	SP	37

Table 3.14: Representative relationships between relative density D_r and friction angle ϕ for granular soils.

State of compaction	Relative density D_r [%]	ϕ [^{o}]
Very loose	0-15	< 25
Loose	15-35	25-30
Medium	35-65	30-37
Dense	65-85	37-43
Very dense	85-100	> 42

3.2.7 Dilatancy angle

It is typically observed in laboratory tests that for a very dense sand the value of the dilatancy angle ψ is about $1/3$ of the peak friction angle ϕ'. In the case of loose sands, the dilatancy angle reduces to a few degrees, where as normally consolidated clays may exhibit no dilatancy at all. For example, Bolton (1986) reports $\psi_{\max} = 14.7^o$ for a dense sand which corresponded to the peak friction angle $\phi'_{\max} = 44.8^o$ derived from a drained, plane strain compression test.

Bolton (1986) proposed that for well-compacted granular soils, the maximal dilatancy angle can be estimated from:

$$\psi = 3.75 I_R \qquad \text{under triaxial conditions} \tag{3.34a}$$

$$\psi = 6.25 I_R \qquad \text{under plain strain conditions} \tag{3.34b}$$

with the relative dilatancy index I_R can be estimated for well-compacted granular soils from:

$$I_R = 5 D_r - 1 \qquad (0 < I_R < 4) \tag{3.35}$$

with D_r denoting the relative density index $\left(= \dfrac{e_{\max} - e}{e_{\max} - e_{\min}} \right)$.

Another reasonable approximation of ψ can be obtained using the following equation:

$$\psi = \phi - 30^o \tag{3.36}$$

for the values of friction angle larger than 30^o.
Notice that the above approximation gives $\psi \approx \phi'/3$ for a dense gravel, whereas small values of ψ will be obtained for the the friction angles that correspond to loose sands (typically $\phi \approx 30^o$ to 32^o).

3.2.8 Coefficient of earth pressure "at rest"

Various relationships can be found in literature for estimation of the coefficient of earth pressure "at rest" for normally consolidated soils. They commonly relate the value of K_0^{NC} to the effective friction angle ϕ', and the most popular are[6]:

$$K_0^{\mathrm{NC}} = 1 - \sin\phi' \tag{3.37a}$$

$$K_0^{\mathrm{NC}} = (\sqrt{2} - \sin\phi')/(\sqrt{2} + \sin\phi') \qquad \text{(Simpson, 1992)} \tag{3.37b}$$

These equations are illustrated in Fig.3.33.

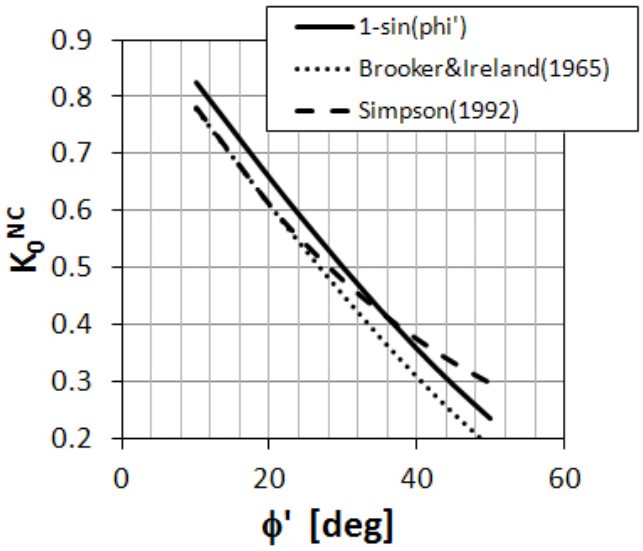

Figure 3.33: Typical relationships between K_0^{NC} and ϕ' observed for soils.

In the case of sands, the notion of preconsolidation pressure is not as meaningful as for cohesive soils, and therefore $\mathrm{OCR} = 1$ (i.e. $K_0^{\mathrm{SR}} = K_0^{\mathrm{NC}}$) can be assumed when calculating parameters H and M.

In the case of running a simulation of **isotropic consolidation** (the case of isotropically consolidated triaxial compression tests, i.e. CIU or CID), the coefficient should be assumed as $K_0^{\mathrm{SR}} = 1$.

[6]Note that Eq.(3.37a) is often erroneously called "Jaky's equation" as it is a simplified form of his original expression $K_0^{\mathrm{NC}} = (1 - \sin\phi')/(1 + \sin\phi')(1 + 2/3\sin\phi')$ (Jaky, 1947) which gives essentially the same results as Eq.(3.87).

3.2.9 Void ratio

Void ratio for a saturated soil can be calculated from:

$$e = w_n G_s \tag{3.38}$$

where w_n is the water content, G_s is the specific gravity of soil solids and S is the saturation ratio.
In the case of partially unsaturated soil, the void ratio can be obtained from:

$$\gamma = \frac{G_s \gamma_w (1 + w_n)}{1 + e} \quad \text{or} \quad e = \frac{G_s \gamma_w}{\gamma_d} - 1 \quad \text{or} \quad e = w_n G_s / S \tag{3.39}$$

where γ_d is the dry unit weight.
Hence, the maximum void ratio e_{max} can be calculated from:

$$e_{max} = \frac{G_s \gamma_w}{\gamma_{d,min}} - 1 \tag{3.40}$$

The maximum void ratio e_{max} can also be estimated according to approximate relationship presented in Figure 3.34 between the void ratio the coefficient of uniformity for different granular soils.

Typical values of void ratios and dry unit weights observed in granular soils are provided in Table 3.15.

Table 3.15: Typical values of void ratio and dry unit weights observed in granular soils (after Das, 2008).

	Voids ratio e [–]		Dry unit weight γ [kN/m^3]	
Soil type	Max	Min	Min	Max
Gravel	0.6	0.3	16	20
Coarse sand	0.75	0.35	15	19
Fine sand	0.85	0.4	14	19
Standard Ottawa sand	0.8	0.5	14	17
Gravelly sand	0.7	0.2	15	22
Silty sand	1	0.4	13	19
Silty sand and gravel	0.85	0.15	14	23

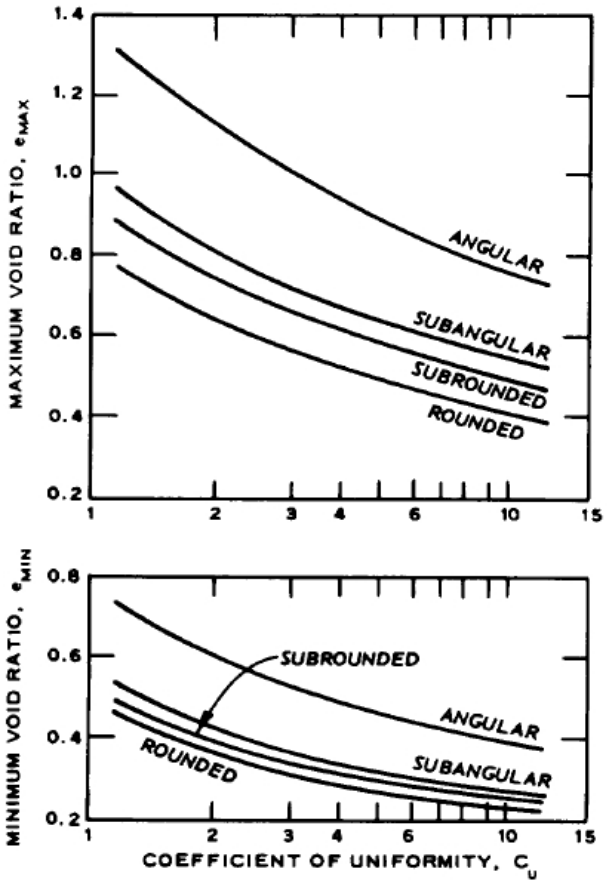

Figure 3.34: Generalized charts for estimating e_{max}, and e_{min} from gradational and particle shape characteristics (from UFC, 2004; Das, 2008).

3.2.10 Overconsolidation ratio

CPT. Estimation of OCR from CPT data in sands can be carried out using a relationship developed based on statistical multiple regression analysis of 26 separate sands worldwide with flexible-walled calibration chambers (Kulhawy and Mayne, 1990; Lunne et al., 1997; Mayne et al., 2001; Mayne, 2007). Primarily clean siliceous (quartz and feldspar) sand samples where subject to normally-consolidated and overconsolidated states $1 \leq \mathrm{OCR} \leq 15$. Sands in the test were usually dry or saturated without back pressures. The obtained empirical equation is the following:

$$\mathrm{OCR} = \left[\frac{0.192 \left(\frac{q_t}{p_a} \right)^{0.22}}{(1 - \sin\phi') \left(\frac{\sigma'_{v0}}{p_a} \right)^{0.31}} \right]^{\left(\frac{1}{\sin\phi' - 0.27} \right)} \tag{3.41}$$

with q_t denoting cone tip resistance, σ'_{v0} effective overburden stress, and atmospheric pressure is $p_a = 100$ kPa.

3.2.11 Coefficient of earth pressure "at rest"

CPT. Estimation of K_0 from CPT data in sands can be carried out using a relationship developed based on statistical multiple regression analysis of 26 separate sands worldwide with flexible-walled calibration chambers (Kulhawy and Mayne, 1990; Lunne et al., 1997; Mayne et al., 2001; Mayne, 2007). Primarily clean siliceous (quartz and feldspar) sand samples where subject to normally-consolidated and overconsolidated states $1 \leq \mathrm{OCR} \leq 15$. Sands in the test were usually dry or saturated without back pressures. The obtained empirical equation is the following:

$$K_0 = 0.192 \left(\frac{q_t}{p_a}\right)^{0.22} \left(\frac{p_a}{\sigma'_{v0}}\right)^{0.31} \mathrm{OCR}^{0.27} \tag{3.42}$$

with q_t denoting cone tip resistance, OCR overconsolidation ratio, and atmospheric pressure is $p_a = 100$ kPa.

DMT-CPT. In 1980's, researchers reported that a unique correlation for K_0 from K_D cannot be established for sands as data points showed that such correlation in sand also depends on ϕ or D_r. Initially developed Marchetti's chart $K_0 - q_c - K_D$ (Marchetti, 1985) was updated by Baldi et al. (1986) by incorporating all subsequent calibration chamber research and converted into a simple algebraic equations:

$$K_0 = 0.376 + 0.095K_D - 0.0017q_c/\sigma'_{v0} \quad \text{for "freshly" deposited sand} \tag{3.43a}$$

$$K_0 = 0.376 + 0.095K_D - 0.0046q_c/\sigma_{v0} \quad \text{for "seasoned" sand)} \tag{3.43b}$$

Marchetti et al. (2001) recommend to use Eq.(3.43a) in "freshly deposited" sand, whereas for "seasoned" sands Eq.(3.43b).

3.3 Alternative parameter estimation for cohesive materials

3.3.1 Initial stiffness modulus and small strain threshold

The present section provides a number of approaches for estimating the initial soil stiffness and the small strain threshold $\gamma_{0.7}$. Some correlations allows to directly approximate the input parameter E_0, the others provide solutions for estimating the initial shear modulus G_0. Then the input parameter E_0 can be obtained through:

$$E_0 = 2(1 + \nu_{\text{ur}})G_0 \tag{3.44}$$

assuming a constant value of the unloading-reloading Poisson's coefficient ν_{ur}.

Geotechnical evidence. Experimental data shows that the initial stiffness of soils may depend on the stress level, soil porosity and overconsolidation. These factors can be taken into account using a modified equation proposed by Hardin and Black (1969):

$$G_0 = A \cdot f(e) \cdot \text{OCR}^k \left(\frac{p'}{p_{\text{ref}}}\right)^m \quad \text{, in [MPa]} \tag{3.45}$$

where G_0 is the maximum small-strain shear modulus in MPa, p' is the mean effective stress in kPa, p_{ref} is the reference stress equal to the atmospheric pressure $p_{\text{ref}} = 100$ kPa, OCR is the overconsolidation ratio and A, $f(e)$, k, m are the correlated functions and parameters which are given in Table 3.16 and 3.18 for different types of soils. It is observed that the empirical exponent k varies from 0 for sands and 0.5 for high plasticity clays. It means that k may increase with soil plasticity and its value can be taken from Table 3.17.

Biarez and Hicher (1994) proposed a simple relationship for all soils with $w_L < 50\%$:

$$E_0 = \frac{140}{e}\left(\frac{p'}{p_{\text{ref}}}\right)^{0.5} \quad \text{, in [MPa]} \tag{3.46}$$

Table 3.16: Parameters for estimation of G_0 in clays using Eq.(3.45).

Soil tested	I_P [%]	A [-]	$f(e)$ [-]	k [-]	m_p [-]	Reference
Quaternary Italian clays (see Fig.3.35)	-	60	$e^{-1.30}$	N/A	0.50	Jamiolkowski et al. (1995)
Avezzano clay (Holocene-Pleistocene)	10-30	74	$e^{-1.27}$	N/A	0.46	Lo Presti and Jamiolkowski (1998)
Fucino clay (Holocene-Pleistocene)	45-75	64	$e^{-1.52}$	N/A	0.40	Lo Presti and Jamiolkowski (1998)
Garigliano clay (Holocene)	10-40	44	$e^{-1.11}$	N/A	0.58	Lo Presti and Jamiolkowski (1998)
Panigaglia clay (Holocene)	44	44	$e^{-1.30}$	N/A	0.50	Lo Presti and Jamiolkowski (1998)
Montaldo di Castro clay (Pleistocene)	15-34	50	$e^{-1.33}$	N/A	0.40	Lo Presti and Jamiolkowski (1998)
Reconstituted Valericca clay (Pleistocene)	27	44	1	N/A	0.85	Rampello et al. (1997)
Pisa clay (Pleistocene)	23-46	50	$e^{-1.43}$	N/A	0.44	Lo Presti and Jamiolkowski (1998)
London clay (reconstituted)	41	13	1	0.25*	0.76	Viggiani and Atkinson (1995)
Speswhite kaolin clay (reconstituted)	24	40	1	0.2*	0.65	Viggiani and Atkinson (1995)
Kaolin clay	35	45	$\frac{(2.97-e)^2}{1+e}$	N/A	0.50	Marcuson and Wahls (1972)
Bentonite clay	60	4.5	$\frac{(4.40-e)^2}{1+e}$	N/A	0.50	Marcuson and Wahls (1972)

*overconsolidation ratio OCR based on the mean stress ($\mathrm{OCR} = p'_c/p'$)

Table 3.17: Overconsolidation ratio exponent k used in Eq.(3.45).

Plasticity Index I_P [%]	Exponent k [-]
0	0.00
20	0.18
40	0.30
60	0.41
80	0.48
≥ 100	0.50

source: Kramer (1996, after Hardin&Drnevich 1972)

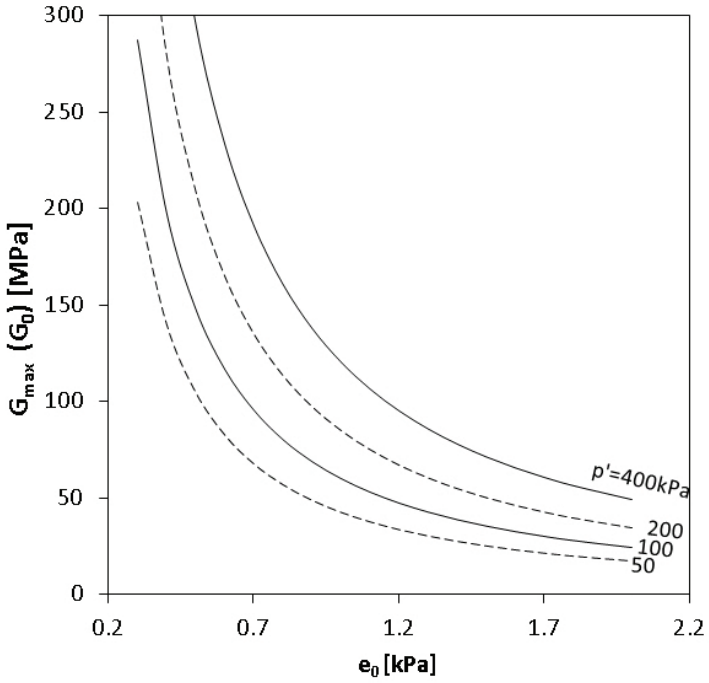

Figure 3.35: Typical void ratio-G_0 dependency using an empirical equation by Jamiolkowski et al. (1995) from Table 3.16.

Table 3.18: Parameters for estimation of G_0 in cohesive soils using Eq.(3.45). The relationships are illustrated in Figure 3.10.

Soil tested	e_{min} [-]	e_{max} [-]	A [-]	$f(e)$ [-]	m_p [-]	Reference
All soils with $w_L < 50\%$	0.4	1.8	58*	$\frac{1}{e}$	0.5	Biarez and Hicher (1994)
Undisturbed clayey soils	0.6	1.5	33	$\frac{(2.97-e)^2}{1+e}$	0.5	Hardin and Black (1969)
Undisturbed cohesive soils	0.6	1.5	16	$\frac{(2.97-e)^2}{1+e}$	0.5	Kim and Novak (1981)
Loess	1.4	4.0	1.4	$\frac{(7.32-e)^2}{1+e}$	0.6	Kokusho et al. (1982)

*obtained from Eq. 3.14 assuming $\nu = 0.2$

Geotechnical evidence. In case of lack of test data at very small strains, E_0 for cohesive soils can be evaluated from an empirical relation proposed by Alpan (1970), see Figure 3.11. The chart relates so-called "static" modulus E_s to the "dynamic" modulus E_d. For the sake of HS-SmallStrain model, E_s can be considered as E_{ur} obtained at engineering strain levels ($\varepsilon \approx 10^{-3}$), whereas E_0 can be considered as $\approx E_d$.

Geotechnical evidence. It can be observed in laboratory test that secant stiffness reduces with mobilization of the shear strength. Mayne (2007) provides a selection of secant modulus curves, represented by the ratio G_s/G_0 or E_s/E_0. The collected results were derived from monotonic laboratory shear tests performed on an sorted mix of clayey ans sandy materials, and they are presented in Figure 3.13.
Geotechnical evidence and authors' experience show that E_0/E_{50} **ratio varies in natural clays from 4.6 to 30** depending on soil aging and particle bonding. The higher values of E_0/E_{50} ratio are suggested for aged, cemented and structured clay, whereas the lower ones for insensitive, unstructured and remoulded clays.

CPT. A relationship between G_0 and corrected tip resistance q_t for clays has been proposed by Mayne and Rix (1993). The correlation also depends upon the inplace void ratio e_0 (cf. Figure 3.36):

$$G_0 = 49.4 q_t^{0.695} e_0^{-1.13} \quad \text{in MPa} \tag{3.47}$$

with q_t in [MPa].
The effective vertical stress σ'_{v0} can used to recalculate the estimated modulus $E_0 = 2G_0(1+\nu_{\text{ur}})$ to the reference one E_0^{ref} using the stiffness dependency power law assuming that minor stress σ_3 equal to $\min(\sigma'_{v0}; \sigma'_{v0} \cdot K_0)$.

CPT. Based on a database for ten Norwegian marine soft clay sites, Long and Shane (2010) proposed an expression obtained by modifying the original expression by Simonini and Cola (2000). The relationship, apart of q_t, also accounts for pore pressure measurements (cf. Figure 3.36). The modification was related to replacing $\Delta u/q_c$ ratio with pore pressure parameter B_q $(= (u_2 - u_0)/(q_t - \sigma_{v0}))$ and tunning empirical coefficients.

$$G_0 = 4.39 q_t^{1.225} (1 + B_q)^{2.53} \quad \pm 50\% \tag{3.48}$$

with G_0, q_t in kPa and B_q is a dimensionless pore pressure parameter.

DMT. G_0 can be estimated based on DMT data using a correlation reported by Hryciw (1990). The correlation was originally proposed for sands, silts and clays, however it seems to underestimate G_0 in sands (cf. Figure 3.37):

$$G_0 = \frac{530}{(\sigma'_{v0}/p_a)^{0.25}} \frac{\gamma_{\text{DMT}}/\gamma_{\text{W}} - 1}{2.7 - \gamma_{\text{DMT}}/\gamma_{\text{W}}} K_0^{0.25} (p_a \sigma'_{v0})^{0.5} \tag{3.49}$$

with G_0, p_a, σ'_{v0} in same units; $\gamma_{\text{DMT}}/\gamma_{\text{W}}$ dilatomter-based unit weight ratio obtained using Marchetti's chart for soil type and unit weight estimation.

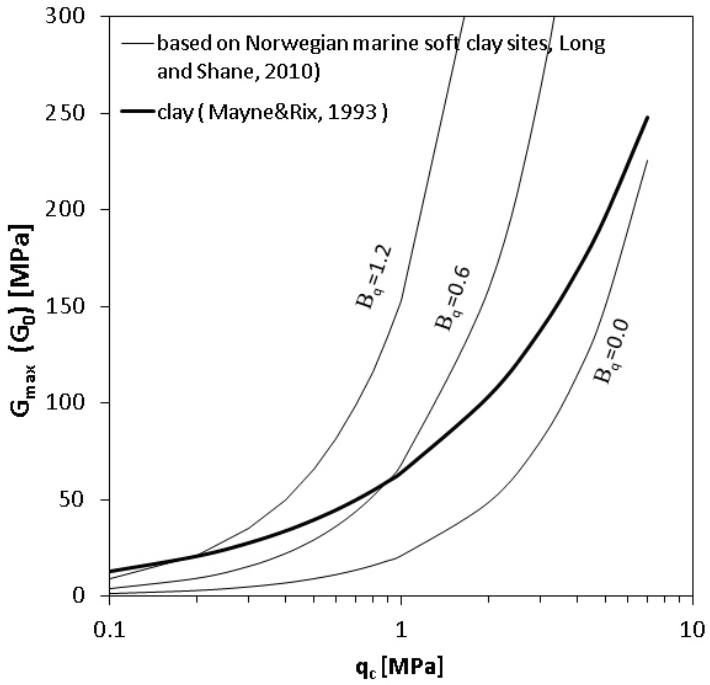

Figure 3.36: Comparison of empirical correlations for estimating G_0 (G_{max}) in clays from CPT data; plot for Eq. (3.47) obtained for $e_0 = 0.8$.

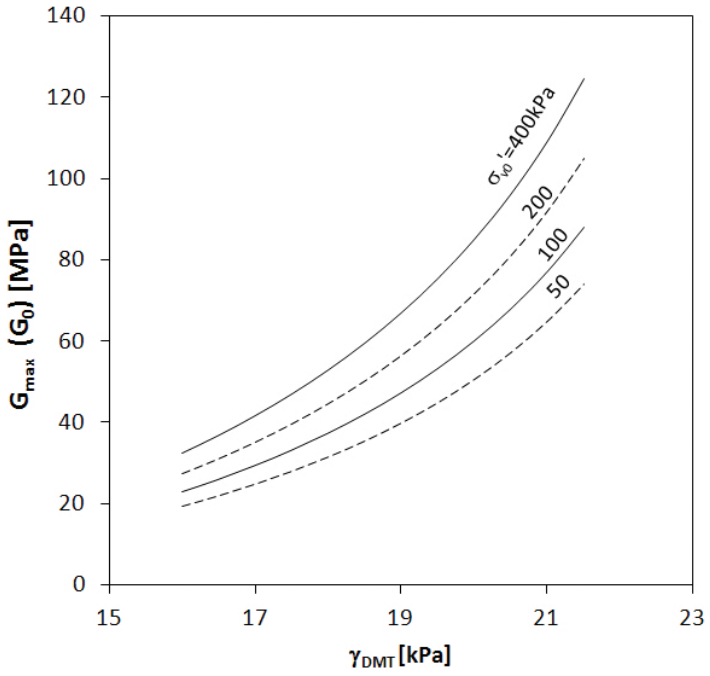

Figure 3.37: Estimating G_0 from DMT data using Eq.(3.49) proposed by Hryciw (1990) (plot obtained for $K_0 = 0.5$).

Geotechnical evidence. Experimental measurements reveal that in the case of fine plastic soils, the reference strain threshold $\gamma_{0.7}$ at which $G_s/G_0 = 0.722$ may be affected by many factors such as soil plasticity, stress history, confining pressure, number of cyclic loadings and others. A well known experimental database reported in Vucetic and Dobry (1991) (Figure 3.38) illustrates the relationship between $\gamma_{0.7}$ and plasticity index I_P. Based on this experimental data, $\gamma_{0.7}$ can be approximated by the following empirical correlation:

$$\begin{array}{ll} \gamma_{0.7} = \gamma_{0.7}^{\text{ref}} + 5 \cdot 10^{-6} I_P & \text{for } I_P < 15 \\ \gamma_{0.7} = 10^{1.15 \log(I_P) - 5.1} & \text{for } I_P \geq 15 \end{array} \tag{3.50}$$

with the reference strain threshold $\gamma_{0.7}^{\text{ref}}\,(I_P = 0) = 1 \cdot 10^{-4}$ and plasticity index I_P in $\%$.
A fit of the above correlation to experimental data is illustrated in Figure 3.38. Since the I_P-dependent chart was compiled from the original data which showed a considerable scatter, a 50% error can be assumed in estimations giving max and min ranges.
Results for $I_P < 100$ have been experimentally proved in many research, whereas extrapolation for soils which exhibit $I_P > 100$ should be treated carefully.

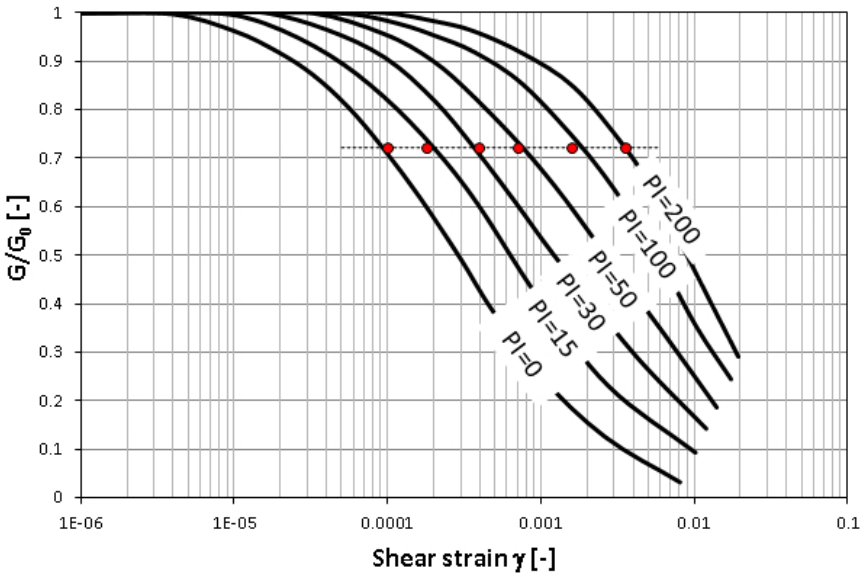

Figure 3.38: Comparison of predictions for $\gamma_{0.7}$ from the plasticity index I_P (PI) using Eq.(3.50) with experimental data reported for cohesive soils (after Vucetic and Dobry, 1991).

Recently, Vardanega and Bolton (2011) reported a database of 20 clays and silts (OCR=1-17) for which a hyperbolic fit to the normalized reduction curve data has been proposed as follows:

$$\frac{G}{G_0} = \frac{1}{1 + \left(\dfrac{\gamma}{\gamma_{0.5}}\right)^{0.74}} \tag{3.51}$$

with the reference threshold parameter $\gamma_{0.5}$ which corresponds to $G_s/G_0 = 0.5$. They also confirmed that strain threshold for cohesive soils depends on the plasticity index I_P (Figure 3.39), liquid limit w_L (Figure 3.41) and plastic limit w_P. Based on these curves, they proposed a number of correlations for prediction of the reference strain threshold $\gamma_{0.5}$. Linear regression

analyzes were characterized by reasonable R^2 values although an error band of $\pm 50\%$ was observed. For the purpose of this report, the original coefficients obtained through regression analyzes for $\gamma_{0.5}$ where recalculated to the model parameter $\gamma_{0.7}$:

$$\gamma_{0.7} = \frac{0.5975 I_P[-]}{1000} \quad \pm 50\%, \quad R^2 = 0.75, \quad n = 61, \quad \text{for } I_P = 10 - 150\% \tag{3.52a}$$

$$\gamma_{0.7} = \frac{0.3442 w_L[-]}{1000} \quad \pm 50\%, \quad R^2 = 0.75, \quad n = 61, \quad \text{for } w_L = 25 - 240\% \tag{3.52b}$$

$$\gamma_{0.7} = \frac{0.7517 w_P[-]}{1000} \quad \pm 50\%, \quad R^2 = 0.57, \quad n = 61, \quad \text{for } w_P = 12 - 90\% \tag{3.52c}$$

Note that the above correlations account for no history stress nor confining pressure effects.

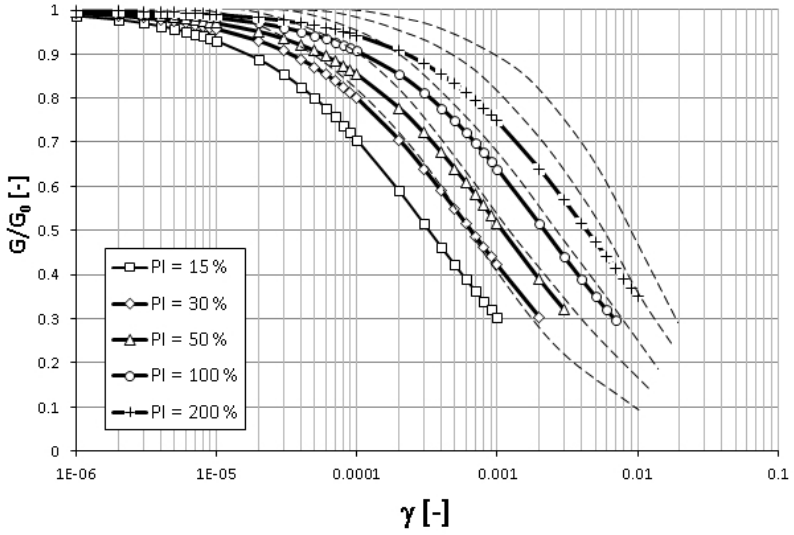

Figure 3.39: Comparison of predictions using Eq.(3.51) and (3.52a) with curves from Vucetic and Dobry (1991).

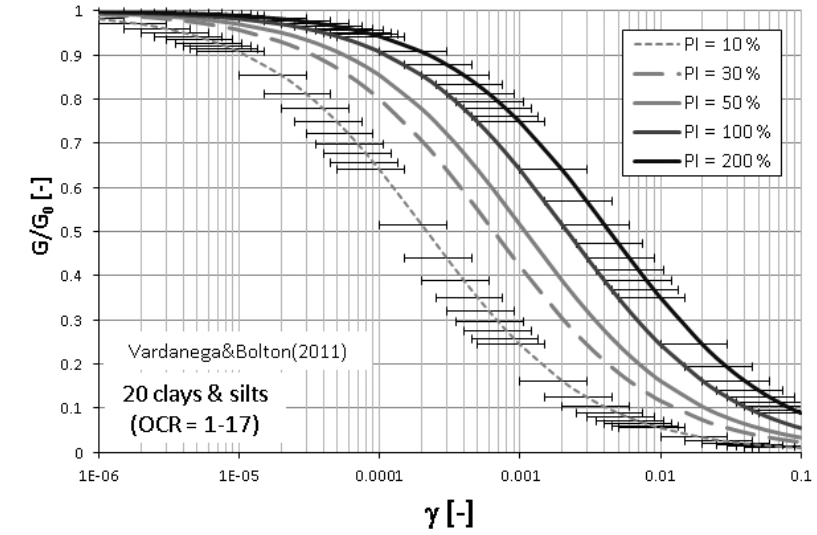

Figure 3.40: I_P-dependent predictions using Eq.(3.51) and (3.52a) with possible 50% error.

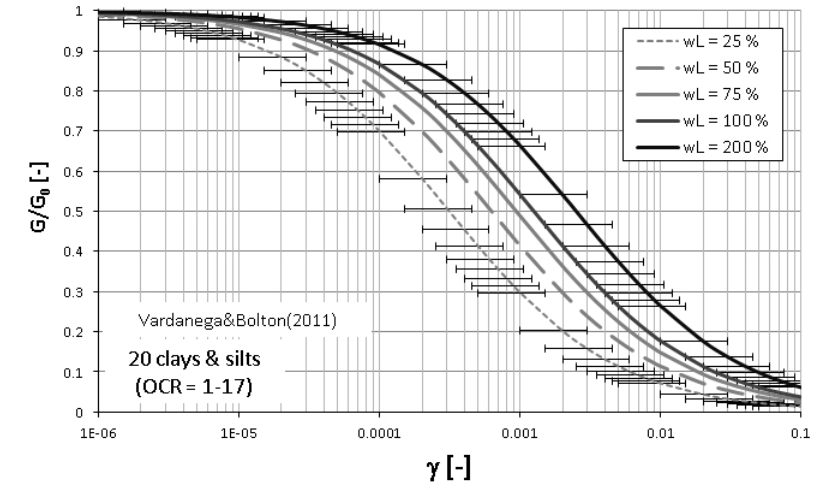

Figure 3.41: w_L-dependent predictions using Eq.(3.51) and (3.52b) with possible 50% error.

Note that the diagrams proposed in Vucetic and Dobry (1991) and Vardanega and Bolton (2011) are independent on stress history. In order to account an observed increase of $\gamma_{0.7}$ with the increasing OCR, Stokoe et al. (2004) proposed the following formula to predict $\gamma_{0.7}$ for plastic soils:

$$\gamma_{0.7} = \gamma_{0.7}^{\text{ref}} + 5 \cdot 10^{-6} I_P \mathrm{OCR}^{0.3} \tag{3.53}$$

with the reference strain threshold $\gamma_{0.7}^{\text{ref}}\,(I_P = 0, \mathrm{OCR} = 1) = 1 \cdot 10^{-4}$.

Darendeli (2001) proposed a correlation for the reference strain threshold which additionally accounts for the effect of confining pressure:

$$\gamma_{0.7} = (a_1 + a_2 I_P \cdot \mathrm{OCR}^{a_3})\, \sigma_0^{a_4} \tag{3.54}$$

Since the original correlation was developed for the reference strain threshold $\gamma_{0.5}$, for the purpose of the HS model, the empirical coefficients a_1, a_2, a_3 and a_4 have been adjusted in order to predict $\gamma_{0.7}$:

$\gamma_{0.7}$ - reference strain threshold in $[\%]$
I_P - plasticity index in $[\%]$
$\sigma_0 = \dfrac{p'_0}{p^{\text{ref}}}$ normalized confining pressure
$p'_0 = \dfrac{(2K_0 + 1)\sigma'_{v0}}{3}$kPa *in situ* mean effective stress
$p^{\text{ref}} \cong 100$kPa (atmospheric pressure)
$a_1 = 1.25e - 2$
$a_2 = 3.7e - 4$
$a_3 = 0.3$
$a_4 = 0.35$

Note that in the current formulation of the HS model no stress dependency for $\gamma_{0.7}$ is considered. If needed, this parameter can be incorporated into boundary value problems through defining average mean effective stresses for defined sub-layers.

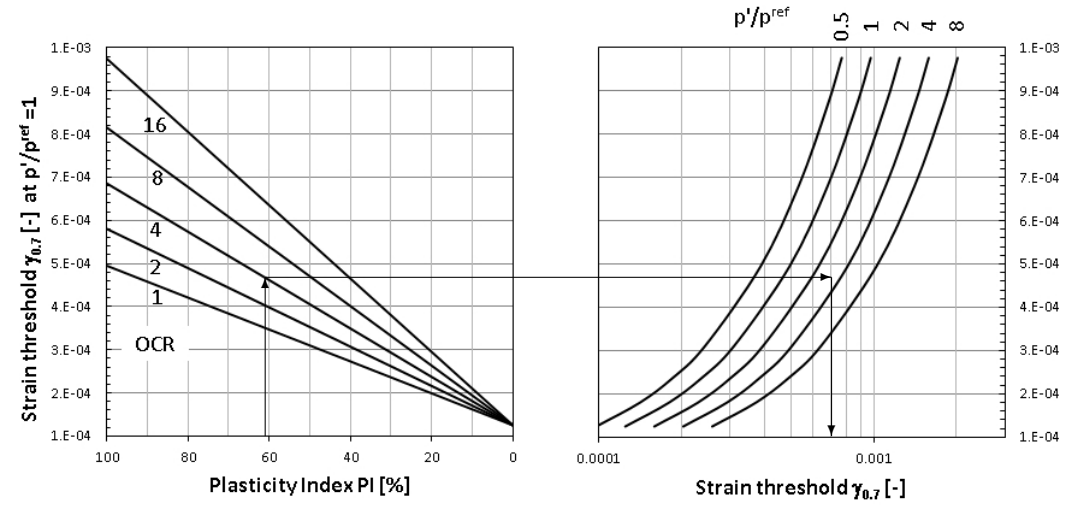

Figure 3.42: A graphical interpretation of Eq.(3.54): an example of estimation of shear strain threshold $\gamma_{0.7}$ for $I_P = 40\%$, $\mathrm{OCR} = 4$ and mean effective stress $p'_0 = 400$kPa.

3.3.2 Strength parameters

It is commonly known that the strength of clays in terms of effective stresses is mostly frictional and the effective cohesion $c' \approx 0$. Small values of cohesion which are observed during testing may appear in partially saturated clays where the meniscus effects (suction) draw soil particles together resulting in inter-particles stresses. Larger magnitudes of cohesion can be often observed in cemented soils due to bonding effects.

Geotechnical evidence. The values of the effective friction angle ϕ' observed for fine soils fall in a wide range from 18^o to 42^o. Some representative values of ϕ' for compacted clays are provided in Table 3.19 after Carter and Bentley (1991).

Table 3.19: Representative values of ϕ' observed in compacted clays (after Carter and Bentley, 1991).

Soil type	UCS class	ϕ [^{o}]
Silty clays, sand-silt mix	SM	34
Clayey sands, sandy-clay mix	SC	31
Silts and clayey silts	ML	32
Clays of low plasticity	CL	28
Clayey silts	MH	25
Clays of high plasticity	CH	19

In fine soils, soil consistency affects the magnitude of the void ratio. Therefore, it seems to be relevant to relate the friction angle with the soil consistency, as the value of friction angle depends on the void ratio. Typical ranges of shear strength parameters for some common soils types given by Senneset et al. (1989) have been extended and are presented in 3.20.

Table 3.20: Typical ranges of shear strength parameters for some common soils types (extended after Senneset et al., 1989).

Soil type	ϕ [^{o}]	c' [^{o}]
Clay		
Silt		

CPTU. The estimation of effective stress parameters from the total stress analysis of undrained penetration is difficult. The solution needs to account for excess pore water pressure for which the distribution around the cone is highly complex and difficult to model analytically. Interpretation methods can be thus viewed as rather approximative.
The effective friction angle ϕ' can be estimated using the solution which is based on the bearing capacity theory (Sandven et al., 1988)[7]:

$$q_t - \sigma_{vo} = N_m(\sigma'_{vo} + a) \quad \text{with} \quad N_m = \frac{N_q - 1}{1 + N_u B_q} \tag{3.55}$$

[7] The approach proposed by researchers from the Norwegian University of Science and Technology (NTNU) is referred to NTNU method.

where a' denotes the attraction ($a' = c' \cot \phi'$), β is the angle of plastification, N_q and N_u are the bearing capacity factors ($N_q = N_q(\phi', \beta)$ and $N_u \cong N_u(\phi)$).
Mayne (2005, 2007) proposed a simplified expression which is applicable to the ranges of $20° \leq \phi' \leq 45°$ and $0.1 \leq B_q \leq 1.0$ (see Figure 3.43). By setting for the above method the effective cohesion intercept $c' = 0$ and plastification angle $\beta = 0$, the values of ϕ' were evaluated line-by-line and the following approximate expression was obtained:

$$\phi' \approx 29.5° B_q^{0.121} \left(0.256 + 0.336 B_q + \log Q_t\right) \tag{3.56}$$

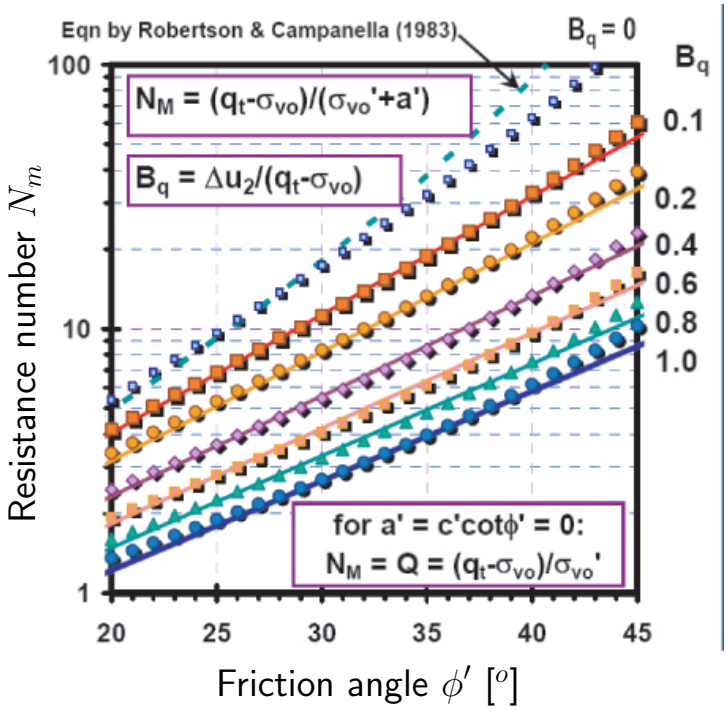

Figure 3.43: Friction angle for sands, silts and clays based on approximation of NTNU original method (from Mayne, 2005).

Strength parameters vs. undrained shear strength. Best-quality predictions of the strength parameters ϕ' and c' for cohesive soils can be essentially derived from laboratory tests. In case of lack of laboratory data, these model parameters can be approximately calibrated based on the undrained shear strength s_u. The magnitude of s_u can be determined from a variety of *in situ* tests such as field vane tests (FVT), pressuremeter tests, cone penetration tests (CPT or CPTU), etc. Some interpretation formula for determining s_u from commonly used field tests are provided in Appendix A.

Considering that the undrained shear strength in the undrained triaxial conditions is defined as:

$$s_u = \frac{1}{2}\left(\sigma_1 - \sigma_3\right)_f = \frac{1}{2} q_f \tag{3.57}$$

the model parameters ϕ and c can be adjusted so that they satisfy the normalized condition:

$$\frac{s_u^{\text{in situ}}}{p_0^{'\,\text{in situ}}} \cong \frac{1/2 q_f^{\text{sim}}}{p_0^{'\,\text{sim}}} \tag{3.58}$$

where $s_u^{\text{in situ}}$ and $p_0^{'\,\text{in situ}}$ denote field test results of the undrained shear strength and the effective mean stress respectively, whereas q_f^{sim} is the failure deviatoric stress obtained through

a numerical simulation of the undrained compression triaxial test at given initial effective mean stress $p_0^{'\,\text{sim}}$. Note that the above relation should be considered as approximative since s_u is not a unique soil parameter as, it depends, among others, on the type of test, which involves particular strain paths related to dominant shear modes appearing during testing (cf. Wroth, 1984; Jamiolkowski et al., 1985).

Conceptually, normalization of data in terms of initial stress conditions removes the effect of depth. Although the mechanisms of particular field test are influenced by both σ'_{h0} and σ'_{v0}, for practical reasons, the normalization can be carried out in terms of σ'_{v0} since there is often little information about σ'_{h0}. Therefore, calibration of the strength parameters can be carried out to satisfy the following relation:

$$\frac{s_\text{u}^{\text{in situ}}}{\sigma_{v0}^{'\,\text{in situ}}} \approx \frac{1/2q_f^{\text{sim}}}{\sigma_{1,0}^{'\,\text{sim}}} \tag{3.59}$$

where $\sigma_{1,0}^{'\,\text{sim}}$ denotes the axial effective stress at the beginning of simulation.
The calibration procedure can be summarized as follows:

1. Assess field values of s_u for, at least, two different depths (different σ'_{v0}) and plot the data on $\sigma'_{v0} - s_\text{u}$ chart.

2. Run two simulations of the undrained triaxial compression test (preferably aniotropically-consolidated with the specified $K_0^{\text{SR}} \neq 1.0$) for different $\sigma_{1,0}^{'\,\text{sim}}$ and corresponding OCRs with an initial guess of parameters ϕ and c, and an assumed failure ratio R_f (note that an explicit ultimate deviatoric stress can be obtained for the dilatancy angle $\psi = 0$, or non-zero ψ with the assumed dilatancy cut-off).

3. Plot numerical results of $1/2q_f$ on $\sigma'_{v0} - s_\text{u}$ chart (as in Figure 3.44) and check the degree of fit for numerical and *in situ* trend lines.

4. Return to step 2 if the degree of fit is not satisfactory and modify parameters ϕ and c. Note that each modification of ϕ and c requires updating K_0^{NC} and evaluating of parameters M and H before the next calculation run.

In the case of overconsolidated material, if the initial mean effective stress p'_0 lies before the mean effective stress p^* which value corresponds to the intersection between deviatoric and isotropic mechanisms (see Figure 3.45), q_f can be estimated directly from the Mohr-Coulomb criterion (cf. Figure 3.1):

$$q_f = \alpha\,(p'_0 + c\cot\phi) \tag{3.60}$$

where α is related to the friction angle ϕ which depends on the dominating shear mode which is appropriate to a given *in situ* test:

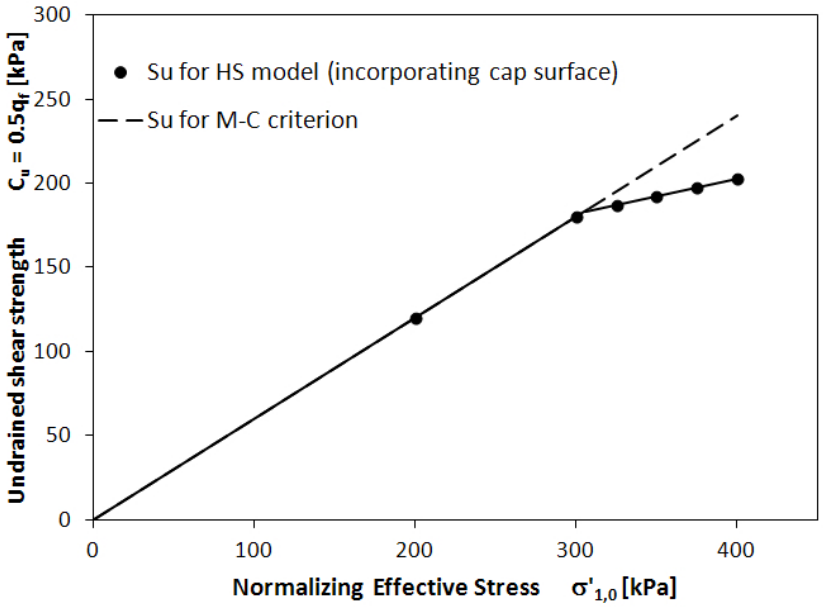

Figure 3.44: Undrained shear strength s_{u} against normalizing effective stress $\sigma_{1,0}^{'\,\mathrm{sim}}$ (p^* denotes the intersection between deviatoric and isotropic mechanisms, see Figure 3.45).

$$\alpha = \frac{6\sin\phi}{3-\sin\phi} \quad \text{for triaxial compression conditions} \tag{3.61a}$$

$$\alpha = \frac{6\sin\phi}{3+\sin\phi} \quad \text{for triaxial extension conditions} \tag{3.61b}$$

$$\alpha = \sqrt{3}\sin\phi \quad \text{for plane strain conditions} \tag{3.61c}$$

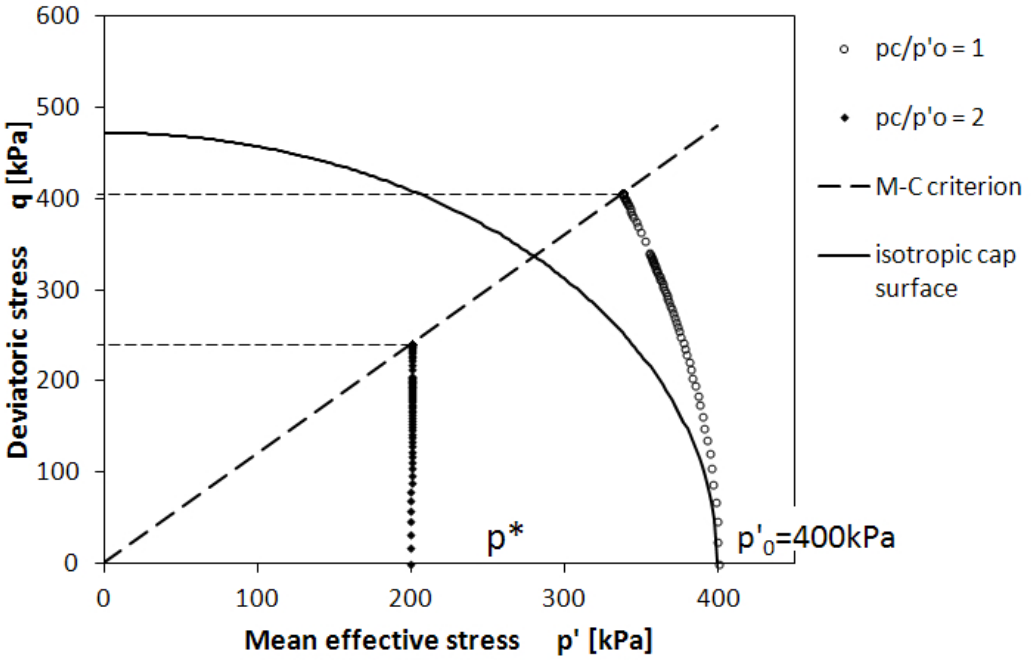

Figure 3.45: Effective stress paths derived from simulations of undrained compression test in normally- and overconsolidated soil.

3.3.3 Failure ratio

For most soils, the value of R_f falls between 0.75 and 1 and an average value of the failure ratio can be taken as $R_f = 0.9$. Kempfert (2006) reported some R_f values derived from triaxial compression tests for three lacustrine soft soils in southern Germany:

- CICD test: $R_f = 0.73 - 0.88$, with the average value of 0.82
- CICU test: $R_f = 0.70 - 0.99$, with the average value of 0.89

3.3.4 Dilatancy angle

While for granular soils the maximal dilatancy angle can be related to the relative density (D_r), an estimation of ψ for clays relies on geotechnical experience. For instance, it can be observed in laboratory tests that normally consolidated clays may exhibit no dilatancy at all. Therefore, it is proposed that for cohesive soils, it can be assumed that dilatancy depends on the preconsolidation state and ψ can be approximately taken as:

- $\psi = 0^o$ for normally- and ligthly-overconslidated soil
- $\psi = \phi'/6$ for overconsolidated soil
- $\psi = \phi'/3$ for heavily overconsolidated soil

Another reasonable approximation of ψ can be obtained using the following equation:

$$\psi = \phi - 30^o \tag{3.62}$$

for the values of friction angle larger than 30^o.
Notice that the above approximation gives $\psi \approx \phi'/3$ for a dense gravel, whereas small values of ψ will be obtained for the the friction angles that correspond to compacted silts or clays(typically $\phi \approx 30^o$ to 35^o).

3.3.5 Stiffness moduli

In general, the relation between the stiffness moduli is as follows:

$$E_{50} < E_s < E_{\text{ur}} \tag{3.63}$$

where E_s denotes "static" modulus or secant modulus taken from the initial part of the $\varepsilon_1 - q$ experimental curve at $\varepsilon_1 = 0.1\%$.

In the case when one of the stiffness moduli cannot be directly determined, it may be relevant for many practical cases to set:

$$\frac{E_{\text{ur}}^{\text{ref}}}{E_{50}^{\text{ref}}} = 3 \text{ to } 6 \qquad \text{(an average can be assumed equal to 4)} \tag{3.64}$$

However, note that the following condition should be satisfied: $\dfrac{E_{\text{ur}}^{\text{ref}}}{E_{50}^{\text{ref}}} > 2$.

The secant modulus E_{50} can be approximated based on the known value of the "static" modulus E_s and according to the approach described in Section 3.2.2, Figure 3.22. A rough approximation of the order of magnitudes for the "static" modulus E_s is given in Table 3.21.

Table 3.21: Typical values for the "static" modulus E_s [MPa] (compiled from Kezdi, 1974; Prat et al., 1995).

	Soil Consistency											
	Very Soft		Soft		Medium		Stiff		Very Stiff		Hard	
Soil Type	Min	Max	Min	Max	Min	Max	Min	Max	Min	Max	Min	Max
Silts												
slight plasticity	2.5	4	5	8	10	15	15	20	20	40	40	80
low plasticity	1.5	3	3	6	6	10	10	15	15	30	30	60
Clays												
low to medium plast.	0.5	3	2	5	5	8	8	12	12	30	30	70
high plasticity	0.35	2	1.5	4	4	7	7	12	12	20	20	32
Silt organic					0.5	5						
Clay organic					0.5	4						

Assuming that during unloading/reloading soil behaves elastically, the modulus E_{ur} can be related with the constrained unloading/reloading oedometric modulus $E_{\text{oed,ur}}$ through:

$$E_{\text{ur}} = E_{\text{oed,ur}} \frac{(1+\nu_{\text{ur}})(1-2\nu_{\text{ur}})}{1-\nu_{\text{ur}}} \tag{3.65}$$

Note, however, that E_{ur} is not a unique value for a given soil in the oedometric test because E_{ur} depends on the previous maximal stress level σ_c' attained before the unloading and the corresponding void ratio e_c, as shown in Figure 3.46. Therefore, assuming an infinitesimal change of the compression stress, i.e. $\Delta\sigma' \to 0$, the unloading/reloading oedometric modulus $E_{\text{oed,ur}}$ should be approximated by similarity with Eq.(3.3) as:

$$E_{\text{oed,ur}} = \frac{2.3(1+e_0)}{C_s}\sigma_c' \tag{3.66}$$

where C_s is the swelling index (Figure 3.46).
Since the $E_{\text{oed,ur}}$ was approximated for the stress point belonging to the primary loading line (K_0^{NC}-line), such a determined reference unloading/reloading modulus $E_{\text{ur}}^{\text{ref}}$ corresponds thus to the reference stress σ^{ref} which can be estimated from:

$$\sigma^{\text{ref}} = K_0^{\text{NC}} \sigma'_c \tag{3.67}$$

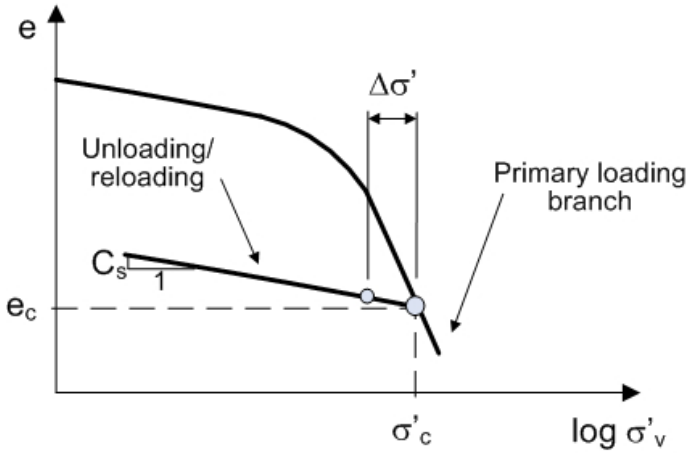

Figure 3.46: Idealized plot of one-dimensional oedometric compression test.

DMT. The "static" modulus corresponding to E_{ur} can be evaluated for cohesive soils the vertical drained constrained modulus M_{DMT} which is derived from three intermediate dilatometer parameters, i.e. the material index I_D, the horizontal stress index K_D, and the dilatometer modulus E_D. Note that M_{DMT} may correspond to $E_{\text{oed}}^{\text{ref}}$ only for normally-consolidated soil. The unloading-reloading modulus E_{ur} can be evaluated assuming that:

$$E_{\text{ur}} = E_s = aE_{\text{oed}} = aM_{\text{DMT}} \tag{3.68}$$

where $a \approx 0.9$ as $a = (1+\nu_{\text{ur}})(1-2\nu_{\text{ur}})/(1-\nu_{\text{ur}})$ and the dilatometer vertical drained constrained modulus M_{DMT} :

$$M_{\text{DMT}} = R_M E_D \tag{3.69}$$

with $E_D = 34.7(p_1 - p_0)$ and R_M depending on soil type behavior, i.e.

- clayey silt to sandy silt ($0.6 < I_D < 1.8$): $R_M = R_{M,0} + (2.5 - R_{M,0}) \log K_D$ and $R_{M,0} = 0.14 + 0.15(I_D - 0.6)$
- clay to silty clays ($I_D \leq 0.6$): $R_M = 0.14 + 2.36 \log K_D$
- if $K_D > 10$: $R_M = 0.32 + 2.18 \log K_D$
- if $R_M < 0.85$: set $R_M = 0.85$

Undrained vs drained moduli - theoretical relationship. In case of lack of drained compression test data, the stiffness moduli can be calibrated based on the results derived from the undrained triaxial compression test (e.g. CIUC or CAUC). Since water filling skeleton

pores has no shear stiffness, the shear modulus is not affected by the drainage condition so one can write:

$$\frac{E_{\mathrm{u}}}{2(1+\nu_{\mathrm{u}})} = G_{\mathrm{u}} = G = \frac{E}{2(1+\nu)} \tag{3.70}$$

where ν_u is the Poisson's coefficient in undrained conditions.
Considering that the undrained conditions imply $\varepsilon_1 = \varepsilon_3$, and therefore $\nu_{\mathrm{u}} = 0.5$, the above equation can be rewritten as:

$$\frac{E_{\mathrm{u}}}{E} = \frac{3}{2(1+\nu)} \tag{3.71}$$

and for the drained Poison's coefficient ranging for most soils between 0.12 and 0.4:

$$\frac{E_{\mathrm{u}}}{E} \approx 1.07 \quad \text{to} \quad 1.34 \tag{3.72}$$

An assumption of $\nu_{\mathrm{u}} = 0.5$ for undrained conditions can also be expressed with the condition of no volume change ($\Delta\varepsilon_v = 0$). Since the undrained bulk modulus K_{u} tends to infinity in such conditions , $\nu_{\mathrm{u}} \to 0.5$:

$$K_{\mathrm{u}} = \frac{\Delta\sigma}{\Delta\varepsilon_v} = \frac{E_{\mathrm{u}}}{3(1-2\nu_{\mathrm{u}})} \tag{3.73}$$

The undrained "static" modulus E_s^{u} can be estimated based on a value of undrained shear strength s_{u} using an empirical correlation:

$$E_{\mathrm{u}} = K_c s_{\mathrm{u}} \tag{3.74}$$

with an empirical correlation coefficient which depends on the plasticity index PI and OCR, and can be estimated from Figure 3.47.

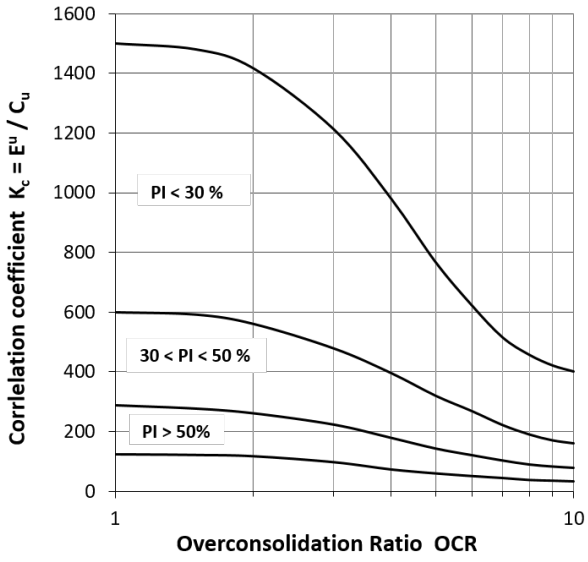

Figure 3.47: Evaluating the undrained modulus from E^{u} from s_{u}: chart for estimating the correlation coefficient K_c in Eq. (3.74) (from Duncan and Buchignani, 1976).

Undrained vs drained moduli - curve fitting. The "drained" model moduli can also be calibrated by means of curve-fitting. It is recommended because in the "undrained" test the effective stress σ'_3 (which corresponds to the reference stress) does not remain constant during compression due to a development of excess pore water pressure. The calibration of "drained" stiffness moduli (E'_{ur}, E'_{50}) from "undrained" test requires fitting laboratory data, i.e. curve $\varepsilon_1 - q$, with the results obtained through an axis-symmetric, one-element simulation of the undrained compression. The flowchart of the parameter calibration is presented in detail in Figure 3.48 and it is described below.

Considering that strength parameters ϕ' and c' can be directly derived from undrained test data, they should be kept unmodified during curve-fitting. In order to avoid excessive gain in material resistance after reaching the failure stress point, the dilatancy angle can be set $\psi = 0^o$ during "undrained" simulations (cf. Truty and Obrzud (2015)). The soil unit weight should be set to $\gamma = 0$ in order to cancel body force loading. As regards the fluid weight the option ☑ *Skip gravity term* should be chosen. A non-zero value for the initial void ratio e_0 should be set.
In order to represent the undrained behavior a finite value of the fluid bulk modulus should be set, e.g. the bulk modulus of water is $2.2e6$ kPa. The ratio between fluid and soil bulk moduli should be of order $K_f/K = 10^5 \div 10^6$. It corresponds to the penalty formulation which may fail to converge if the penalty factor is too large. In such a case computation will be terminated and some null pivots will be reported in the $^*.log$ file. In order to remedy such a problem, the value of the fluid bulk modulus should be decreased. Note that the two-phase stabilization should not be activated in the single-element test as no pressure oscillation is observed (pore pressure is constant over the element). No initial pressure BC need to be introduced.
The simulation should be carried out using `Axisymmetry` analysis type,
`Deformation+Flow` problem type and `Consolidation` driver should be set for when running compression of the element.

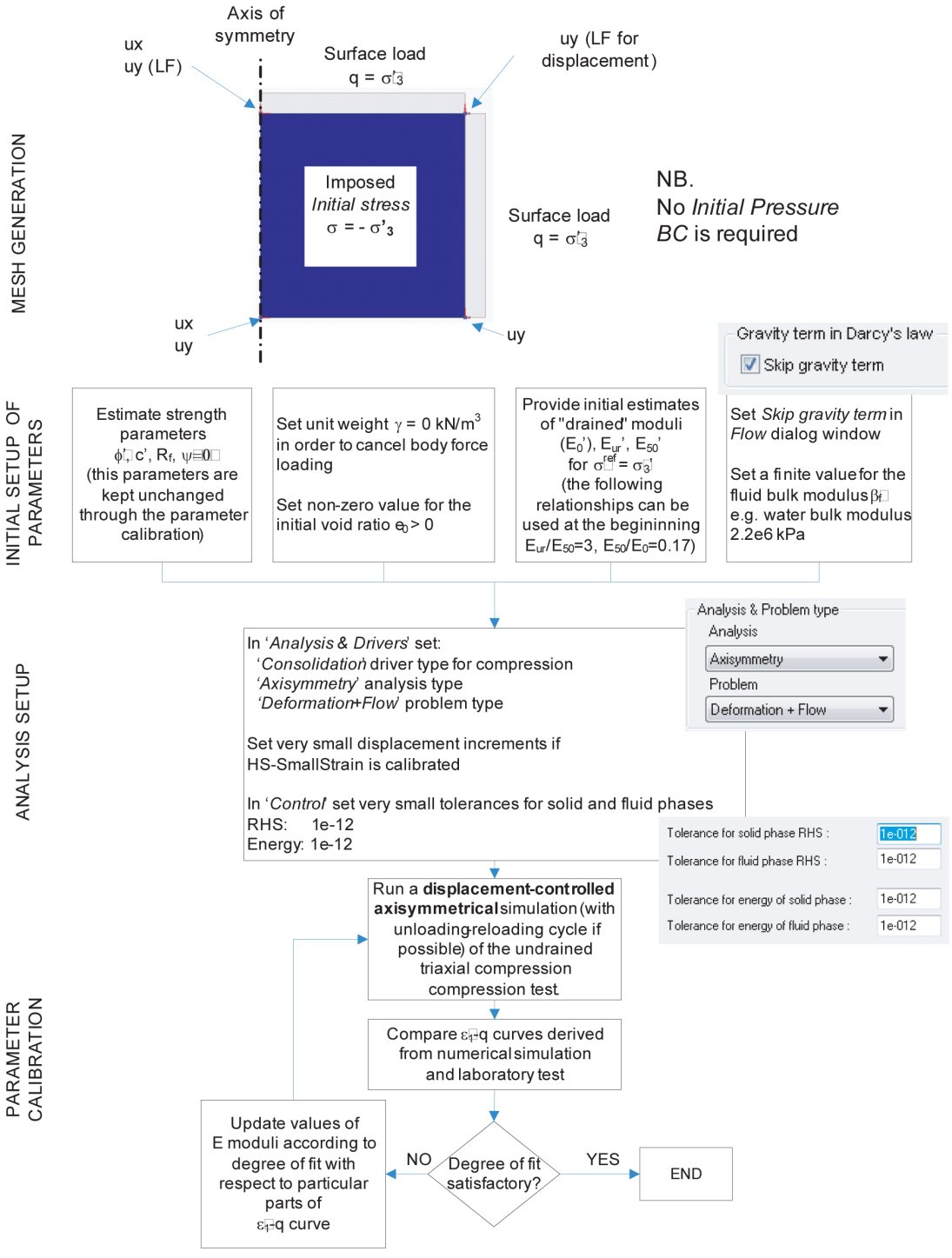

Figure 3.48: Flowchart for calibration of stiffness moduli E_0, E_{ur}, E_{50} based on $\varepsilon_1 - q$ curve derived from the undrained compression triaxial test (CU) and a single-element test.

Geotechnical evidence. Kempfert (2006) have provided typical results for the ratios between stiffness moduli. These ratios are presented below in Tables 3.22 and 3.23.

Table 3.22: Relationship between triaxial stiffness moduli and oedometric moduli for three lacustrine clays in Germany, from Kempfert (2006).

	E_i/E_{oed}	E_{50}/E_{oed}	$E_{\text{ur}}/E_{\text{oed,ur}}$	$E_{\text{oed,ur}}/E_{\text{oed}}$
Soil 1	2.08	1.03	2.33-2.52	2.60
Soil 2	1.63	0.77	1.29-2.09	3.63
Soil 3	2.82	1.45	1.32-2.51	6.65
Average	2.17	1.08		4.29

E_i was derived from the initial slope of the triaxial curve $\varepsilon_1 - q$
$E_{\text{oed,ur}}$ denotes unloading/reloading oedometer modulus

Table 3.23: Relationship between stiffness moduli derived from drained and undrained triaxial tests for three lacustrine clays in Germany, from Kempfert (2006).

	Drainage conditions	E_i/E_{50}	E_{ur}/E_i	E_{ur}/E_{50}
Soil 1	drained	2.02	3.20	5.93
	undrained	1.48		
Soil 2	drained	2.17	3.10	6.72
	undrained	1.84		
Soil 3	drained	1.94	6.55	12.66
	undrained	3.02		
Average	drained	2.04	4.28	8.43
	undrained	2.11		

E_i was derived from the initial slope of the triaxial curve $\varepsilon_1 - q$

3.3.6 Oedometric modulus

The one-dimensional constrained tangent modulus E_{oed} (which, in literature, is often assigned as M_D when determined from *in situ* tests) is obtained for steady state measurements based on the oedometer test through the expression:

$$E_{\text{oed}} = M_{\text{D}} = \frac{\delta\sigma'_v}{\delta\varepsilon_{\text{v}}} \tag{3.75}$$

which can also be expressed as:

$$E_{\text{oed}} = \frac{2.3(1+e)\sigma'_v}{C_c} = \frac{(1+e)\sigma'_v}{\lambda} \tag{3.76}$$

where C_c is the compression index($C_c = 2.3\lambda$). A number of empirical correlations which can be used to evaluate C_c are given in Appendix B.

In case of lack of relevant data the oedometric modulus can be approximately taken as:

$$E^{\text{ref}}_{\text{oed}} \cong E^{\text{ref}}_{50} \tag{3.77}$$

In such a case, the oedometric vertical reference stress $\sigma^{\text{ref}}_{\text{oed}}$ should be matched to the reference minor stress σ_{ref} since the latter typically corresponds to the confining (horizontal) pressure $\sigma_{\text{ref}} = \sigma_3 = \sigma'_h$:

$$\sigma^{\text{ref}}_{\text{oed}} = \sigma_{\text{ref}}/K_0^{\text{NC}} \tag{3.78}$$

As an example, Kempfert (2006) reports $E^{\text{ref}}_{50}/E^{\text{ref}}_{\text{oed}}$ ratio for three lacustrine clays in Germany which varies from 0.77 to 1.45 with the average 1.08 (see Table 3.22) .

Important note. In the case of the HS model, $E^{\text{ref}}_{\text{oed}}$ can be taken as equal to M_{D} if the latter has been derived from CPT, CPTU or DMT but **only for normally-consolidated soil**. In such a case σ_{oed} can be taken as σ'_{v0} which corresponds to the testing depth for which M_{D} has been evaluated.

CPT. The constrained modulus for clays can be interpreted from the CPT or CPTU test using the measured cone resistance q_c and an empirical coefficient α_m. Lunne et al. (1997) quote the values of α_m for different types of soils proposed by Sanglerat (1972).

CPTU. The constrained modulus can be interpreted from the CPTU using the net cone resistance $q_t - \sigma_{v0}$ (q_t denotes the corrected cone resistance):

$$M_{\text{D}} = \alpha_n(q_t - \sigma_{v0}) \tag{3.79}$$

where α_n is observed for most clays between 5 and 15 while for normally consolidated clays, it is between 4 to 8 (Sandven et al., 1988; Senneset et al., 1989). A more general correlation was suggested by Kulhawy and Mayne (1990) (cf. Figure 3.49):

$$M_{\text{D}} = 8.25(q_t - \sigma_{v0}) \tag{3.80}$$

As discussed be Lunne et al. (1997), the estimation of "drained" parameter M_{D} from an undrained penetration test using general empirical correlations may suffer from errors as large as $\pm 100\%$. An individual site-specific calibration is thus recommended for α_n. They also concluded that it is difficult to correlate "drained" parameters without accounting for the pore pressure measurements as the cone resistance is measured in total stress.

DMT. The constrained modulus M_{D} can be interpreted from three intermediate dilatometer parameters, i.e. the material index I_D, the horizontal stress index K_D, and the dilatometer modulus E_D, by applying the correlation presented in Eq.(3.69).

Table 3.24: Estimation of constrained modulus M_{D} for clays (after Lunne et al. (1997)).

$M_{\mathrm{D}} = \alpha_m \cdot q_c$		
$q_c < 0.7$ MPa	$3 < \alpha_m < 8$	Clay of low plasticity (CL)
$0.7 < q_c < 2.0$ MPa	$2 < \alpha_m < 5$	
$q_c > 2.0$ MPa	$1 < \alpha_m < 2.5$	
$q_c < 2.0$ MPa	$1 < \alpha_m < 3$	Silts of low plasticity (ML)
$q_c > 2.0$ MPa	$3 < \alpha_m < 6$	
$q_c < 2.0$ MPa	$2 < \alpha_m < 6$	Highly plastic silts and clays (MH, CH)
$q_c < 1.2$ MPa	$2 < \alpha_m < 8$	Organic silts (OL)
$q_c < 0.7$ MPa		Peat and organic clay (P_t,OH)
$50 < w < 100$	$1.5 < \alpha_m < 4$	(w-water content [%])
$100 < w < 200$	$1 < \alpha_m < 1.5$	
$w > 200$	$0.4 < \alpha_m < 1$	

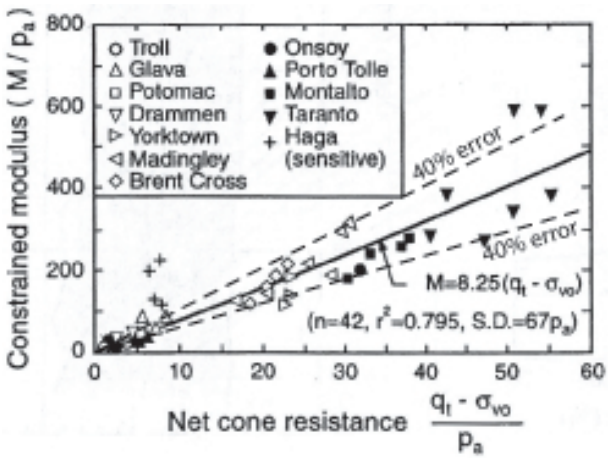

Figure 3.49: General M_{D} correlation for CPTU data proposed by Kulhawy and Mayne (1990) (from Lunne et al., 1997).

3.3.7 Stiffness exponent

Geotechnical evidence. The formulation of HS models assumes the same exponent m for four different stiffness moduli, i.e. E_0, E_{50}, E_{ur} and E_{oed}. Kempfert (2006) demonstrated that in reality, the following relation may appear $m_0 < m_{50} < m_{\text{ur}}$; they also provide some typical values derived from drained tests (oedometer loading and triaxial tests) for three lacustrine soft soils:

	m_{oed}	$m_{\text{oed}}^{\text{avg}}$ (no. of tests)	m_0	m_0^{avg} (no. of tests)	m_{50}	m_{50}^{avg} (no. of tests)	m_{ur}	$m_{\text{ur}}^{\text{avg}}$ (no. of tests)
Soil 1	0.73-0.76	0.75 (2)	0.3-0.42	0.34 (3)	0.39-0.51	0.45 (3)	0.74	0.74 (1)
Soil 2	0.58-0.69	0.64 (2)	0.52-0.79	0.68 (4)	0.66-0.84	0.72 (4)	0.61-0.67	0.64 (2)
Soil 3	0.58	0.58 (1)	0.42-0.56	0.51 (3)	0.38-0.54	0.48 (3)	0.79-0.89	0.84 (3)

Kempfert (2006) also highlighted that the exponent m for undrained tests can be generally higher than for drained tests.

Viggiani and Atkinson (1995) reports the exponent numbers m for different clays at very small strains as a function of the plasticity index I_P(see Figure 3.50(a)) whereas Hicher (1996) presents them as a function of the liquid limit w_L (see Figure 3.50(b)).

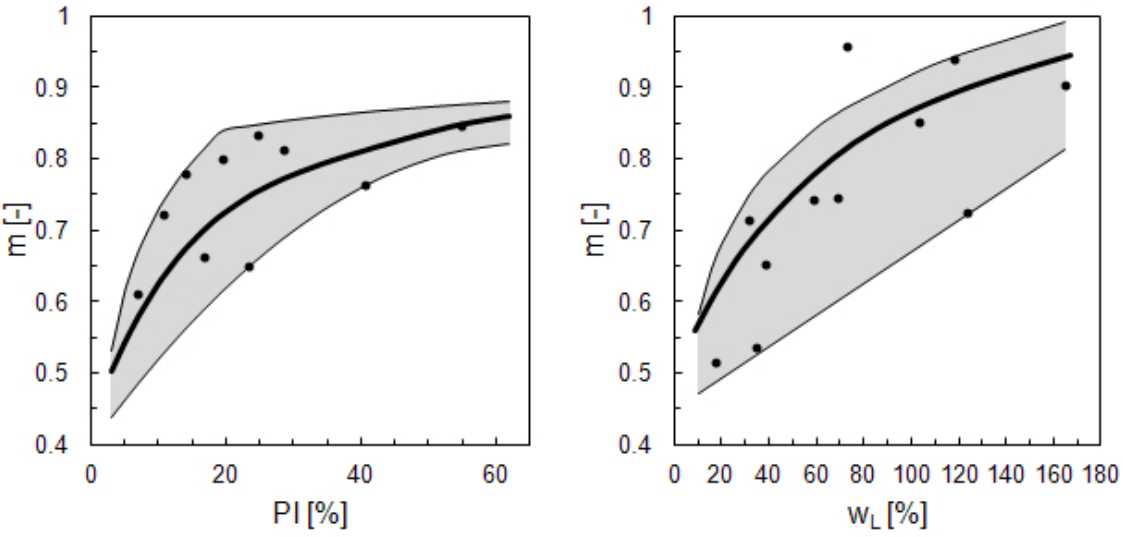

(a) (b)

Figure 3.50: Power law exponent m related to (a) plasticity index I_P (Viggiani and Atkinson, 1995), and (b) liquid limit w_L (Hicher, 1996).

Table 3.25: Typical values for m_p* observed in clays for the shear modulus G_0 (from Benz, 2007).

Soil tested	I_P [%]	m_p [-]	Reference
Avezzano clay (Holocene-Pleistocene)	10-30	0.46	Lo Presti and Jamiolkowski (1998)
Fucino clay (Holocene-Pleistocene)	45-75	0.40	Lo Presti and Jamiolkowski (1998)
Garigliano clay (Holocene)	10-40	0.58	Lo Presti and Jamiolkowski (1998)
Panigaglia clay (Holocene)	44	0.50	Lo Presti and Jamiolkowski (1998)
Montaldo di Castro clay (Pleistocene)	15-34	0.40	Lo Presti and Jamiolkowski (1998)
Recon. Valericca clay (Pleistocene)	27	0.85	Rampello et al. (1997)
Pisa clay (Pleistocene)	23-46	0.44	Lo Presti and Jamiolkowski (1998)
London clay (reconstituted)	41	0.76	Viggiani and Atkinson (1995)
Speswhite kaolin clay (reconstituted)	24	0.65	Viggiani and Atkinson (1995)
Kaolin clay	35	0.50	Marcuson and Wahls (1972)
Bentonite clay	60	0.50	Marcuson and Wahls (1972)

The number m_p was obtained for the relation $G_0 \propto \left(\frac{p'}{\sigma_{\text{ref}}}\right)^{m_p}$

Table 3.26: Suggested ranges of stiffness exponent m observed for oedometric modulus E_{oed} (von Soos, 1991).

Soil type	m [-]
Silt: low plasticity	$0.6 \div 0.8$
Silt: medium and high plasticity	$0.7 \div 0.9$
Clay: low plasticity	$0.9 \div 1.0$
Clay: medium plasticity	$0.95 \div 1.0$
Clay: high plasticity	1.0
Silt or clay: organic	$0.85 \div 1.0$
Peat	1.0
Mud	$0.9 \div 1.0$

3.3.8 Overconsolidation ratio

In the case of a soil which is located below the ground water table, a qualitative estimation of the overconsolidation ratio can be done based on the Atterberg limits and the natural moisture content. Assuming that the soil is saturated, it can be expected that smaller void ratios have less water space and w_n would be smaller Bowles (1997). From this observation, the following may be deduced:

if w_n is close to w_L	soil is normally consolidated
if w_n is between w_P and w_L	soil is lightly overconsolidated
if w_n is close to w_P	soil is lightly- to heavily overconsolidated
if w_n is larger than w_L	soil is on verge of being a viscous liquid

In the latter case ($w_n > w_L$), stability of soil in *in situ* conditions may be ensured by overburden pressure and interparticle bonds, unless visual inspection indicates a liquid mass.

Geotechnical evidence. Mayne (1988) provides empirical upper and lower limits derived from laboratory tests:

- undrained shear strength s_u determined under anisotropically consolidated-undrained triaxial conditions (CIUC):

$$\left(1.82\frac{s_\mathrm{u}}{\sigma'_{v0}}\right)^{1.43} \leq \mathrm{OCR} \leq \left(4\frac{s_\mathrm{u}}{\sigma'_{v0}}\right)^{1.43} \tag{3.81}$$

- s_u determined under isotropically consolidated-undrained triaxial conditions (CAUC):

$$\left(3.70\frac{s_\mathrm{u}}{\sigma'_{v0}}\right)^{1.25} \leq \mathrm{OCR} \leq \left(5.26\frac{s_\mathrm{u}}{\sigma'_{v0}}\right)^{1.25} \tag{3.82}$$

CPTU. One of the best working approaches relates the overconsolidation ratio OCR to the net cone resistance $q_t - \sigma_{v0}$:

$$\mathrm{OCR} = k_{\sigma t}\frac{q_t - \sigma_{v0}}{\sigma'_{v0}} \tag{3.83}$$

where $k_{\sigma t}$ is an empirical coefficient which falls in the interval from 0.1 to 0.5 for non-fissured clays (Larsson and Mulabdić, 1991; Hight and Leroueil, 2003). The higher values are suggested for cemented, aged and heavily consolidated soils (between 0.9 and 2.2). For good-quality interpretation, this coefficient needs to be calibrated for specific site conditions based on the benchmark values derived from oedometer test. However, the first-order approximates of OCR can be obtained using the values of $k_{\sigma t}$ from multiple regression analyzes which are based on historical syntheses from many characterization sites (see Table 3.27). Mayne (2006b) suggests assuming $k_{\sigma t} = 0.30$ for first-order estimates.
Another approach combines measurements of cone resistance q_t and pore pressure u_2 measured behind the cone:

$$\mathrm{OCR} = k_{\sigma e}\left(\frac{q_t - u_2}{\sigma'_{v0}}\right) = k_{\sigma e}\frac{q_e}{\sigma'_{v0}} \tag{3.84}$$

with $k_{\sigma e}$ being obtained through site-specific correlations. By analogy to the previous approach, the first-order approximates of OCR can be obtained using the values of $k_{\sigma e}$ through

Table 3.27: Comparison of the empirical coefficients obtained from multiple regression analyzes for non-fissured clays.

Ref.	Geographical region	Results of regression analysis					
		Number of sites/points	$k_{\sigma t}$	R^2	Number of sites/points	$k_{\sigma e}$	R^2
[1]	Sweden	9/110	0.292	-	9/110	0.50	-
[2]	Canada	31/153	0.294	0.90	31/153	0.546	0.96
[3]	Worldwide	123/1121	0.305	0.84	84/811	0.50	0.75

[1] Larsson and Mulabdić (1991); [2] Demers and Leroueil (2002);
[3] Chen and Mayne (1994, 1996)

regression analyzes (see Table 3.27). Mayne (2006b, 2007) suggested assuming $k_{\sigma e} = 0.60$ for the first-order estimates. This approach is often used as a comparative to the previous one and local correlations are strongly recommended. The formula is also viewed as less reliable in soft, lightly overconsolidated clays the q_t results accompanied by large values of u_2 yield in a small number for $q_t - u_2$ (Houlsby and Hitchman, 1988; Lunne et al., 1997).

DMT. Based on dilatometer measurements, estimation of OCR for clays can be carried out with the formula proposed by Marchetti which relates the horizontal stress index[8] K_D to OCR from oedometer tests with the following correlation:

$$\mathrm{OCR} = (0.5K_D)^{1.56} \tag{3.85}$$

The application of this correlation is restricted to materials with $I_D < 1.2$, free of cementation which have experienced simple one-dimensional stress histories (Totani et al., 2001).

An improved relationship which takes into account a large range of soil plasticity in the exponent was proposed by Lacasse and Lunne (1988):

$$\mathrm{OCR} = 0.225K_D^{1.35 \div 1.67} \tag{3.86}$$

where the exponent varies from 1.35 for plastic clays, up to 1.67 for low plasticity materials.

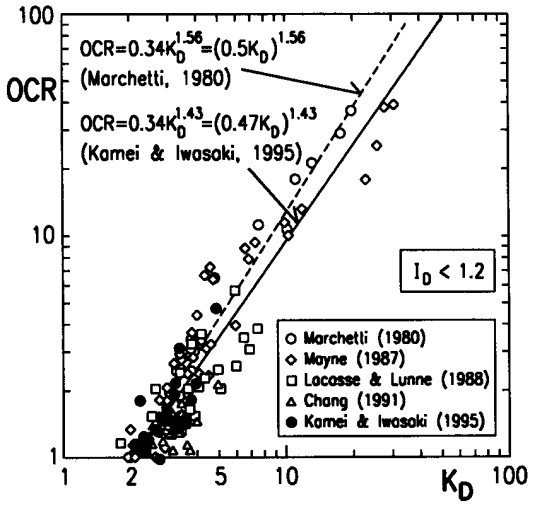

Figure 3.51: Various correlations $K_D - \mathrm{OCR}$ for cohesive soils from various geographical areas (from Totani et al., 2001).

[8] Horizontal stress index which is calculated based on the first dilatometer reading p_0, i.e. $K_D = (p_0 - u_0)/\sigma'_{v0}$.

3.3.9 Coefficient of earth pressure "at rest"

The coefficient of earth pressure "at rest" for normally-consolidated clays can be estimated through Eq.(3.37a) or the similar expression suggested in Brooker & Ireland (1965):

$$K_0^{\mathsf{NC}} = 0.95 - \sin\phi' \tag{3.87}$$

For cohesive soils, K_0^{NC} can also be related through empirical correlations with soil plasticity:

$$K_0^{\mathsf{NC}} = 0.19 + 0.233 \log I_P \qquad \text{(Alpan, 1967)} \tag{3.88a}$$

and similar

$$K_0^{\mathsf{NC}} = 0.44 + 0.0042 I_P \qquad \text{(Holtz \& Kovacs, 1981)} \tag{3.88b}$$

where I_P is the plasticity index in $\%$.

It is commonly known that in cohesive soils the preconsolidation plays an important role and K_0 typically increases with the overconsolidation ratio OCR. Estimations of the initial stress state for overconsolidated soil take a general form:

$$K_0 = K_0^{\mathsf{NC}} \mathrm{OCR}^m \tag{3.89}$$

where m is a coefficient which for estimation of K_0^{NC} for most practical purposes can be taken as:

$$m = 0.5 \qquad \text{suggested by Meyerhof (1976)} \tag{3.90a}$$

$$m = \sin\phi' \qquad \text{suggested in Mayne \& Kulhawy (1982)} \tag{3.90b}$$

However, the upper bound value for K_0 should be limited by the passive lateral earth pressure coefficient:

$$K_p = \frac{1 + \sin\phi}{1 - \sin\phi} \tag{3.91}$$

The equations are presented graphically in Fig.3.52 (K_0^{NC} was calculated using Eq. (3.37a)).

SBPT. Approximation of K_0 from the self-boring pressuremeter test requires determination of the horizontal effective stress σ'_{h0} since the vertical effective stress σ'_{vo} can be estimated based on depth, unit weight and groundwater information. In the case of SBPT, the in situ total horizontal stress can be directly estimated from the "lift-off" pressure (Jamiolkowski et al., 1985; Clough et al., 1990; Amar et al., 1991). The "lift-off" pressure corresponds to the internal cavity pressure ψ_0 when the membrane starts to deform the wall of a borehole, therefore $\psi_0 \cong \sigma'_{h0} + u_0$ (Figure 3.53). The "lift-off" is typically estimated based on the averaging procedure including the measurements of three feeler arms spaced at $120°$ around the instrument (Dalton and Hawkins, 1982; Mair and Wood, 1987). In general, the lateral stress measurements can be considered as fairly accurate in clays, particularly in soft deposits (Jamiolkowski et al., 1985).

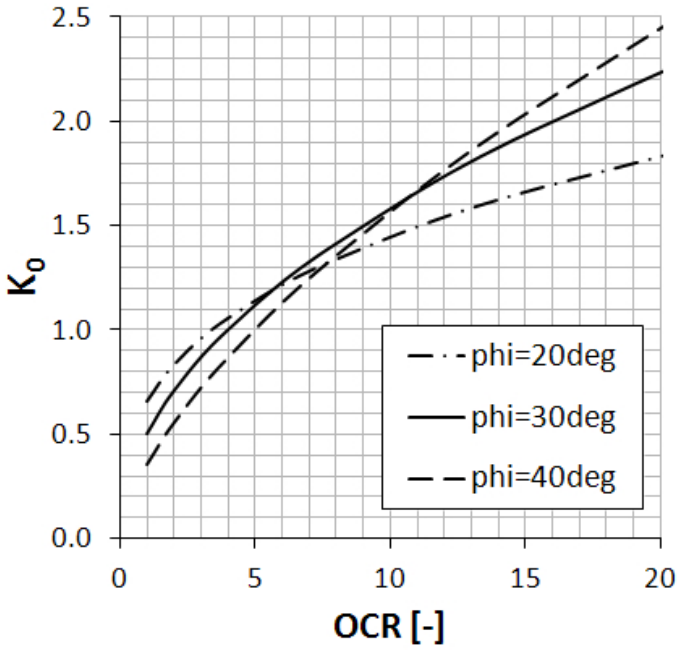

Figure 3.52: Typical relationships between K_0 and OCR observed for clays based on the correlation proposed by Mayne and Kulhawy (1982).

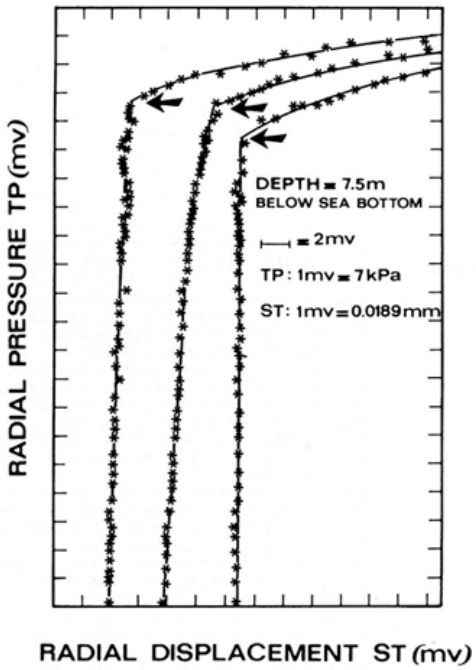

Figure 3.53: Example of the total horizontal stress estimation from the lift-off pressure in soft clay at Panigaglia site (after Jamiolkowski et al., 1985).

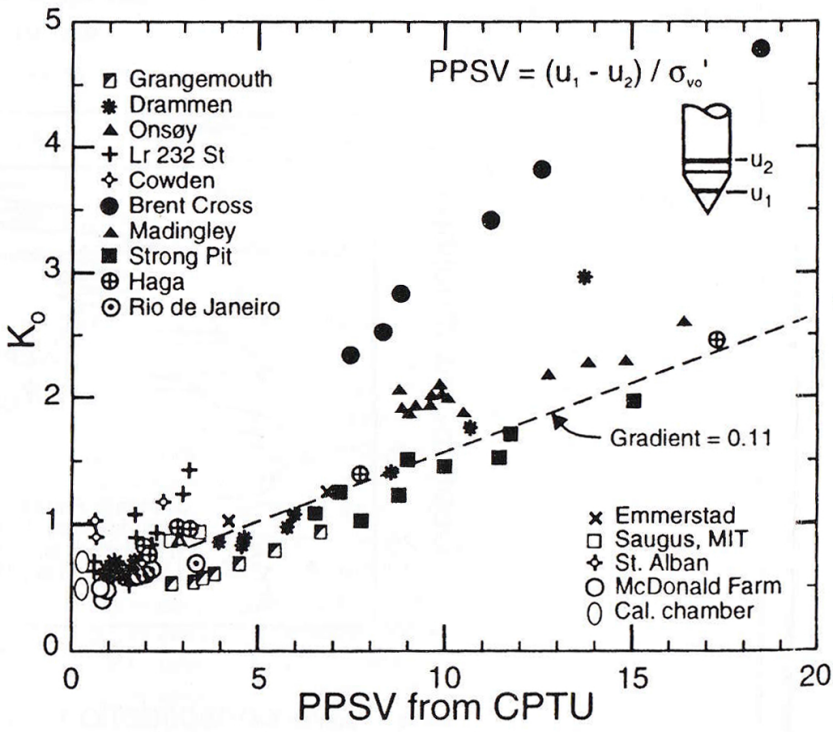

Figure 3.54: Approximation of K_0 based on the normalized pore pressure difference PPSV from dual sensor cone (after Sully and Campanella, 1991).

CPTU. At present, no reliable method exists for interpretation K_0 from CPT data. Rough evaluations related directly to CPTU measurements can be made using various approximative methods.

Observing that the pore pressure distribution around the cone is a function of σ'_{ho}, Sully and Campanella (1991) proposed to approximate K_0 based on a linear regression analysis using the normalized difference between pore pressure measured at the cone tip u_1 and behind the tip at the sleeve shoulder u_2:

$$K_0 = 0.11 \cdot \text{PPSV} + 0.5 \tag{3.92}$$

where PPSV$= (u_1 - u_2)/\sigma'_{v0}$ and the empirical coefficient a_K was obtained equal to 0.11, see Figure 3.54. Note that the regression analysis reveals a considerable scatter and this identification approach should be used carefully.

Masood and Mitchell (1993) proposed the estimation of K_0 based on measurements at the friction sleeve f_s. In this method, K_0 is a function of the normalized sleeve friction f_s/σ'_{v0} and the overconsolidation ratio OCR, as presented in Figure 3.55. Thus the approach requires prior evaluation of OCR and reliable measurements of f_s.

The most common technique for estimating K_0 employs an empirical formula which is based on the normalized cone resistance:

$$K_0 = k_K \left(\frac{q_t - \sigma_{vo}}{\sigma'_{vo}} \right) \tag{3.93}$$

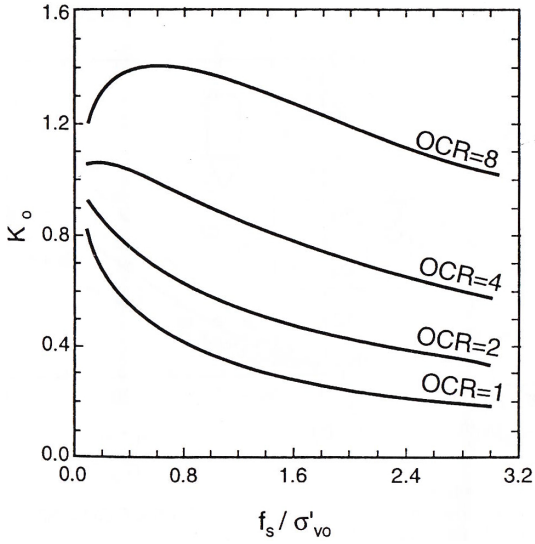

Figure 3.55: Proposed relationship between K_0, f_s and OCR Masood and Mitchell (after 1993).

where k_K is an empirical coefficient. Using the regression analysis, Kulhawy and Mayne (1990) obtained the value of $k_K = 0.1$ for several K_0 values estimated from the self-boring pressuremeter test (SBPT), see Figure 3.56.

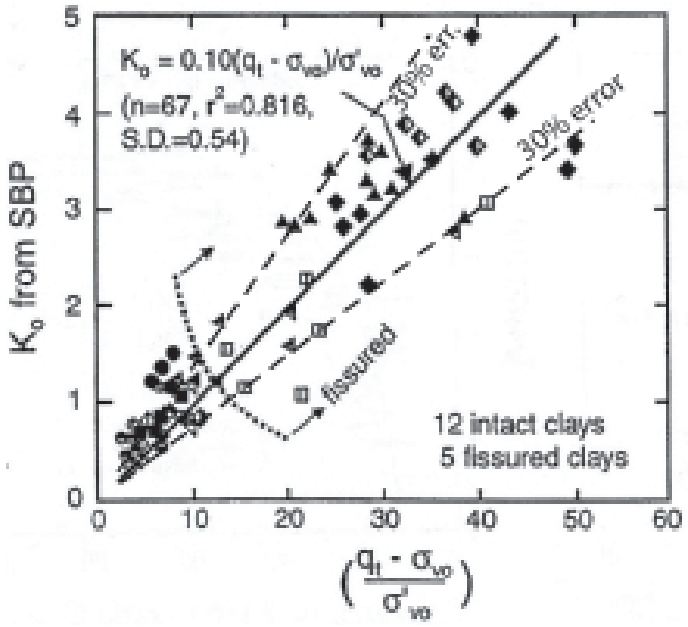

Figure 3.56: General K_0 correlation for CPTU data proposed by Kulhawy and Mayne (1990) (adapted from Lunne et al., 1997).

DMT. The original correlation for K_0 based on the dilatometer data, relative to uncemented clays is (Marchetti, 1980):

$$K_0 = \left(\frac{K_D}{1.5}\right)^{0.47} - 0.6 \tag{3.94}$$

In highly cemented clays, the above equation may significantly overestimate K_0, since part of K_D is due to the cementation.

DMT. K_0 can also be interpreted from dilatometer test data. Since the original Marchetti relationship tends to overestimate K_0, its estimation can be carried out through the correlation suggested in Lacasse and Lunne (1988):

$$K_0 = 0.34 K_D^{0.44 \div 0.64} \tag{3.95}$$

where the lower exponent value is associated with highly plastic clays, whereas higher values are suggested for for low plasticity materials.

3.3.10 Void ratio

Typical values of voids ratio and dry unit weights observed for cohesive soils are provided in Table 3.28 and 3.29.

Table 3.28: Typical values of void ratios and dry unit weights observed in cohesive soils (from Hough, 1969).

	Voids ratio e [–]	
Soil type	Min	Max
Silty or sandy clay	0.25	1.8
Gap-graded silty clay w. gravel or larger	0.2	1
Well-graded gravel/sand/silt/clay	0.13	0.7
Clay (30 to 50% of 2microns size)	0.5	2.4
Colloidal clay (over 50% of 2microns size)	0.6	12
Organic silt	0.55	3
Uniform, inorganic silt	0.4	1.1
Organic clay (30 to 50% of 2microns size)	0.7	4.4

Table 3.29: Typical values of void ratios and unit weights observed in granular soils (from Terzaghi et al., 1996).

Soil type	Voids ratio e [–]	Dry unit weights [kN/m^3]	Wet weights [kN/m^3]
Glacial till, very mixed grained	0.25	20.8	22.7
Soft glacial clay	1.2	12	17.4
Stiff glacial clay	0.6	16.7	20.3
Soft slightly organic clay	1.9	9.1	15.5
Soft very organic clay	3	6.7	14.4
Soft bentonite	5.2	4.2	12.5

3.4 Automated assistance in parameter determination

Virtual Lab v2023 is a highly-interactive module which provides users with:

- assistance in selecting a relevant constitutive law with regards to the general behavior of the real material
- first-guess parameter estimation based on field test records
- automated parameter selection (first-guess values of model parameters for soil for any incomplete or complete specimen data)
- user-engaged parameter selection (interactive parameter selection which involves browsing different parameter correlations including field tests data)
- ranges of parameter values which can be considered in parametric studies
- automated parameter identification from laboratory experimental data
- possibility of running numerical simulations of elementary laboratory tests in order to visualize the constitutive model response for the defined model parameters
- possibility of comparing numerical simulations of elementary laboratory tests with curves obtained in the laboratory

A separated report provides **Help** to **Virtual Lab**.

The toolbox is initialized by clicking on Virtual Lab which is visible once one of the following continuum models has been chosen as the material definition (Figure 3.57):

- Mohr-Coulomb
- Hardening-Soil Small Strain
- Cam-Clay
- Cap

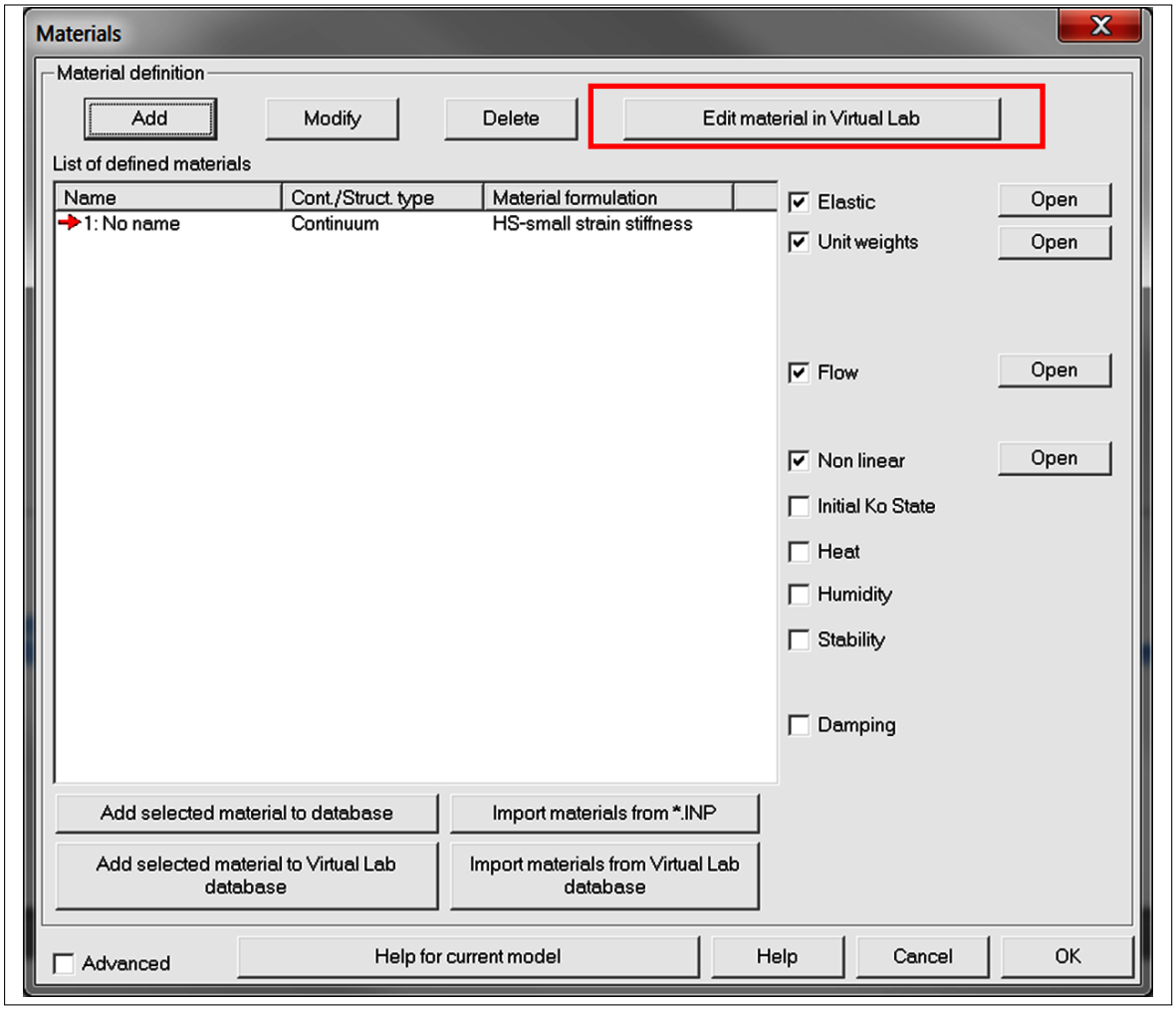

Figure 3.57: Initializing Virtual Lab from the *Materials* window

Chapter 4

Benchmarks

4.1 Triaxial drained compression test on dense Hostun sand

Files:
HS-std-dh-sand-100kPa.inp,
HS-small-dh-sand-100kPa.inp,
HS-brick-dh-sand-100kPa.inp
HS-std-dh-sand-300kPa.inp,
HS-small-dh-sand-300kPa.inp,
HS-brick-dh-sand-300kPa.inp
HS-std-dh-sand-600kPa.inp,
HS-small-dh-sand-600kPa.inp,
HS-brick-dh-sand-600kPa.inp

The following section presents a validation of all HS model versions ie. HS-standard, HS-small, HS-Brick on a triaxial drained compression test for Hostun sand. Material properties are taken from PhD thesis by Benz (2007) and are given in the following table:

Parameter	Unit	Value	Parameter	Unit	Value
$E_{\text{ur}}^{\text{ref}}$	[kPa]	90000	ψ	[^{o}]	16.0
E_{50}^{ref}	[kPa]	30000	f_t	[kPa]	0.0
σ^{ref}	[kPa]	100	D	[–]	0.0/0.25[1]
m	[–]	0.55	M	[–]	1.5656/1.5597
ν_{ur}	[–]	0.25	H	[kPa]	51649/52339
R_f	[–]	0.9	OCR	[–]	1.0
c	[kPa]	0.0	E_0^{ref}	[kPa]	270000
ϕ	[^{o}]	42.0	$\gamma_{0.7}$	[–]	0.0002

Parameters M and H were estimated automatically by the code assuming $K_0^{\text{NC}} = 0.4$ and $E_{\text{oed}} = 30000$ kPa at reference stress equal to 100 kPa. It must be emphasized that M and H values will not be equal to the ones given by Benz because of the different form of the hardening law for the preconsolidation pressure p_c. All results obtained with Z_Soil match very well results published by Benz.

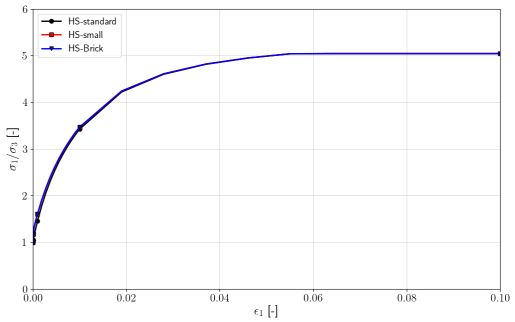

(a) $\frac{\sigma_1}{\sigma_3}(\varepsilon_1)$ (Z_Soil)

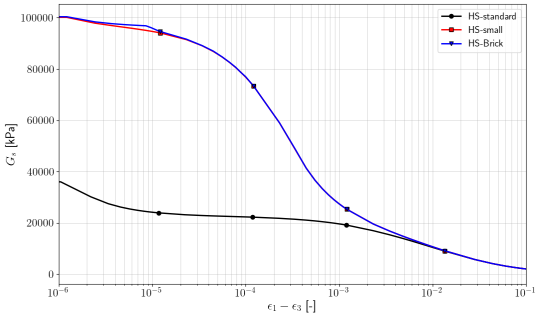

(b) $G(\gamma)$ (Z_Soil)

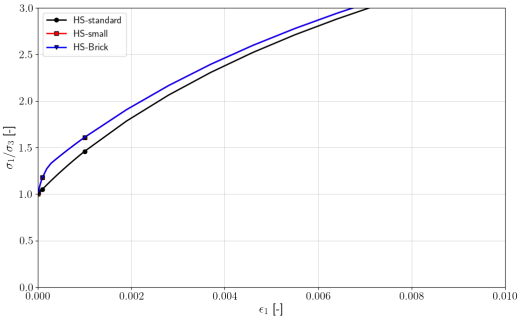

(c) $\frac{\sigma_1}{\sigma_3}(\varepsilon_1)$ (zoom) (Z_Soil)

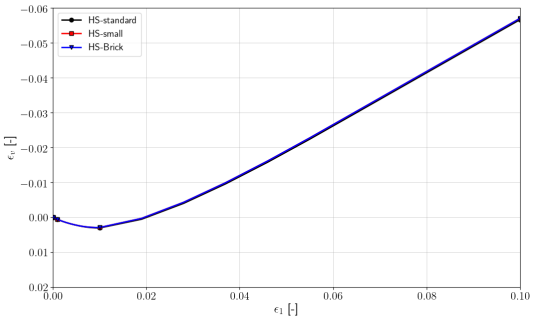

(d) $\varepsilon_v(\varepsilon_1)$ (Z_Soil)

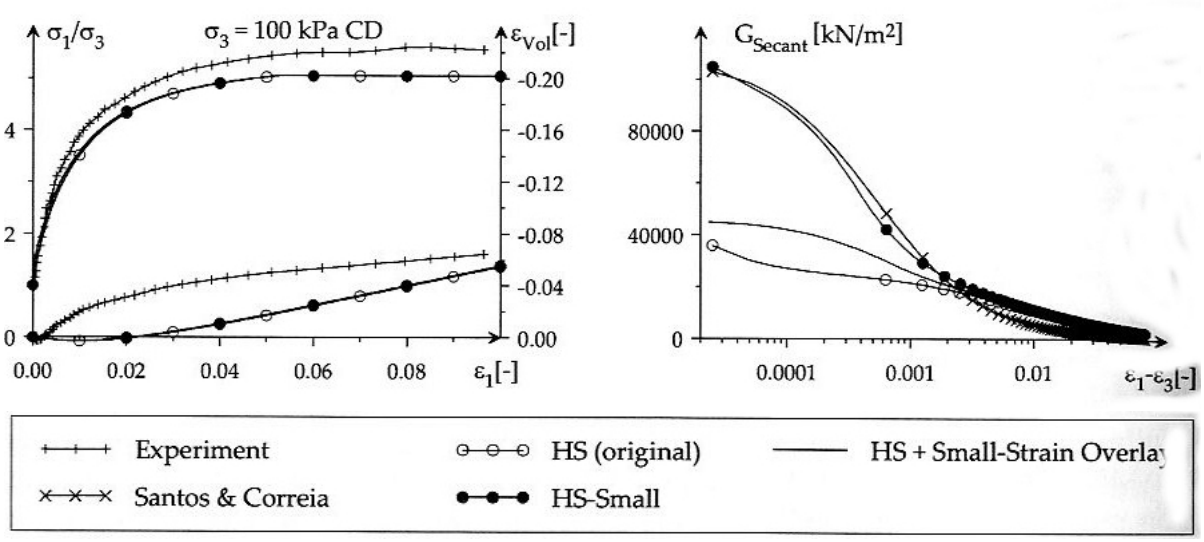

(e) Solution by Benz Benz (2007)

Figure 4.1: Results for the confining pressure $\sigma_3 = 100$ kPa

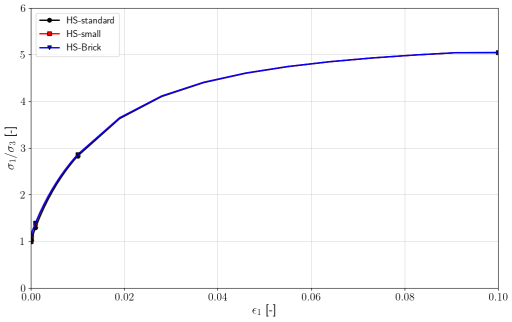

(a) $\frac{\sigma_1}{\sigma_3}(\varepsilon_1)$ (Z_Soil)

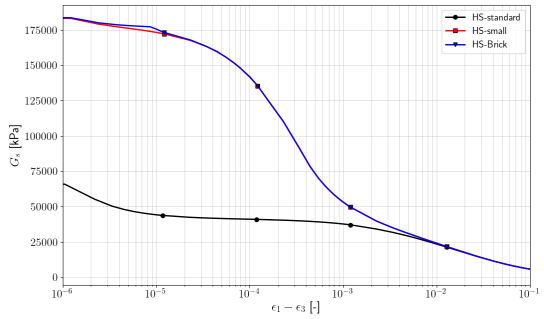

(b) $G(\gamma)$ (Z_Soil)

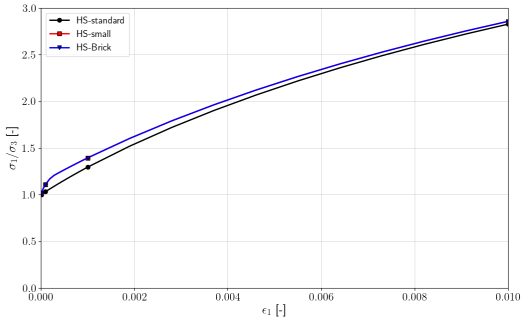

(c) $\frac{\sigma_1}{\sigma_3}(\varepsilon_1)$ (zoom) (Z_Soil)

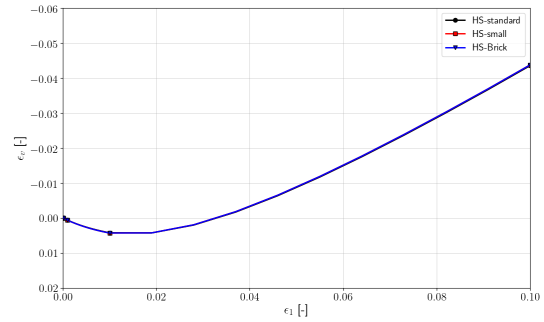

(d) $\varepsilon_v(\varepsilon_1)$ (Z_Soil)

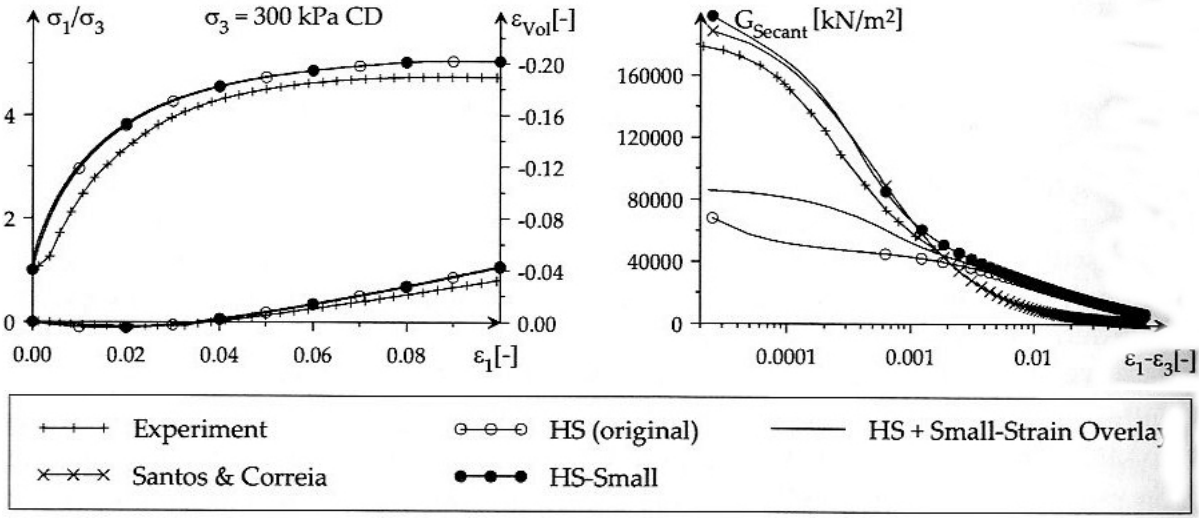

(e) Solution by Benz Benz (2007)

Figure 4.2: Results for the confining pressure $\sigma_3 = 300$ kPa

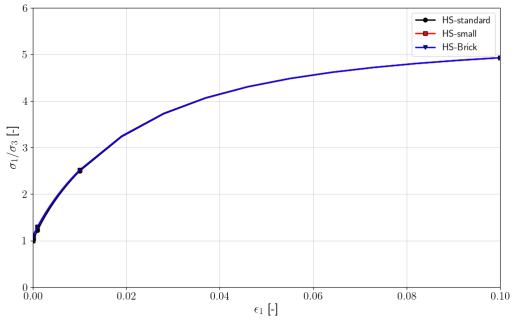

(a) $\frac{\sigma_1}{\sigma_3}(\varepsilon_1)$ (Z_Soil)

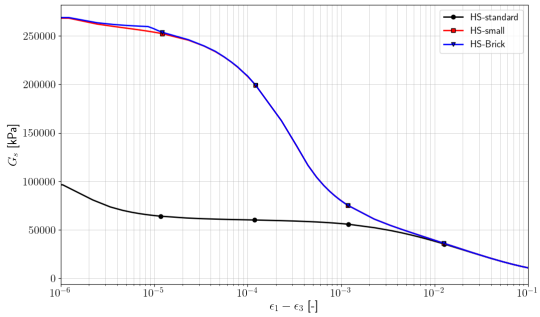

(b) $G(\gamma)$ (Z_Soil)

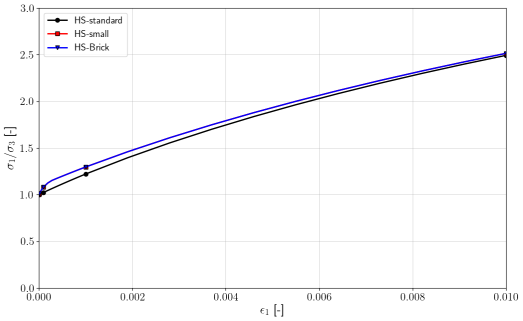

(c) $\frac{\sigma_1}{\sigma_3}(\varepsilon_1)$ (zoom) (Z_Soil)

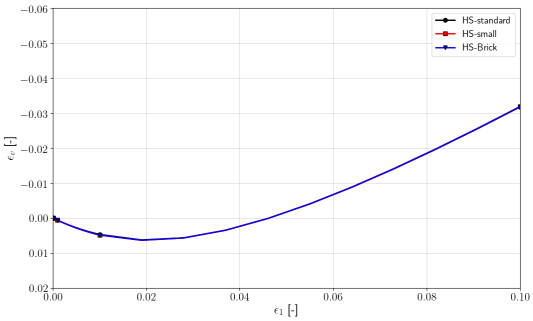

(d) $\varepsilon_v(\varepsilon_1)$ (Z_Soil)

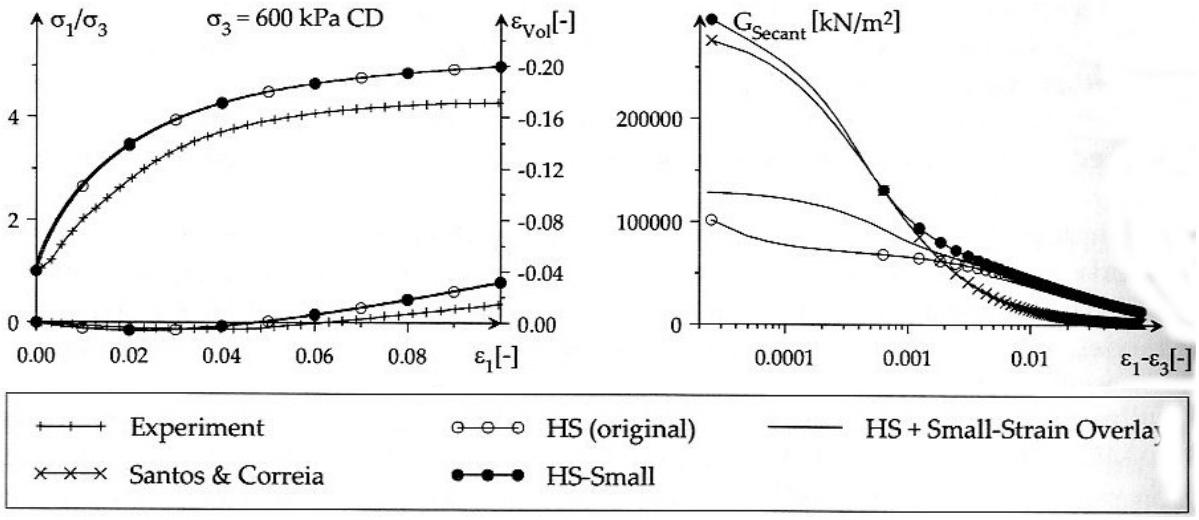

(e) Solution by Benz Benz (2007)

Figure 4.3: Results for the confining pressure $\sigma_3 = 600$ kPa

4.2 Isotropic compression of dense Hostun sand

File: HS-isotropicCompr.inp

This benchmark is solved analytically for the HS-standard model with classical stress dependency function using $(\sigma_3 + c\ \cot\phi)$ term. The decomposed total strain increments for the elastic and plastic part in isotropic compression conditions $(p = p_c)$ are presented in the following expression (NB. the increment of total volumetric strain is measured from the initial configuration of equilibrium $p_0 = p_{c0}$ to the current one):

$$\Delta\varepsilon_v^p = \frac{\dfrac{\sigma^{ref}}{1-m}\left[\left(\dfrac{p_c}{\sigma^{ref}}\right)^{1-m} - \left(\dfrac{p_{co}}{\sigma^{ref}}\right)^{1-m}\right]}{H} \tag{4.1}$$

$$\Delta\varepsilon_v^e = \frac{3(1-2\nu_{ur})}{E_{ur}^{ref}}\left(\frac{\sigma^{ref} + c\ \cot\phi}{1-m}\right)\left[\left(\frac{p_c + c\ \cot\phi}{\sigma^{ref} + c\ \cot\phi}\right)^{1-m} - \left(\frac{p_{co} + c\ \cot\phi}{\sigma^{ref} + c\ \cot\phi}\right)^{1-m}\right] \tag{4.2}$$

$$\Delta\varepsilon_v = \Delta\varepsilon_v^e + \Delta\varepsilon_v^p \tag{4.3}$$

Verification was carried out on an single axisymmetric finite element which is subject to an external uniformly distributed load varying from $q = 50$ kN/m2 to $q = 250$ kN/m2. The initial effective stresses are $\boldsymbol{\sigma}_o = \{-50, -50, 0, -50\}^{\mathsf{T}}$ kPa. Material data for the dense Hostun sand (see section (4.1)) is used in the simulation. Numerical and analytical solutions are compared in in the following figure.

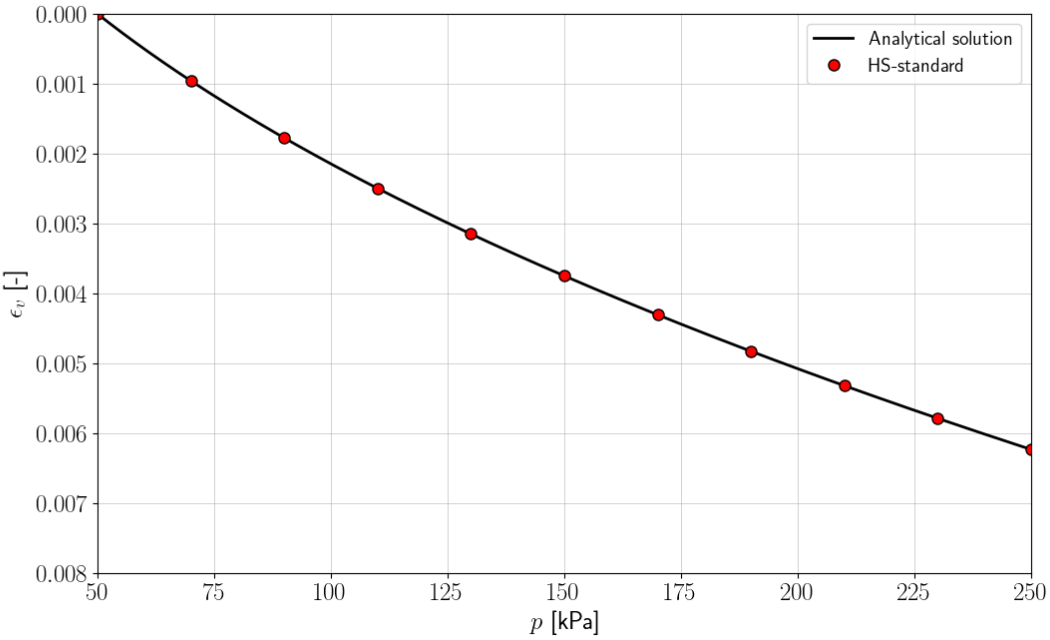

4.3 Oedometric compression test

Files: HS-oedometer.inp,HS-oedometer-5steps.inp, HS-oedometer-2steps.inp, HS-oedometer-1.inp

This single-element axisymmetric benchmark demonstrates that using the HS-standard model an assumed $E_{\text{oed}} = 30000$ kPa at the reference stress $\sigma^{\text{ref}}_{\text{oed}}$ kPa and K_0^{NC}=0.4 are correctly reproduced. This benchmark uses material data for dense Hostun sand presented in Section 4.1.
In the first 3 tests an element is loaded vertically by an uniformly distributed load which varies from $q = 75$ kN/m2 to $q = 275$ kN/m2 and is applied in 10, 5 and 2 steps respectively. Stress strain diagram and the resulting K_0^{NC} coefficient are shown in the next two figures.
In the last test, a stress driven program is run using a single step in which vertical traction varies from 99.99 kPa to 100.01 kPa. The initial effective stress state is defined as $\boldsymbol{\sigma}_o = \{-99.99 * 0.4, -99.99, 0, -99.99 * 0.4\}^{\text{T}}$ kPa.
The result of this test yields the tangent oedometric modulus at $\sigma_{\text{ref}} = 100$ kPa which is computed using central finite difference scheme as follows $E_{\text{oed}} = \dfrac{\Delta\sigma_y}{\Delta\varepsilon_y} = \dfrac{0.02}{6.6367e-7} = 30135$ kPa, which is close to the assumed value. A small error (below 0.5%) results from the assumed tolerance in M and H estimation procedure.

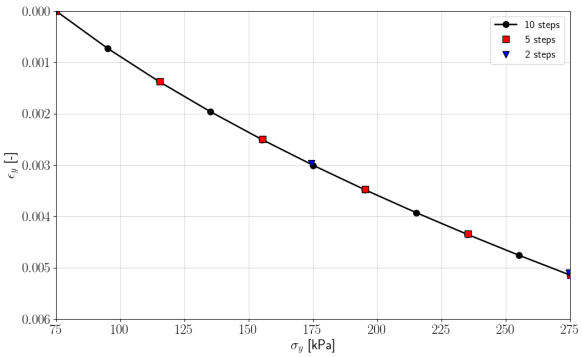

$\sigma_y - \varepsilon_y$ plot for different number of load increments

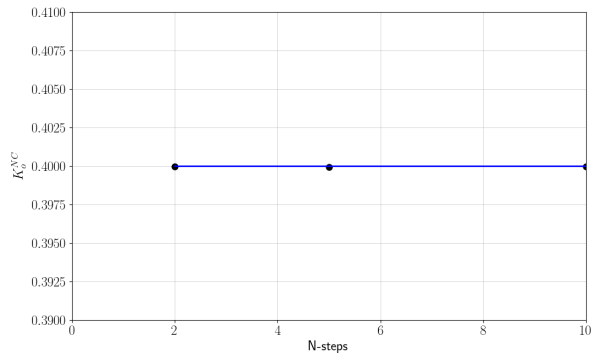

Estimated K_0^{NC}

4.4 Oedometric compression test - K_0^{NC}-path test

Files: KoNC-HS-std.inp,HS-oedometer-5steps.inp, HS-oedometer-2steps.inp, HS-oedometer-1.inp

This single-element benchmark shows that HS-standard model is able to correctly reproduce K_0^{NC}-path for the oedometric test for different values of the friction angle. The results are compared with the data obtained with other constitutive models.

The oedometric test on the normally-consolidated soil ($\text{OCR} = 1$) is modeled in axisymme-

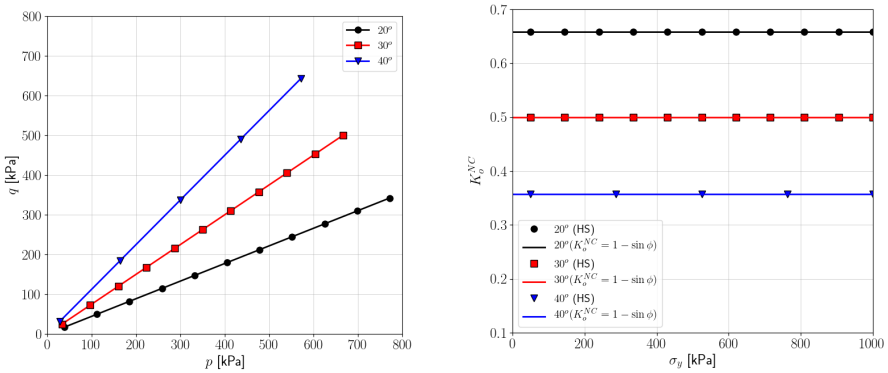

(a) (b)

Figure 4.4: K_0^{NC}-path test for the HS-standard model and different values of the friction angle $\phi = 20^o, 30^o, 40^o$: a) stress paths in $p' - q$ plane, b) K_0^{NC} with increasing loading.

try, with a single element subject to an external, uniformly distributed load which varied from $q = 50$ kN/m^2 to $q = 1000$ kN/m^2. The initial stress state corresponds to the $K_0^{\text{NC}} = 1 - \sin\phi$ value. Results which are presented in Figure 4.4 show that HS-standard model correctly reproduces K_0^{NC} stress paths which obey the empirical expression $K_0^{\text{NC}} = 1 - \sin\phi$ for three different values of the friction angle. It is worth noting that during whole loading history the K_0^{NC} is constant.

The same model is used to compare the results from the oedometric test using different constitutive models: the Modified Cam clay (MCC), the standard Mohr-Coulomb (M-C) and the Cap model (CAP). Simulations for different models were carried out for the same value of the friction angle $\phi = 30^o$ (and equivalent $M = 1.2$ for the MCC model). Hence, the value of cohesion was assumed as $c = 0$ kPa. The value of Poisson's ratio was assumed $\nu_{\text{ur}} = 0.2$ for the HS model and $\nu = 0.3$ for other models. Figure 4.5 shows that starting from the initial "zero" stress setup and gradually increasing the vertical stress, only the HS model is able to reproduce expected σ'_h/σ'_v path. It is so because the parameter M which defines the shape of the cap surface in the HS-model, is optimized so that the tangent to the cap surface at the stress reversal point is perpendicular to K_0^{NC} stress path.

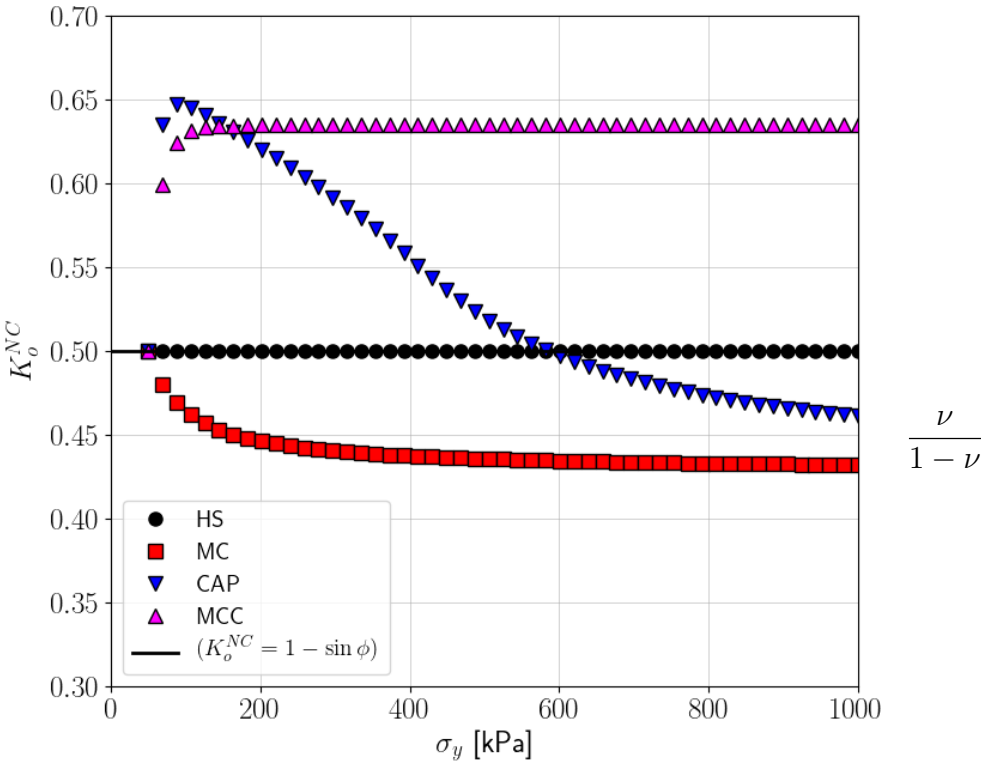

Figure 4.5: K_0^{NC}-path test using different models for $\phi = 30^o$ ($K_0^{\text{NC}} = 0.5$): Hardening Soil (HS), Modified Cam Clay (MCC), standard Mohr-Coulomb (M-C) and Cap model (CAP).

Chapter 5

Case studies

5.1 Excavation in Berlin Sand

File: HS-std-Exc-Berlin-Sand-2phase.inp
File: HS-small-Exc-Berlin-Sand-2phase.inp
File: MC-Exc-Berlin-Sand-2phase.inp

This example demonstrates the importance of modeling excavation problems using Hardening Soil model. The study case presents an analysis of main differences between HS-standard, HS-small, HS-Brick and Mohr-Coulomb models based on numerical simulation of deep excavation in Berlin Sand.

An engineering draft of the problem and the sequence of both excavation and construction steps, are given in Figure 5.1. Material data for calibration of sand was taken from Benz (2007) and Schweiger (2002). The data with standard MC model was generated assuming that stiffness of sand varies according to the power law:

$$E = 20000\sqrt{y} \text{ kPa} \quad \text{for} \quad y \leq 20m$$
$$E = 60000\sqrt{y} \text{ kPa} \quad \text{for} \quad y > 20m$$

where y is the depth expressed in [m]. The same strength parameters apply to both the MC model and HS models.

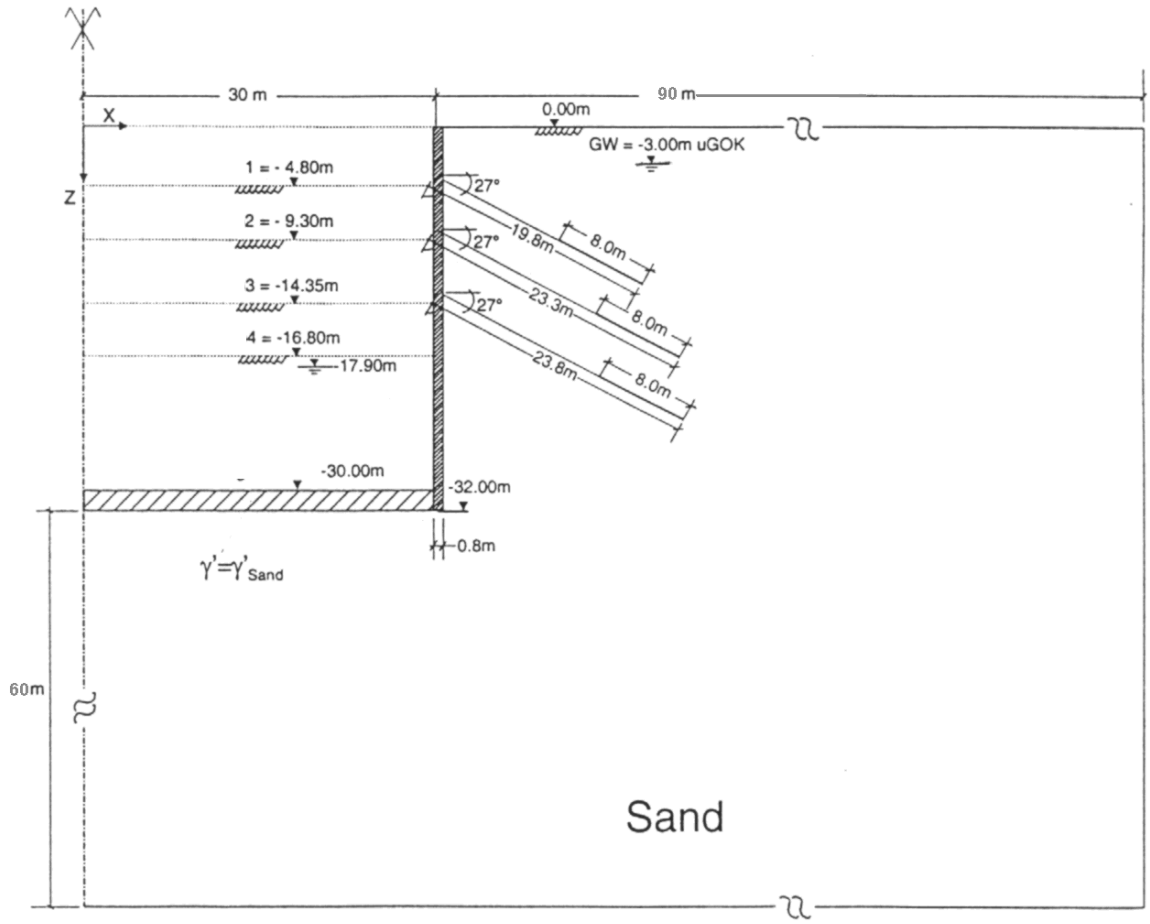

Figure 5.1: An engineering draft and the sequence of both excavation and construction stages for the deep excavation in Berlin sand.

Sequence of stages:

1. Generating an initial stress state for an assumed $K_0^{\text{in situ}}$ in sand layers
2. Installation of the diaphragm wall
3. Lowering the ground water level in the excavated zone up to the elevation -17.90m
4. Excavation step 1 (up to -4.80m)
5. Introducing the first row of anchors (distance 2.30 m) and applying the prestress $P_0 = 768$ kN
6. Excavation step 2 (up to -9.30m)
7. Introducing of the second row of anchors (distance 1.35 m) and and applying the prestress $P_0 = 945$ kN
8. Excavation step 3 (up to -14.35m)
9. Introducing of the third row of anchors (distance 1.35 m) and and applying the prestress $P_0 = 980$ kN
10. Excavation step 4 (up to -16.80m)

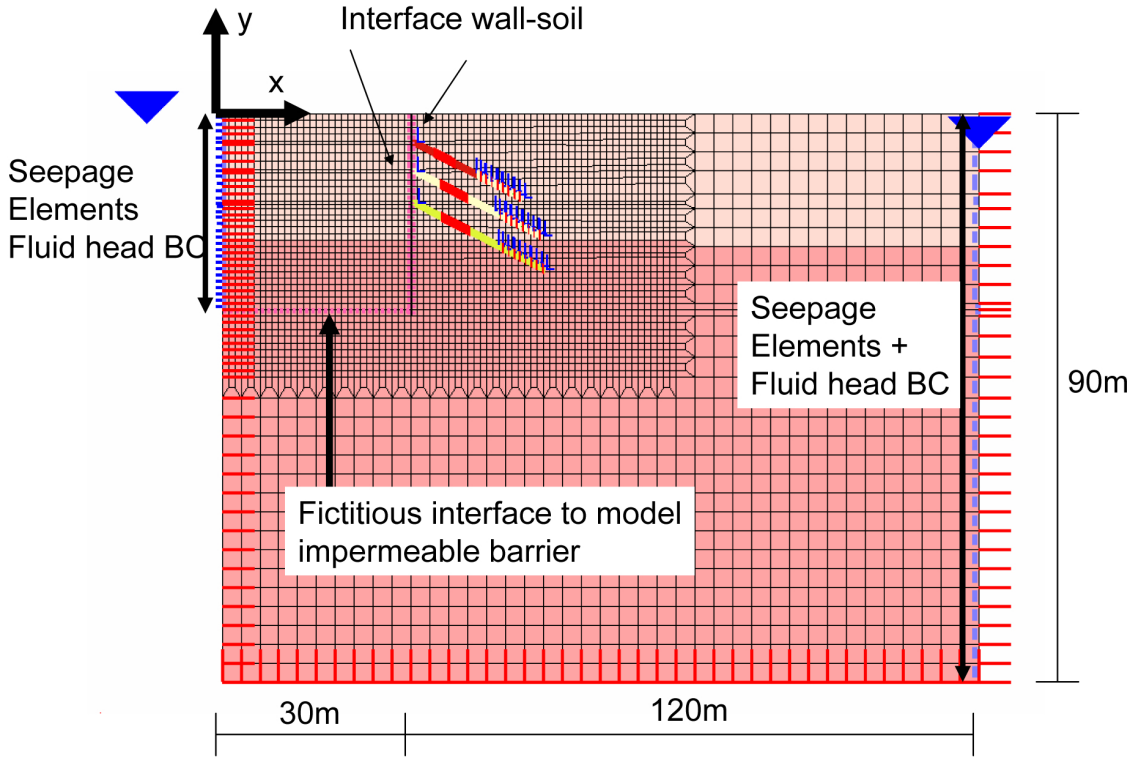

Figure 5.2: Excavation in Berlin Sand: FE mesh.

A **finite element model** of the problem is shown in the figure below. The mesh represents:

- deposits consisting of two sand layers which are described with two different groups of stiffness characteristics
- three rows of prestressed anchors
- diaphragm wall
- contact interfaces between sand and the wall
- zone of artificial contact elements which are used to model a hydraulic barrier (preserving continuity of displacement field and discontinuity of pore pressure)
- external displacement boundary conditions (BC) (box type)
- pressure BC which are applied via fluid head and set up along the right hand side boundary, as well as along the left hand boundary up to the level of impermeable barrier (pressure fluid head BC is applied with the aid of seepage elements)

Table 5.1: Excavation in Berlin Sand: material properties for soils

Material	Model	Data group	Properties	Unit	Value
1 Sand (-20m↑)	HS-small	Elastic	E_{ur}	[kN/m^2]	180000
			σ_{ref}	[kN/m^2]	100.0
			ν_{ur}	–	0.2
			m	–	0.50
			σ_L	–	10.0
			E_0^{ref}	[kN/m^2]	405000
			$\gamma_{0.7}$	–	0.0002
		Density	γ_D	[kN/m^3]	16
			γ^F	[kN/m^3]	10
			e_0	–	0.66
		Non-linear	ϕ	[°]	35
			ψ	[°]	5
			c	[kN/m^2]	1
			E_{50}^{ref}	[kN/m^2]	45000
			R_f	–	0.9
			D	–	0.25/0.0(HS-std)
			f_t	–	0.0
			M	–	1.85
			H	[kN/m^2]	129305
			K_0^{NC}	–	0.426
			p_{c0}^{min}	[kN/m^2]	10.0
		Initial K_0 state	K'_{0x}/K'_{0z}	–	0.43
2 Sand (-20m↓)	HS-small	Elastic	E_{ur}	[kN/m^2]	300000
			σ_{ref}	[kN/m^2]	100
			ν_{ur}	–	0.2
			m	–	0.55
			σ_L	–	10.0
			E_0^{ref}	[kN/m^2]	675000
			$\gamma_{0.7}$	–	0.0002
		Density	γ_D	[kN/m^3]	16
			γ^F	[kN/m^3]	10
			e_o	–	0.66
		Non-linear	ϕ	[°]	38
			ψ	[°]	6
			c	[kN/m^2]	1
			E_{50}^{ref}	[kN/m^2]	75000
			R_f	–	0.9
			D	–	0.25/0.0(HS-std)
			f_t	–	0.0
			M	–	2.955
			H	[kN/m^2]	128964
			K_0^{NC}	–	0.38
			p_{c0}^{min}	[kN/m^2]	10.0
		Initial K_0 state	K'_{ox}/K'_{oz}	–	0.38

Table 5.2: Excavation in Berlin Sand: material properties for the diaphragm wall, anchors and interfaces

Material		Model	Data group	Properties	Unit	Value
3	Wall	Beams	Elastic	E	[kN/m^2]	30000000
				ν	–	0.15
			Density	Unit weight	[kN/m^3]	24
			Geometry	Interval	[m]	1.0
				A	[m^2]	0.8
				I_z	[m^4]	0.0426667
4	Anchors	Truss	Elastic	E	[kN/m^2]	210000000
			Density	Unit weight	[kN/m^3]	0.0
			Geometry	Interval	[m]	2.3
				A	[m^2]	0.0015
5	Anchors	Truss	Elastic	E	[kN/m^2]	210000000
			Density	Unit weight	[kN/m^3]	0.0
			Geometry	Interval	[m]	1.35
				A	[m^2]	0.0015
6	Anchors	Truss	Elastic	E	[kN/m^2]	210000000
			Density	Unit weight	[kN/m^3]	0.0
			Geometry	Interval	[m]	1.35
				A	[m^2]	0.0015
7	Interface	Contact	Non-linear	ϕ	[°]	28
				ψ	[°]	0
				c	[kN/m^2]	0.0

The chart below presents four unloading functions which are defined and associated with the excavated elements in order to gradually unload each excavated region. Note that the same unloading functions must be applied to interface elements adjacent to the excavated continuum. All existence functions and unloading functions which are applied for excavated zones of sand are shown in the chart below.

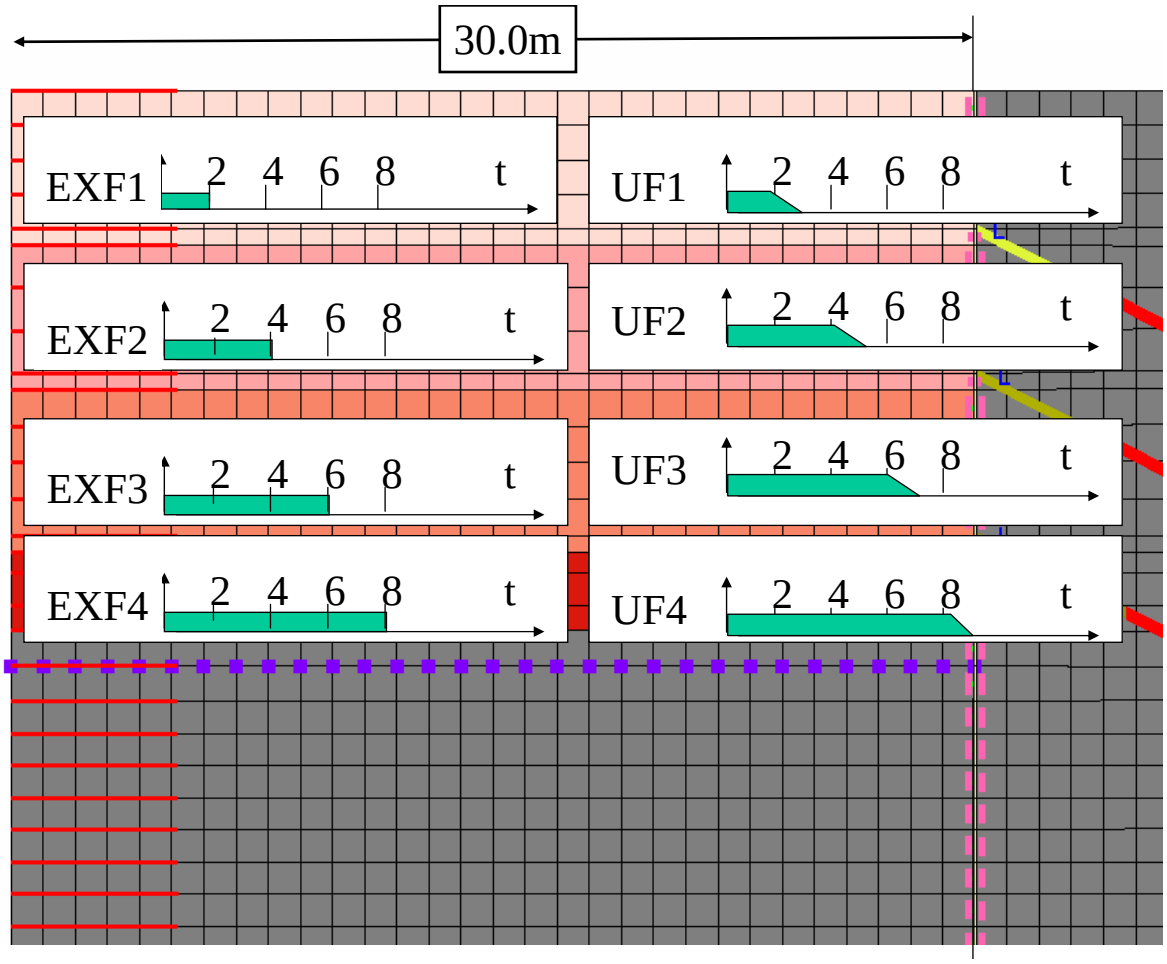

Figure 5.3: Excavation in Berlin Sand: unloading functions

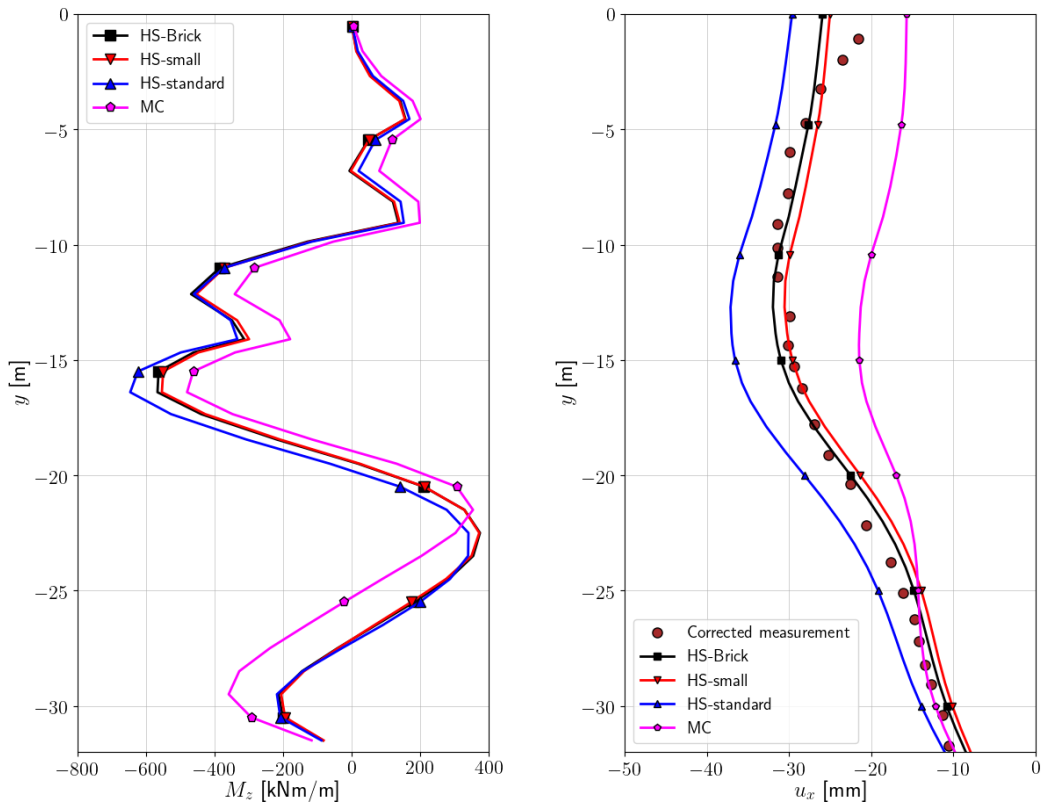

(a) (b)

Figure 5.4: Excavation in Berlin Sand: Bending moments and wall deflections at the last stage of excavation

Remarks:

1. The largest bending moments are generated by HS-standard model due to excessive plastic soil deformation caused by lack of small strain stiffness. The shape of the M diagrams is similar for all models.

2. The most significant overshoot is observed in the bottom part of the wall. In the basic MC model elastic stiffness remains unchanged and insensitive to the current stress state while HS-standard and HS-small/HS-Brick models exhibit strong stress dependency (cf. Eq.(2.6)).

3. Predictions of wall deflection by the HS-small/HS-Brick models match *in situ* measurements. A certain discrepancy is observed at the top part of the wall. This effect can be explained by the fact that creep neither cracking of concrete is not included.

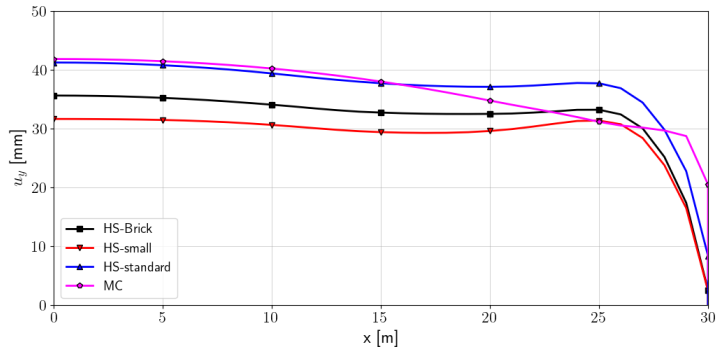

(a)

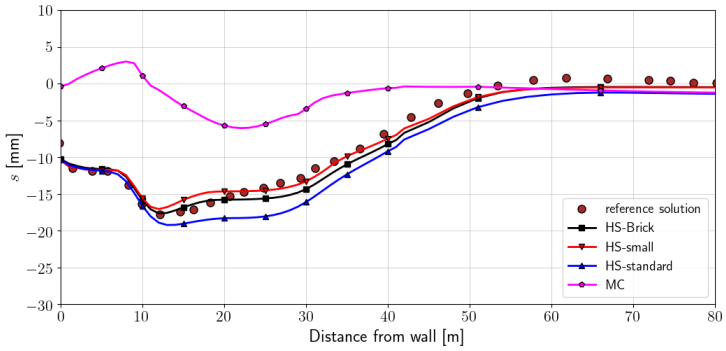

(b)

Figure 5.5: Excavation in Berlin Sand: Soil deformations at last stage of excavation (a) vertical heaving of subsoil, (b) settlements of the ground behind the wall ($y = 0$ m)

Remarks:

1. The HS-Standard and MC models with variable stiffness generate similar heaving.
2. Vertical heaving generated by the HS-small and HS-Brick models is significantly reduced with respect to results which are generated by HS-Standard and MC models; the HS-Brick model yields larger heaving than the HS-small (because of spurious strain history reset)
3. The MC model results in an unrealistic lifting of the retaining wall associated with unloading of the bottom of an excavation. Settlements behind the wall are realistically generated with HS-standard and HS-small/HS-Brick models.

5.2 Twin tunnels excavation in London Clay

File: HS-Brick-Exc-London-Clay-2phase.inp

This example demonstrates the importance of modeling tunnel construction problems using advanced constitutive models such as Hardening Soil models which enable one to consider pre-failure non-linear stiffness. The study highlights the differences in predictions of subsurface displacements during tunnel excavations in the stiff, heavily overconsolidated London Clay modeled using:

- Non-linear elastic, perfectly plastic models: HS-Brick and HS-small.

This study reanalyzes the excavation model of the twin Jubilee Line Extension Project tunnels beneath St James's Park (London, UK) which has been reported in the original paper by Addenbrooke et al. (1997). Predictions of displacements obtained using Hardening Soil models are additionally compared with the results obtained by Addenbrooke et al. (1997) for the isotropic non-linear elastic model J4 and field data.

The problem statement, i.e. subsurface stratigraphy and tunnels orientation is presented in Figure 5.6. The following paragraphs present the analysis details, excavation/construction stages and the material data assumed in the analyzes.

Analysis details

- analysis type: `Plane Strain: Deformation + Flow`
- driver type: `Consolidation`
- mesh: Figure 5.7
- constitutive models:
  - ⋆ Sand: HS-Brick
  - ⋆ Thames Gravel: HS-Brick
  - ⋆ London Clay: HS-Brick
  - ⋆ Woolwich and Reading Bed Clay: M-C

Excavation/construction stages

1. Generating the initial state in subsoil for the assumed K_0^{insitu} across the FE mesh presented in Figure 5.7
2. Adding seepage elements around the westbound tunnel which permits water outflow and excavation of the westbound tunnel with gradual unloading - 100% unloading within period of 8 hours
3. Installation of the westbound tunnel lining at 63% of unloading (this corresponds to the assumed volume loss level of 3.3 $\%$ achieved with the HS-Brick model) and removing seepage elements; parameters for tunnel lining are given in Table 5.7
4. Consolidation during 8.5 months
5. Adding seepage elements around the eastbound tunnel which permits water outflow and excavation of the eastbound tunnel during 8 hours with gradual unloading within period of 8 hours
6. Installation of the westbound tunnel lining at 62.8% of unloading and removing seepage elements; this unloading level corresponds to the assumed volume loss of 2.9% achieved with the HS-Brick model
7. Consolidation

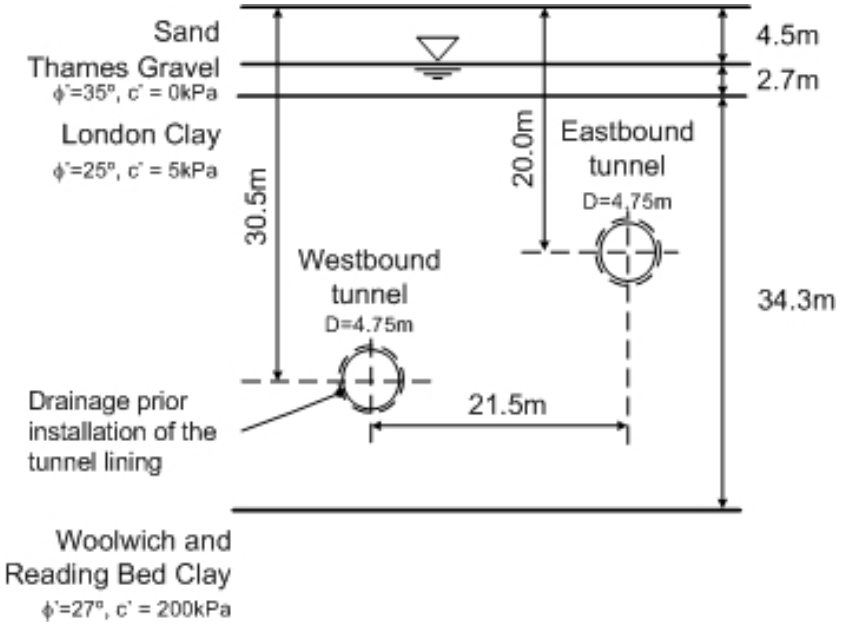

Figure 5.6: Soil stratigraphy and diagonally oriented tunnels at St James's Park, London, UK.

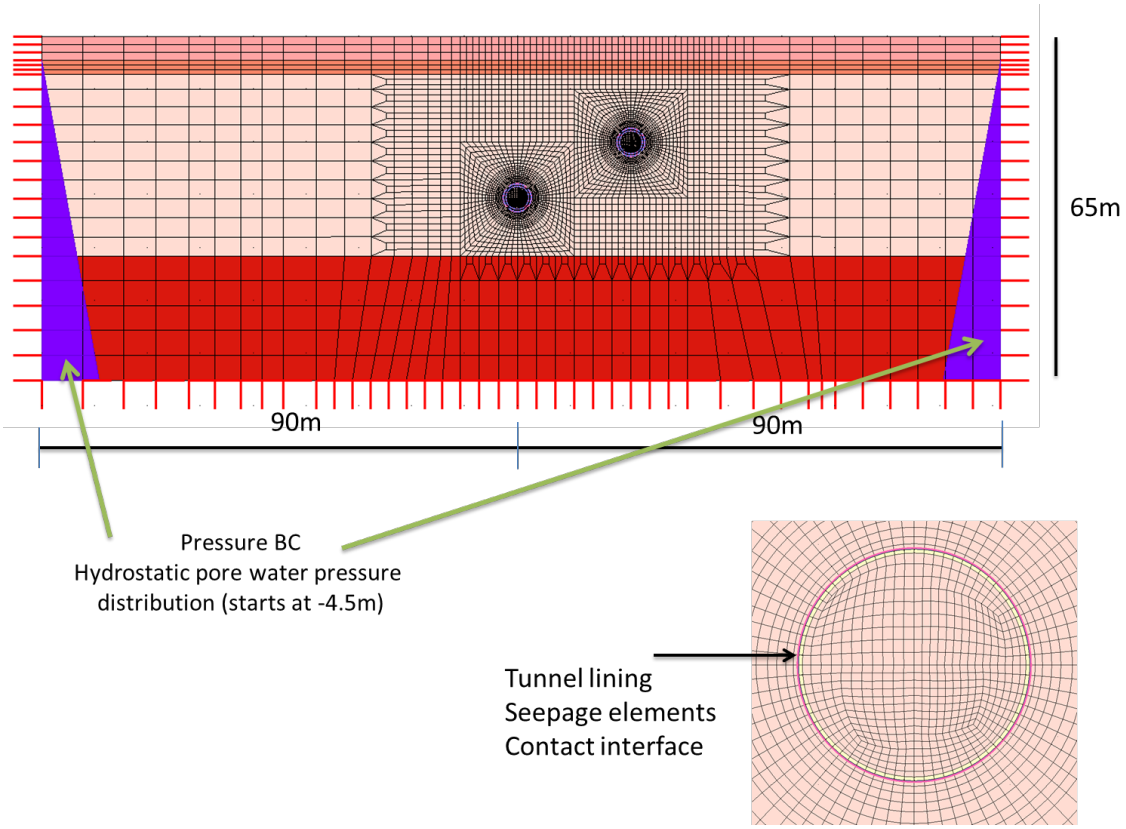

Figure 5.7: Finite element mesh

Material data

- Unit weights - see Table 5.3
- Stiffness parameters
  - ⋆ for HS models - E_0, E_{ur}, E_{50} and $\gamma_{0.7}$ calibrated using laboratory $\varepsilon_1 - q$ data points for the isotropically consolidated undrained extension triaxial test (CIUE) at $p'_0 = 750$ kPa, as shown in Figure 5.9. The constant m was assumed for London Clay equal to 0.7 which is little lower than the one (0.75) reported in Viggiani and Atkinson (1995). The stiffness parameters are given in Table 5.4. The E_0 value was calibrated to fit as best as possible the $\varepsilon_1 - q$ curve for the aforementioned triaxial undrained extension test and resulting degradation curve.
- Strength and plastic potential parameters - typical values for London Clay (see Table 5.3) have been adapted from the original paper (Addenbrooke et al., 1997) for all considered models. The reported very high dilatancy angles (unrealistic in practice) were significantly reduced for all soil layers.
- Initial state parameters (see Table 5.6)
  - ⋆ the value of the overconsolidation ratio OCR for London Clay was assumed equal to 5.
  - ⋆ although the estimates of $K_0^{\text{in situ}}$ for the London Clay are typically reported of around 1.5, the value $K_0 = 1.0$ has been adopted in the analysis. It was observed that the isotropic Hardening Soil models may give incorrect predictions for $K_0 >> 1.0$. The comparative results produced by model J4 in Addenbrooke et al. (1997) were obtained for $K_0 = 1.5$.
- Permeability - sand and gravel were modelled as highly permeable materials, whereas clayey soils were attributed with an anisotropic permeability decreasing with depth, as shown in Figure 5.8. The fluid bulk modulus was assumed equal to $\beta_f = 2.2$ GPa.
- Characteristics for the tunnel lining which were adopted after the original paper are summarized in Table 5.7.

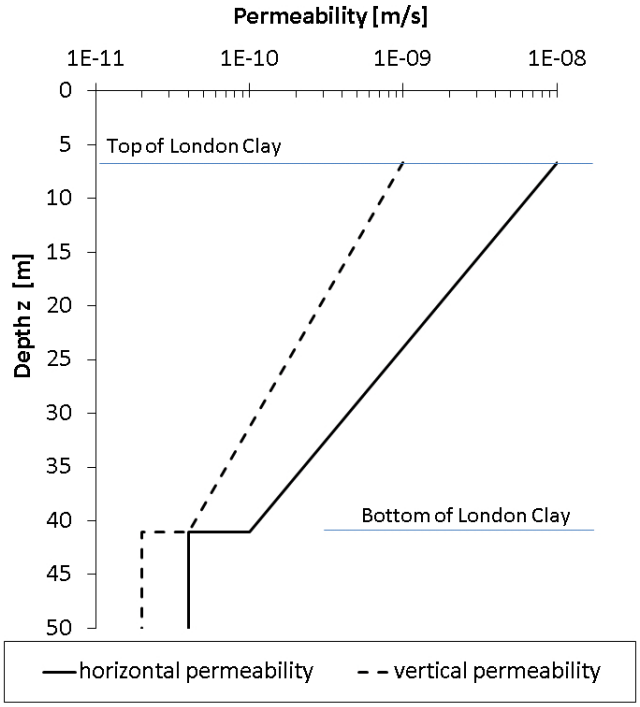

Figure 5.8: Permeability profile assumed in the analysis.

Comments:

- The HS-Brick model matches quite well the laboratory data points (in red) both in the range of very small strains (up to 0.01%) and in the range of small strains (between 0.01 and 0.4%).

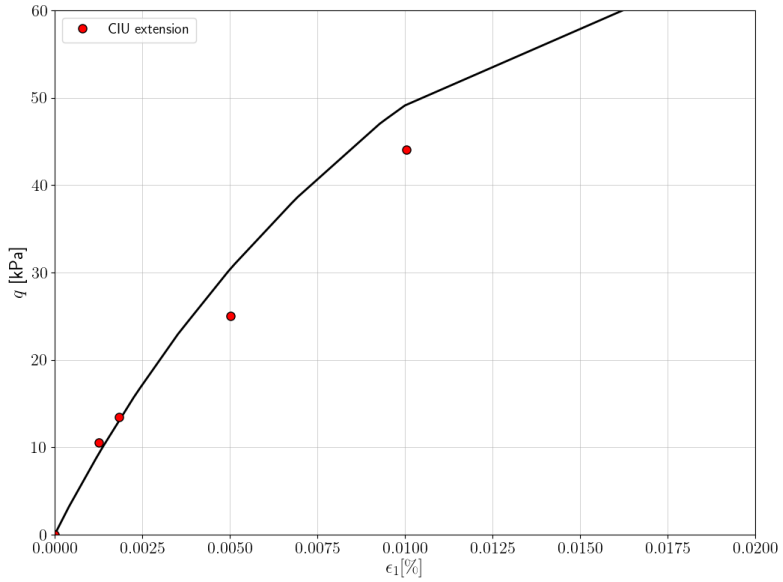

(a) Very small strains

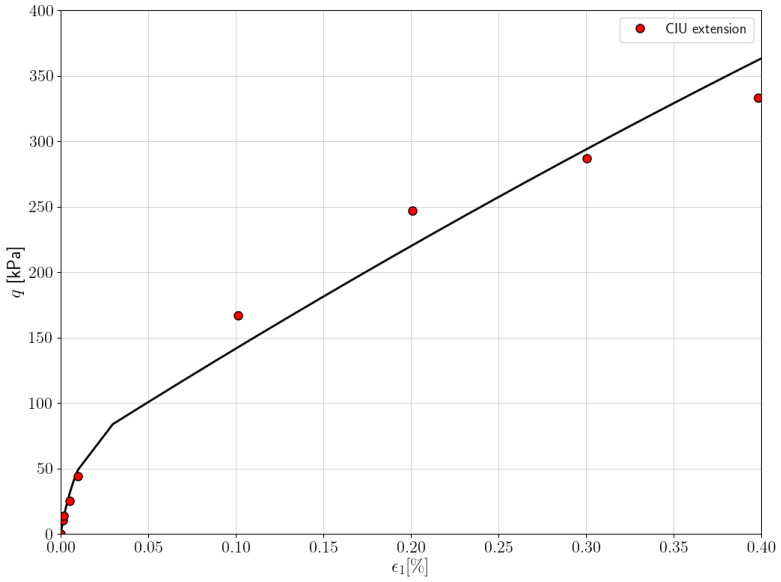

(b) Small strains

Figure 5.9: Stress-strain curves: HS-Brick vs experiment (isotropically consolidated undrained extension test ($p'_0 = 750$ kPa)).

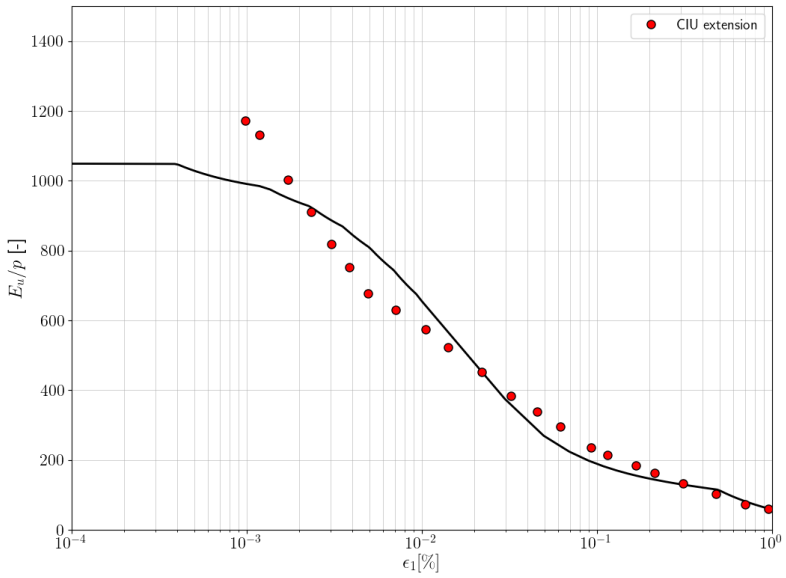

Figure 5.10: Variation of the undrained secant stiffness-strain curve $\varepsilon_1 - E_s^{\text{ud}}$: HS-Brick model response vs laboratory data points obtained in the isotropically (CIEU) consolidated undrained extension tests ($p'_0 = 750$ kPa).

Comments:

- Volume loss is understood here as a fraction $\frac{\int u_y(x)\mathrm{d}x}{\pi\ R^2} * 100\%$ computed at ground surface

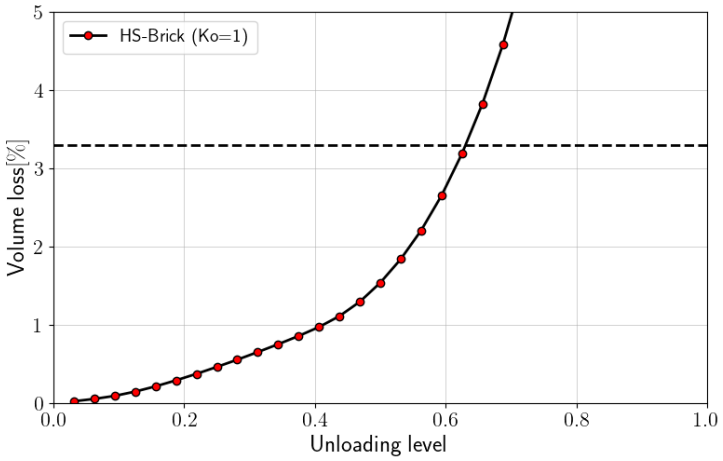

(a) westbound tunnel (volume loss 3.3% achieved at unloading level of 63 $\%$)

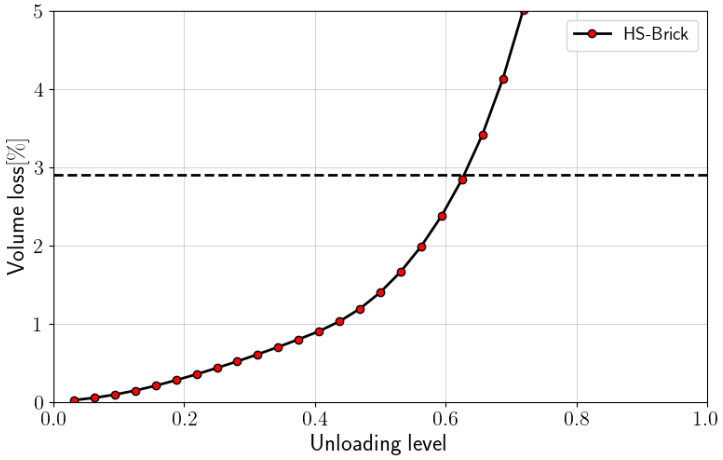

(b) eastbound tunnel (volume loss 2.9% achieved at unloading level of 62.8 $\%$)

Figure 5.11: Evolution of the volume loss with the unloading level for the westbound and the eastbound tunnels

Comments:

- The HS-Brick and HS-small yield a similar shape of surface settlements with the maximum value of about 15 mm; this result is better than the one obtained using the J4 model which is also isotropic; this result clearly shows an anisotropic behavior of London clay

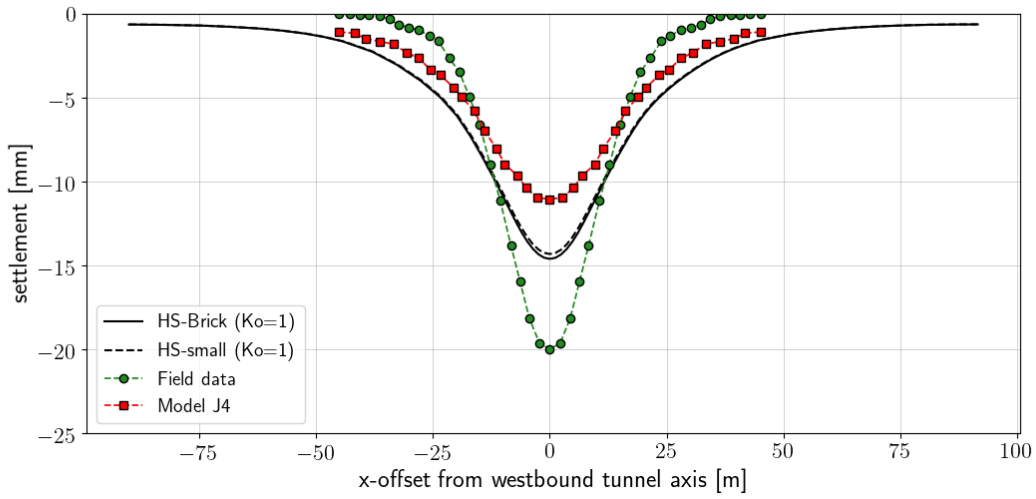

Figure 5.12: Surface settlement profiles after excavation of the westbound tunnel: comparison of different models.

Comments:

- The HS-Brick model yields a better prediction than the HS-small model and the J4 one. Problem of the stiffness overshooting in the HS-small model is here well visible.

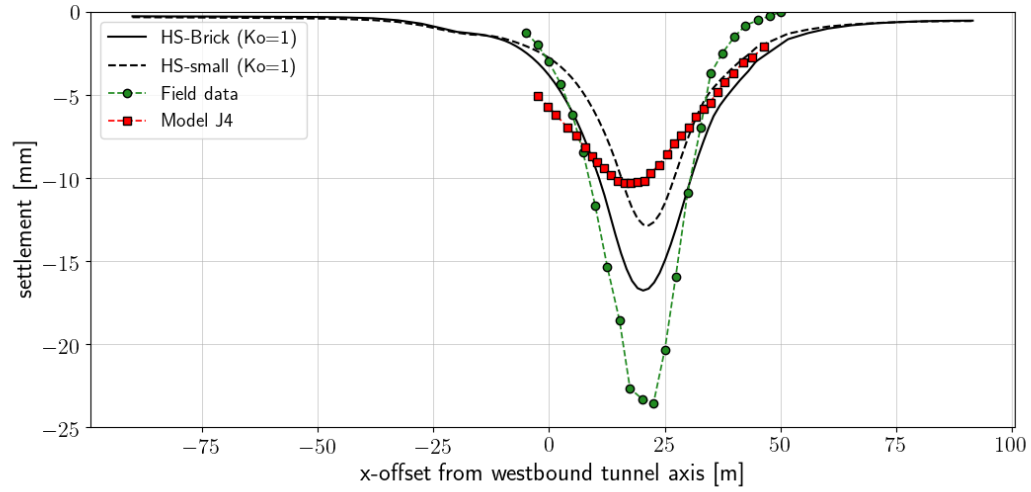

Figure 5.13: Surface settlement profiles after excavation of eastbound tunnel: comparison of different models.

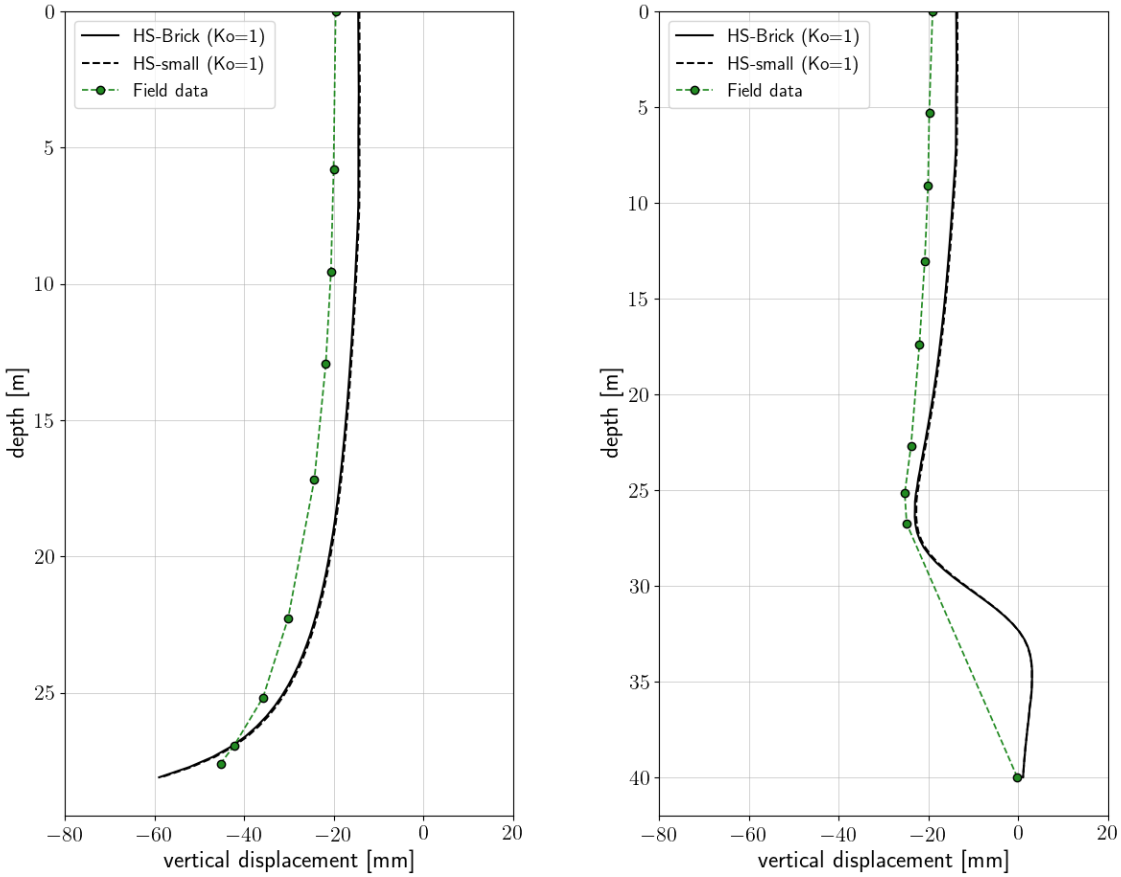

(a) (b)

Figure 5.14: Excavation of the westbound tunnel (a) vertical displacements profile at the tunnel axis (b) vertical displacements profile 4m (left) from the axis.

Table 5.3: Unit weight, permeability, yield surface and plastic potential parameters for Mohr-Coulomb and HS-models.

	Sand	Gravel	London Clay	Woolwich and Reading Clay
Strength parameters	$c' = 1$ kP $\phi' = 30^o$	$c' = 0$ kPa $\phi' = 35^o$	$c' = 5.0$ kPa $\phi' = 25^o$	$c' = 200$ kPa $\phi' = 27^o$
Dilatancy angle	$\psi = 0^o$	$\psi = 5^o$	$\psi = 5^o$	$\psi = 5^o$
Bulk unit weight kN/m^3	$\gamma_{dry} = 18$ $\gamma_{sat} = 20$	$\gamma_{sat} = 20$	$\gamma_{sat} = 20$	$\gamma_{sat} = 20$
Permeability coefficient m/s	10^{-5}	10^{-4}	see Fig. 5.8	see Fig. 5.8

Table 5.4: Stiffness parameters for London Clay, gravel and sands for HS models at the reference stress $\sigma_{\text{ref}} = 100$ kPa.

Layer	E_0 [MPa]	$\gamma_{0.7}$ [-]	E_{ur} [MPa]	E_{50} [MPa]	m [-]	ν [-]
London Clay	160	0.0001	18	4	0.7	0.25
Gravel	300	0.0002	100	33	0.5	0.20
Sands	150	0.0002	50	16.7	0.5	0.25

Table 5.5: Stiffness parameters for Woolwich and Reading Bed Clay

Layer	E [MPa]	ν [-]
Woolwich and Reading clay	800	0.25

Table 5.6: Initial state parameters assumed in this study.

	K_0^{NC} [-]	K_0^{SR} [-]	K_0 [-]	OCR [-]
London Clay	0.577	0.577	1.0	5
Sand	0.5	0.5	0.5	1.1
Gravel	0.5	0.5	0.5	1.1
Woolwich and Reading Clay			1.0	-

Table 5.7: Tunnel lining characteristics.

Young's modulus E	Poisson's ratio υ	Cross sectional area A	Momentum of inertia I_z	Lining-soil interface friction angle ϕ_i
28 GPa	0.15	0.168 m^2/m	3.95136$\cdot 10^{-4}$ m^4/m	20^o

5.3 Spread footing on overconsolidated Sand

File: HS-small-Footing-Texas-Sand-2phase.inp
File: HS-Brick-Footing-Texas-Sand-2phase.inp
File: MC-Footing-Texas-Sand-2phase_EurVar.inp

A verification of the HS-small/HS-Brick models for a square footing load test is demonstrated in this section. This load test examines the model in terms of its sensitivity to loading and unloading modes applied to overconsolidated sand. This simple boundary value problem also illustrates:

- Combined parameter identification from triaxial tests and dilatometer tests
- Interpretation of laboratory and *in situ* measurements
- Imposing soil stress history through the q^{POP} (obtaining a variable OCR profile)
- Imposing a variable K_0 profile
- Sensitivity of numerical prediction to small-strain stiffness parameters
- Sensitivity of numerical prediction to initial stress setup

The study case demonstrates main differences between HS-standard, HS-small, HS-Brick and standard Mohr-Coulomb (MC) for the analyzes of footing.

Problem statement.

A number of load tests on square footing were performed at Texas A&M University's National Geotechnical Site (Briaud and Gibbens, 1997). In this example, the measurements derived from a load test of 3x3m "North" footing are compared to numerical predictions. The test setup and soil stratigraphy is presented in Figure 5.15. The subsoil mainly consists of sandy clay to silty sand layers and it has been confirmed by the interpreted DMT data (see Figure 5.21(a)). Vertical displacements were measured at the corners of the square footing.

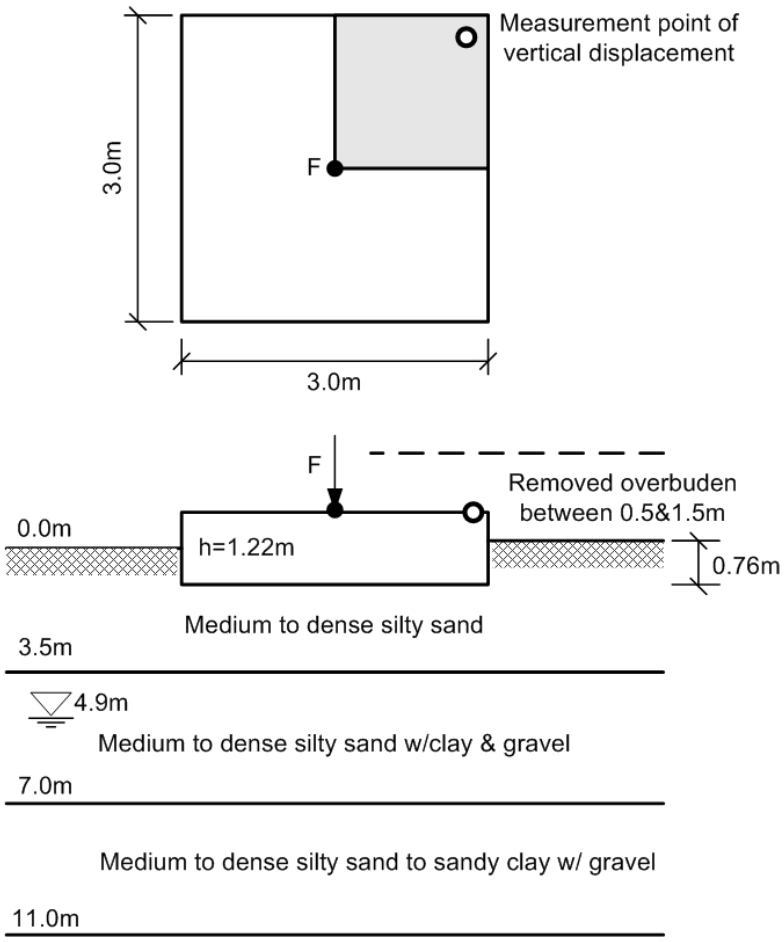

Figure 5.15: A draft of the test setup and soil stratigraphy at A&M University's National Geotechnical Site in Texas.

Parameter identification from a triaxial test. The parameters for the HS model have been determined from available triaxial compression tests for two sampling depths 0.6m and 3.0m, and three confining pressures 34.5, 138 and 345 kPa. The results from several resonant column tests with the confining pressure 100kPa have been used to evaluate the order of magnitude of small strain characteristics. The reader can analyze parameter identification in the spreadsheet presented in Table 5.8. Note that the determination of ϕ' and c' was carried out only for 34.5kPa and 138kPa tests since the ultimate state (failure deviatoric stress q_f) was not achieved at 345kPa.
A comparison of numerical results and experimental data derived from triaxial compression tests is presented in Figure 5.17. Note that the preconsolidated state of soil specimens was taken into account in the triaxial test simulations by applying the initial value of the minimal preconsolidation pressure $p_{c0} = 250$kPa. The value was evaluated assuming that:

$$\sigma'_{v0} = 14.9\text{kN/m}^3 \times 3.0\text{m} = 44.7\text{kPa}$$

and applying an estimated q^{POP} (see Figure 5.20):

$$\sigma_y^{\text{'SR}} = \sigma'_{vc} = \sigma'_{v0} + q^{\text{POP}} = 44.7\text{kPa} + 350kPa = 394.7kPa \qquad \text{cf. Eq.(2.28a)}$$

$$\sigma_x^{\text{'SR}} = \sigma'_{v0} \cdot K_0^{\text{SR}} = 394.7\text{kPa} \times 0.41 = 161.8\text{kPa}$$

$$p_{c0} = (2\sigma_x^{'SR} + \sigma_y^{'SR})/3 \approx 250\text{kPa}$$

Note that prescribing the initial preconsolidation state may have an influence on the results of the numerical simulation of the triaxial compression test. In the presented example, the volumetric mechanism is not activated during the triaxial compression test for the confining pressures 34.5kPa and 138kPa because the specimens are preconsolidated, i.e. the initial stress state p'_0 is largely inferior with respect to p'_{c0}. On the other hand, the simulation for 345kPa is affected by both shear and cap mechanisms as the specimen is normally consolidated. In the other words, one may expect less stiffness at 50% of q_f, where the volumetric straining also occurs. Note that in the case of the full scale simulation of the footing load test, the initial preconsolidation state will be prescribed through the preoverburden pressure q^{POP} which imposes the preconsolidation pressure with respect to the initial effective vertical stress σ'_{v0} (see Figure 5.20).

Since the results derived from resonant columns present a considerable scatter (even for the same confining pressure 100kPa, see Figure 5.17 in the right hand bottom corner), they were used to evaluate the first guess of small-strain stiffness parameters. It is commonly recognized that the small-strain stiffness derived from *in situ* seismic probes is typically larger compared to that measured with laboratory devices. This is typically attributed to specimen disturbances during soil sampling.
The results derived from numerical simulations presented in Figure 5.17 illustrate the sensitivity analysis of the HS-small/HS-Brick model to two parameters E_0 and $\gamma_{0.7}$ which define the model behavior for very small amplitudes of shear strain. It can be noticed that a considerable scatter of the results derived from resonant columns does not allow performing a precise parameter calibration, especially for parameter $\gamma_{0.7}$. Considering probable disturbances due to sampling, the simulations of triaxial tests were conducted for lower small-strain stiffness parameters, whereas higher values of parameters were assumed to simulate *in situ* load test.

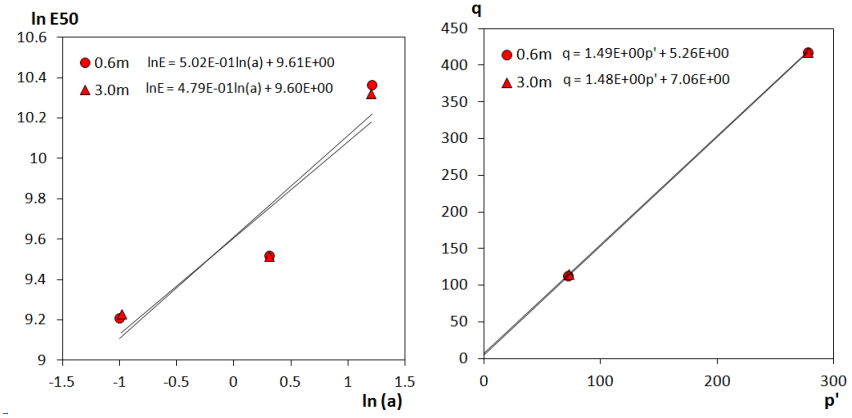

(a) Identification of slope m (b) Identification of slope M^* and intercept c^*

Figure 5.16: Interpretation of triaxial compression test data from A&M test site (sampling depths: 0.6m and 3.0m, refer to Table 5.8).

Table 5.8: Parameter identification spreadsheet for the triaxial test - spread footing benchmark.

Sample	0.6m			3.0m				Ref.
Confining pressure σ_3 [kPa]	34.5	138	345	34.5	138	345		Fig.5.17
Ultimate dev. stress q_f [kPa]	112.3	417.7	994.4$^{\#}$	114.9	417.9	994.9$^{\#}$		
Vertical stress σ_1 [kPa]	146.8	555.7	1339.4	149.4	555.9	1339.9		
Mean stress at failure [kPa]	71.9	277.2	676.5	72.8	277.3	676.6		
$^{\#}$ q_f not achieved, identification of ϕ and c for 34.5kPa and 138kPa								
Identification of ϕ and c							Mean	
Slope M^* [-]	1.488			1.482				Fig. 5.16(b)
Intercept in $p' - q$ plane c^* [kPa]	5.262			7.06				Fig. 5.16(b)
Friction angle ϕ [deg]	36.6			36.5			36.5	cf. Fig.3.1
Cohesion c [kPa]	2.6			3.5			3.1	cf. Fig.3.1
Identification of R_f and $E_{50}(\sigma_3)$							Mean	
Slope a [-]	8.48e-03	2.12e-03	8.82e-04	8.40e-03	2.11e-03	8.75e-04		Fig.5.18
Intercept b [-/kPa]	5.01e-05	3.68e-05	1.57e-05	4.90e-05	3.68e-05	1.65e-05		Fig.5.18
Failure ratio $R_f(= b \cdot q_f)$ [-]	0.95	0.89	0.88	0.97	0.88	0.87		
Secant modulus $E_{50}(= 1/2b)$ [kPa]	9988	13605	31786	10210	13576	30358		
Identification of E_{50}^{ref} and m							Mean	
$\ln E_{50}$	9.21	9.52	10.37	9.23	9.52	10.32		
Reference stress σ_3 [kPa]		100			100		100	
$a = (\sigma_3 + c\cot\phi)/(\sigma_{\text{ref}} + c\cot\phi)$	0.367	1.367	3.366	0.375	1.363	3.339		
$\ln a$	-1.001	0.313	1.214	-0.981	0.309	1.206		
Stiffness exponent m [-]		0.521			0.494		0.51	Fig.5.16(a)
Ref. secant modulus E_{50}^{ref} [kPa]		16013			15821		15917	
Identification of ψ							Mean	
Slope d	4.88e-02	3.92e-02	9.86e-03	4.82e-02	3.70e-02	1.11e-02		
Dilatancy angle ψ [deg]	1.37	1.10		1.35	1.04		1.27	

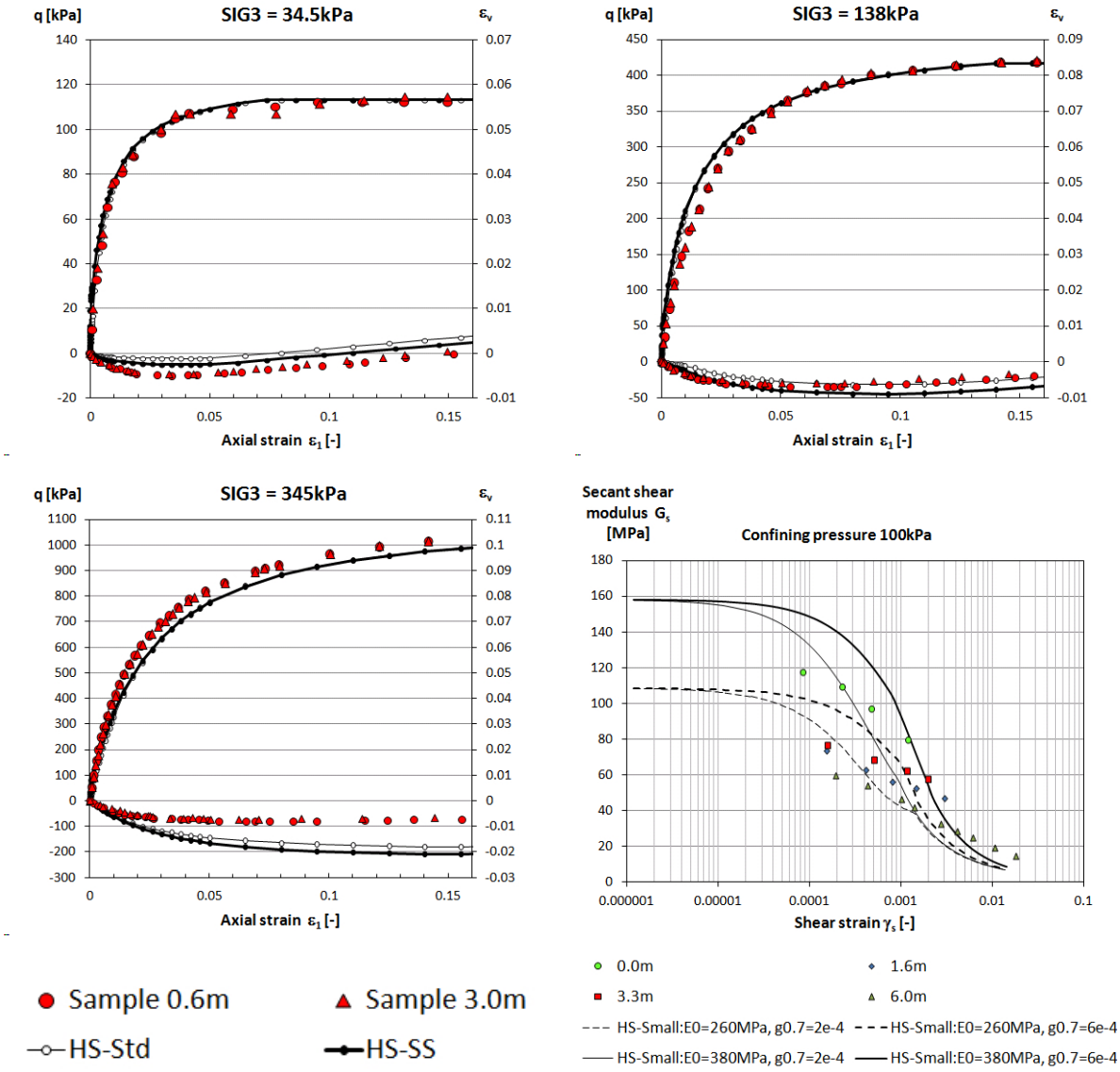

Figure 5.17: Triaxial compression test data from A&M test site (sampling depths: 0.6m and 3.0m) and numerical results for HS-small and HS-standard. Parameters for HS-Std model were derived from parameter identification presented in Table 5.8; the results for different small-strain parameters are compared to the results from a couple of resonant column tests (right hand bottom corner: $\gamma_s = \varepsilon_1 - \varepsilon_3$ and $G_{50} = \Delta q / 2\Delta\gamma_s$). The other parameters used for numerical simulations are summarized in Table 5.9.

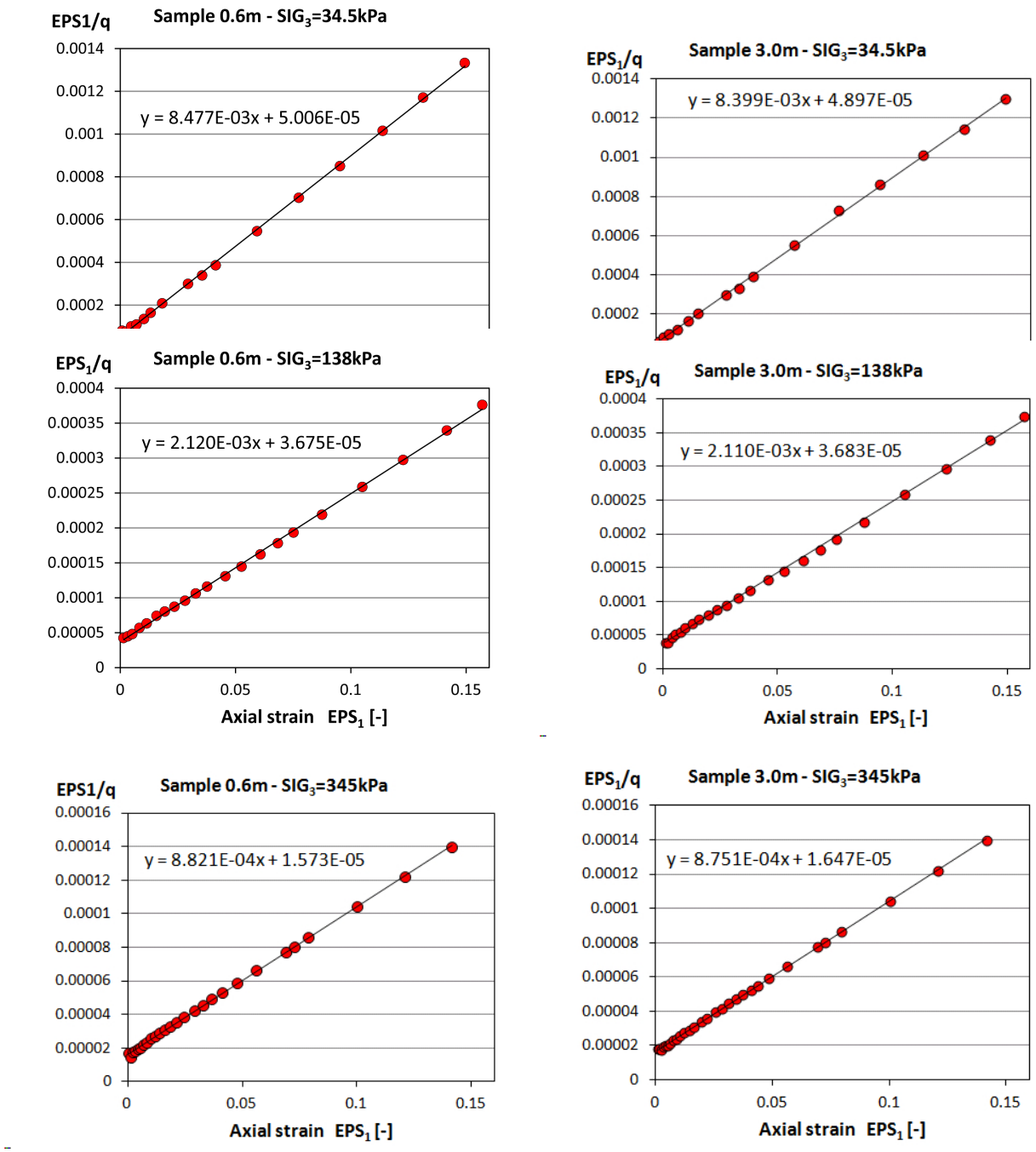

Figure 5.18: Interpretation of triaxial test data in $\varepsilon_1 - \varepsilon_1/q$ plane: samples 0.6m and 3.0m. Note that slope a is used to calculate R_f whereas the intercept b is used to compute E_{50} as shown in Figure 3.3 (sampling depths: 0.6m and 3.0m, refer to Table 5.8).

Parameter estimation from the dilatometer test.

Records derived from two dilatometer tests (DMT-1 and DMT-2) were used for profiling silty sand. The field tests, i.e. CPT, pressuremeter and Marchetti's dilatometer, showed that the silty sand site is overconsolidated due to removal of an overburden surcharge and soil aging. Estimation of two initial state variables OCR and K_0 was carried out based on the interpreted results of the horizontal stress index K_D (see Figure 5.19(a)). It can be noticed that the OCR decreases with increasing depth which is characteristic to superficial layers of subsoil which may be directly subject to mechanical unloading such as erosion, excavations, changes in ground water level, or due to other phenomena such as dessication or formation of particle bonds.
In addition, the profile of the effective friction angle ϕ' which has been obtained applying empirical correlations for DMT data, was compared to ϕ' derived from the triaxial test (see Figure 5.19(b)). The following correlations were used for parameter profiling:

- OCR: Eq.(3.86) with the exponent value for low plastic materials equal to 1.67,
- K_0: Eq.(3.95) with the exponent value for low plastic materials equal to 0.64,
- E_{ur}: Eq.(3.25),
- ϕ': upper bound Eq.(3.32), lower bound Eq.(3.33), and the mean value as the average of both.

While the profile ϕ' derived from DMT was used to verify the values obtained with triaxial tests, OCR and K_0 profiles assumed in the model were directly interpreted from *in situ* data. As regards OCR, the variable profile which is illustrated in Figure 5.20(a) was obtained based on the effective vertical stress by applying preoverburden pressure q^{POP}, see Figure 5.20(b):

$$\sigma_y^{\mathrm{'SR}} = \sigma'_{vc} = \sigma'_{v0} + q^{\mathrm{POP}} \qquad \text{cf. Eq.(2.28a)}$$

and

$$\mathrm{OCR} = \sigma'_{vc}/\sigma'_{v0}$$

where:
σ'_{vc} - preconsolidation pressure
σ'_{v0} - effective vertical stress

Clearly, the stress history (soil overconsolidation) could be also obtained by applying and removing a surcharge before the installation of the footing. However, such manipulation leaves behind a strain history. Typically, a strain history in natural deposits may be erased relatively fast due to stress relaxation and soil aging effects such as cementing of soil particles. Therefore, most boundary value problems should be started from zero initial strains which is a default setting in ZSoil® . Applying the stress history through q^{POP} option allows the user to account for the overconsolidation effect (variable OCR typically observed at superficial layers of subsoil) with zero strains at the beginning of the analysis.
As regards K_0, the profile assumed in the model was obtained by fitting DMT interpretation, as shown in Figure 5.22.

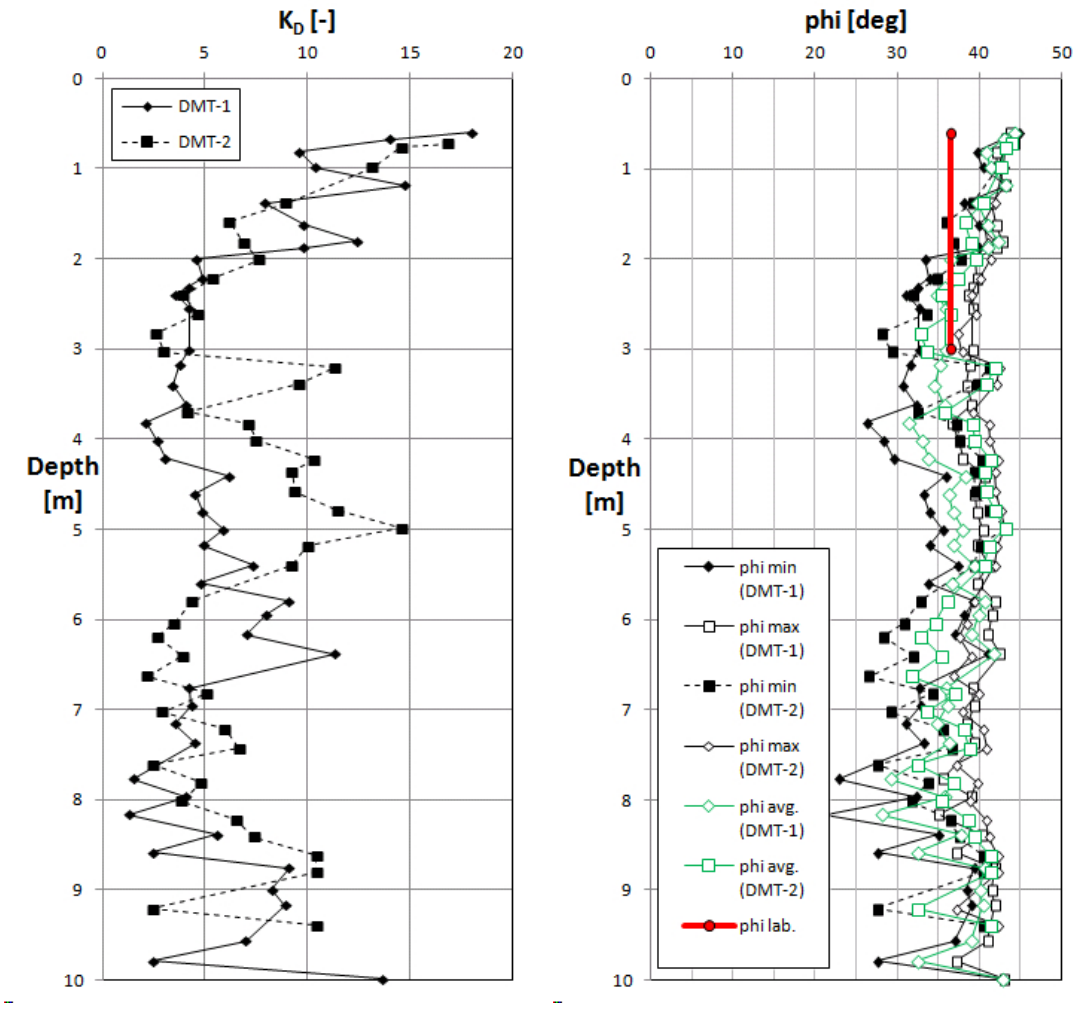

Figure 5.19: Interpretation of dilatometer test data: a) profile of horizontal stress index K_D, b) DMT-based profiling of the effective friction angle compared to ϕ' derived from the triaxial test

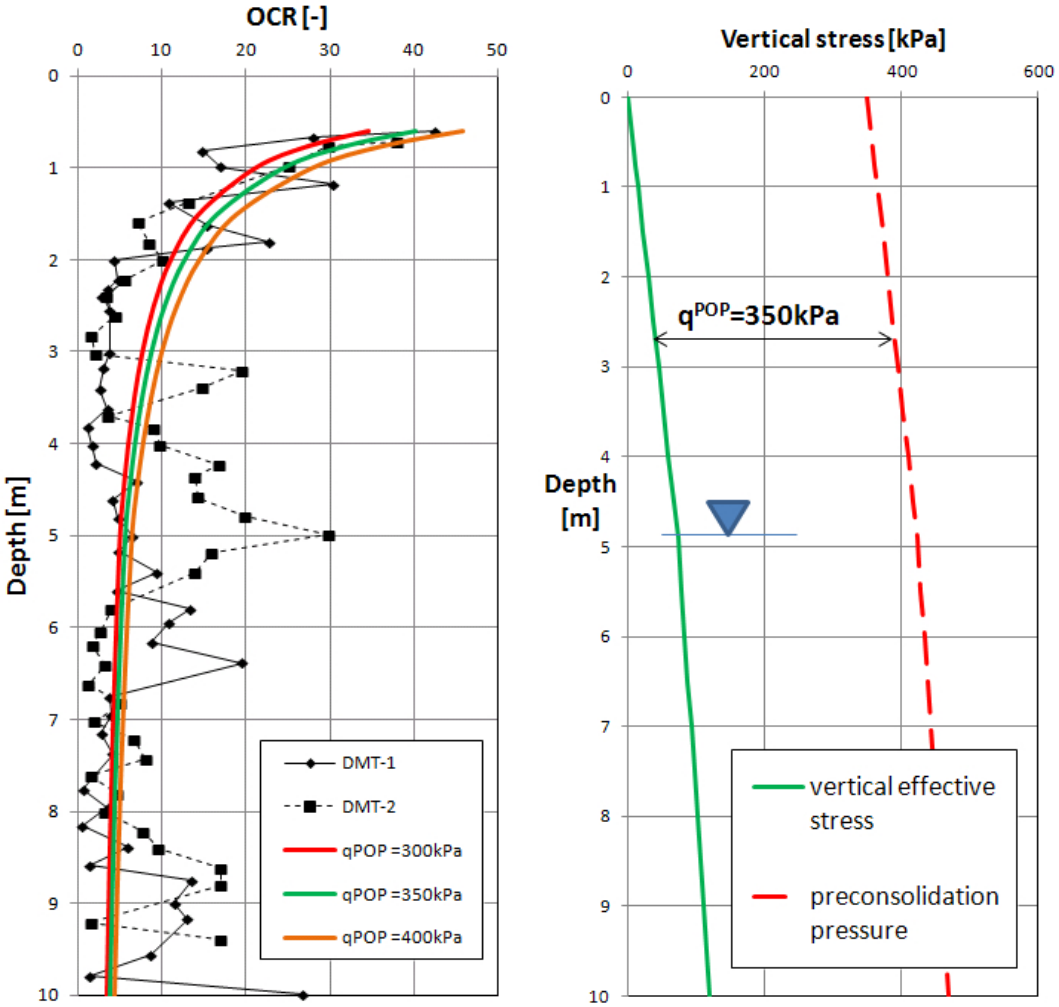

Figure 5.20: Initial stress state profiling: a) OCR profile derived from DMT data and OCR profiles by applying different q^{POP} (in the reference simulation $q^{\mathrm{POP}} = 350$kPa has been considered), b) the vertical effective stress and the preconsolidation stress profiles assumed in the analysis.

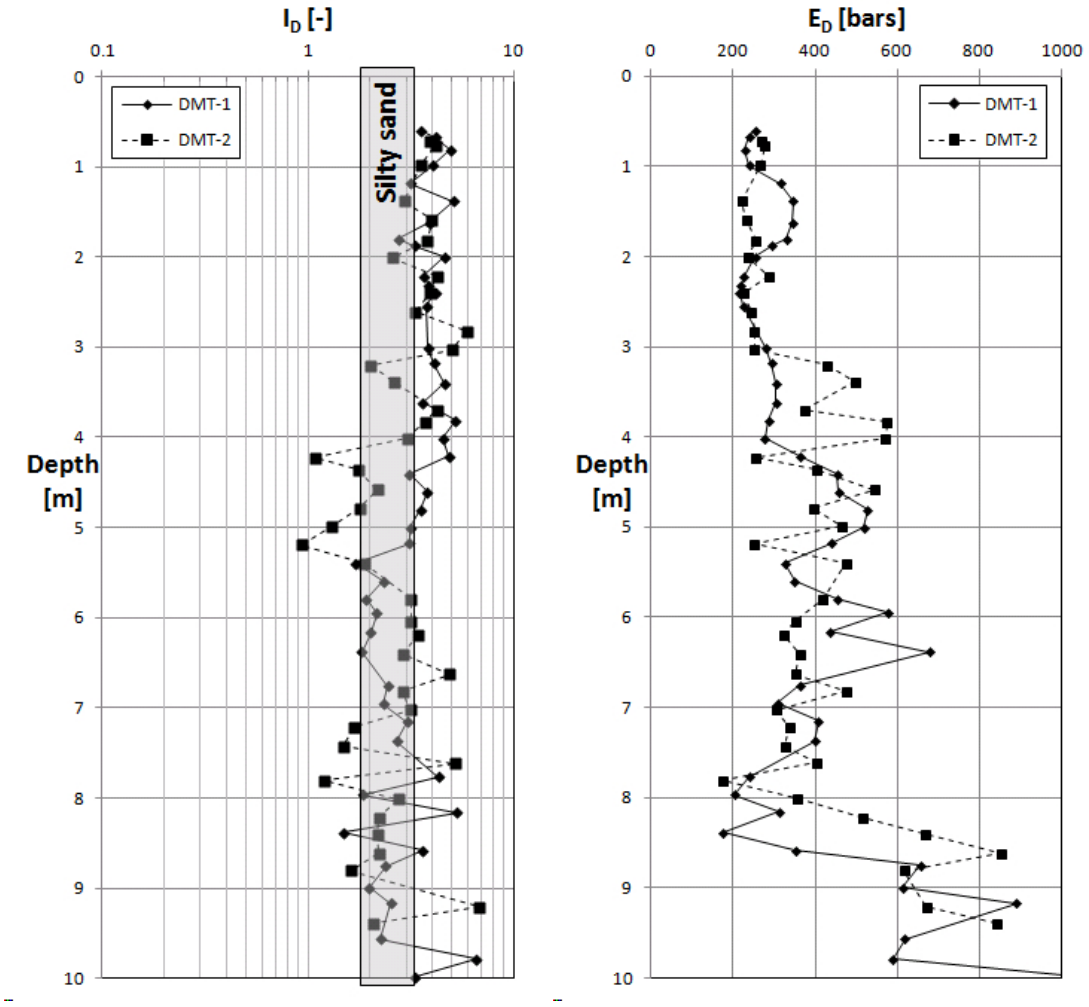

Figure 5.21: Dilatometer test data: a) profile of material index I_D, b) profile of dilatometer modulus E_D (both profiles have been used to determine E_{ur} profile based on an empirical solution given in Eq.3.25).

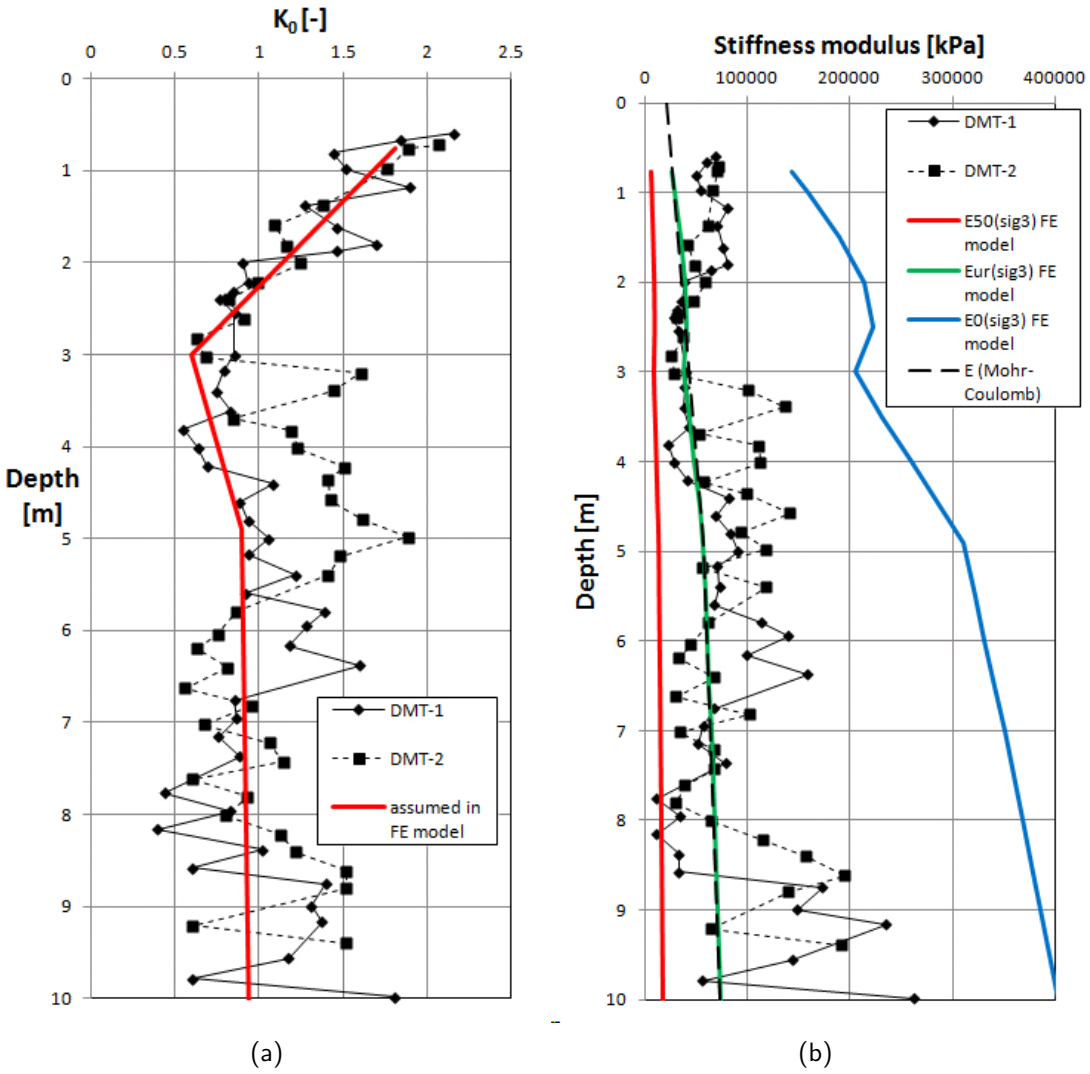

Figure 5.22: Profiles interpreted from DMT data and assumed profiles for in FE model: a) coefficient K_0, b) stiffness modulus interpreted from DMT data, stiffness moduli assumed for HS-small/HS-Brick (E_{50}, E_{ur} and E_0) and the Young modulus E assumed for the Mohr-Coulomb model.

Material data. Material data which was assumed for numerical simulation of footing test loading are summarized in Table 5.9.

- *Physical properties* - taken from the original report (Briaud and Gibbens, 1997)
- *Small strain properties* - evaluated from the resonant column tests
- *Deformation characteristics* - E_{50} derived from triaxial compression test data, and E_{ur} double-checked with DMT data
- *Strength characteristics* - derived from triaxial compression test data
- *Initial state variables* - evaluated from DMT data

Table 5.9: Model parameters used in simulations of the spread footing at Texas site.

Parameter symbol	Unit	Hardening-Soil		Mohr-Coulomb
		Sand (triaxial test)	Sand (in situ simulation)	Sand (in situ simulation)
Physical properties				
γ_D	[kN/m^3]	-	14.9	14.9
e_0	[-]	0.75	0.75	0.75
γ'	[kN/m^3]	-	9.2	9.2
e_{max}	[-]	0.91	0.91	0.91
Small strain properties				
E_0	[kPa]	260000	380000	-
$\gamma_{0.7}$	[kN/m^3]	0.0002	0.00045	-
Deformation characteristics				
E_{ur}	[kPa]	70000	70000	imposed profile for E: Fig.5.22(b)
E_{50}	[kPa]	16000	16000	-
σ_{ref}	[kPa]	100	100	-
ν	[-]	0.2	0.25	0.3
m	[-]	0.51	0.51	-
Strength characteristics				
ϕ	[^{o}]	36.5	36.5	36.5
c	[kPa]	3	3	3
ψ	[^{o}]	1.3	1.3	1.3
R_f	[-]	0.92	0.92	-
Oedometric test characteristics				
K_0^{NC}	[-]	0.41	0.41	-
E_{oed}	[kPa]	20000	16000	-
$\sigma_{\text{oed}}^{\text{ref}}$	[kPa]	100	247	-
Initial state variables				
q^{POP}	[kPa]	-	350	-
p_{c0}	[kPa]	250	-	-
K_0 (in situ)	[-]	1	variable	variable
K_0^{SR}	[-]	1	0.41	-

Numerical simulation of the footing problem. A 3D model of the footing problem which is shown in Figure 5.23 was considered in the analysis. The 3D mesh can represent a quarter of the real setup thanks to the two symmetry planes. The mesh includes:

- simplified stratigraphy of the subsoil deposits consisting of one sand layer; mesh dimension 19.8m×19.8m×17m
- quarter of 3x3m footing which is embedded in the soil at 0.76m and its thickness is equal to 1.22m
- interface between footing faces and soil
- external displacement boundary conditions (BC) (box type)
- pressure BCs which are applied via fluid head and set up along the external boundaries; ground water level is set to 4.9m below soil surface
- nodal force representing a hydraulic jack (due to two symmetry planes the applied nodal is equal to $0.25 \times F$

In addition, Figure 5.24 illustrates how to impose a variable profile of K_0 by means of the INITIAL STRESSES option. Note that an existence function is attributed to the superelements describing the initial stresses. It means that the effect of imposed initial stress applies only to the first analysis step, i.e. during the generation of the initial state. This intervention is needed to avoid imposing soil's initial stress onto the material which replaces excavated soil.

Analysis details

- analysis type: 3D deformation+flow
- driver type: steady state
- constitutive models:
  - ⋆ Sand: four variants: HS-standard, HS-small, HS-Brick, Standard Mohr-Coulomb
  - ⋆ Footing: elastic material $E = 20$GPa, $\nu = 0.2$

The following stages are considered in the model:

1. Generating an initial stress state for an assumed $K_0^{\text{in situ}}$ in sand layer and initial pore pressure BC
2. Installation of the square footing with simultaneous replacement of soil's material in the embedded part of footing
3. Gradual application of test load at the square footing

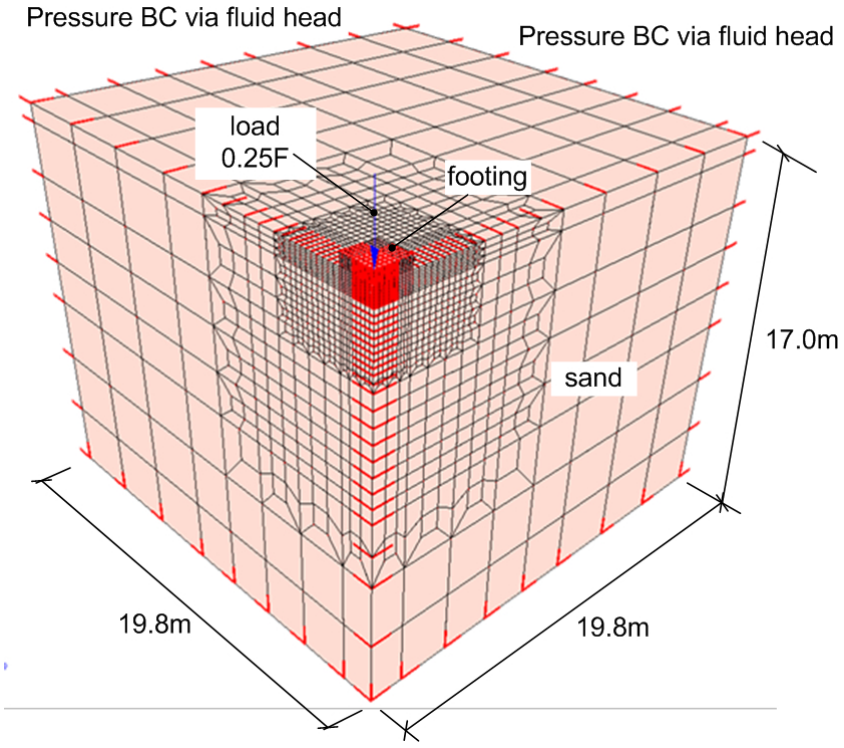

Figure 5.23: 3D mesh representing a quarter of 3x3m footing.

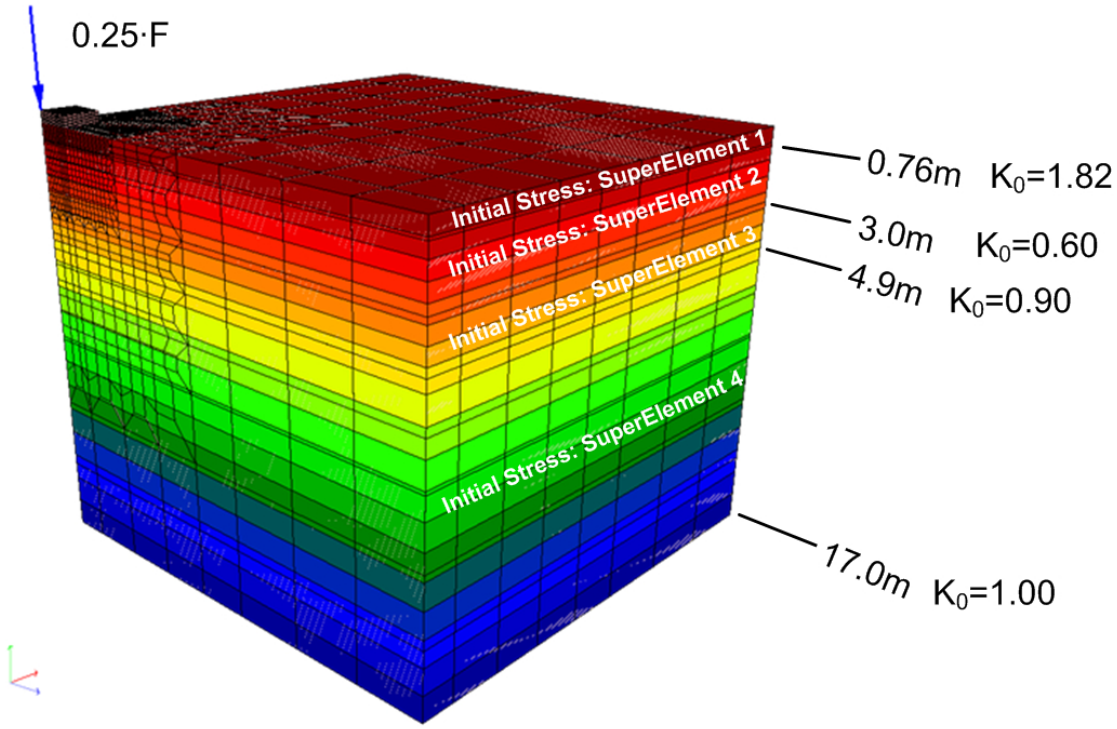

Figure 5.24: Imposing a variable K_0 profile by means of the INITIAL STRESSES option.

Analysis of results. The following paragraph presents the results derived from numerical simulations.

Figure 5.25(a) shows that the HS-small/HS-Brick satisfactorily reproduce the overall load settlement curve. The charts also show that failing to account for small strain stiffness by using the HS-standard model may lead to overestimation of settlements in overconsolidated sand.

Figure 5.25(b) demonstrates the incapability of the standard Mohr-Coulomb model to realistically reproduce the evolution of settlements under mixed loading conditions. In this analysis, an imposed profile of Young modulus E corresponding to E_{ur} has been chosen to describe stiffness of the M-C model (see Figure 5.22(b)).

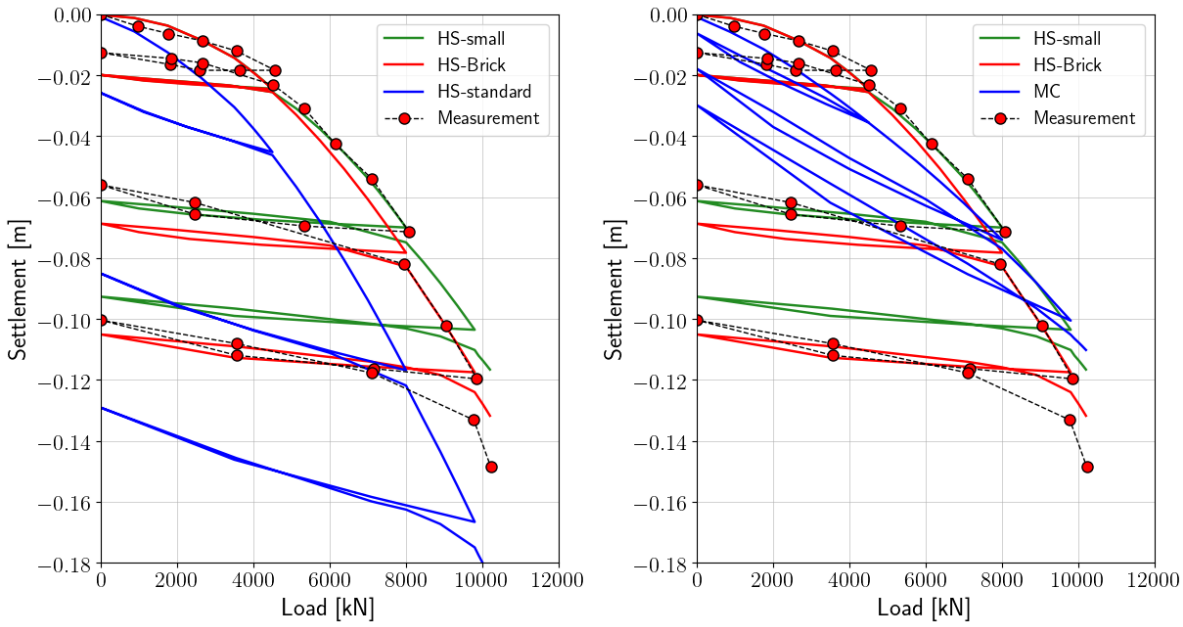

(a) HS-small/HS-Brick vs HS-standard

(b) HS-small/HS-Brick vs Mohr-Coulomb

Figure 5.25: Experimental and computed load-settlement results for 3x3m footing test on sand at A&M site: comparison of models.

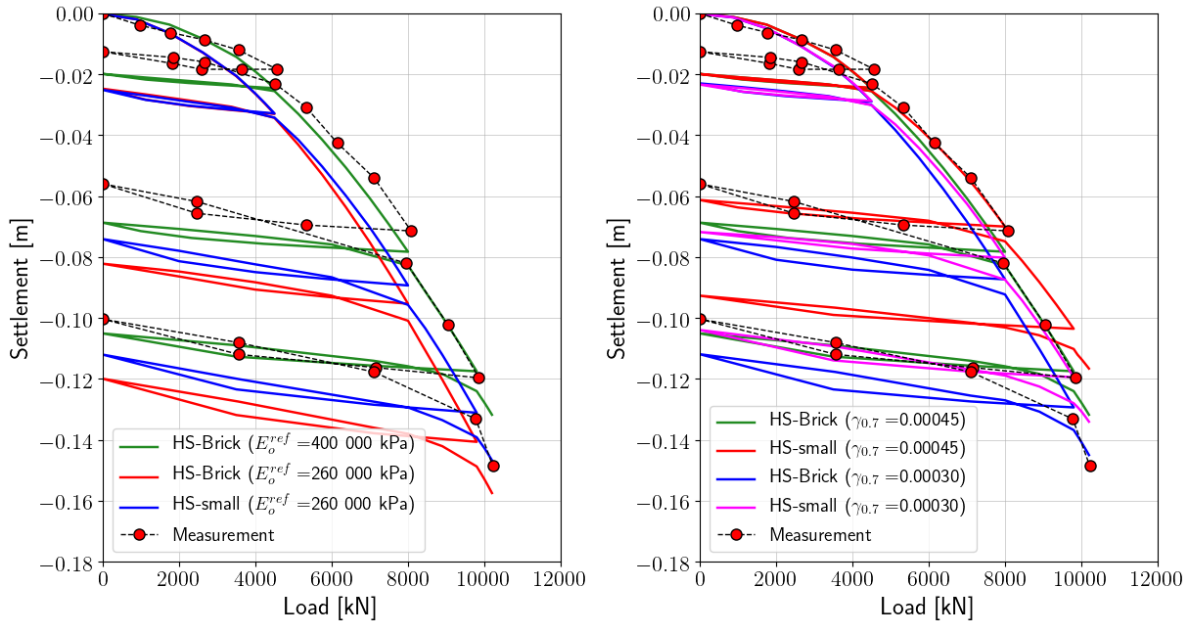

(a) HS-small/HS-Brick: sensitivity to E_0

(b) HS-small/HS-Brick: sensitivity to $\gamma_{0.7}$

Figure 5.26: Experimental and computed load-settlement results for 3x3m footing test on sand at A&M site: sensitivity to small-strain stiffness parameters.

Figure 5.26(a) demonstrates sensitivity of HS-small/HS-Brick to E_0. It can be noticed that underestimating small-strain stiffness may lead to an overestimation of settlements, affecting especially the initial part of the load-settlement curve.

Figure 5.26(b) illustrates the sensitivity of HS-small/HS-Brick to the small-strain threshold parameter $\gamma_{0.7}$. It can be noticed that the lower value of this parameter allows an earlier degradation of small-strain stiffness.

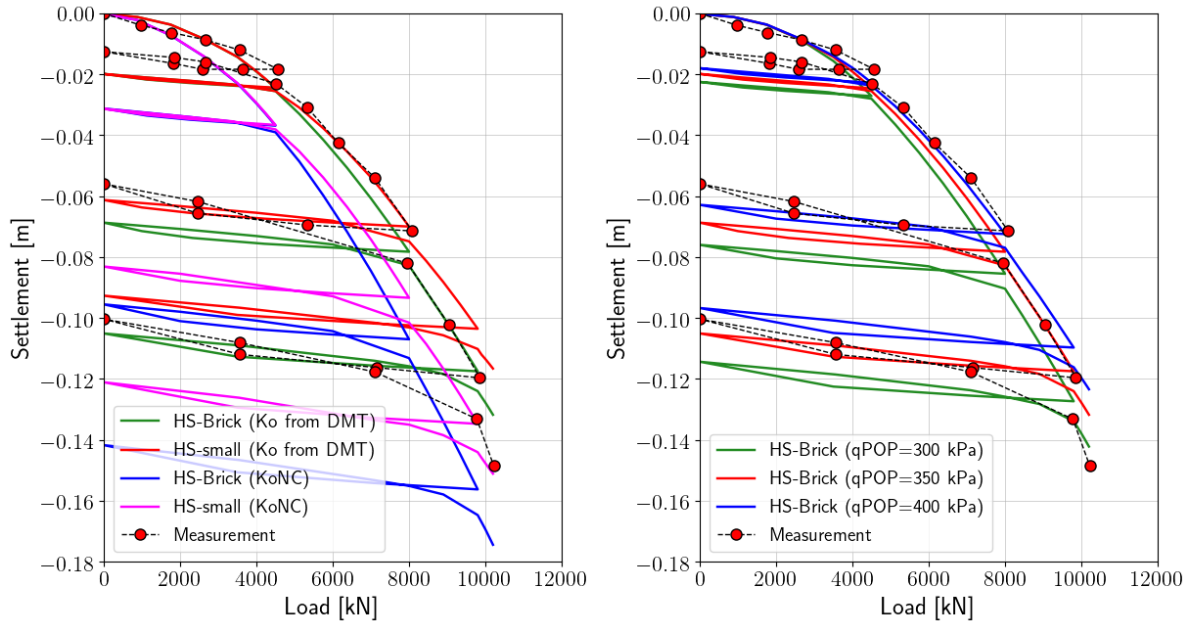

(a) HS-small/HS-Brick: sensitivity to the initial stress setup

(b) HS-Brick: sensitivity to q^{POP}

Figure 5.27: Experimental and computed load-settlement results for 3x3m footing test on sand at A&M site: sensitivity to the initial stress setup.

Figure 5.27(a) illustrates the sensitivity of numerical predictions to the initial setup of the coefficient of earth pressure "at rest". In the reference simulation, the profile of K_0 for over-consolidated soil has been evaluated by means of the Marchetti's dilatometer test (DMT), whereas in the second simulation a constant profile of K_0 equal to $K_0^{\mathrm{NC}} = 1 - \sin(\phi)$ has been assumed. This analysis reveals slightly larger settlements for $K_0^{\mathrm{NC}} = 0.41$ which is attributed to lower initial soil stiffness. Note that soil stiffness in the HS model depends on the minor effective stress so in the case where $K_0 = K_0^{\mathrm{NC}}$ the initial stiffness is defined by σ'_{h0}, whereas for the reference simulation, the initial soil stiffness is defined by σ'_{v0} up to around 2.2m as $K_0 > 1$. The user should be aware that soil stiffness in the HS model evolves during simulation with amplitudes of stress level.

Finally, Figure 5.27(b) reveals the sensitivity of a numerical simulation to the initial preconsolidation setup. The chart presents numerical predictions for three q^{POP} values: 350kPa (reference simulation), 300kPa and 400kPa. The sensitivity of the OCR profile to the specified values of q^{POP} is presented in Figure 5.20(a).

Appendix A

Determination of undrained shear strength

A.1 Non-uniqueness of undrained shear strength

It has been widely recognized that the *in situ* behavior of soils may be significantly different from that of laboratory samples. This can be mainly attributed to the quality of the intact specimens which may depend on drilling and sampling methods and sample geometry (DeGroot and Sandven, 2004). The disturbance of samples may increase during their insertion into a sampling tube, transportation, relaxation of stresses, drying, temperature changes, trimming and, finally, their installation in the testing cells, etc. (Hight et al., 1992). Different sampling devices such as piston samplers, thin walled tubes or downhole block samplers can provide specimens for which different magnitudes of preconsolidation pressure or undrained shear strength s_{u} are measured (e.g. Hight et al., 1992; Tanaka and Tanaka, 1999). Experience shows that sample disturbance may lead to underestimation of the apparent preconsolidation pressure or undrained shear strength (Karlsrud, 1999; Fioravante, 2004).
Inconsistencies in s_{u} values measured by laboratory and field tests may also stem from the non-uniqueness of this property. The undrained shear strength s_{u} is not a unique soil parameter (Wroth, 1984; Jamiolkowski et al., 1985), as it depends on the type of test, which involves particular strain paths (cf. Figure 1.1).

The differences in interpreted results also stems from the time-dependent behavior of soils (e.g. Vaid and Campanella, 1977; Leroueil, 1988; Sheahan et al., 1996; Penumadu et al., 1998). The undrained shear strength increases linearly with the logarithm of the shear strain (Bjerrum, 1972; Nakase and Kamei, 1986). For instance, the testing speed for SBPT or CPTU can be one or more orders of magnitude greater than that used in the triaxial compression test TC ($\dot{\varepsilon} = 0.01\%/\mathrm{min}$), see Figure 1.2. Laboratory tests with the use of a model pressuremeter in clays have revealed an increase of s_{u} of about 10% for every tenfold increase of strain rate (Prapaharan et al., 1989). While the overstimation of s_{u} derived from pressuremeter test due to the strain rate effect can be reasonably small, in the order of 10-20%, the differences for CPTU can be much larger. The extrapolated results of Bjerrum (1972) (Figure 1.2) can indicate that neglecting the strain effect in the analysis of penetration may lead to the considerable overestimation of s_{u} of about 40% with respect to the value obtained for the conventional triaxial compression. Since the undrained shear strength is a function of the stress history, the similar effects can be observed for the derived values of preconsolidation pressure σ'_p. The study carried out by Leroueil et al. (1983b) revealed the increase of

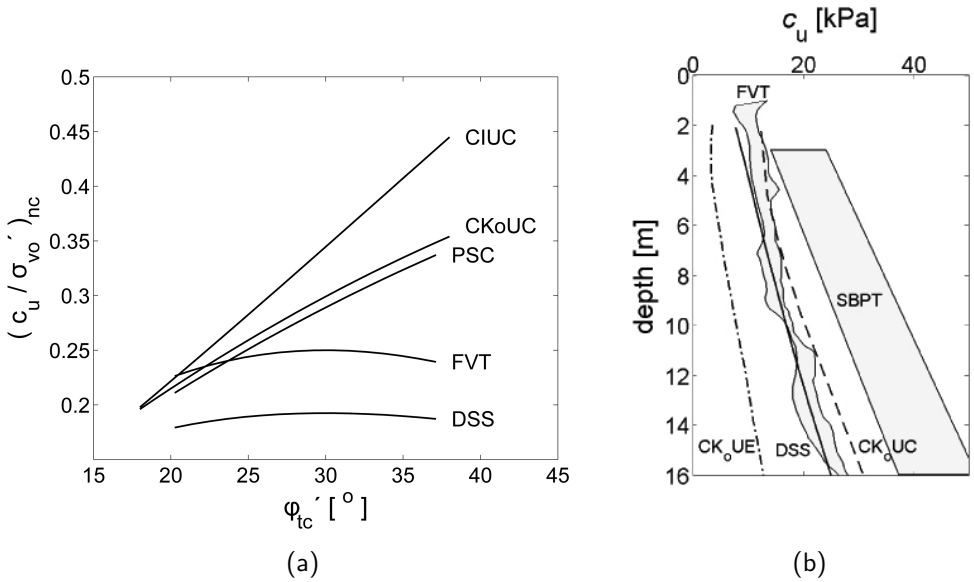

Figure 1.1: Undrained shear strength in normally consolidated soil (a) as a function of shear modes for various tests: triaxial undrained compression tests (CIUC and $\mathrm{CK_0UC}$), plain strain compression test (PSC), direct simple shear test (DSS) and field vane test (FVT) (after Wroth, 1984), (b) profiles for field and laboratory tests on Onsøy clay (from Lacasse et al., 1981).

.

about 10-14% for σ_p' per log cycle of volumetric strain rate $\dot{\varepsilon}_\mathrm{v}$ in the constant rate of strain oedometer test (CRS).

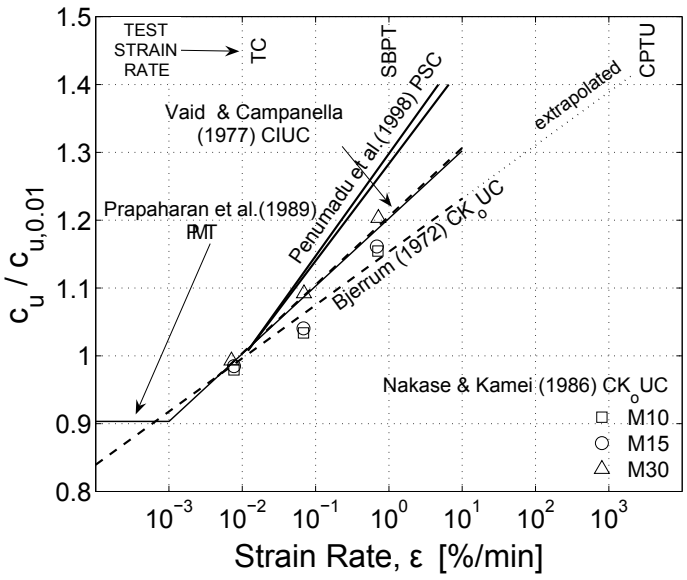

Figure 1.2: The strain rate effect on undrained shear strength s_u for different shear modes and a schematic comparison of test strain rates for triaxial compression (TC), self-boring pressuremeter (SBPT) and piezocone (CPTU).

A.2 Determination of s_u from field tests

FVT. The interpretation of s_u from the standardly used field vane test (see Figure 1.3) can be carried out with the conventional formula:

$$s_u = \frac{6M}{7\pi D^3} = 0.2728\frac{M}{D^3} \tag{1.1}$$

in which M is the maximum recorded torque, and D is the diameter of vane.
Since the values of s_u obtained with the above equation can be too conservative, Chandler (1988) suggested increasing the factor 0.2728 to 0.2897.

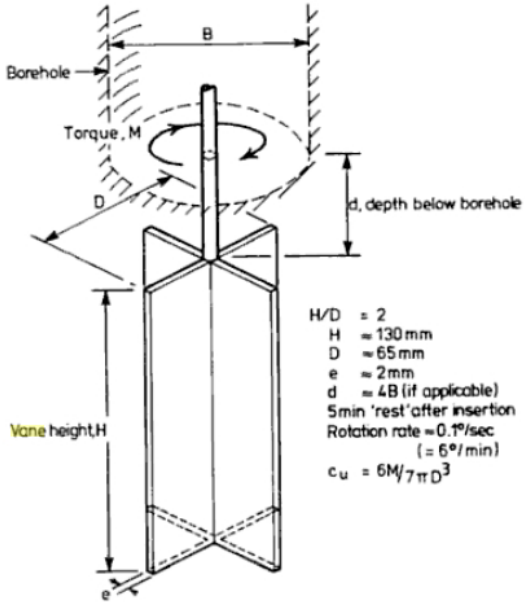

Figure 1.3: Standard dimensions of the most commonly used field vane test (from Chandler, 1988).

DMT. The values of s_u can be correlated with the Marchetti's dilatometer data through the original formula suggested by Marchetti (1980):

$$s_u = 0.22\sigma'_{v0}(0.5K_D)^{1.25} \tag{1.2}$$

where K_D is the horizontal stress index which is calculated based on the first dilatometer reading p_0 ($K_D = (p_0 - u_0)/\sigma'_{v0}$).

Appendix B

Estimation of compression index

Table B.1: Some correlation equations for estimating consolidation parameters (after Holtz et al., 1986; Bowles, 1997; Kempfert, 2006).

Compression index	Applicability	Reference
$C_c = 0.009(w_L - 10)$	Normally consolidated clays of low to medium sensitivity and $w_L < 100$($\pm 30\%$ error)	Terzaghi and Peck (1967)
$C_c = 0.141 G_s(\gamma_{\mathrm{SAT}}/\gamma_D)$	All clays	Rendon-Herrero (1983)
$C_c = 0.141 G_s^{1.2}[(1+e_0)/G_s]^{2.38}$	All clays (94 data points)	Rendon-Herrero (1983)
$C_c = 1.15(e_0 - 0.35)$	All clays, uniformly packed	Nishida (1956)
$C_c = 1.15(e - 0.91)$	All clays, loosely packed $e > 0.9$	Nishida (1956)
$C_c = 0.009 w_n + 0.005 w_L$	All clays	Koppula (1986)
$C_c = 0.00234 w_L G_s$	All inorganic clays	Nagaraj and Murthy (1985)
$C_c = 0.37(e_0 + 0.003 w_L + 0.0004 w_n - 0.34)$	678 data points	Azzouz et al. (1976)
$C_c = 0.00917(w_L - 13)$	56 data points	Mayne (1980)
$C_c = -0.156 + 0.411 e + 0.00058 w_L$	72 data points	Al-Khafaji and Andersland (1992)
$C_c = 0.156 e + 0.0107$	Remoulded all clays	Azzouz et al. (1976)
$C_c = 0.208 e + 0.0083$	Chicago clays	Azzouz et al. (1976)
$C_c = 0.007(w_L - 10)$	Remoulded clays	Skempton (1944)
$C_c = 0.007(w_L - 7)$	Remoulded clays	Azzouz et al. (1976)
$C_c = 0.005 G_s I_P$	Remoulded clays	Wroth and Wood (1978)
$C_c = 0.5(I_P/100) G_s$	Remoulded clays	Wroth and Wood (1978)
$C_c = 0.046 + 0.0104 I_P$	Best for $I_P < 50\%$	Nakase (1988)
$C_c = 1.15 e$	Deformable but incompressible soil	Nishida (1956)
$C_c = 0.0115 w_n$	Organic soils - meadow mats, peats, and organic silt and clay	Azzouz et al. (1976)
$C_c = 0.75(e_0 - 0.50)$	Soils with low plasticity	Azzouz et al. (1976)
$C_c = 0.30(e_0 - 0.27)$	Inorganic silty sand-silty clay	Hough (1969)
$C_c = \mathrm{PI}/74$	Data from different soils	Kulhawy and Mayne (1990)

$C_c = 0.0093 w_n$	Chicago clays and Alberta Province in Canada (109 data points)	Koppula (1981)
$C_c = 17.66/100000 w_n^2 + 0.00593 w_n - 0.135$	Chicago clays	Azzouz et al. (1976)
$C_c = 0.015(w_n - 8)$	Soils in Taipei	Moh et al. (1989)
$C_c = 0.54(e - 0.23)$	Soils in Taipei	Moh et al. (1989)
$C_c = 0.0046(w_L - 9)$	Brazilian clays	Azzouz et al. (1976)
$C_c = 1.21 + 1.005(e - 1.87)$	Motley clays from Sao Paulo	Azzouz et al. (1976)
$C_c = 0.0037(w_L + 25.5)$	Cincinnati and Northern Kentucky	Dayal (2006)
$C_c = 0.0135 w_n - 0.1169$	Cincinnati and Northern Kentucky	Dayal (2006)
$C_c = 0.0042 I_P + 0.165$	Cincinnati and Northern Kentucky	Dayal (2006)
$C_c = 0.46e - 0.049 G_s + 0.0023$	Cincinnati and Northern Kentucky	Dayal (2006)
$C_c = 0.4965e - 0.0014 w_n - 0.123$	Cincinnati and Northern Kentucky	Dayal (2006)
$C_c = -0.247e + 0.004 w_L + 0.01 w_n + 0.021$	Cincinnati and Northern Kentucky	Dayal (2006)
$C_c = 0.0018/(1 - 0.0109n)$	Remoulded clays in Japan (Ariake)	Park and Koumoto (2004)
$C_c = 0.00269/(1 - 0.0115n)$	Undisturbed clays in Japan (Ariake)	Park and Koumoto (2004)
$C_c = 0.02 + 0.014 I_P$	North Atlantic clays	Nacci et al. (1975)
$C_c = 0.02 + 0.014 I_P$	North Atlantic clays	Nacci et al. (1975)
$C_c = 0.011(w_L - 6.36)$	East coast of Korea	Yoon et al. (2004)
$C_c = 0.01(w_n + 2.83)$	East coast of Korea	Yoon et al. (2004)
$C_c = 0.39(e - 0.13)$	East coast of Korea	Yoon et al. (2004)
$C_c = -0.16\gamma_D + 2.4$	East coast of Korea	Yoon et al. (2004)
$C_c = 0.0098 w_n + 0.194e - 0.0025 I_P - 0.256$	East coast of Korea	Yoon et al. (2004)
$C_c = 0.012(w_L + 16.4)$	South coast of Korea	Yoon et al. (2004)
$C_c = 0.013(w_n - 3.85)$	South coast of Korea	Yoon et al. (2004)
$C_c = 0.54(e - 0.37)$	South coast of Korea	Yoon et al. (2004)
$C_c = -0.0003 w_n + 0.538e + 0.002 w_L - 0.3$	South coast of Korea	Yoon et al. (2004)
$C_c = 0.165 + 0.01 I_P$	South coast of Korea	Yoon et al. (2004)
$C_c = 0.01(w_L - 10.9)$	West coast of Korea	Yoon et al. (2004)
$C_c = 0.011(w_n - 11.22)$	West coast of Korea	Yoon et al. (2004)
$C_c = 0.37(e - 0.28)$	West coast of Korea	Yoon et al. (2004)
$C_c = -0.066\gamma_D + 1.15$	West coast of Korea	Yoon et al. (2004)
$C_c = 0.0038 w_n + 0.12e + 0.0065 w_L - 0.248$	West coast of Korea	Yoon et al. (2004)

Table B.2: Some correlation equations for estimating recompression index (after Holtz et al., 1986; Bowles, 1997; Kempfert, 2006).

Recompression index	Regions of applicability	Reference
$C_s = 0.000463 w_L G_s$		Nagaraj and Murthy (1985)
$C_s = 0.00194(\text{PI} - 4.6)$	Best for PI$< 50\%$	Nakase (1988)
$C_s = \text{PI}/370$	Data from different soils	Kulhawy and Mayne (1990)
C_r/C_c is observed between 0.05 and 0.5, with typical values between 0.1-0.25 and the average 0.2 (cf. Mayne, 1980, 2007; Kempfert, 2006); lower values are observed for cemented soils		

PI - plastic index in [%], w_L - liquid limit in [%], w_n natural water content in [%] .

Appendix C

Estimation of shear wave velocity

Table C.1: Typical values of shear wave velocity and density for different geomaterials (after Lavergne, 1986).

	Shear wave velocity V_s [m/s]		Dry unit weight γ [g/cm^3]	
Soil type	Min	Max	Min	Max
Screes, organic topsoil	100	300	1.7	2.4
Dry sands	100	500	1.5	1.7
Wet sands	400	1200	1.9	2.1
Clays	200	800	2.0	2.4
Marls	750	1500	2.1	2.6
Sandstones	1200	2800	2.1	2.4
Lime stones	2000	3300	2.4	2.7
Chalk	1100	1300	1.8	2.3
Salt	2500	3100	2.1	2.3
Anhydrite	2200	3100	2.9	3.0
Dolomite	1900	3600	2.5	2.9
Granite	2500	3300	2.5	2.7
Basalte	2800	3400	2.7	3.1
Carbon	1000	1400	1.3	1.8
Ice	1700	1900	0.9	0.9

Table C.2: Typical values of shear wave velocity for different geomaterials (after FOWG, 2003).

	Shear wave velocity V_s [m/s]	
Soil type	Min	Max
Top soil layers (3 to 6m), lightly compact., desagregated, unsat.	110	480
Ballast (gravelly or sandy), unsaturated	220	450
Ballast, saturated	400	600
Ballast cemented	1000	1500
Silt from the lake bottom, not completely saturated	290	540
Silt from the lake bottom, saturated	390	530
Silt at banks, unsaturated	120	400
Moraine	500	1150
Loess	150	300
Marl and mollase sandstone, soft, desagregated	520	1050
Marl , not desagregated	1000	1900
Sandstone, hard	1100	2200
Molasse at plateau	600	2500
Schist	1100	3100
Limestone	1800	3700
Gneiss	1900	3500
Granite	2500	3900

Table C.3: Typical values of shear wave velocity for different geomaterials (after Lindeburg, 2001).

	Shear wave velocity V_s [m/s]	
Soil type	Min	Max
Hard rocks	>1400	
Firm to hard rocks	700	1400
Gravelly soils and soft to firm rocks	375	700
Stiff clays and sandy soils	200	375
Soft soils	100	200
Very soft soils	50	100

Table C.4: Typical values of shear wave velocity for different geomaterials (after NAVFAC, 1986).

	Shear wave velocity V_s [m/s]	
Soil type	Min	Max
Hard rock	1500	
Rock	760	1500
Very dense soil and soft rock ($N_{60} > 50$, $s_u > 100$kPa)	360	760
Stiff soil ($15 > N_{60} < 50$, $50 < s_u < 100$kPa)	180	360
Soft soil ($N_{60} < 15$, $s_u < 50$kPa)		180
Any soil with PI> 20%,w> 40%, $s_u < 25$kPa	site eveluation	

SPT. Most published correlations for SPT are based on uncorrected N-values. These correlations are given in:

- for all soil types: Table C.5 (insight prrovided in 3.1),
- for sands: Table C.6 (Figure 3.2),
- for silts: Table C.7 (Figure 3.3),
- for clays: Table C.8 (Figure 3.4).

Table C.5: SPT-Based correlations for **all type of soils**.

Reference	Country	Soil Type	Equation	Correlation coefficient
Ohba & Toriumi (1970)[1]	Japan	Alluvium	$V_s = 84N_{60}^{0.31}$	–
Fujiwara (1972)[2]	Japan	–	$V_s = 92.1N_{60}^{0.337}$	–
Ohsaki & Iwasaki (1973)[1]	Japan	–	$V_s = 81.3N_{60}^{0.39}$	0.886
Imai and Yoshimura (1975)	Japan	–	$V_s = 76N_{60}^{0.333}$	–
Imai (1977)[2]	Japan	Quaternary and Pleistocene Alluvium	$V_s = 91N_{60}^{0.337}$	–
Ohta and Goto (1978)	Japan	Quaternary and Pleistocene Alluvium	$V_s = 85.34N_{60}^{0.348}$	0.719
Imai & Tonouchi (1982)[1]	Japan	–	$V_s = 97N_{60}^{0.314}$	0.868
Seed et al. (1983)	–	–	$V_s = 56N_{60}^{0.5}$	–
Jinan (1987)	Shanghai	Soft Holocene Deposits	$V_s = 116.1(N_{60} + 0.3185)^{0.202}$	0.7
Athanasopoulos (1995)	Greece	–	$V_s = 107.6N_{60}^{0.36}$	–
Sisman (1995)[2]	–	–	$V_s = 32.8N_{60}^{0.51}$	–
Iyisan (1996)[2]	–	–	$V_s = 51.5N_{60}^{0.516}$	–
Kiku *et al.* (2001)[2]	Turkey	–	$V_s = 68.3N_{60}^{0.292}$	–
Hasancebi and Ulusay (2007)	Turkey	Quaternary Alluvium and Detritus	$V_s = 90N_{60}^{0.308}$	0.73

[1] Referenced by Sykora (1987)
[2] Referenced by Hasancebi and Ulusay (2007)

Table C.6: SPT-Based correlations for **sands**.

Reference	Country	Soil Type	Equation	Correlation coefficient
Shibata (1970)	–	–	$V_s = 31.7N_{60}^{0.54}$	–
Ohta et al. (1972)	Japan	–	$V_s = 87.2N_{60}^{0.36}$	–
Imai (1977)[2]	Japan	Quaternary and Pleistocene Alluvium	$V_s = 80.6N_{60}^{0.331}$	–
Ohta & Goto (1978b)[1]	Japan	Quaternary and Pleistocene Alluvium	$V_s = 88.4N_{60}^{0.333}$	0.719
Imai & Tonouchi (1982)[1]	Japan	Quaternary and Pleistocene Alluvium	$V_s = 87.8N_{60}^{0.314}$	0.69
Sykora & Stokoe (1983)[1]	–	–	$V_s = 100.5N_{60}^{0.29}$	0.84
Okamoto et al. (1989)	Japan	–	$V_s = 125N_{60}^{0.3}$	–
Lee (1990)	Taiwan	–	$V_s = 57.4N_{60}^{0.49}$	0.62
Lee (1992)	Taiwan	–	$V_s = 157.13 + 4.74N_{60}$	0.691
Pitilakis et al. (1999)	Greece	Alluvium	$V_s = 145N_{60}^{0.178}$	0.70
Hasancebi and Ulusay (2007)	Turkey	Quaternary Alluvium and Detritus	$V_s = 90.82N_{60}^{0.319}$	0.65
Dikmen (2009)	Western central Anatolia, Turkey	–	$V_s = 73N_{60}^{0.33}$	–

[1] Referenced by Sykora (1987)
[2] Referenced by Hasancebi and Ulusay (2007)

Table C.7: SPT-Based correlations for **silts**.

Reference	Country	Soil Type	Equation	Correlation coefficient
Lee (1990)	Taiwan	–	$V_s = 105.64N_{60}^{0.32}$	0.73
Lee (1992)	Taiwan	–	$V_s = 103.99(N_{60} + 1)^{0.334}$	0.798
Pitilakis et al. (1999)	Greece	Alluvium	$V_s = 145N_{60}^{0.178}$	0.70
Dikmen (2009)	Western central Anatolia, Turkey	–	$V_s = 60N_{60}^{0.36}$	–

Table C.8: SPT-Based correlations for **clays**.

Reference	Country	Soil Type	Equation	Correlation coefficient
Imai (1977)[2]	Japan	Quaternary and Pleistocene Alluvium	$V_s = 80.2N_{60}^{0.292}$	–
Ohta & Goto (1978b)[1]	Japan	Quaternary and Pleistocene Alluvium	$V_s = 86.9N_{60}^{0.333}$	0.719
Imai & Tonouchi (1982)[1]	Japan	Quaternary and Pleistocene Alluvium	$V_s = 107N_{60}^{0.274}$	0.721
Lee (1990)	Taiwan	–	$V_s = 114.43N_{60}^{0.31}$	0.62
Lee (1992)	Taiwan	–	$V_s = 138.36(N_{60}+1)^{0.242}$	0.695
Athanasopoulos (1995)	Greece		$V_s = 76.55N_{60}^{0.445}$	–
Pitilakis et al. (1999)	Greece	Alluvium	$V_s = 132N_{60}^{0.271}$	0.75
Hasancebi and Ulusay (2007)	Turkey	Quaternary Alluvium and Detritus	$V_s = 97.89N_{60}^{0.269}$	0.75
Dikmen (2009)	Western central Anatolia, Turkey	–	$V_s = 44N_{60}^{0.48}$	–

[1] Referenced by Sykora (1987)
[2] Referenced by Hasancebi and Ulusay (2007)

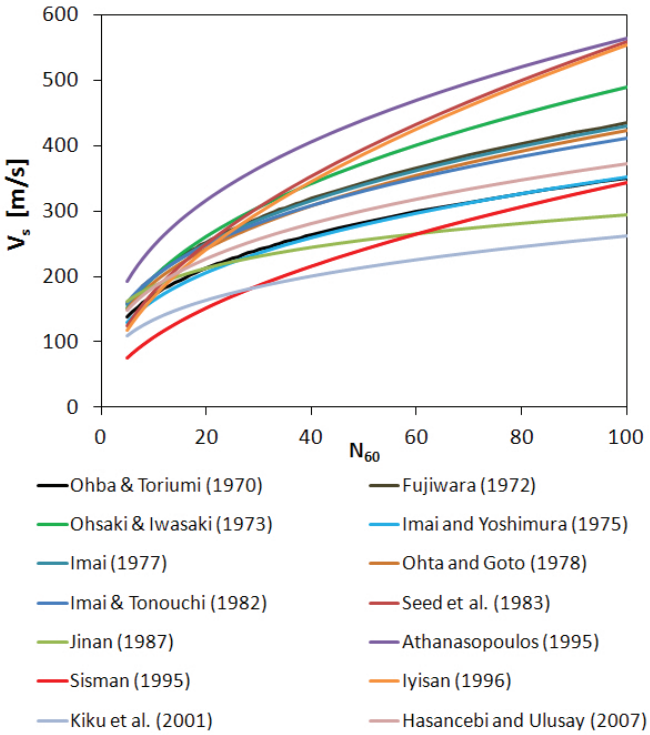

Figure 3.1: Comparison of **"all soil type"**-correlations for estimating V_s from SPT data (correlations are given in Table C.5).

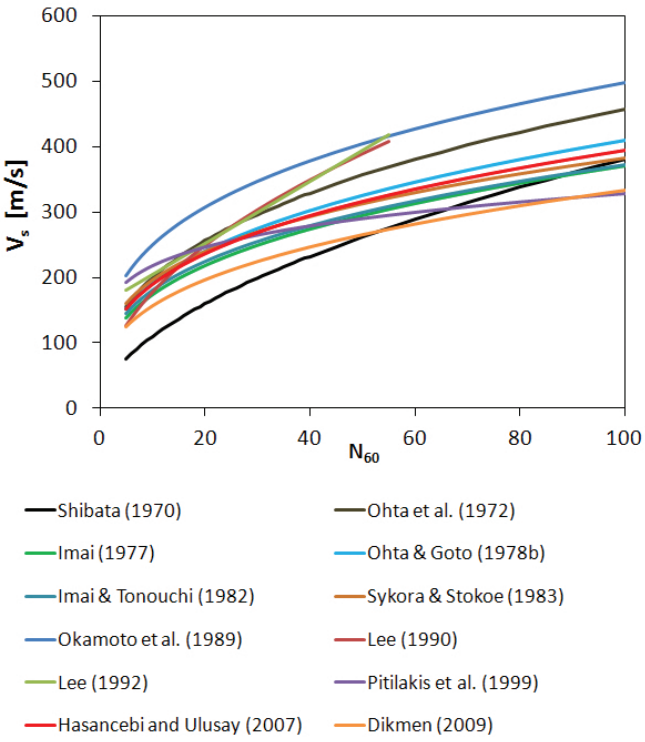

Figure 3.2: Comparison of -correlations for estimating V_s in **sands** from SPT data (correlations are given in Table C.6).

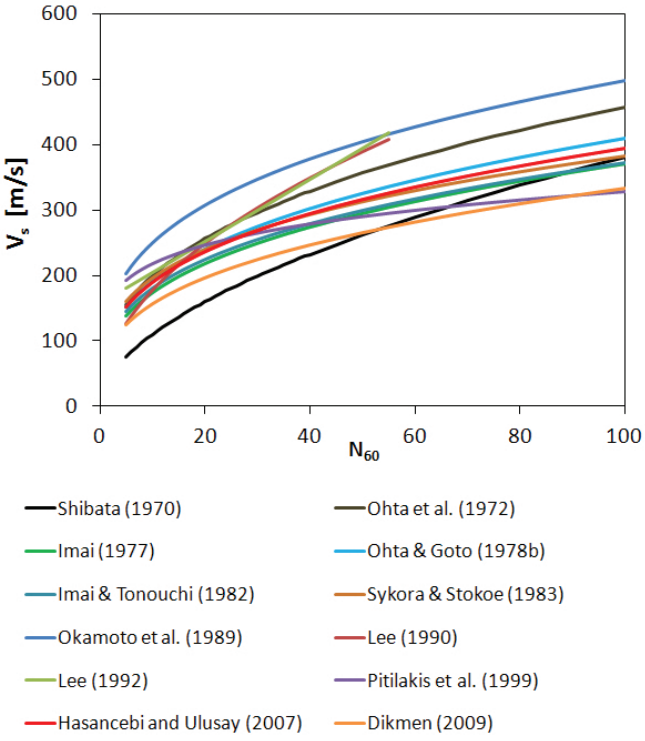

Figure 3.3: Comparison of -correlations for estimating V_s in **silts** from SPT data (correlations are given in Table C.7).

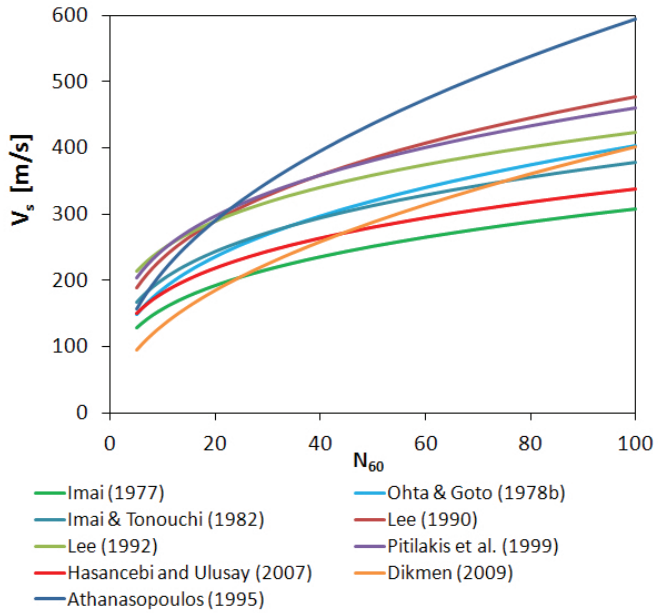

Figure 3.4: Comparison of -correlations for estimating V_s in **clays** from SPT data (correlations are given in Table C.8).

CPT. A number of correlations can be used to estimate shear wave velocity based on CPT data. Correlations were developed for a generic soil types: Table C.9, for sands: Table C.10, for clays: Table C.11. Graphical comparisons of these correlations are presented in Figure for sands

Table C.9: CPT-based correlations for **all soil types**.

Reference	Soil Type	V_s [m/s]	Remarks
Hegazy and Mayne (1995)	sands, silts, clays, mixed soil types	$(10.1 \log q_t - 11.4)^{1.67}(f_s/q_t \cdot 100)^{0.3}$	q_t, f_s in kPa
Mayne (2006a)	saturated clays, silts, and sands	$118.8 \log f_s + 18.5$	f_s in kPa

Table C.10: CPT-based correlations for **sands**.

Reference	Soil Type	V_s [m/s]	Remarks
Baldi et al. (1989)	Giola Taura Sand w/Gravel, Po River sands	$277 q_t^{0.13} \sigma'^{0.27}_{v0}$	q_t, σ'_{v0} in MPa
Hegazy and Mayne (1995)	–	$13.18 q_t^{0.192} \sigma'^{0.179}_{v0}$	q_t, σ'_{v0} in kPa
Hegazy and Mayne (1995)	–	$12.02 q_t^{0.319} f_s^{-0.0466}$	q_t, f_s in kPa

Table C.11: CPT-based correlations for **clays**.

Reference	Soil Type	V_s [m/s]	Remarks
Mayne and Rix (1993)	soft to firm to stiff intact clays to fissured clays, Piedmont silts	$9.44 q_t^{0.435} e_0^{-0.532}$	q_t in kPa
Mayne and Rix (1993)	–	$1.75 q_t^{0.627}$	q_t in kPa, $n = 481, R = 0.86$
Hegazy and Mayne (1995)	–	$14.13 q_t^{0.359} e_0^{-0.473}$	q_t in kPa
Hegazy and Mayne (1995)	–	$3.18 q_t^{0.549} f_s^{0.025}$	q_t, f_s in kPa

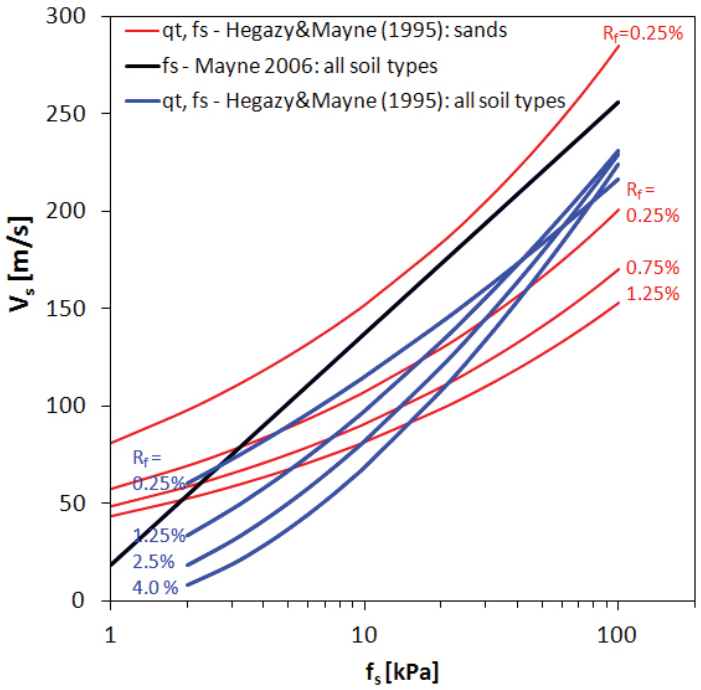

Figure 3.5: Comparison of empirical correlations for estimating V_s from CPT data: q_t and f_s, plotted for different values of friction ratio $R_f = f_s/q_t \times 100$ (correlations are given in Table C.9 and C.10).

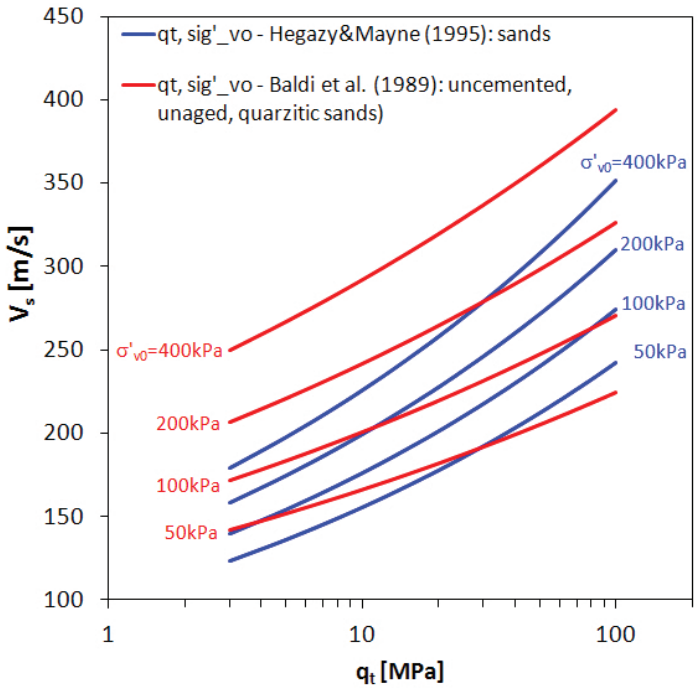

Figure 3.6: Comparison of empirical correlations for estimating V_s in sands from CPT data (correlations are given in Table C.10).

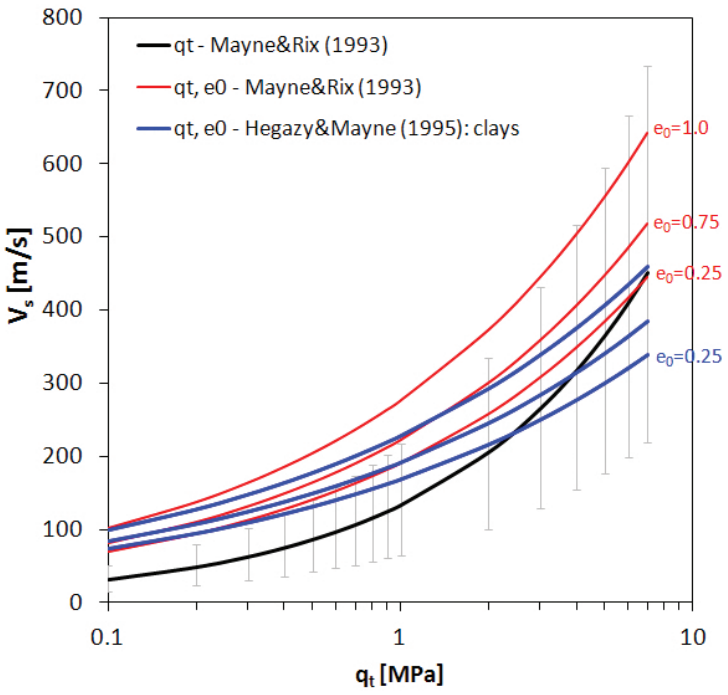

Figure 3.7: Comparison of empirical correlations for estimating V_s in sands from CPT data (correlations are given in Table C.11).

References

Addenbrooke, T., Potts, D., and Puzrin, A. (1997). The influence of pre-failure soil stiffness on the numerical analysis of the tunnel construction. *Géotechnique*, 47(3):693–712.

Al-Khafaji, A. and Andersland, O. (1992). Equations for compression index approximation. *J Geotech Eng ASCE*, 118(1):148–153.

Alpan, I. (1970). The geotechnical properties of soils. *Earth-Science Reviews*, 6:5–49.

Amar, S., Clarke, B., Gambin, M., and Orr, T., editors (1991). *The application of pressuremeter test results to foundation design in Europe. Part 1: Predrilled pressuremeters/self-boring pressuremeters*. Balkema, Rotterdam.

Athanasopoulos, G. A. (1995). Empirical correlations vs-nspt for soils of greece: a comparative study of reliability. In Cakmak, A., editor, *7th Int Conf on Soil Dynamics and Earthquake Engineering*, pages 19–36, Chania, Crete.

Atkinson, J. and Sallfors, G. (1991). Experimental determination of soil properties. In *Proc. 10th ECSMFE*, volume 3, pages 915–956, Florence, Italy.

Azzouz, A., Krizek, R., and Corotis, R. (1976). Regression analysis of soil compressibility. *Soils and Foundations*, 16(2):19–29.

Baldi, G., Bellotti, R., Ghionna, V., Jamiolkowski, M., and Lo Presti, D. (1989). Modulus of sands from cpts and dmts. In *Proc. 12th International Conference on Soil Mechanics and Foundation Engineering*, volume 1, pages 165–170, Rio de Janeiro, Brazil. Balkema, Rotterdam.

Baldi, G., Bellotti, R., Ghionna, V., Jamiolkowski, M., Marchetti, S., and Pasqualini, E. (1986). Flat dilatometer tests in calibration chambers. In *In Situ 86, ASCE Spec. Conf. on "Use of In Situ Tests in Geotechn Engineering"*, volume GSP 6, pages 431–436. ASCE.

Begemann, H. (1974). General report for central and western europe. In *European Symp. on Penetration Testing*, Stockholm, Sweden.

Belotti, R., Ghionna, V., Jamiolkowski, M., Lancellotta, R., and Manfredini, G. (1986). Deformation characteristics of cohesionless soisl in in situ tests. In ASCE, editor, *In Situ 86, Geotechnical Special Publications*, pages 47–73, New York. ASCE.

Benz, T. (2007). *Small-strain stiffness of soils and its numerical consequences*. Phd, Universitat Sttutgart.

Biarez, J. and Hicher, P. (1994). *Elementary mechanics of soil behaviour. Saturated remoulded soils.* Balkema, Rotterdam.

Bjerrum, L. (1972). Embankments on soft ground. In *Proc. Am.Soc. Civ Engs Specialty Conf. on Perfomence of Earth and Earth supported Structures.*, volume 2, pages 1–54, Perdue University.

Bolton, M. (1986). The strength and dilatancy of sands. *Géotechnique*, 36(1):65–78.

Bowles, J. (1997). *Foundation analysis and design*. McGraw-Hill.

Briaud, J.-L. and Gibbens, R. (1997). Large scale load test and data base of spread footings on sand. Technical Report Publication No. FHWA RD-97-068, Texas A&M University.

Brinch Hansen, J. and Lundgren, H., editors (1958). *Geoteknik*. Teknisk Forlag, Kopenhagen.

Carter, M. and Bentley, S. (1991). *Correlations of soil properties*. Penetech Press Publishers, London.

Casagrande, A. (1936). The determination of the pre-consolidation load and its practical significance. In Casagrande, A., editor, *In Proc. 1st Int Soil Mech and Found Engng Conf, 22-26 June 1936*, volume 3, pages 60–64, Cambridge, Mass. Graduate School of Engineering, Harvard University, Cambridge, Mass.

Chandler, R. (1988). The in-situ measurements of the undrained shear strength of clays using the field tests. Technical report, ASTM.

Chaudary, S., Kuwano, J., and Hayano, Y. (2004). Measurement of quasi-elastic stiffness parameters of dense toyoura sand in hollow cylinder apparatus and triaxial apparatus with bender elements. *Geotechnical Testing Journal*, 27(1):1–13.

Chen, B. and Mayne, P. (1994). Profiling the OCR of clays by piezocone tests. Technical Report Rep. No. CEEGEO-94-1, Georgia Institute of Technology.

Chen, B. and Mayne, P. (1996). Statistical relationships between piezocone measurements and stress history of clays. *Can Geotech J*, 33:488–498.

Clough, G., Briauld, J., and Hughes, J. (1990). The developement of prssuremeter testing. In *Pressuremeters, 3^{rd} Int Symp on Pressuremeters*, pages 25–45, Oxford. Thomas Telford, London.

Cudny, M. and Truty, A. (2020). Refinement of the hardening soil model within the small strain range. *Acta Geotechnica*, accepted for publication (https://doi.org/10.1007/s11440-020-00945-5).

Dalton, J. and Hawkins, P. (1982). Fields of stress - some measurements of the in-situ stress in a meadow in the Cambridgeshire countryside. *Ground Engineering*, 15(4):15–23.

D'Appolonia, D., D'Appolonia, E., and Brissette, R. (1970). Closure: Settlement of spread footing on sand. *J Soils Mechanics and Foundation Division ASCE*, 96(2):754–762.

Darendeli, M. (2001). *Development of a New Family of Normalized Modulus Reduction and Material Damping Curves*. PhD thesis, University of Texas.

Darendeli, M. and Stokoe, K. (2001). Development of a new family of normalized modulus reduction and material damping curves. Technical report, University of Texas.

Das, B. (2008). *Advanced Soil Mechanics*. Taylor & Francis, London & New York.

Dayal, I. (2006). Consolidation analyses of greater cincinnati soils. *MSc*. Technical report, University of Cincinnati.

DeGroot, D. and Sandven, R. (2004). General report: Laboratory and field comparisons. In de Fonseca, V. and Mayne, editors, *Proc. ISC-2 on Geotechnical and Geophysical Site Characterization*, pages 1775–1789, Porto, Portugal. Millpress, Rotterdam.

Demers, D. and Leroueil, S. (2002). Evaluation of preconsolidation pressure and the overconsolidation ratio from piezocone tests of clay deposits in quebec. *Can Geotech J*, 39:174–192.

Dikmen, U. (2009). Statistical correlations of shear wave velocity and penetration resistance for soils. *Journal of Geophysics and Engineering*, 6:61–72.

Duncan, J. and Buchignani, A. (1976). An engineering manual for settlement studies. Technical report, University of California.

Fahey, M. and Carter, J. (1993). A finite element study of the pressuremeter in sand using a nonlinear elastic plastic model. *Canadian Geotechnical Journal*, 30(2):348–362.

Finno, R. and Calvello, M. (2005). Supported excavations: the observational method and inverse modeling. *J Geotech Geoenv Engng ASCE*, 131(7):826–836.

Fioravante, V. (2000). Anisotropy of small-strain stiffness of ticino and kenya sands from seismic wave propagation measured in traixial testing. *Soils and Foundations*, 40(4):129–142.

Fioravante, V. (2004). General report: Enhanced characterization by combined *in situ* testing. In de Fonseca, V. and Mayne, editors, *Proc. ISC-2 on Geotechnical and Geophysical Site Characterization*, pages 1585–1596, Porto, Portugal. Millpress, Rotterdam.

FOWG (2003). Documentation de base pour la vérification des ouvrages d'accumulation aux séismes. Technical report, Swiss Federal Office for Water and Geology.

Hardin, B. and Black, W. (1969). Closure to vibration modulus of normally consolidated clays. *J Soils Mechanics and Foundation Division ASCE*, 95(6):1531–1537.

Hardin, B. and Richart Jr, F. (1963). Elastic wave velocities in granular soils. *J Soils Mechanics and Foundation Division ASCE*, 89(1):33–65.

Hasancebi, N. and Ulusay, R. (2007). Empirical correlations between shear wave velocity and penetration resistance for ground shaking assessments. *Bulletin of Engineering Geology and theEnvironment*, 66:203–213.

Hatanaka, M. and Uchida, A. (1996). Empirical correlation between penetration resistance and phi of sandy soils. *Soils and Foundations*, 36(4):1–9.

Hegazy, Y. and Mayne, P. (1995). Statistical correlations between vs and cone penetration data for different soil types. In Society, S. G., editor, *Cone Penetration Testing (CPT'95)*, volume 2, pages 173–8.

Hicher, P. (1996). Elastic properties of soils. *J Geotech Eng ASCE*, 122(8):641–648.

Hight, D., Böese, R., Butcher, A., Clayton, C., and Smith, P. (1992). Disturbance of the Bothkennar clay prior to laboratory testing. *Géotechnique*, 42(2):199–217.

Hight, D. and Leroueil, S. (2003). Characterisation of soils for engineering purposes. In Tan, T., Phoon, K., Hight, D., and Leroueil, S., editors, *Characterisation and engineering properties of natural soils*, volume 1, pages 254–360, Singapore. Swets and Zeitlinger.

Holtz, R., Jamiolkowski, M., and Lancellotta, R. (1986). Lessons from oedometer tests on high quality samples. *J Geotech Eng ASCE*, 112(8):768–776.

Hoque, E. and Tatsuoka, F. (2000). Kinematic elasticity of granula material. In *GeoEng 2000*, Melbourne.

Hoque, E. and Tatsuoka, F. (2004). Effects of stress ratio on small-strain stiffness during triaxial shearing. *Géotechnique*, 54(7):429–439.

Hough, B. (1969). *Basic soil engineering*. Ronald Press Company, New York.

Houlsby, G. and Hitchman, R. (1988). Calibration chamber tests of a cone penetrometer in sand. *Géotechnique*, 38(1):39–44.

Hryciw, R. (1990). Small-strain-shear modulus of soil by dilatometer. *J Geotech Eng ASCE*, 116(11):1700–16.

Imai, T. and Tonouchi, K. (1982). Correlation on n-value with s-wave velocity and shear modulus. 57-72.

Imai, T. and Yoshimura, Y. (1975). The relation of mechanical properties of soils to p and s-wave velocities for ground in japan. technical note. Technical report, OYO Corporation.

Iwasaki, T. and Tatsuoka, F. (1977). Effects of grains size and grading on dynamic shear moduli of sands. *Soils and Foundations*, 17(3):19–35.

Jamiolkowski, M., Ladd, C., Germaine, J., and Lancellotta, R. (1985). New developments in field and laboratory testing of soils. In *Proc. 11th ICSMFE*, volume 1, pages 57–153, San Francisco. Balkema.

Jamiolkowski, M., Lo Presti, D., and Pallara, O. (1995). Role of in-situ testing in geotechnical earthquake engineering. In *Proc. 3rd Int Conf on Recent Advances in Geotechnical Earthquake Engineering and Soil Dynamics*, volume 2, pages 1523–1546, Missouri.

Janbu, N. (1963). Soil compressibility as detrmined by oedometer and triaxial tests. In *Proc. ECSMFE*, volume 1, pages 19–25, Wiesbaden.

Jinan, Z. (1987). Correlation between seismic wave velocity and the number of blow of spt and depth. *Selected Papers from the Chinese Journal of Geotechncial Engineering (ASCE)*, pages 92–100.

Kallioglou, T., Papadopoulou, A., and Pitilakis, K. (2003). Shear modulus and damping of natural sands. In Di Benedetto, H., Doanh, T., Geoffroy, H., and Sauzeat, C., editors, *Deformation characteristics of geomatrials*, pages 401–407, Lyon. Balkema.

Karlsrud, K. (1999). General aspects of transportation infrastructure. In Barends, e. a., editor, *12th European Conf on Soil Mech and Geotech Engng*, volume 1, pages 17–30, Amsterdam. Balkema.

Kempfert, H. (2006). *Excavations and foundations in soft soils*. Springer, Heidelberg.

Kezdi, A. (1974). *Handbook of Soil Mechanics*. Elsevier, Amsterdam.

Kim, T. and Novak, M. (1981). Dynamic properties of some cohesive soils of ontario. *Can Geotech J*, 18(3):371–389.

Kokusho, T., Yoshida, Y., and Yasuyuki, E. (1982). Dynamic properties of soft clay for wide strain range. *Soils and Foundations*, 22(4):1–18.

Koppula, S. (1981). Stastical estimation of compression index. *Geotechnical Testing Journal*, 4(2):68–73.

Koppula, S. (1986). Discussion: Consolidation parameters derived from index tests. *Géotechnique*, 36(2):291–292.

Kramer, S. (1996). *Geotechnical Earthquake Engineering*. Civil Engineering and Engineering Mechanics. Prentice Hall, New Jersey.

Kulhawy, F. and Mayne, P. (1990). Manual on estimating soil properties for foundation design. Technical report, Electric Power Research Institute.

Kuwano, R. and Jardine, R. (2002). On the application of cross-anisotropic elasticity to granular materials at very small strains. *Géotechnique*, 52(10):727–749.

Lacasse, S., Jamiolkowski, M., Lancellotta, R., and Lunne, T. (1981). In situ characteristics of two Norwegian clays. In *Proc. 10th Int Conf Soil Mech and Found Engng*, volume 2, Stockholm.

Lacasse, S. and Lunne, T. (1988). Calibration of dilatometer correlations. In *Penetration Testing 88, ISOPT-1*, volume 1, pages 539–548, Orlando, Florida.

Larsson, R. and Mulabdić, M. (1991). Piezocone tests in clay. Technical Report Report No.42, Swedish Geotechnical Institute.

Lavergne, M. (1986). *Méthodes sismiques*. Technip, Paris.

Lee, S. H. (1990). Regression models of shear wave velocities. *J Chin Inst Eng*, 13:519–32.

Lee, S.-H. (1992). Analysis of the multicollinearity of regression equations of shear wave velocities. *Soils and Foundations*, 32(1):205–214.

Leroueil, S. (1988). Tenth Canadian Geotechnical Colloquium: Recent developments in consolidation of natural clays. *Can Geotech J*, 25:85–107.

Leroueil, S., Tavenas, F., and Le Bihan, J.-P. (1983a). Propriétés caractéristiques des argiles de l'est du Canada. *Can Geotech J*, 20(4):681–705.

Leroueil, S., Tavenas, F., Samson, L., and Morin, P. (1983b). Preconsolidation pressure of champlain clays. part II. laboratory determination. *Can Geotech J*, 20(4):803–816.

Li, X. and Dafalias, Y. (2000). Dilatancyfor cohesionless soils. *Géotechnique*, 50(4):449–460.

Liao, S. and Whitman, R. (1986). Overburden correction factors for. spt in sand. *J Geotech Eng ASCE*, 112(3):373–377.

Lindeburg, M. (2001). *Civil Engineering Reference Manual for the PE Exam*. Professional Publications, Belmont, California.

Lo Presti, D. and Jamiolkowski, M. (1998). Discussion: Estimate of elastic shear modulus in holocene soil deposits. *Soils and Foundations*, 38:263–265.

Lo Presti, D., Pallara, O., Fioravante, V., and Jamiolkowski, M. (1998). Assessement of quasi-linear models for sands. In Jardine, R., Davies, M., Hight, D., Smith, A., and Stallebras, S., editors, *Pre-failure Deformation of Geomaterials*, pages 363–372, London. Thomas Telford.

Lo Presti, D., Pallara, O., Lancellotta, R., Armandi, M., and Maniscalco, R. (1993). Monotonic and cyclic loadin behaviour of two sands at small strains. *Geotechnical Testing Journal*, 16(4):409–424.

Long, M. and Shane, D. (2010). Characterization of norwegian marine clays with combined shear wave velocity and piezocone cone penetration test (cptu) data. *Can Geotech J*, 47(7):709–718.

Lunne, T., Robertson, P., and Powell, J. (1997). *Cone penetration testing in geotechnical practice*. Blackie Academic & Professional, London.

Mair, R. and Wood, D. (1987). *Pressuremeter testing. Methods and interpretation.* Butterworths, London.

Marchetti, S. (1980). In situ tests by flat dilatometer. *J Geotech Eng ASCE*, 106(3):299–321.

Marchetti, S. (1985). On the field determination of k0 in sand. discussion session no. 2a. In *XI ICSMFE*, volume 5, pages 2667–2673, San Francisco.

Marchetti, S., Monaco, P., Totani, G., and Calabrese, M. (2001). The flat dilatometer test (dmt) in soil investigations. In TC16, I. C., editor, *IN SITU 2001, Int Conf On In situ Measurement of Soil Properties*, Bali. ISSMGE.

Marcuson, W. and Wahls, H. (1972). Time effects on dynamic shear modulus of clays. *J Soils Mechanics and Foundation Division ASCE*, 98(12):1359–1373.

Masood, T. and Mitchell, J. (1993). Estimation of in situ lateral stresses in soils by cone-penetration test. *J Geotech Eng ASCE*, 119(10):1624–1639.

Mayne, P. (1980). Cam-clay predictions of undrained strength. *J Geotech Engng ASCE*, 106(GT11):1219–1242.

Mayne, P. (1988). Determining OCR in clays from laboratory strength. *J Geotech Engng ASCE*, 114(1):76–92.

Mayne, P. (2005). Versatile site characterization by seismic piezocone. In *Proc. 16th ICSMGE*, volume 2, Osaka. Millpress.

Mayne, P. (2006a). The 2nd james k. mitchell lecture: Undisturbed sand strength from seismic cone tests. *Geomechanics and Geoengineering*, 1(4):239–247.

Mayne, P. (2006b). In-situ test calibrations for evaluating soil parameters. In Tan, Phoon, Hight, and Leroueil, editors, *Characterisation and Engineering Properties of Natural Soils*, volume 3, pages 1601–1652, Singapore. Taylor & Francis Group, London.

Mayne, P. (2007). Cone penetration testing. a synthesis of highway practice. Technical report, Transportation Research Board.

Mayne, P., Barry, R. C., and DeJong, J. (2001). Manual on subsurface investigations. Technical Report Publication No. FHWA NHI-01-031, Federal Highway Administration.

Mayne, P., Coop, M., Springman, S., Huang, A.-B., and Zornberg, J. (2009). State-of-the-art paper (soa-1): Geomaterial behavior and testing. In ICSMGE, editor, *17th Int Conf Soil Mech And Geotech Engng*, volume 4, pages 2777–2872, Alexandria, Egypt. Millpress/IOS Press Rotterdam.

Mayne, P. and Kulhawy, F. (1982). $K_o - OCR$ relationship in soils. *J Geotech Engng ASCE*, 108(6):851–872.

Mayne, P. and Rix, G. (1993). Gmax-qc relationships for clays. *Geotechnical Testing Journal*, 16(1):54–60.

Meyerhof, G. (1956). Penetration tests and bearing capacity of cohesionless soils. *J Soils Mechanics and Foundation Division ASCE*, 82(SM1).

Modoni, G., Flora, A., Anh Dan, L., Macuso, C., Koseki, J., Balakrishnaier, K., and Tatsuoka, F. (1999). A simple experimental procedure for the complete characterization of small strain stiffness of gravels. In Jamiolkowski, M., Lancellotta, R., and Lo Presti, D., editors, *Pre-failure Deformation Characteristics in Geomaterials*, pages 123–130, Torino. Balkema.

Moh, Z., Chin, C., Lin, C., and Woo, S. (1989). Engineering correlations for soil deposits in taipei. *J Chinese Institute of Engineers*, 12(3):273–283.

Mróz, Z., Norris, V. A., and Zienkiewicz, O. C. (1981). An anisotropic, critical state model for soils subject to cyclic loading. *Géotechnique*, 31(4):451–469.

Nacci, V. A., Wang, A. M., and Demars, K. R. (1975). Engineering behavior of calcareous soils. In *In Civil Engineering in the Oceans III*, volume 1, pages 380–400. Am Soc Civ Eng.

Nagaraj, T. and Murthy, B. (1985). Prediction of the preconsolidation pressure and recompression index of soils. *Geotechnical Testing Journal*, 8(4):199–202.

Nakase, A. (1988). Constitutive parameters estimated by plasticity index. *J Geotech Engng ASCE*, 114(GT7):844–858.

Nakase, A. and Kamei, T. (1986). Influence of strain rate on undrained shear characteristics of k_o-consolidated cohesive soils. *Soils and Foundations*, 26(1):85–95.

NAVFAC (1986). Foundations and earth structures: Design Manual DM-7.02. Technical report, Naval Facilities Engineering Command Publications Transmittal.

Niemunis, A. and Cudny, M. (2018). Discussion on "Dynamic soil-structure interaction: A three-dimensional numerical approach and its application to the Lotung case study". Poor performance of the HSS model. *Computers and Geotechnics*, 98:243–245.

Nishida, Y. (1956). A brief note on compression index of soils. *J Soils Mechanics and Foundation Division ASCE*, 82(SM3):1027.

Ohta, H. and Goto, N. (1976). Estimation of s-wave velocity in terms of characteristic indices of soil *(in Japanese)*. *Buturi-tansa*, 29:251–261.

Ohta, T., Hara, A., Niwa, M., and Sakano, T. (1972). Elastic shear moduli as estimated from n-value. In *7th Ann. Convention of Japan Society of Soil Mechanics and Foundation Engineering*, pages 265–8.

Ohta, Y. and Goto, N. (1978). Empirical shear wave velocity equations in terms of characteristic soil indexes. *Earthquake Engineering and Structural Dynamics*, 6:167–187.

Okamoto, T., Kokusho, T., Yoshida, Y., and Kusuonoki, K. (1989). Comparison of surface versus subsurface wave source for p-s logging in sand layer. In Engineers, J. S. C., editor, *Proc. 44th Ann. Conf.*, volume 3, pages 996–7 (in Japaneese).

Pacheco-Silva, F. (1970). A new graphical construction for determination of the pre-consolidation stress of a soil sample. In *4th Brazilian Conf on Soil Mech and Found Engng*, volume 1, pages 225–232, Rio de Janeiro.

Park, J. and Koumoto, T. (2004). New compression index equation. *J Geotech Geoenv Eng ASCE*, 130:223.

Peck, R., Hanson, W., and Thornburn, T. (1974). *Foundation Engineering Handbook*. Wiley, London.

Penumadu, D., Skandarajah, A., and Chameau, J. (1998). Strain-rate effects in pressuremeter testing using a cuboidal shear device: experiments and modeling. *Can Geotech J*, 35:27–42.

Pitilakis, K., Raptakis, D., Lontzetidis, K., Tika-Vassilikou, T., and Jongmans, D. (1999). Geotechnical and geophysical description of euro-seistests, using field, and laboratory tests and moderate strong ground motions. *Journal of Earthquake Engineering*, 3(3):381–409.

Prapaharan, S., Chameau, J., and Holtz, R. (1989). Effect of strain rate on undrained strength derived from pressuremeter tests. *Géotechnique*, 39(4):615–624.

Prat, M., Bisch, E., Millard, A., Mestat, P., and Cabot, G. (1995). *La modelisation des ouvrages*. Hermes, Paris.

Rampello, S., Viggiani, G., and Amorosi, A. (1997). Small-strain stiffness of reconstituted clay compresses along constant traiaxial effective stress ratio paths. *Géotechnique*, 47(3):475–489.

Rendon-Herrero, O. (1983). Closure: Universal compression index equation. *J Geotech Engng ASCE*, 109(GT5):755–761.

Rix, G. and Stokoe, K. (1992). Correlation of initial tangent modulus and cone resistance. In *Int Symp. on Calibration Chamber Testing*, pages 351–62, Postdam. Elsevier, New York.

Robertson, P. and Campanella, R. (1983). Interpretation of cone penetration tests. part I: Sand. *Can Geotech J*, 20(4):718–33.

Sandven, R., Senneset, K., and Janbu, N. (1988). Interpretation of piezocone tests in cohesive soils. In De Ruiter, J., editor, *ISOPT-1 Penetration Testing*, pages 939–953. Balkema, Rotterdam.

Sanglerat, G. (1972). *The penetrometer and soil exploration*. Elsevier, Amsterdam.

Schanz, T. (1998). Zur modellierung des mechanischen verhaltens von reibungsmaterialien. *Mitt. Inst. fÃ¼r Geotechnik, Universitat Stuttgart, 1998*, 45.

Schanz, T. and Vermeer, P. (1998). On the stiffness of sands. In Jardine, R., Davies, M., Hight, D., Smith, A., and Stallebras, S., editors, *Pre-failure deformation behaviour of geomaterials*, pages 383–387, London. Thomas Telford.

Schanz, T., Vermeer, P., and Bonier, P., editors (1999). *Formulation and verification of the Hardening Soil model*. Beyond 2000 in Computational Geotechnics. Balkema, Rotterdam.

Schmertmann, J. (1975). Measurement of insitu shear strength. In *In-situ Measurement of Soil Properties*, volume 2. ASCE.

Schmertmann, J. (1978). Guidlines for cone penetration test, performance and design. Technical report, US Federal Highway Admininstration.

Schultze, E. and Menzenbach, E. (1961). Standard penetration test and compressibility of soils. In 5^{th} *ICSMFE*, volume 1, pages 527–532, Pari.

Schweiger, H. (2002). Benchmarking in geotechnics. part I: Results of benchmarking. part II reference solution and parametric study. Technical report, Institute for Slil Mechnaics and Foundation Engineering, Graz University of Technology.

Seed, H., Idriss, I., and Arango, I. (1983). Evauluation of liquefaction potential using field performance data. *Journal Geotechnical Engineering*, 109(3):458–482.

Senneset, K., Sandven, R., and Janbu, N. (1989). The evaluation of soil paramters from piezocone tests. *Transportation Research Record*, 1235:24–37.

Sheahan, T., Ladd, C., and Germaine, J. (1996). Rate-dependent undrained shear behavior of saturated clay. *J Geotech Eng ASCE*, 122(2):99–108.

Shibata, T. (1970). Analysis of liquefaction of saturated sand during cyclic loading. *Disaster Prevention Res. Inst. Bull.*, 13:567–70.

Shioi, Y. and Fukui, J. (1982). Application of n-value to design of foundations in japan. In *2nd ESOPT*, volume 1, pages 159–164.

Simonini, P. and Cola, S. (2000). Use of piezocone to predict maximum stiffness of venetian soils. *J Geotech Geoenv Engng ASCE*, 126(4):378–382.

Simpson, B. (1992). Retaining structures: displacement and design, 32nd Rankine Lecture. *Géotechnique*, 42(4):541–576.

Simpson, B., O'Riordan, N. J., and Croft, D. D. (1979). A computer model for the analysis of ground movements in London clay. *Géotechnique*, 29(2):149–175.

Skempton, A. (1944). Notes on the compressibility of clays. *Quarterly Journal of Geotechnical Society, London.*, pages 119–135.

Stokoe, K., Derendeli, M., Gilbertl, R., Menq, F., and Choi, W. (2004). Development of a new family of normalized modulus reduction and material damping curves. In *Int Workshop on Uncertainties in Nonlinear Soil Properties and their Impact on Modeling Dynamic Soil Response*, UC Berkley.

Sully, J. and Campanella, R. (1991). Effect of lateral stress on CPT penetration pore pressures. *J Geotech Eng ASCE*, 117(7):1082–1088.

Sykora, D. (1987). Examination of existing shear wave velocity and shear modulus correlations in soils. miscellaneous paper gl-87-22. Technical report, Department of the Army, Waterways Experiment Station, Corps of Engineers.

Tanaka, H. and Tanaka, M. (1999). Kay factors governing sample quality. In *Int Symp on Coastal Engng in Practice*, pages 57–82, Yokohama.

Teixeira, A. (1996). Projeto e execuadao de fundacoes. In *Seminario de Engenharia de Fundacoes Especiais e Geotecnica III*, volume 1, pages 33–50, Sao Paolo.

Terzaghi, K. and Peck, R. (1967). *Soil mechanics in engineering practice*. Wiley and Sons, New York.

Terzaghi, K., Peck, R., and Mesri, G. (1996). *Soil Mechanics in Engineering Practice*. Wiley, New York.

Totani, G., Marchetti, S., Monaco, P., and Calabrese, M. (1999). Impiego della prova dilatometrica (dmt) nella progettazione geotecnica. In *XX National Geotechnical Congress*, volume 1, pages 301–308, Parma.

Totani, G., Marchetti, S., Monaco, P., and Calabrese, M. (2001). Use of the flat dilatometer test (dmt) in geotechnical design. In Rahardjo, P. and Lunne, T., editors, *$IN\ SITU$ 2001 Int Conf In Situ Measurement of Soil Properties and Case Histories*, Bali, Indonesia.

Townsend, F. C., Anderson, J. B., Horta, E., and Sandoval, J. (2003). Development of deep foundations test site. Technical report, University of Central Florida.

Tromienkov, Y. (1974). Penetration testing in western europe. In *Europ. Symp. on Penetration Testing*, Stockholm, Sweden.

Truty, A. (2008). Hardening soil model with samll strain stiffness. Technical report, Zace Services Ltd.

Truty, A. and Obrzud, R. (2015). Improved formulation of the hardening soil model in the contex of modeling the undrained behavior of cohesive soils. *Studia Geotechnica et Mechanica*, 37(2):61–68.

UFC (2004). Unified facilities criteria: Soils and geology procedures for foundation design of buildings and other structures (except hydraulic structures). technical manual TM 5-818-1/AFM 88-3. Technical report, Joint Departments of the Army and Air Force USA.

Vaid, Y. and Campanella, R. (1977). Time-dependent behavior of undisturbed clay. *J Geotech Eng ASCE*, 103(7):693–709.

Vardanega, P. J. and Bolton, M. (2011). Practical methods to estimate the non-linear shear stiffness of fine grained soils. In *Int Symp on Deformation Characteristics of Geomaterials*, pages 372–379, Seoul, Korea.

Viggiani, G. and Atkinson, J. (1995). Stiffness of fine grained soil at very small strain. *Géotechnique*, 45(2):249–265.

von Soos, P. (1991). *Grundbataschenbuch. Part 4*. Ernst & Sohn, Berlin.

Vucetic, M. and Dobry, R. (1991). Effect of soil plasticity on cyclic response. *J Geotech Eng ASCE*, 117(1):89–107.

Webb, D. (1969). Settlement of structures on deep alluvial sandy sediments in duran, south africa. In Engineers, I. o. C., editor, *Conf. on In Situ Behaviour of Soil and Rock*, pages 181–188, London.

Wichtmann, T. and Triantafyllidis, T. (2004). Influence of a cyclic and dynamic loading history on dynamic properties of dry sand, part i: cyclic and dynamic torsional prestraining. *Soil Dynamics and Earthquake Eng.*, 24(2):127–147.

Wroth, C. (1984). The interpretation of in situ tests. *Géotechnique*, 34(4):449–489.

Wroth, C. and Wood, B. (1978). The correlation of index properties with some basic engineering properties of soils. *Canadian Geotechnical Journal*, 15(2):137–145.

Yoon, G., Kim, B., and Jeon, S. (2004). Empirical correlations of compression index for marine clay from regression analysis. *Can Geotech J*, 41:1213–1221.

ZACE (2010). Zsoil pc2010, user manual, soil, rock and structural mechanics in dry or partially saturated media. Technical report, ZACE Services Ltd, Software Engineering.